DEVELOPMENT OF NON-INVASIVE TECHNIQUES FOR BLADDER CANCER DIAGNOSIS AND THERAPY

A thesis presented for the degree of

Doctor of Philosophy

to the University of Dundee by

Scott Gordon Palmer B.Sc.

Division of Cancer Research

School of Medicine

Ninewells Hospital and Medical School

University of Dundee

July 2016

TABLE OF CONTENTS

LIST OF FIGURES **7**

LIST OF TABLES **11**

LIST OF EQUATIONS **12**

ACKNOWLEDGMENTS **13**

DECLARATION **15**

PUBLICATION LIST **16**

CONFERENCE PARTICIPATION **17**

SUMMARY OF RESEARCH **18**

LIST OF ABBREVIATIONS **20**

1. INTRODUCTION **22**

1.1 Introduction to bladder cancer ***22***

1.1.1 Bladder anatomy *22*

1.1.2 Bladder cancer incidence *24*

1.1.3 Diagnosis, staging and grading *25*

1.1.4 Photodynamic diagnosis and therapy *28*

1.1.5 Nuclear Matrix Protein 22 (NMP22) and other urine analysis techniques *33*

1.1.6 Diagnosis and therapy in the context of "The Hallmarks of Cancer" *34*

1.1.7 Next generation diagnosis and therapy *37*

1.1.8 Autofluorescence Spectroscopy *41*

1.1.9 Light-Oxygen Effect *56*

1.2 Light-tissue interactions ***57***

1.2.1 Scattering of light *58*

1.2.2 Absorption of light *59*

1.2.3 Energy release *63*

1.2.4 Second harmonic generation *65*

1.2.5 Modelling light tissue interactions *65*

1.3 Multi-Functional Laser Based Non-Invasive Diagnostic Systems (MLNDS) ... ***66***

1.4 Aims and objectives ***79***

2. CELLULAR FLUORESCENCE ANALYSIS **82**

2.1 Background ***82***

2.2 Methods ***84***

2.2.1 LAKK-M System *84*

2.2.2 Cuvettes *86*

2.2.3 Fluorophore Analysis *89*

2.2.4 Cell Culture *90*

2.2.5 Cell Fluorescence Analysis – Confocal Microscopy *92*

2.2.6 Cell Fluorescence Analysis – Flow Cytometry *93*

2.2.7 Cell Fluorescence Analysis – LAKK-M *94*

2.2.8 Urine Fluorescence Analysis 95

2.3 Results 96

2.3.1 Comparison of Background Fluorescence in Cuvettes 96

2.3.2 Fluorophore Fluorescence Spectroscopy 99

2.3.3 Confocal Analysis of Cell Fluorescence 105

2.3.4 Flow Cytometric Analysis of ORR 106

2.3.5 LAKK-M Cell Autofluorescence Analysis 108

2.3.6 Urine Fluorescence Analysis 114

2.4 Discussion 116

2.5 Conclusion 122

3. ORGANOID DEVELOPMENT 124

3.1 Introduction 124

3.2 Methods 126

3.2.1 Porcine bladder scaffold 126

3.2.2 Cell culture 127

3.2.3 Fluorescence spectroscopy 127

3.2.4 Confirmation of invasion 128

3.2.5 Data analysis 130

3.2.6 Second harmonic generation imaging 131

3.2.7 Classification algorithms......133

***3.3 Results*......134**

3.3.1 Fluorescence spectra......134

3.3.2 Optical redox ratio......135

3.3.3 Elastin relative to metabolic cofactors......135

3.3.4 Development of Diagnostic Algorithm......139

3.3.5 Second Harmonic Imaging......140

***3.4 Discussion*......146**

***3.5 Conclusion*......151**

4. ANALYSIS OF HUMAN TISSUE......152

***4.1 Introduction*......152**

***4.2 Methods*......156**

4.2.1 “LAKK-M” Setup......156

4.2.2 Fluorophore Fluorescence Spectroscopy......156

4.2.3 Patient Recruitment......156

4.2.4 Tissue Fluorescence Spectroscopy......157

4.2.5 Histopathology as reference standard......158

4.2.6 Data Analysis......159

***4.3 Results*......160**

4.3.1 Analysis of fluorophore contribution to tissue fluorescence *160*

4.3.2 Fluorophore analysis *165*

4.3.3 ROC calculations *167*

4.4 Discussion ***168***

4.5 Conclusion ***173***

5. LIGHT-OXYGEN EFFECT **174**

5.1 Introduction ***174***

5.2 Methods ***178***

5.2.1 Cell culture *178*

5.2.2 Laser Setup *179*

5.2.3 Irradiation of singlet oxygen sensor and cancer cells *181*

5.2.4 Detecting apoptosis *182*

5.2.5 Detecting necrosis *183*

5.3 Results ***183***

5.3.1 Singlet oxygen generation in aqueous media *183*

5.3.2 Cell death analysis by Annexin-V expression *185*

5.3.3 Cell death analysis by Trypan blue exclusion dye *186*

5.4 Discussion ***188***

5.5 Conclusion ***193***

6. TISSUE COMPUTER MODELLING 195

6.1 Introduction 195

6.2 Materials and Methods 196

6.2.1 Literature Search 196

6.2.2 Creation of tissue simulation 196

6.2.3 Experimental Comparison 198

6.3 Results 199

6.3.1 Literature Review 199

6.3.2 Monte-Carlo Modelling of photon transport in tissue 201

6.3.3 Comparison with measured fluorescence 202

6.4 Discussion 203

6.5 Conclusion 206

7. CONCLUSION AND FUTURE PERSPECTIVES 207

REFERENCES 218

LIST OF FIGURES

Figure 1 Cross-section diagram of the bladder showing major anatomical features 23
Figure 2 The main layers of the bladder wall 23
Figure 3 Diagram showing the layers of bladder tissue along with progressing stages of BCa from CIS to invasive stage T4 27
Figure 4 Diagram showing the standard technical setup for tumour PDD. Tumour area selectively accumulates PS agents, strongly fluorescing red under blue excitation. 30
Figure 5 Comparison of cystoscopic images of BCa obtained using WLC (left) and PDD (right) courtesy Cauberg Evelyne et al.[33] (reproduced with permission under a CC Attribution Non-commercial Share Alike License) 31
Figure 6 Molecular pathways following PDT leading to apoptosis. Photosensitiser (PS) excited by 405nm light enters a stable triplet state, donating energy to molecular oxygen to form singlet oxygen. Effects of singlet oxygen on mitochondria causes release of apoptotic messengers to the nucleus, leading to quiescent apoptotic cell death. 32
Figure 7 Molecular pathways following PDT leading to necrotic cell death. Photosensitiser (PS) excited by 405nm light enters excited triplet state, donating energy to form singlet oxygen and ROS. Interaction between singlet oxygen and ROS with cell membrane and lysosomal membrane, leading to membrane rupturing, necrotic cell death and release of danger signals. . 33
Figure 8 The "Hallmarks of Cancer", according to Hanahan and Weinberg[57] (reproduced with permission from Elsevier) 35
Figure 9 Comparison of TCC of urinary bladder imaged using WLC (left) and NBI (right) courtesy Cauberg Evelyne et al.[33] (reproduced with permission under a CC Attribution Non-Commercial Share Alike License) 39
Figure 10 Emission profiles of the most common endogenous fluorophores under 366nm excitation (reproduced with permission under Creative Commons attribution non-commercial license, courtesy Croce et al.[180]) 51
Figure 11 Cross section of the urinary bladder showing the main layers and related fluorophores (adapted from Wikiwand and included under a public domain license) 52
Figure 12 Molecular and cellular consequences of the Warburg Effect, adapted partially from text by Vander Heiden et al.[187] and text and figures by Chiarugi et al.[188]. Glycolytic switch in cancer cells causes a shutdown of the electron transport chain and an accumulation of NADH.54
Figure 13 Fates of light entering tissue: light can either be scattered (A), for instance by cellular components such as nuclei; absorbed (B), for instance by hemoglobin, water and tissue fluorophores; or transmitted through full tissue (C) 57
Figure 14 Jablonski diagram denoting the absorption of light by a molecule (purple arrow) and energy release (blue arrow) 59
Figure 15 Absorption spectra of NAD+ (solid black line) and reduced counterpart NADH (dashed black line) between 240-360nm (courtesy Cronholm114 via Wikipedia.org, reproduced through public domain access (By Cronholm144 - Own work, Public Domain, https://commons.wikimedia.org/w/index.php?curid=3258108)) 60
Figure 16 Electromagnetic spectrum showing the wavelengths of UV and visible light (reproduced freely under CC-BY license, courtesy Philip Ronan via commons.wikimedia.org (https://commons.wikimedia.org/wiki/File:EM_spectrum.svg)) 61
Figure 17 Diagram of the "Tissue Optical Window" displaying absorption of light by oxygenated blood (cyan line), deoxygenated blood (red line) and water (blue line) between the wavelength range of 600-1100nm (reproduced with permission from Nature Publishing Group, courtesy Phan & Bullen, 2010[200] 63
Figure 18 Range of commercially available lasers, reproduced freely under a CC-BY-SA license (original figure created by Danh, via Wikipedia.org: https://en.wikipedia.org/wiki/Laser#/media/File:Commercial_laser_lines.svg) 68

Figure 19 Experimental setup of the LAKK-M system 69
Figure 20 Layout of the LAKK-M optical probe including the source and detector fibres: (2.1) Green laser; (2.2) UV laser; (2.3) NIR laser; (2.4) Blue laser; (2.5) Red laser; (2.6) LDF detector; (2.7) TRO detector; (2.8) LDF detector; (2.9) AS detector. Separation distance between fibres = 1mm, diameter of each fibre = 100µm (120µm including cladding). NA for each fibre = 0.22. 71
Figure 21 Annotated screenshot of the LAKK-M spectrometer showing back-scattered laser light, fluorescence across 380-820nm and the measured parameters of fluorescence intensity for each fluorophore. 73
Figure 22 Example of a fluorescence spectrum recorded from the finger under UV excitation at 365nm 74
Figure 23 Example of a fluorescence spectrum recorded from the finger under blue excitation (450nm)... 74
Figure 24 Fluorescence spectrum recorded from finger tissue excited using green light (535nm) 75
Figure 25 Fluorescence spectrum recorded from finger tissue excited using red light (633nm) 75
Figure 26 Annotated screenshot of the LDF and TRO channel of the LAKK-M, including measured graphs and recorded values for index of microcirculation (perfusion), tissue oxygenation and relative blood volume 78
Figure 27 Experimental setup including LAKK-M system, attached laptop and cuvette........... 86
Figure 28 Cuvette types used for comparison: (a) conventional clear plastic cuvette; (b) 3D printed matte black cuvette; (c) custom made matte black cuvette... 88
Figure 29 Setup of custom black cuvette on Gilson LabStir containing magnetic stir bar......... 88
Figure 30 Cuvette setup for fluorophore and cell analysis: (a) solutions are pipetted into the top of the empty cuvette; (b) the stainless steel lid is screwed into place; (c) the optical probe of the LAKK-M device is placed into the holder in the lid.. 90
Figure 31 Background fluorescence recorded from standard plastic cuvette (black line), 3D printed cuvette (red line) and custom built cuvette (blue line) under UV (a), blue (b), green (c) and red excitation (d). 97
Figure 32 PBS fluorescence measured in standard plastic cuvette (black line), 3D printed cuvette (red line) and custom built cuvette (blue line) under UV (a), blue (b), green (c) and red (d) excitation. 98
Figure 33 Figure 34 Background fluorescence measured from empty cuvette (black line) and cuvette containing magnetic stir bar (red line) under UV (a), blue (b), green (c) and red (d) excitation.. 99
Figure 34 Fluorescence intensity of 1M solutions of tryptophan (a) and 1M tyrosine (B) in PBS measured under UV excitation (black line), blue excitation (blue line), green excitation (green line) and red excitation (red line). 100
Figure 35 Fluorescence spectra of 1M NADH (a) and 1M flavin (b) under UV (black line); blue (blue line); green (green line) and red excitation (red line) 100
Figure 36 1M PpIX fluorescence under UV (black line); blue (blue line); green (green line) and red (red line) excitation 101
Figure 37 Fluorescence measured from flavin solutions under blue (450nm) excitation. Black line depicts a 3.75uM solution, red line depicts a 7.5uM solution and blue line depicts a 15uM solution... 103
Figure 38 Fluorescence spectra of 1M NADH (black line), 1M flavins (red line) and a 50:50 mix of NADH and flavins (blue line) under uv (a) and blue (b) excitation............................. 104
Figure 39 Chart of ORR values measured at increasing NADH: Flavin ratios with flavins measured at ex365em550 (black line), ex450em510 (red line) and ex450em550 (blue line) .. 105
Figure 40 Confocal Microscopy images from bladder cancer cells showing localisation of (a) MitoTracker Red, (b) NADH and (c) flavins.. 106

Figure 41 Bivariate dot plots of (A, top row) healthy bladder and (B, bottom row) bladder cancer cells measured in triplicate, charting cellular content of NADH (x-axis) and flavins (y-axis) showing differences between population distributions 107
Figure 42 Comparison of ORR mean +/- SEM for healthy bladder cells (pale shaded) and bladder cancer cells (dark shaded). ORR measured as ex360em425-475/ex488em515-545. .. 108
Figure 43 Cell fluorescence averaged from 5 measurements of 10^6 cells: cells (black line) under UV excitation (a) overlaid with NADH (blue line) and flavins (red line); cells under blue excitation (b) overlaid with flavins (red line); cells under green excitation (c); cells under red excitation (d) overlaid with porphyrins (red line). 109
Figure 44 Fluorescence spectra of 15 separate measurements of cellular fluorescence from individually prepared bladder cancer cells under UV excitation, showing signal variability... 110
Figure 45 Fluorescence spectra of 15 separate measurements of cellular fluorescence under blue excitation showing signal variability 111
Figure 46 Dose dependence of bladder cancer cell spectra using UV (a) and blue (b) excitation at concentrations ranging from 1.25 x 10^6 to 1 x 10^7 cells/ml in PBS 111
Figure 47 ORR mean +/- SEM values measured from bladder cancer (pale shaded) and healthy bladder (dark shaded) cells. ORR measured as ex365em490/ex450em550 112
Figure 48 Scatter diagram charting ORR values of repeated measures from bladder cancer cells calculated in 3 ways (ex365em490/ex365em550 (“UV”); ex365em490/ex450em510 (“Blue”); ex365em490/ex450em550 (“Blue 550”)) 113
Figure 49 Average +/- SEM ORR values of bladder cancer cells measured at 5 minute intervals up to 35 minutes following initial measurement (ORR measured as ex365em490/ex365em550). 114
Figure 50 Spectra recorded from urine on days 1, 2 and 3 (black, red and blue lines) measured using UV (a) and blue excitation (b).. 115
Figure 51 comparison of the UV (a) and blue fluorescence (b) of PBS (black line); total urine fluorescence average (red line); urine cells in PBS (blue line) and average urine without cells (green line) 115
Figure 52 Fluorescence under UV (a) and blue excitation (b) arising from PBS (black line); 12.5% urine in PBS (red line); 25% urine in PBS (blue line); 50% urine in PBS (green line) and 100% urine (magenta line)... 116
Figure 53 Diagrams of fluorescence spectroscopy using the LAKK-M system (a) and conventional spectrofluorimetry (b)... 121
Figure 54 Experimental setup of organoid measurement showing cross-section (A) and top-down view (B) of optical probe (1) touched to urothelial surface (2) overlaying connective tissue (3) and muscle layer (4) 127
Figure 55 H & E stained sections of control (A), attachment of cancer cells (B) and invasion of cells into tissue (C) with tissue scaffold and cancer cell labelled as appropriate..................... 129
Figure 56 Comparison of H & E stained human healthy tissue (A) with organoid control (B) and human TCC (C) with cancer organoid (D) 129
Figure 57 General setup of confocal imaging system used to generate SHG images, showing combination of SHG signal at 440nm with transmitted light at 488nm. 133
Figure 58 Sectioning of SHG image to remove background signal and include areas of strong SHG signal for analysis (image generated as montage of fields of view from one healthy sample)... 133
Figure 59 Average UV spectra of control (orange line) and organoid (blue line) on days 0 (A) and 21 (B). Orange and blue lines on A represent n = 10; orange line on B represents n = 7; blue line on B represents n = 10. 134
Figure 60 Day to day variations in elastin fluorescence measured from samples at ex365em450. Black line depicts control average (n = 10 on days 0 &1, n = 9 on days 4, 7, 11 & 14, n = 7 on

days 18 & 21), red line depicts organoid average (n = 10 on each day). Error bars depict standard error of the mean (SEM)....... 136
Figure 61 Day to day variations in NADH fluorescence measured from samples at ex365em490. Black line depicts control average (n = 10 on days 0 &1, n = 9 on days 4, 7, 11 & 14, n = 7 on days 18 & 21), red line depicts organoid average (n = 10 on each day). Error bars depict standard error of the mean (SEM)....... 137
Figure 62 Day to day variation in flavin fluorescence measured from samples at ex365em550. Black line depicts control average (n = 10 on days 0 &1, n = 9 on days 4, 7, 11 & 14, n = 7 on days 18 & 21), red line depicts organoid average (n = 10 on each day). Error bars depict standard error of the mean (SEM)....... 137
Figure 63 Average ORR values for control (solid line) and bladder cancer organoid (dashed line) across the 21 day measurement period (+/- SEM). Organoid n = 10 on each day. Control n = 10 on days 0 & 1, n = 9 on days 4, 7, 11 & 14 and n = 7 on days 18 & 21....... 138
Figure 64 Average elastin/NADH ratios for control (solid line) and cancer organoids (dashed line) across the 21 day study (+/- SEM). Organoid n = 10 on each day. Control n = 10 on days 0 & 1, n = 9 on days 4, 7, 11 & 14 and n = 7 on days 18 & 21. 138
Figure 65 Average elastin/flavins ratios for control (solid line) and cancer organoids (dashed line) across the 21 day measurement period (+/- SEM). Organoid n = 10 on each day. Control n = 10 on days 0 & 1, n = 9 on days 4, 7, 11 & 14 and n = 7 on days 18 & 21....... 139
Figure 66 ROC curves for ORR (A) and elastin/NADH (B) values....... 140
Figure 67 Screenshot of diagnostic interface showing measured parameters of AUC, ORR and elastin/NADH along with tissue classification 140
Figure 68 Merged SHG + transmitted light of control sample slide showing connective tissue and urothelium 142
Figure 69 Combined SHG + Transmitted light image of control sample slide showing connective tissue and muscle 143
Figure 70 Combined SHG + Transmitted light image of cancer organoid slide showing bladder cancer cells adhering and invading into tissue scaffold 144
Figure 71 Bar charts depicting mean +/- SEM for energy (A), entropy (B), contrast (C), correlation (D), average brightness (E) and pixel ratio (F) comparing control with organoid (in each case, healthy n = 24, cancer n = 29) 145
Figure 72 Screenshot of MATLAB diagnostic interface designed to classify images based on measured GLCM parameters 146
Figure 73 Cross section of tissue fluorescence measurement showing optical probe (1) containing individual excitation and detection fibres, in contact with the mucosal surface of biopsy tissue (2) held in matte black cuvette (3)....... 158
Figure 74 Comparison between healthy average (solid black line, n = 33) and cancer average (dashed black line, n = 89) under UV excitation (a) and red excitation (b). Figure 74a overlaid with spectra from 1M NADH (solid red line) and 1M FAD (dotted red line). Figure 74b overlaid with 1M protoporphyrin IX (solid red line) 162
Figure 75 Comparison of healthy tissue fluorescence spectra (black line, n = 33) compared to cancer average (red line, n = 89) and cancer samples broken down into CIS (blue line, n = 6), TCC (magenta line, n = 76) and SCC (orange line, n = 7) 162
Figure 76 Average spectra +/- SD for healthy tissue (blue line +/- blue shading, n = 33) and cancer tissue (orange line +/- orange shading, n = 89) under UV (a) and red excitation (b).... 163
Figure 77 Average fluorescence spectra of healthy bladder tissue (black line, n = 32) and bladder cancer tissue (red line, n = 89) excited using green (532nm) laser....... 164
Figure 78 Average fluorescence spectra +/- SD values for healthy (blue line +/- blue shading, n = 32) and cancer (orange line +/- orange shading, n = 89) under green excitation. 165

Figure 79 Bar charts depicting mean +/- SEM for UV ORR (a); porphyrin amplitude of fluorescence (b) and NADH/porphyrin ratio (c) for healthy (white bars) and cancer (light grey bars). 166
Figure 80 Mean +/- SEM values for integrated fluorescence intensity under green (532nm) excitation for healthy tissue (pale grey, n = 32) and bladder cancer tissue (dark grey, n = 89) 167
Figure 81 ROC curves for UV ORR (a), UV ORR healthy vs CIS (b), porphyrin (c) and NADH/porphyrin ratio (d), including AUC values 168
Figure 82 Basic experimental setup of laser showing laser diode connected to lensing apparatus via optical fibre 180
Figure 83 Laser schematic showing optical fibre, diverging lens and neutral density filter. Approximate beam diameter at sample = 20mm 180
Figure 84 Fluorescence spectra of 1uM solution of ADPA measured using UV excitation following preparation (black line) and following 30 minutes (red line) and 60 minutes on bench without irradiation (blue line) 184
Figure 85 ADPA fluorescence recorded at 365nm excitation for 1ml ADPA solution irradiated for increasing periods 185
Figure 86 Confocal microscopy of cells stained with MitoTracker Green (green) and Annexin V-APC (red): (A) non-irradiated control; (B) sample irradiated for 10 minutes; (C) sample irradiated for 20 minutes; (D) sample irradiated for 30 minutes 186
Figure 87 Average +/- Standard deviation values for cell viability in control (blue) and following 10 minute irradiation at 200mW optical power (orange), 300mW optical power (grey) and 400mW optical power (yellow) 187
Figure 88 Temperature increase in media irradiated for 4 minutes using 1268nm laser with set optical power of 100mW (black line), 200mW (red line), 300mW (blue line) and 400mW (green line). Lines represent average of 3 measurements each. 187
Figure 89 Average +/- standard deviation values of cell viability for control (blue), for cells submerged for 10 minutes in a 42oC water bath (orange) and for cells irradiated for 10 minutes using 400mW optical power (grey) 188
Figure 90 Optical model of bladder tissue generated in TracePro: (a) cross section of tissue; (b) 3D simulation 202
Figure 91 Comparison of the measured UV fluorescence (black line) with theoretical fluorescence simulated from TracePro model (dotted black line) 203

LIST OF TABLES

Table 1 BCa grades and descriptions 26
Table 2 BCa stages and descriptions 26
Table 3 Common endogenous tissue fluorophores (courtesy Wikipedia.org) 42
Table 4 Wavelength, source and optical power of the lasers used by the LAKK-M system 70
Table 5 Excitation sources on the LAKK-M for AS 72
Table 6 Relative NADH concentrations used to measure ORR using LAKK-M system 89
Table 7 Wavelengths at which metabolic fluorophores were studied (excitation and emission) using the LAKK-M 95
Table 8 Common tissue fluorophores measured using the LAKK-M system 130
Table 9 Parameters derived from GLCM 132
Table 10 Examples of effects of optical power and irradiation period on delivered dose 181
Table 11 Optical properties of human bladder tissue 199
Table 12 Optical properties of porcine bladder tissue 200

Table 13 Parameters used for the generation of each layer in the Monte Carlo model, including thickness, coefficient of absorption, coefficient of scattering, anisotropy, fluorophore type, coefficient of fluorophore absorption, fluorophore optical cross section and molar extinction coefficient, ... 201

LIST OF EQUATIONS

Equation 1 Calculation of the optical redox ratio (ORR) ... 53
Equation 2 Calculation of dose applied to sample ... 181
Equation 3 Calculation of tissue absorption of light using Beer-Lambert law ... 197
Equation 4 Scattering phase function using Henyey-Greenstein function ... 197
Equation 5 Probability distribution ... 197
Equation 6 Coefficient of absorption ... 198
Equation 7 Path length before absorption ... 198

ACKNOWLEDGMENTS

The list of people to whom I owe thanks is far too long to detail in these pages. I am grateful to have worked with so many special people and to have made a number of friends during my years writing this thesis.

First and foremost, I would like to dedicate this thesis, and any promising findings within it, to my mother, Katie Palmer, who passed away during the writing of this work. My mother and father, John, have always supported me in all of my endeavours and encouraged me to always do my best, do what makes me happy and to treat others well. It is due to their tireless support that I have been in the position to undertake this research and see it through. Thank you both for everything, a son could not have wished for better parents.

To my wonderful partner, Lizzie, without whom I never would have completed this work: thank you for being so patient, loving and understanding, especially when I was still proof-reading manuscripts or checking emails at 2 a.m. Thank you for always reminding me that this was a marathon, that I should pace myself. I would have burned out a long time ago without you by my side.

To my primary supervisor Professor Ghulam Nabi, I will never forget the help and support you have provided me, especially during some very difficult times. Thank you for having the faith in me to allow me to grow as an independent thinker and achieve so much in these four years. I'm glad to have been able to share in these successes together. To Dr David McGloin, thank you for helping this biologist traverse the tricky world of photonics and for your invaluable feedback on so many pieces of written work, including this thesis. To Professor Edik Rafailov and the photonics and nanoscience group, thank you for stimulating my interest in biophotonics from the very beginning.

Particularly, to Dr Andrey Dunaev and Dr Karina Litvinova, thank you both for these years of friendship and successful collaboration, and for sharing with me your expertise, experience and sense of humour. Last, but by no means least, to Mike Groves, thank you for your now famous pep-talks. Nothing cheered me up more after a failed experiment than bumping into you in the lab. I hope you are sincerely considering a secondary career as a motivational speaker!

To everyone on this list, and the countless others I have met over the years, thank you from the bottom of my heart for your help and support to complete this huge project, I honestly would have been lost without you.

DECLARATION

I, Scott Gordon Palmer, certify that this thesis has been written by me as a record of work carried out by me, that it has not been submitted in any previous application for a higher degree and that all references cited have been consulted by me. Chapter 6 (Tissue computer modelling) is a record of relevant joint research, to which I contributed to tissue preparation, literature review, spectrophotometry, fluorescence spectroscopy and manuscript preparation.

Signature of candidate……………………. Date……………….

I confirm that Scott Palmer has completed the minimum period of registration for full-time study at the University of Dundee and has fulfilled the conditions of the University of Dundee, thereby qualifying him to submit his thesis in application for the degree of Doctor of Philosophy.

Signature of supervisor………………….. Date………………..

PUBLICATION LIST

2016

Palmer, S., Litvinova, K., Dunaev, A., Ji, Y., McGloin, D. & Nabi, G., "Optical redox ratio and endogenous porphyrins in the detection of urinary bladder cancer: a patient biopsy analysis", J. Biophotonics (October 2016) epub ahead of print, doi: 10.1002/jbio.201600162

Ling, Y., Li, C., Feng, K., Palmer, S., Appleton, P. L., McGloin, D., Huang, Z. & Nabi, G., "Second harmonic generation (SHG) imaging of microstructural heterogeneity in ultrasound guided biopsies of prostate in men with suspected prostate cancer", J. Biophotonics (August 2016) epub ahead of print, doi: 10.1002/jbio.201600090

Palmer, S., Litvinova, K., Dunaev, A., Fleming, S., McGloin, D. & Nabi, G., "Changes in autofluorescence based organoid model of muscle invasive urinary bladder cancer", Biomed. Opt. Express **7**(4), 1193-1200 (April 2016)

2015

Belotti, Y., Conneely, M., Palmer, S., Huang, T., Campbell, P., McKenna, S., Nabi, G. & McGloin, D., "Hydrodynamic stretching for prostate cancer detection", Proc. SPIE 9518 (June 2015)

Dunaev, A., Dremin, V., Zherebtsov, E., Rafailov, I., Litvinova, K., Palmer, S., Stewart, N., Sokolovski, S. & Rafailov, E., "Individual variability analysis of fluorescence parameters measured in skin with different levels of nutritive blood flow", Med. Eng. Phys. **37**(6), 574-583 (April 2015)

Palmer, S., Litvinova, K., Rafailov, E. & Nabi, G., "Discrimination of healthy and cancer cells of the bladder by metabolic state, based on autofluorescence", Proc. SPIE 9303:93030T-1 (March 2015)

Palmer, S., Litvinova, K., Rafailov, E. & Nabi, G., "Detection of urinary bladder cancer cells using redox ratio and double excitation wavelengths autofluorescence", Biomed. Opt. Express **6**(3), 977-86 (March 2015)

Rafailov, I., Palmer, S., Litvinova, K., Dremin, V., Dunaev, A. & Nabi, G., "A novel excitation-emission wavelength model to facilitate the diagnosis of urinary bladder diseases", Proc. SPIE 9303 (February 2015)

2014

Dunaev, A., Sidorov, V., Krupatkin, A., Rafailov, I., Palmer, S., Stewart, N., Sokolovski, S. & Rafailov, E., "Investigating tissue respiration and skin microhaemocirculation under adaptive changes and the synchronisation of blood flow and oxygen saturation rhythms", Physiol. Meas. **35**(4), 607-21 (April 2014)

2013

Palmer, S., Sokolovski, S., Rafailov, E. & Nabi, G., "Technologic developments in the field of photonics for the detection of urinary bladder cancer", Clin. Genitourin. Cancer **11**(4), 390-6 (December 2013) (Review paper)

CONFERENCE PARTICIPATION

Palmer, S., “Organoid model for the diagnosis of urinary bladder cancer”, British Association of Urological Surgeons annual meeting, Royal College of Surgeons, London, UK, December 2015 (Contributed talk)

Palmer, S., “Autofluorescence flow cytometry for voided urine cytology”, British Association of Urological Surgeons annual meeting, University of Cambridge, Cambridge, UK, January 2014 (Contributed talk)

Palmer, S., “Autofluorescence spectroscopy for bladder cancer detection”, “Physics meets biology” summer school, Hersonissos, Greece, October 2013 (Poster presentation)

Palmer, S., “Multi-functional laser system for disease diagnosis”, “Photonics as an enabling technology” conference, Aston University, Birmingham, UK, September 2013 (Poster presentation)

SUMMARY OF RESEARCH

Bladder cancer is among the most common cancers in the UK, responsible for significant patient morbidity. Current techniques for detection suffer from low sensitivity, particularly for early stage disease, therefore new techniques are urgently sought.

Among the suggested techniques to augment bladder cancer detection is the use of autofluorescence spectroscopy. Autofluorescence arises from a number of molecules in human tissue, giving a wealth of structural and metabolic information. Autofluorescence spectroscopy has previously been applied to the detection of a wide range of cancers, however clinical implementation of the technique to bladder cancer diagnosis is inhibited by a poor understanding of the contributions of individual fluorophores to autofluorescence. I sought primarily to use the multi-functional laser based diagnostic system “LAKK-M” to study the autofluorescence profiles of bladder cancer at the cell and tissue level, with the aim of developing a better understanding of bladder autofluorescence characteristics in health and disease. The significant findings of this research are threefold:

1. Autofluorescence flow cytometry of cell optical redox ratio reveals metabolic abnormalities in bladder cancer cells, specifically a glycolytic switch in bladder cancer cells culminating in an increased optical redox (NADH/flavin, ex360em425-475/ex488em515/545) ratio relative to healthy bladder cells.
2. Lab grown bladder cancer organoids show progressive changes in autofluorescence ratios relative to control samples – specifically reductions in the NADH/flavin (ex365em490/ex365em550), elastin/NADH (ex365em450/ex365em490) and elastin/flavin ratio

(ex365em450/ex365em550), suggestive of structural and metabolic changes in developing cancer.

3. Analysis of human bladder tissue reveals significant differences in key fluorophores and diagnostic ratios between healthy and cancer tissue, amounting to increased porphyrin fluorescence and a decreased optical redox ratio (ex365em490/ex365em550) in cancer tissue compared to healthy control.

These findings better inform our understanding of the autofluorescence properties of the bladder in health and disease at both the cell and tissue level, contributing to future development of diagnostic techniques. Additionally, in this thesis, I discuss the diagnostic worth of collagen analysis in bladder cancer using second harmonic generation imaging, the application of bladder tissue computer simulation to better elucidate fluorophore properties, and progress in novel laser therapy techniques for bladder cancer. The ultimate goal of this research is the development of a combined laser-based system for bladder cancer diagnosis and therapy.

LIST OF ABBREVIATIONS

5-ALA – 5-aminolaevulinic acid

ADPA – Anthracene 9,10 dipropionic acid

Af – Amplitude of fluorescence

AS – Autofluorescence spectroscopy

ATP – Adenosine triphosphate

AU – Arbitrary units

AUC – Area under the curve

BCa – Bladder cancer

BTA – Bladder tumour antigen

CCD – Charge coupled device

CIS – Carcinoma in situ

DMEM – Dulbecco’s modified eagle medium

ECM – Extracellular matrix

EDTA – Ethyldiaminetetraacetic acid

EPR – Enhanced permeability and retention

FAD – Flavin adenine dinucleotide

FBS – Fetal bovine serum

FISH – Fluorescence in-situ hybridisation

GLCM – Grey level co-occurrence matrix

H & E – Haematoxylin and eosin

HAL – Hexaminolaevulinate

HUC – Human urothelial cell

Il-6 – Interleukin 6

Kf – Coefficient of fluorescence

LDF – Laser Doppler flowmetry

LED – Light emitting diode

LOE – Light-oxygen effect

MIBC – Muscle invasive bladder cancer

MLNDS – Multi-functional laser-based non-invasive diagnostic system

MMP – Matrix metalloproteinase

MPM – Multi-photon microscopy

NADH – Reduced nicotinamide dinucleotide

NBI – Narrow band imaging

NIR – Near infra-red

NMIBC – Non-muscle invasive bladder Cancer

NMP22 – Nuclear matrix protein 22

NRES – National research ethics service

OCT – Optical coherence tomography

ORR – Optical redox ratio

PBS – Phosphate buffered saline

PDD – Photodynamic diagnosis

PDT – Photodynamic therapy

PIS – Participant information sheet

PMT – Photomultiplier tube

PpIX – Protoporphyrin 9

PS – Photosensitiser

QD – Quantum dot

ROC – Receiver operating characteristic

ROS – Reactive oxygen species

SCC – Squamous cell carcinoma

SEM – Standard error of the mean

SHG – Second harmonic generation

TASC – Tayside medical science centre

TCC – Transitional cell carcinoma

TRO – Tissue reflectance oximetry

TURBT – Transurethral resection of bladder tumour

UV – Ultraviolet

VUC - Voided urine cytology

WLC - White light cystoscopy

1. INTRODUCTION

1.1 Introduction to bladder cancer

1.1.1 Bladder anatomy

The human urinary bladder is the organ responsible for storage and excretion of human waste products in the form of urine. Anatomically, it consists of walls of functional detrusor muscle surrounding a trigone area containing the urethral opening. Alongside the urethral opening are two ureteric orifices. The ureteric orifices transport urine produced by the kidneys to the bladder for storage. Upon bladder emptying, the detrusor muscles contract, pushing urine through the urethral sphincter and out through the urethra. Due to the physiological nature of the bladder in the storage of urine, it has immense contractile and expansive properties, afforded by the bladder rugae (series of internal folds). The structure of the bladder is detailed below in Fig.1.

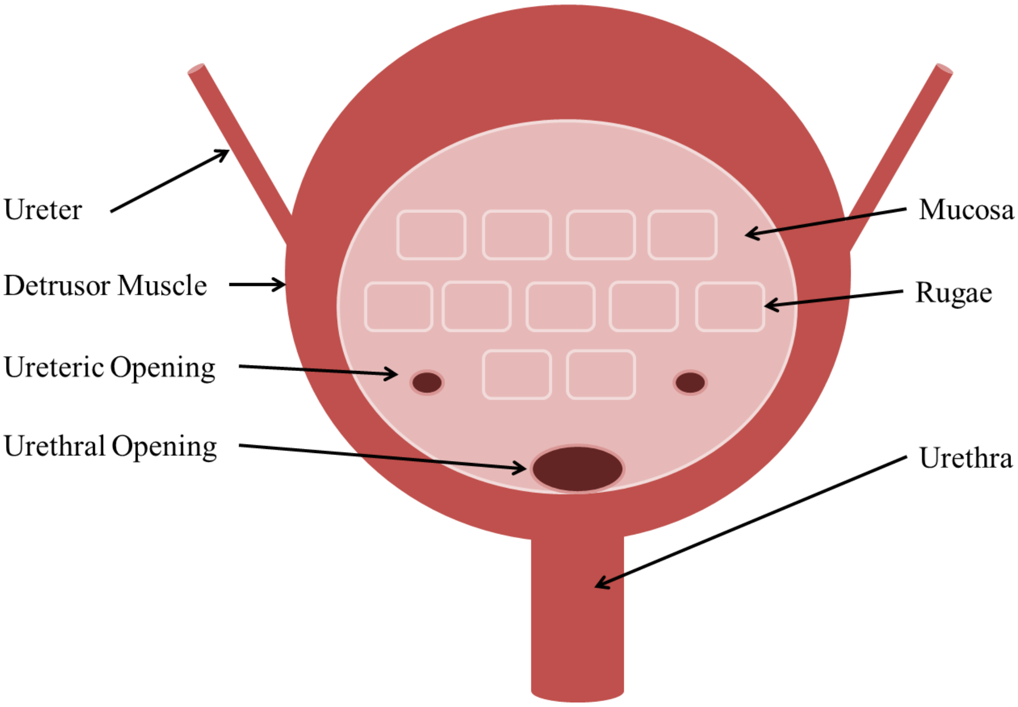

Figure 1 Cross-section diagram of the bladder showing major anatomical features

On a tissue level, the bladder is composed of three main layers: the mucosal layer, containing the transitional epithelium/urothelium; submucosa, containing blood vessels and the underlying connective tissue of the lamina propria; and the muscular layer, containing the detrusor muscle which forms the main bladder wall (Fig.2).

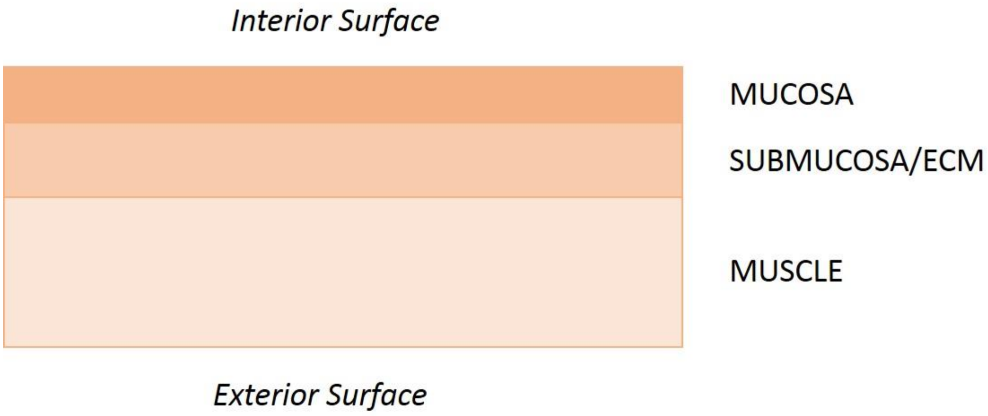

Figure 2 The main layers of the bladder wall

The role of the muscle layer is to promote bladder constriction upon voiding, while the urothelium is crucial for its function in maintaining a barrier between the tissue and the outside world. The urothelium is similar to many other epithelial cell types in similar locations in contact with the outside world - such as the oral cavity – however it displays high elasticity to allow for the contractive and expansive properties of the bladder. Due to its location, the transitional cells which make up the urothelium are repeatedly exposed to toxins and potential pathogens on a day-to-day basis, leaving the bladder susceptible to infection, inflammation and malignant transformation.

1.1.2 Bladder cancer incidence

Bladder cancer (BCa) is among the most common cancers worldwide. In the UK, 10,341 new BCa diagnoses are made each year, making it the 9th most common cancer in the UK, 4th most common in men[1]. Of the new cases of BCa reported each year, some 90% affect the transitional cells of the urothelium, referred to as transitional cell carcinoma (TCC). The remaining 10% of diagnosed BCa cases consist primarily of squamous cell carcinomas (much more common in developing countries)[2] and adenocarcinoma[3]. The 10 year survival rate of bladder cancer is around 50% and decreases with age (all incidence and mortality statistics taken from Cancer Research UK[1]). There are a number of risk factors suggested and proven to play significant roles in the development of BCa, including gender[4,5] and race[5]. Cigarette smoking in particular has been demonstrated as an important prognostic factor in BCa development[5,6] and shown to have an effect on disease recurrence and progression[7]. BCa risk is also known to be associated with occupation[8] - possibly due to exposure to chemicals such as polycyclic aromatic hydrocarbons (PAHs)[9] – risk is also associated with incidence of diabetes (in men)[10]. Toxins contained in cigarette smoke and PAHs are excreted in the urine – therefore the bladder, particularly the transitional cells at the luminal surface, as an interface with these toxins represents a common target for mutagenic effects and malignant transformation.

1.1.3 Diagnosis, staging and grading

The gold standard methods for diagnosing BCa are as follows: patients presenting with pain and haematuria (blood in their urine) submit urine samples for voided urine cytology (VUC) by a trained pathologist[11]. VUC involves microscopic examination of slides containing urothelial cells shed in the urine, allowing pathologists to identify cellular abnormalities such as nuclear enlargement. Patients with positive urine cytology are scheduled for a routine cystoscopic examination using a fibre optic white light source, allowing the consultant to view inside the bladder for suspicious areas and lesions. This process, known as white light cystoscopy (WLC), is the most commonly used modality. Furthermore, WLC can be used in conjunction with surgical techniques to remove suspicious tissue by a process called trans-urethral resection of bladder tumour (TURBT). The tissue removed during TURBT is then sent to expert pathologists for detailed staging and grading.

Of the ~9500 cases of TCC identified in the UK each year, some 75-80% will be classified as non-muscle-invasive bladder cancer (NMIBC), meaning the tumour, which has arisen in the urothelium, has not penetrated into the underlying muscular layer. By contrast, the remaining 20-25% of cases will be muscle invasive and penetrate through the urothelium into the underlying muscle. Muscle invasive bladder cancer, if not adequately dealt with, has the potential to be fatal. Muscle invasion in bladder cancer largely dictates the course of therapy. Often, small papillary lesions from NMIBC can be adequately dealt with by TURBT followed by intravesical instillation of chemotherapeutic agents such as Mitomycin C. By contrast, muscle invasive disease can often only be adequately dealt with by removing the entire bladder to prevent the spread of disease to lymph nodes and metastatic sites[12]. Radical cystectomy, the removal of the entire bladder, is a life-changing procedure for patients with muscle invasive disease, with associated risks such as infection, blood clots and impotence, therefore it is imperative that bladder cancer is detected and treated as quickly as possible.

NMIBC itself can pose a threat to patients, owing to its potential to recur and progress. NMIBC is a broad category which contains many stages and grades of cancer with varying degrees of aggressiveness. Reliable staging and grading of tumours is carried out on resected biopsy tissue by experienced pathologists. Grading and staging nomenclature for BCa are listed below (tables 1 & 2) and disease stages are depicted in Figure 3:

Table 1 BCa grades and descriptions

Grade	**Description**
Grade 1	Normal appearance and slow growing
Grade 2	Moderately aggressive and abnormal
Grade 3	Extremely abnormal; poorly differentiated

Table 2 BCa stages and descriptions

Stage	**Description**
Carcinoma in Situ (CIS)	High grade flat lesion which exists only in the urothelium with aggressive potential
Ta	A tumour, often papillary, which exists only on the luminal lining of the bladder
T1	Invasion into the lamina propria
T2	Muscle invasion

T3	Invasion through muscle into adipose layer
T4	Invasion out-with the bladder

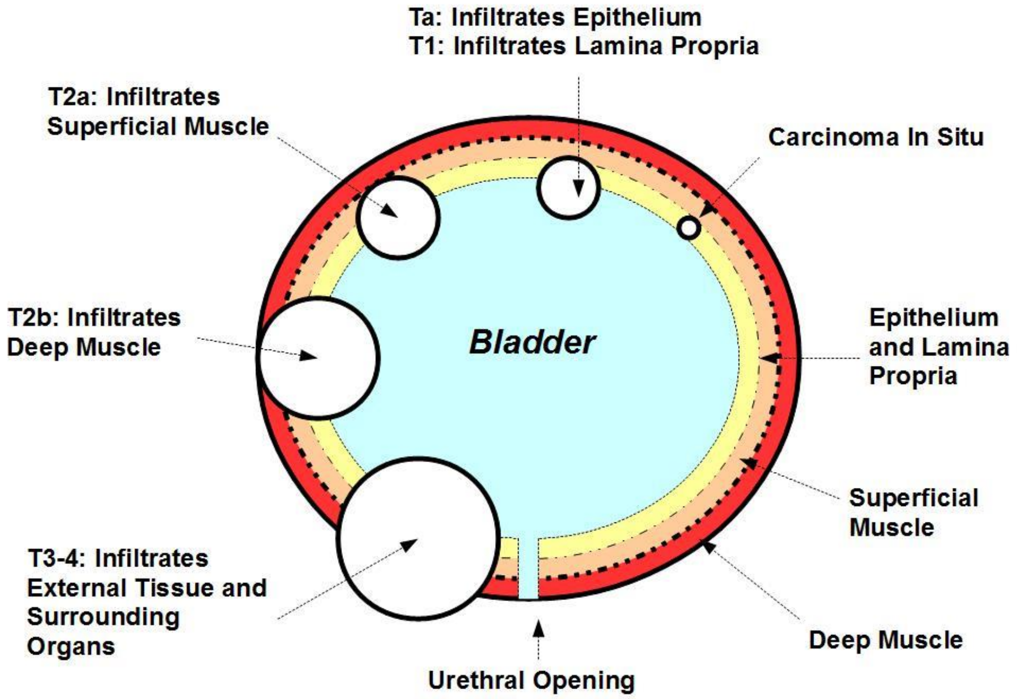

Figure 3 Diagram showing the layers of bladder tissue along with progressing stages of BCa from CIS to invasive stage T4

Therefore, although NMIBC, and although early stage, CIS presents a dangerous flat dysplasia stage owing to its high grade and invasive potential[13]. BCa can also be characterised by incidence of metastasis and by local lymph node involvement.

Although widely accepted as gold standard diagnostic procedures owing to their high specificity and low false positive rates, WLC and VUC often suffer from low sensitivity, particularly for early stage NMIBC. WLC is a useful technique for the detection and observation of papillary lesions but less so for flat lesions, including CIS, and for small tumour margins during resection. It is estimated that the overall sensitivity of VUC for TCC cases is between 25%[14] and 50%[15] depending on the study, particularly lacking sensitivity for low grade cancer[15]. For WLC detection of TCC, sensitivity ranges from 60%[16] to 70%[17] but can be as low as 4% for CIS[18]. The lack of sensitivity of these gold standard techniques means many otherwise preventable early cancers are allowed to recur and progress to more dangerous forms. According to CRUK statistics in 2014, 42% of preventable BCa cases were missed[1]. The high rates of recurrence and progression associated with BCa mean it is essential to provide diagnosed patients with stringent follow-up monitoring months and years after initial diagnosis and intervention. These factors significantly affect patient quality of life and, furthermore, put a considerable burden on the health service each year. Monitoring and intervention strategies, along with patient lay-up time in hospitals and the necessity of having experienced consultants and pathologists on hand make BCa an expensive disease to manage[19]. BCa is estimated to be the single most expensive cancer to treat per patient on a lifetime basis, amounting to roughly £65 million pounds in costs per year in the UK. It is evident, then, that new avenues must be sought to improve the sensitivity of diagnostic techniques for BCa - particularly aggressive, early stage NMIBC such as CIS – to promote early diagnosis, effective monitoring and reliable identification of surgical margins.

1.1.4 Photodynamic diagnosis and therapy

In recent years, many efforts have been made to improve on the sensitivity of current gold standard techniques to promote earlier diagnosis and more effective disease follow-up. Progress has been made in improving the sensitivity of both urinary and cystoscopic examinations for bladder cancer, but at a cost.

The advent of photodynamic diagnosis (PDD) using photosensitising dyes (PS) has seen improvements to sensitivity for both cystoscopic and urinary examination for BCa detection. PS agents, including Hexaminolaevulinate (HAL) and 5-Aminolaevulinic Acid (5-ALA) have been developed to preferentially accumulate in tumours. The preferential accumulation of PS agents in tumours can be explained by the enhanced permeability and retention effect (EPR), whereby cancer cells lose lymphatic drainage and expression of adhesion molecules[20], causing them to be more loosely distributed and creating “leaky” gaps between cells. It is thought that this morphological change in cancer cells allows them to participate more freely in invasion and metastasis. Changes in environmental pH in cancer cells also contribute to the preferential uptake and retention of PS agents. PS agents such as HAL and 5-ALA are precursors in the process of the heme biosynthetic pathway. Heme metabolism is often elevated in cancer cells, therefore inundating cells with HAL and 5-ALA causes accumulation of the fluorescent heme precursor Protoporphyrin IX (PpIX) in cancer cells[21]. PpIX strongly absorbs and emits blue and red light, respectively (PpIX also strongly absorbs red light)[21,22]. Instillation of the bladder with PS, followed by illumination with blue light during cystoscopy, enables surgeons to clearly visualise tumours owing to their bright red fluorescence. Although we will cover the subject in much greater detail in the following section, fluorescence can broadly be described as a process by which an excited molecule can release energy to return to a relaxed state. The absorption of energy, in the form of blue light, by PS agents causes them to emit energy in the form of red light (Figure 4).

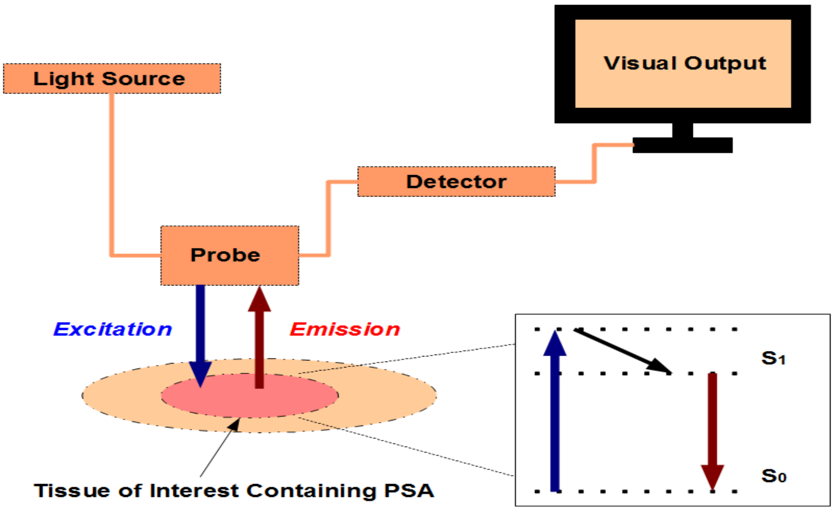

Figure 4 Diagram showing the standard technical setup for tumour PDD. Tumour area selectively accumulates PS agents, strongly fluorescing red under blue excitation.

PDD has been shown to significantly increase sensitivity of detection of bladder cancer, leading to lower recurrence rates compared to WLC[23,24], also dramatically increasing the sensitivity of CIS diagnosis[16,18,25]. PDD using HAL has recently been recommended by a panel of urologists in the USA for diagnosis and surveillance of NMIBC[26]. Furthermore, PDD has shown diagnostic worth as an adjunct to urinary cytology, with voided urine cells from carcinoma displaying increased porphyrin fluorescence compared to healthy cells[27,28]. Bladder tumour detection by WLC (left) and PDD (right) is shown in Figure 5.

Tumours are not the only tissue type which display leaky architecture, however: it is often noted that inflamed and infected tissue contains loosely packed epithelial cells, permitting the accumulation of PS agents. Several studies have now recognised that, although significantly more sensitive for bladder cancer diagnosis, PDD is a less specific methodology than its counterpart, WLC[17,19]. Reduced specificity and increased false positive rate of PDD is particularly noticeable after previous intravesical therapy[29].

As a result of the practicalities of PS instillation and the increased false positive rates seen with PDD, it is considered a more costly option than WLC[30] – the costliness of PDD is suggested for further review[31]. The monetary and diagnostic costs to using PDD must therefore be carefully weighed against the benefits of increased sensitivity. There is ongoing work in the field by many research groups to increase the specificity of PS localisation for PDD regimens[32].

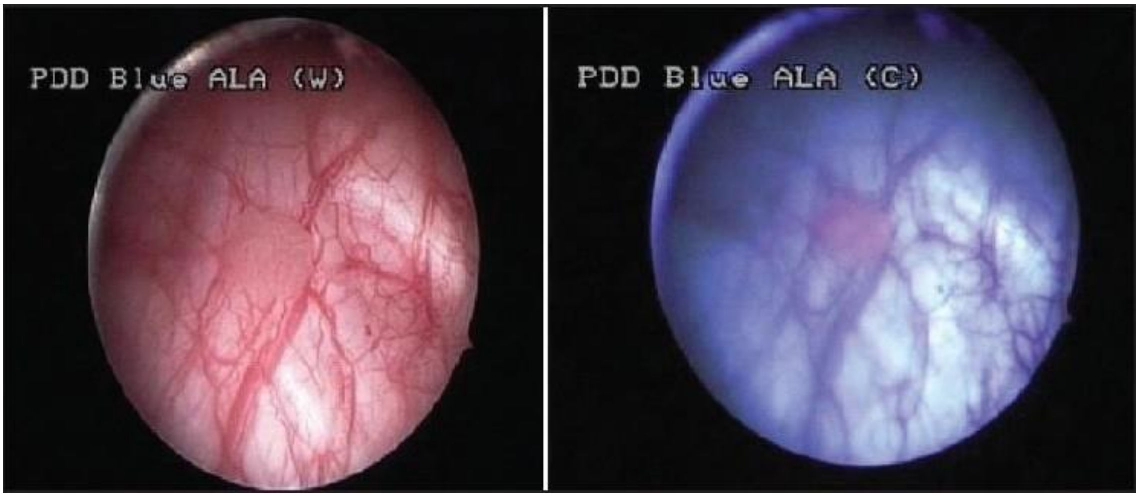

Figure 5 Comparison of cystoscopic images of BCa obtained using WLC (left) and PDD (right) courtesy Cauberg Evelyne et al.[33] (reproduced with permission under a CC Attribution Non-commercial Share Alike License)

The same processes of absorption of light which contribute to tissue fluorescence in photodynamic diagnosis can also be utilised to selectively kill cancer cells, in a process known as photodynamic therapy (PDT), covered expertly here[34]. PS agents possess a strong probability to enter a longer-lived excited triplet state, allowing time for the excited PS to interact with molecular oxygen and cellular components. Entry of the PS into a longer-lived triplet state is necessary for effective PDT While PDD relies on excited singlet state PS agents relaxing to ground state by emitting fluorescence, PDT relies on the donation of molecular energy from the excited triplet state PS agent to surrounding molecules via type I and type II reactions. The reactions between excited PS agents and nearby molecules generate reactive oxygen species (ROS). The generation of high levels of ROS within cells is associated with cell toxicity[35] owing to modification and denaturation of fatty acids[36], DNA[37] and peptides[38]. Of particular importance in PDT are type II reactions, whereby excited PS agents donate energy directly to molecular oxygen to form singlet oxygen ($^1O_2$). Singlet oxygen is potently reactive and rapidly affects surrounding cell organelles, particularly the mitochondria[39,40], leading to apoptosis (Figure 6), necrosis (Figure 7) and long lasting anti-tumour immune response[41,42]. It has been suggested that the mechanism of PS action can have an effect on the mode of death a cell experiences (apoptosis or necrosis)[41]. Targeting of the mitochondria during PDT via messengers such as Bax and Bcl-2 has been suggested to lead to quiescent apoptotic cell death through the release of apoptotic messengers to the nucleus (Figure 6). Conversely, targeting of the lysosome or cell membrane during PDT has been suggested to lead to necrotic cell death and the release of danger signals, promoting inflammation (Figure 7). PDT has enjoyed ongoing success in cancers other than BCa, including skin cancer[43]. In BCa, PDT enjoys considerable success as a tissue sparing therapeutic modality, particularly in patients who fail to respond to intravesical Mitomycin C instillation.

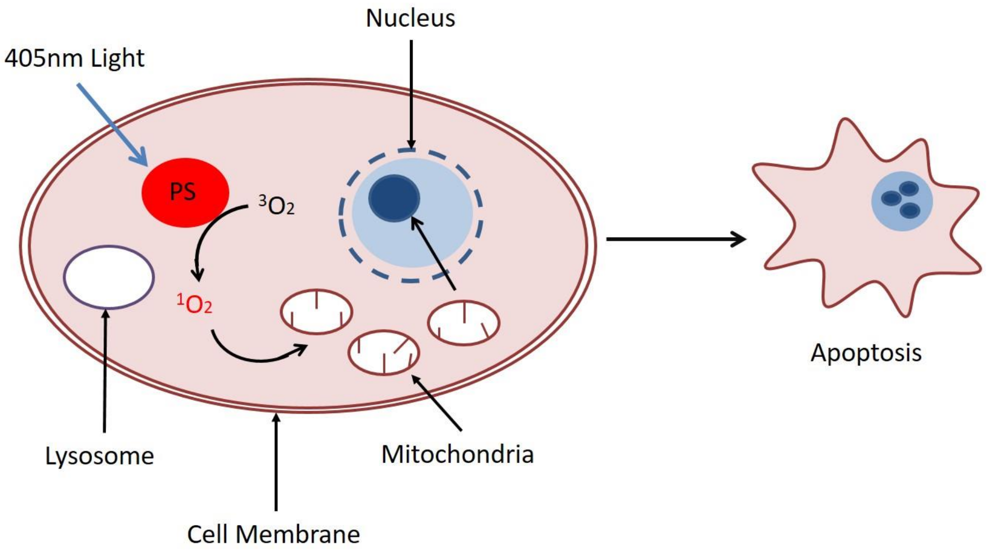

Figure 6 Molecular pathways following PDT leading to apoptosis. Photosensitiser (PS) excited by 405nm light enters a stable triplet state, donating energy to molecular oxygen to form singlet oxygen. Effects of singlet oxygen on mitochondria causes release of apoptotic messengers to the nucleus, leading to quiescent apoptotic cell death.

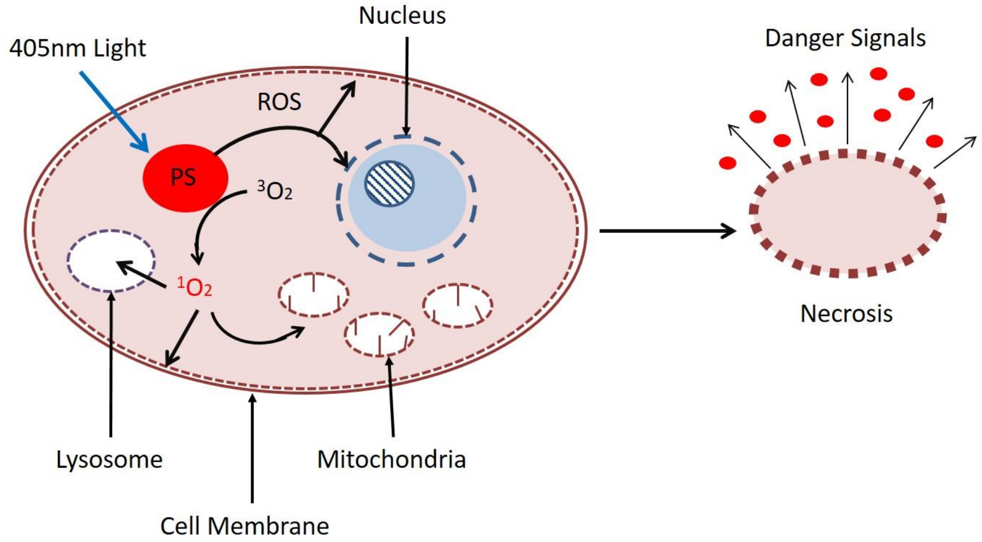

Figure 7 Molecular pathways following PDT leading to necrotic cell death. Photosensitiser (PS) excited by 405nm light enters excited triplet state, donating energy to form singlet oxygen and ROS. Interaction between singlet oxygen and ROS with cell membrane and lysosomal membrane, leading to membrane rupturing, necrotic cell death and release of danger signals.

Alongside the specificity issues associated with PDD using PS agents, PDT efficacy, especially for deeper lying tumours, can be hampered both by the penetration of PS dye and activating light into tissue, leading to incomplete clearance of tumour areas. 633nm light can penetrate up to 20mm into bladder tissue[44], which may cause limited tumour clearance in areas of extensive epithelial thickening. Recurrence at 30 months was found to be around 40% for PDT treated NMIBC patients[45]. Furthermore, high fluence rates can cause healthy tissue necrosis and inflammation[46]. In an animal model of PDT, irradiation was associated with tissue fibrosis, epithelial sloughing and haemorrhaging, depending on the light dose[47]. New technologies are therefore required for PDT, possibly at longer wavelengths, to increase tissue penetration and avoid aberrant side effects on tissue.

1.1.5 Nuclear Matrix Protein 22 (NMP22) and other urine analysis techniques

Similarly, efforts are ongoing to increase the sensitivity of urine analysis modalities for BCa, especially for early stages such as CIS. Urine analysis presents an attractive alternative to WLC for diagnosis and follow up of disease as it is completely non-invasive and can be performed in an out-patient environment, reducing patient morbidity and associated costs. These tests rely on the detection of shed urinary biomarkers such as nuclear matrix protein 22 (NMP22)[48], chromosomal abnormalities (Urovysion)[49] or bladder tumour antigen (BTA stat)[50]. The NMP22 test has been shown to display increased sensitivity compared to VUC[48] while also being cost effective[51], however it displays reduced specificity compared to VUC[52,53] and is adversely affected by a number of factors, including urinary tract infection[54]. Due to confounding factors which may cause false positives and the need for experienced operators, NMP22 test has been suggested as not recommendable for application as a point of care test[55] or as a follow up test to replace WLC[56]. Similarly, BTA stat does not possess adequate sensitivity for follow up[56].

1.1.6 Diagnosis and therapy in the context of "The Hallmarks of Cancer"

In 2000, Hanahan and Weinberg published the seminal paper "The hallmarks of cancer"[57], updated in 2011 as "The next generation"[58]. In these comprehensive reviews, the fundamental differences between healthy and cancer cells are discussed, with the aim of exploiting these differences to develop new methods for cancer diagnosis and therapy. The key features highlighted by Hanahan and Weinberg are reproduced below (Figure 8):

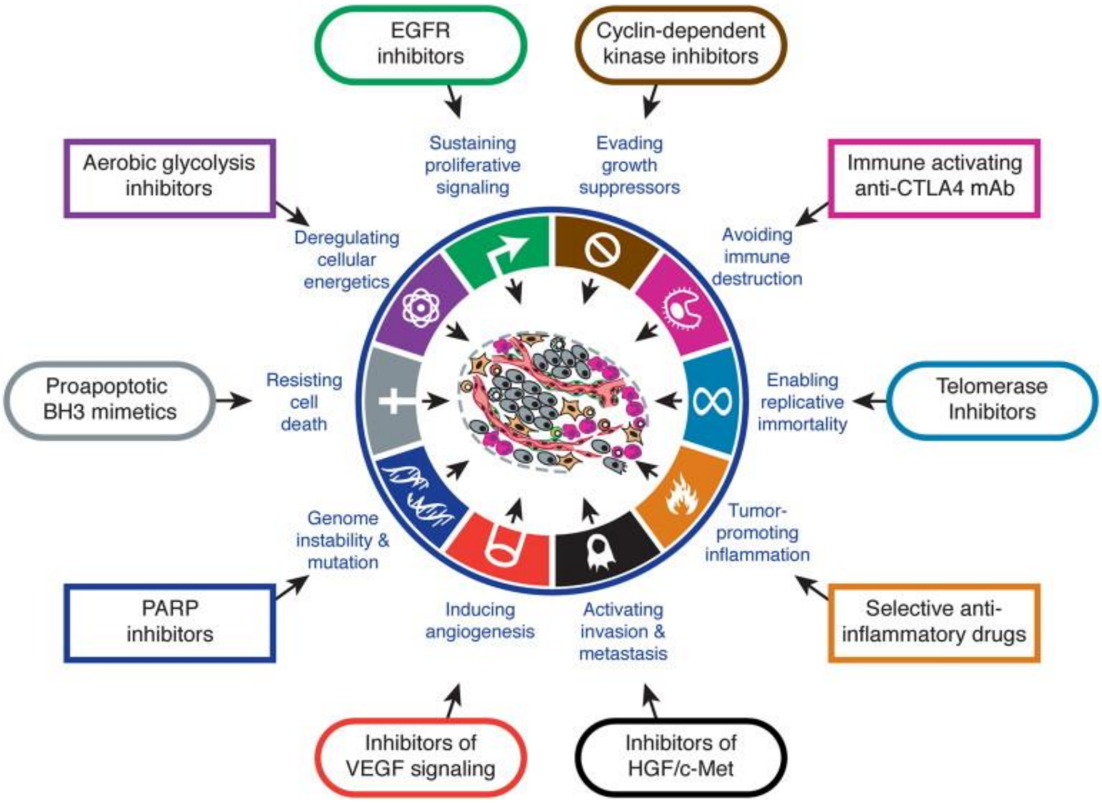

Figure 8 The "Hallmarks of Cancer", according to Hanahan and Weinberg[57]

(reproduced with permission from Elsevier)

Broadly, cancer cells will drive genetic instability and mutation and deregulate their metabolism to enable them to adapt to new environments, often the poorly oxygenated environments of the tumour inner core. This, coupled with inducing angiogenesis and invasive behaviour allows cancer cells to escape their native environment and migrate (metastasise to distant regions of the body). In addition to promoting metastasis, angiogenesis also provides cells in growing tumours with the nutrients they require to continue replicating (aided by enabling replicative immortality). From this we can see a wide range of factors which could contribute to the malignant and invasive phenotype of aggressive BCa, the scope of which is far too large to adequately cover here. Below is a quick summary of how some of the classical hallmarks of cancer may apply to BCa, and how these may be used to better diagnose and treat the disease.

1. As briefly discussed earlier, the induction of angiogenesis by developing tumours – a hallmark of cancer – is a factor which is taken advantage of by the use of photosensitising agents and other drugs. The weak, leaky vessel walls of tumours is much more penetrable to PS agents than are the surrounding healthy tissues, leading to preferential uptake of PS into tumours.
2. The theoretical basis of urinary fluorescence in situ hybridisation (FISH) tests such as Urovysion is that of genomic instability in cancer cells. By targeting mutations in bladder cancer cells, including to the p16 tumour suppressor gene, pathologists can non-invasively assess the presence of bladder cancer from patient urine[49]. Tests such as the NMP22 test also rely on genomic instability – alongside cancer cell ability to enable replicative immortality – by targeting nuclear matrix proteins, which are expressed at much higher levels in rapidly replicating bladder cancer cells[59].
3. Inflammation associated with tumours can provide a strong indicator of suspicious lesions when inspecting the bladder using WLC. Often, bladder tumours show up visibly redder than healthy tissue, however this can also prove misleading in cases of benign inflammation such as urinary tract disease. Furthermore, tissue inflammation can contribute to blood vessel leakiness (to promote immune cell extravasation), enhancing tissue uptake of PS agents. Inflammation has been implicated in pathogenesis of many cancers, including breast cancer (through mediators including cyclooxygenase and prostaglandins)[60], ovarian cancer (via C-reactive protein)[61] and gastric cancer (via Toll-like receptors)[62]. In particular, IFN-y induced inflammatory mediators have been implicated in a wide range of cancers[63]. COX-2 has been suggested to play a role in bladder cancer[64], as has C-reactive protein[65]. C-reactive protein levels can also be used to predict outcomes in bladder cancer[66].

Two of the main hallmarks of cancer which will provide the focus of this thesis are the deregulation of cellular energetics (through the Warburg effect) and the invasion of tissue by growing tumours. As will be seen, these hallmarks provide ways with which to study the onset and progression of bladder cancer, with promising real world applications for disease detection.

1.1.7 Next generation diagnosis and therapy

To improve diagnosis and reduce patient morbidity and associated treatment costs, there has been a great deal of research in recent years with the aim of improving the sensitivity of BCa diagnosis without having to compromise on specificity. The need for diagnostic tools which balance sensitivity and specificity has opened up many new avenues of research, some displaying strong promise.

The PS agent Hypericin, taken from St. John's wort, has been suggested as an upgrade on conventional PS agents such as 5-ALA and HAL[67], owing to its improved specificity compared to these agents. HY uptake by tumours is hypothesised to occur by different mechanisms than those which dictate conventional PS uptake. These are likely structural changes in tissue, possibly including changes in Cadherin and Catenin levels[68]. Specificity of BCa diagnosis using Hypericin has been recorded as high as 98%[69], a considerable upgrade on the specificity levels achieved by conventional PDD. Hypericin can also be instilled directly into the bladder, offering an improvement on the systemic administration of first generation PS agents by avoiding the risk of non-specific toxicity and skin photosensitivity (although HY can still display phototoxic effect on healthy tissue[70]). Furthermore, HY possesses an increased absorption maximum compared to conventional PS agents (540-590nm vs 400nm for HAL/5-ALA) - as it does not rely on PpIX accumulation – allowing for deeper tissue penetration by activating light. Direct instillation of HY into the bladder is, however, associated with increased patient lay-up time, for up to several hours prior to inspection. D’Hallewin *et al.* discuss this[69] as one of the drawbacks of Hypericin use – Hypericin must also be in direct contact with all bladder areas during instillation, excluding the use of this technique for patients presenting with diverticula or other related health issues. A further drawback to the use of Hypericin is its lipophilicity, meaning it forms aggregates in aqueous solutions. This is a significant issue to the clinical application of Hypericin based diagnosis, with several research groups focussing on the development of new strategies to better solubilise Hypericin[71,72].

Many research groups have focussed their attentions on nano-applications for photo-diagnosis and therapy of BCa. In particular, functionalised quantum dots (QD) have been suggested as a suitable theranostic tool owing to the high quantum yield of QDs, along with their high degree of specificity afforded by functionalisation with monoclonal antibodies against tumour specific antigens. QD excitation and emission profiles can be tightly regulated by particle size, allowing wavelength specific targeting of molecules and tissues of choice. A major concern which has limited the implementation of nano-medicine is the accumulation and systemic toxicity of quantum dots, gold nano-rods and others. Valizadeh *et al.* discuss in great detail the synthesis, potential applications and toxicity concerns associated with QDs[73]. The development of biocompatible QDs for clinical application is considered by Rosenthal *et al.*[74].

Along with improving the sensitivity and specificity of diagnosis, a major aim of current research should be working towards non- or minimally-invasive techniques which are capable of grading and staging tumours without the needs for repeat cystoscopy and biopsy. In recent years a major focus has been on the development of diagnostic imaging techniques which rely on inherent structural or molecular properties of tissue. These techniques aim to create “fingerprints” of tissues of interest, corresponding to particular structural or molecular contributions. Within this field there is a wide scope of techniques available for the analysis of tissue constituents. Liu *et al.* expertly cover the current standing of a wide range of novel diagnostic techniques, including laser endomicroscopy, optical coherence tomography (OCT) and narrow band imaging (NBI), particularly focusing on the need for clinical prospective studies using these techniques[75]. We ourselves have also reviewed the current standing of novel optical techniques for bladder cancer diagnosis[76]. Some of the most promising endogenous imaging techniques for BCa will be discussed here. Firstly, NBI is a technique which relies upon differential absorption and scattering of light by blood vessels, permitting straightforward observation of tumour vasculature and increased urothelial contrast to clinicians. NBI is gaining recognition and beginning to become implemented in clinical settings by affording improved sensitivity of BCa detection[77,78], increased quality of TURBT[79] and reduced recurrence rates after TURBT (comparable to PDD)[80]. An NBI image is compared to the same tissue site under WLC in Fig. 9.

Figure 9 Comparison of TCC of urinary bladder imaged using WLC (left) and NBI (right) courtesy Cauberg Evelyne et al.[33] (reproduced with permission under a CC Attribution Non-Commercial Share Alike License)

NBI requires detailed post-processing and image analysis by trained professionals to obtain useful diagnostic information. In addition, NBI provides little information on a molecular level, therefore it may not be a suitable technique for providing optical biopsies including staging and grading reports.

To obtain detailed molecular information about tissues of interest, Raman spectroscopy is undergoing development into a potential clinical modality, demonstrating diagnostic worth in the detection of cervical[81], oral[82], skin[83] and brain cancer[84] as well as bladder cancer at the tissue[85,86] and cellular level[87,88]. Raman spectroscopy relies on the process of "Raman scattering", by which molecular components of cells and tissues interact with light, causing specific energy shifts in accordance with the specific molecular properties of tissue. Raman spectroscopy can therefore give detailed information on the presence and quantity of amino acids, carbohydrates and lipids, etc. in tissue, allowing analyses of any differences between the levels of these components in healthy and cancerous tissue. Crow et al. have demonstrated reliably high sensitivity and specificity BCa diagnosis (>90%) using a Raman microscopy setup[89], indicating potential as a diagnostic modality to provide the sensitivity lacking from conventional WLC alongside specificity missing from PDD. Crucially, *In vivo* application of Raman spectroscopy can be hampered by out of focus signals which reduce the specificity of diagnosis (discussed by Barman *et al.*[90]). Steps are being made to improve the specificity of *In vivo* imaging modalities by reducing the out of focus signal[90] but this remains a major barrier in the clinical application of Raman spectroscopy to BCa diagnosis.

Another useful technique for structural imaging of tissue is second harmonic generation (SHG) imaging, generally using pulsed femtosecond infrared lasers. This process relies on the inelastic interactions between light and molecules with non-centrosymmetric surfaces. The biophysical processes by which SHG occurs will be discussed later. By far the largest contributor to SHG in human tissue is type I collagen[91], with collagen destruction or modification leading to a loss in SHG signal intensity. Changes in SHG signal intensity can therefore be used as a non-invasive indicator of cancer. Furthermore, changes to the orientation of collagen fibrils during carcinogenesis can be identified and used as diagnostic markers, as demonstrated in breast[92] and ovarian cancer diagnosis[93]. Conklin *et al.* discovered hallmark signatures, known as “tumour associated collagen signatures” in SHG imaging of breast cancer, suggesting the worth of these signatures for disease diagnosis[94]. Conventional setups used for SHG imaging generally also allow for multi-photon fluorescence microscopy, therefore multi-modal imaging of epithelial cells and underlying connective tissue is afforded by this methodology[95]. Non-linear imaging, particularly SHG, is still poorly investigated in BCa, with preliminary studies setting out optimal measurement techniques in mouse models[96] or clinical studies with small sample sizes[97,98]. The clinical data derived from patient biopsy in[97] and[98] show good correlation with histopathology data, suggesting the diagnostic worth of this modality for bladder cancer, particularly CIS. Larger scale studies are undoubtedly required into SHG imaging of BCa, to determine the true diagnostic worth and clinical application of this modality. Thomas *et al.* consider that, in general, there are very few studies applying clinical SHG imaging to an *In Vivo* setting (with the exception of skin cancer) and that this is the next big step towards developing it as a clinical modality[99].

1.1.8 Autofluorescence Spectroscopy

A useful method for incorporating the structural elements of SHG with the detailed molecular profiling provided by applications such as Raman spectroscopy is the use of autofluorescence spectroscopy (AS)[100]. AS works similarly to PDD, with the exception that no PS is added to tissue. Instead, the signals received from tissue arise entirely from inherent molecules of interest. Tissue autofluorescence spectroscopy can give information on the presence and quantity of a wide range of diagnostically relevant molecules, including amino acids, lipids, metabolic cofactors and heme precursors. Molecules of interest can be specifically targeted and studied in tissues (either using lasers or broadband illumination sources) based on the intrinsic excitation and emission properties of the molecule of interest. The most commonly studied endogenous fluorophores in human tissue are listed in table 3 below:

Table 3 Common endogenous tissue fluorophores (courtesy Wikipedia.org)

Molecule	**Excitation (nm)**	**Emission (nm)**	**Role**
Tyrosine	270	300	Amino acid, protein component
Tryptophan	270-280	300-350	Amino acid, protein component
Collagen	270-370	300-450	Structural protein
Elastin	340-390	400-450	Structural protein
NADH	350-400	450-490	Metabolic cofactor
Flavin	350-450	500-600	Metabolic cofactor
Lipofuscin	410-530	500-700	Lysosomal pigment
Porphyrin	550-650	700-710	Heme pathway

Therefore fluorescence spectroscopy of tissue using different wavelengths of excitation light will provide spectral information with very different molecular information about tissue. UV spectroscopy provides structural and metabolic information based on fluorescence from contributors such as collagen, elastin, NADH and flavins, while at longer wavelengths, red light can be used to study heme pathway precursors.

Autofluorescence imaging in animal tissue was first described in the early 1900s, using microscopy setups with UV excitation sources to capture the fluorescence properties of cartilage, bone, skin and other tissues[101]. In the 1980s, researchers including Alfano *et al.* had begun to utilise UV light sources to demarcate breast cancer based on autofluorescence imaging[102]. Autofluorescence imaging has previously successfully been applied to detection and analysis of ulcerative colitis[103], diabetes[104] and macular degeneration[105] in addition to a wide range of cancers[106,107], being comprehensively reviewed by Ramanujam[100]. AS has been reported to greatly improve the accuracy of laryngeal cancer detection[108]. He *et al.* report a greatly improved sensitivity but reduced specificity of AS for lung cancer compared to gold standard white light bronchoscopy[109], lack of specificity of AS has been corroborated in oral cancer by Awan *et al.*[110]. The first recorded application of autofluorescence spectroscopy to BCa analysis was by D’Hallewin *et al.*[111]. In the intervening years, many subsequent analyses of bladder cancer autofluorescence have been published[112-114]. Rokahr *et al.* noted an increased accuracy of tumour margin demarcation using autofluorescence imaging of bladder tissue compared with PDD[115]. In a spectrofluorometric analysis of ex vivo bladder samples, Zheng *et al.* demonstrated that the most useful excitation wavelengths for bladder cancer detection were 280nm and 330nm[114]. The In vivo application of a 150W light source (similar to that used in the study by Zheng *et al.*) to the human bladder would cause tissue damage through heating, so it is imperative for us to determine how bladder tissue responds to light of reduced optical power. One recurring theme of several AS studies of bladder cancer is a decrease in the area under the curve (AUC) fluorescence in bladder cancer samples excited using UV and blue light[112,116,117]. This is attributed to thickening of urothelium in bladder cancer tissue, obscuring underlying fluorescence signals from structural proteins such as collagen. D’Hallewin *et al.* have discussed this phenomenon[118], from which it can be concluded that this technique may prove little worth in the detection of CIS, which does not cause noticeable tissue thickening. Non-specific spectral ratio analysis has also been applied to bladder cancer detection, with promising diagnostic ratios including 335/440nm at 308nm excitation[119] and 385/455nm at 337nm excitation[113]. Recently, a comparative study with PDD demonstrated both increased sensitivity and moderately increased specificity of AS for bladder cancer[120]. Promising laboratory and pre-clinical results are yet to be fully realised clinically, however. This may be due to the inability to separate distinct fluorophores in complex spectra, and the inability to apply in vitro results – using bulky laboratory equipment – *in vivo*. Limited applicability to CIS detection is a contributing factor. Additionally, autofluorescence is known to vary considerably even among healthy individuals due to natural differences in tissue composition and function. More work in the field is required, therefore, to uncover new optical disease biomarkers which are independent of tissue thickening. Anidjar *et al.* attempted to address this issue by studying tryptophan levels in healthy and cancerous bladder mucosa[121], indicating a new biomarker which may be of worth for CIS detection.

Recent work has sought to delineate fluorophore contributions using multi-photon microscopy (MPM). A recent MPM study of ex vivo human bladder tissue showed strong autofluorescence from the urothelial layers (corresponding to NADH and flavins) with a strong SHG signal underneath from collagen in the connective tissue[97]. Mukherjee *et al.* demonstrated that structural and functional tissue imaging using MPM could differentiate between healthy mucosa and bladder cancer, similar to haematoxylin and eosin (H & E) staining of fixed pathology slides. Although this study did not focus on autofluorescence intensity, it demonstrates the increasing worth of AS applications for optical biopsy.

Another factor of tissue autofluorescence which can provide diagnostic worth is fluorescence lifetime, the duration of time for which a molecule fluoresces following excitation before returning fully to ground state. Fluorescence lifetime imaging (FLIM) studies allow for very specific analysis of cell and tissue status as changes in pH and oxygenation can all influence the fluorescence lifetimes of molecules of interest such as NADH, and id independent of molecular concentration. In theory, detection of fluorescence lifetimes outside of "normal" parameters for a molecule of interest may point towards a cellular abnormality such as cancer. FLIM is of interest in cancer research because it is less affected by heterogeneity in tissue thickness than other quantitative fluorescence analysis techniques, therefore it may be of use for CIS detection. Furthermore, FLIM can be used to delineate between fluorophores with overlapping spectra - for instance NADH vs NADPH and free vs bound NADH – and to study a range of the fluorophores discussed previously in this thesis (including tryptophan[122] and flavins[123]). FLIM has been utilised widely since the development of applicable systems in the early 1990s which allowed for simultaneous lifetime measurement and fluorescence localisation through imaging[124]. The use of FLIM for tissue analysis has been reviewed comprehensively[125-127] and has enjoyed application to the study of oral carcinoma, Barrett's oesophagus and colon adenoma among others[125]. Although decay dynamics have been found to differ between healthy and cancerous tissue, specific details vary between tissues: for instance colon adenoma spectra were found to decay faster than healthy colon, while oral carcinoma spectra have been found to decay much less quickly than healthy tissue. To date, FLIM studies of bladder tissue are limited to one time resolved autofluorescence study of CIS[98], therefore there remains great scope in the field to apply FLIM to the study of bladder cancer in future.

Application of FLIM *In Vivo* has previously been limited by bulky, expensive equipment, however in recent years FLIM probes have started to receive attention as a means by which to study dynamics in intact tissue, an example being FLIM confocal endomicroscopes[128]. FLIM probe studies have revealed a great deal about the autofluorescence dynamics of healthy and tumour tissue: a decrease in the mean fluorescence lifetime in colon neoplasia compared to healthy colon in an *Ex Vivo* study[129]; a decrease in fluorescence lifetime in oral cancer in an *In Vivo* hamster model[130] and increased NADH fluorescence lifetime in apoptotic tissue compared to necrotic in an *In Vivo* study of mouse keratinocytes[131]. FLIM probes have also been and applied to the study of exogenous dye uptake by tumour tissue[132], and combined with Raman probes for *In Vivo* application[133]. In future, FLIM studies may help to further elucidate the profiles and dynamics of fluorophores of interest in the bladder both in health and disease.

A further limitation to our understanding of AS is that multi-parametric non-invasive analyses of bladder tissue using multiple excitation sources are few in number, with most studies relying on single excitation sources, usually in the UV wavelength range. As we will discuss in later sections, UV spectroscopy can often be hampered by the low penetration of the short wavelength, especially in the detection of deep and flat lesions. One further factor impeding the clinical application of autofluorescence diagnosis of bladder cancer is a poor understanding of changing autofluorescence profiles as tumours grow and develop. Organoids (in vitro mimics of tissues or cell systems) have recently enjoyed application to study cellular responses to drugs[134]. Bladder organoids have previously been derived from porcine[135] and human tissue[136] and provide a useful platform with which to study progressive changes in cells and tissues over time. Work is also underway into the development of organoids which accurately recapitulate cancer[137]. The application of AS to developing bladder cancer organoids may serve to address the issue of our poor understanding of changes in autofluorescence profiles as tumours develop, however this has so far not been achieved.

Previous biochemical studies into bladder cancer have shed new light on the structural and molecular makeup of the disease, yielding information which could better help the design of AS systems for bladder cancer diagnosis.

With regards to structural proteins, the role of collagen in cancer progression has been studied extensively. Collagen in connective tissue surrounding epithelial tissues is known to be modified by progressing tumours in order to provide space and the opportunity for tumour invasion. It is well-known that developing tumours secrete matrix metalloproteinases (MMPs) which break down collagen in surrounding tissues, facilitating tumour growth and invasion[138,139], resulting in reduced local collagen levels. MMP-1 in particular has been well studied in bladder cancer, potentially playing a driving role in pathogenesis[140] while MMP-9 detection has also shown prognostic value in bladder cancer[141] and MMP-7 has shown promise for predicting bladder cancer metastasis[142]. The larger picture of collagen involvement in cancer is not so clear, however, as discussed by Fang *et al.*[143], with clinical implications in breast cancer[144]. Positive feedback signalling between cancer cells and local collagen may therefore also serve to facilitate cancer progression and invasion. Autofluorescence imaging of collagen has previously been used to study tissue repair[145] and to shed light on cancers of the prostate[146] and cervix[147]. Interestingly, both of these studies have reported reductions in the relative levels of collagen. Collagen fluorescence properties in bladder cancer have not been extensively studied, however the role of collagen in bladder extracellular matrix (ECM) and its architectural modifications during disease has been comprehensively reviewed[148]. It is known that invading cancer cells actively adhere to collagen fibrils in the ECM and utilise these fibrils to facilitate their invasion deeper into tissue[149].

Likewise, elastin is a major component of the ECM, partially responsible for providing the functional properties of bladder tissue. Genetically modified mice which lack elastin in the bladder were shown to present with altered bladder function[150]. Elastin fibre arrangement and modification has previously been studied to great effect in Marfan syndrome – a genetic condition affecting connective tissue production and distribution in the body - using two-photon excited autofluorescence[151]. Furthermore, autofluorescence imaging of elastin in the dermis has been used to elucidate a wealth of information about skin disorders[152]. Elastin fluorescence properties in bladder cancer have not been extensively studied, however it has been reported that elastin fluorescence (alongside collagen fluorescence) can be used to characterise bladder tissue in an ex vivo study of mouse organs[153].

The autofluorescence information received from collagen and elastin, particularly using spectroscopy, may be obscured somewhat by the presence of the amino acids tryptophan and tyrosine, which possess similar excitation and emission profiles. These amino acids are used by cells for the production of structural and functional proteins, therefore the enhanced activity of cancer cells compared to normal may give rise to increases in local amino acid levels. Tryptophan has been shown to accumulate in breast cancer, studied using native autofluorescence, at both the cellular[154] and tissue level[155]. Increased tryptophan fluorescence has also been demonstrated in colon cancer[156], while chemotherapy studies have shown decreases in tryptophan fluorescence in bladder cancer cells in response to drug treatment[157]. In addition, tyrosine phosphorylation of proteins has been found to increase in bladder cancer[158], therefore tyrosine may play an as-yet unknown role in bladder cancer progression.

The metabolic cofactors NADH and flavins have been studied in a wide range of cancers. Metabolic anomalies in cancer cells often cause alterations to the way these cells generate energy, resulting in changes to endogenous NADH and Flavin levels. NADH and NADPH fluorescence is often referred to as “NAD(P)H”, due to the close structural and spectral similarities between NADH and the related NADPH. While NADH is involved in energy metabolism, NADPH is often involved in cellular antioxidant defence[159]. As these molecules are spectroscopically indistinguishable[160], understanding of the redox profile of a cell or tissue can be influenced by the presence of NADPH, therefore being skewed by its antioxidant defences. One way to individually localise and quantify NADH and NADPH is to take advantage of their differing fluorescence lifetimes. For instance, bound NADPH has been shown to possess a longer fluorescence lifetime than bound NADH[161]. Blacker and Duchen suggest that the ratio between NADH and NADPH lifetimes could serve as a useful tool for the detection of pathological conditions[161].

Much of the work in the field on NADH and flavins concentrates on the optical redox ratio (ORR), which will be discussed in greater detail shortly. NADH and Flavin levels are very sensitive to perturbations in tissue thickness associated with cancer progression, therefore it is often much more suitable to apply a diagnostic ratio to account for this. NADH exists in both free and bound (proteins, etc.) forms, which possess slight differences in their emission profiles and considerable differences in their fluorescence lifetimes[160] due to the physical properties of the fluorophore. Fluorescence lifetime of NAD(P)H has been shown to increase upon binding with a protein. This increase has been shown to range from 1-6.5ns, depending on the molecule NAD(P)H binds to[160]. Multi-photon microscopy has been used to differentiate between free and bound NADH, detailing relative levels of both forms of NADH during an animal model of ischaemia[162]. Free to bound NADH ratios have recently been used to identify oral squamous cell carcinomas[163] and bound NADH lifetime imaging has been used to detect pre-cancerous epithelia[164]. NADH FLIM has also been used to monitor breast cancer cell response to drug treatment[165]. The role of NADH levels alone in bladder cancer have not been extensively studied, although one previous study using fluorescence microscopy of fixed slides has suggested that NADH fluorescence alone is not suitable for bladder cancer detection[166]. Flavin fluorescence has been used to characterise glioblastoma cell lines[167].

Lipofuscin pigments are well known for their involvement and increased presence in aged and damaged tissues as a marker of “wear and tear”. Lipofuscin accumulation has previously been linked to macular degeneration[168] and Alzheimer’s disease[169], among others. The inherent autofluorescence of lipofuscin pigments across 560-730nm has proved a useful tool with which to study these diseases[170]. The presence of lipofuscin granules in urothelial cells was only recently discovered[171], and may provide an opportunity with which to study tissue inflammatory status due to its apparent link with oxidative stress. Lipofuscin levels were found to increase with both age and disease stage in a multi-photon microscopy study of ovarian cancer[172].

Finally, porphyrins are a class of molecule involved in heme production, with the most common form in humans being Protoporphyrin IX (PpIX). Porphyrins are perhaps best known for their selective accumulation in cancer tissue following administration of PS agents such as 5-ALA (covered earlier), however endogenous porphyrins also show some promise in the detection of cancer. Porphyrin like fluorescence has previously been identified for its diagnostic worth in oral cancer[173]. Furthermore, baseline PpIX levels were demonstrably lower in healthy renal cells compared to renal carcinoma cells[174] (without addition of PS) and in the blood[175] and tumour area[176] of mice implanted with renal cell carcinoma. So far, no studies have demonstrated differences in the baseline porphyrin levels of non-sensitised healthy and cancerous bladder tissue, however the efficacy of PDD using PS agents suggests a deficiency in the heme biosynthetic pathway of bladder cancer cells which may also result in changes in autofluorescence. Koenig *et al.* previously concluded that porphyrin presence should be expected in the majority of aerobic tissues owing to its key role in heme/haemoglobin biosynthesis for oxygen transport[177], therefore we consider that endogenous porphyrin quantification may be of worth in the disease. Porphyrin possesses several absorption peaks, thereby allowing fluorescence to be excited both at its excitation maximum

(405nm) and closer to the tissue optical window (630nm), theoretically allowing deeper tissue penetration. Longer wavelength excitation of porphyrins has been utilised in studies of PDD for bladder TCC[178] and in the study of endogenous porphyrins in oral mucosa[179], therefore it is a reliable methodology for future study.

The emission profiles of several endogenous fluorophores under 366nm excitation have been collected by Croce *et al.*[180] (Fig. 10). We can see that a great deal of endogenous fluorophores are excited to fluoresce under UV illumination, thereby contributing to complex fluorescence spectra. Delineation of individual fluorophores contributing to the spectra of healthy and cancerous tissue is therefore crucial. In this review, Croce *et al.* also discuss the essential need for light-tissue modelling using techniques such as Monte-Carlo modelling (this technique will be covered in greater detail later).

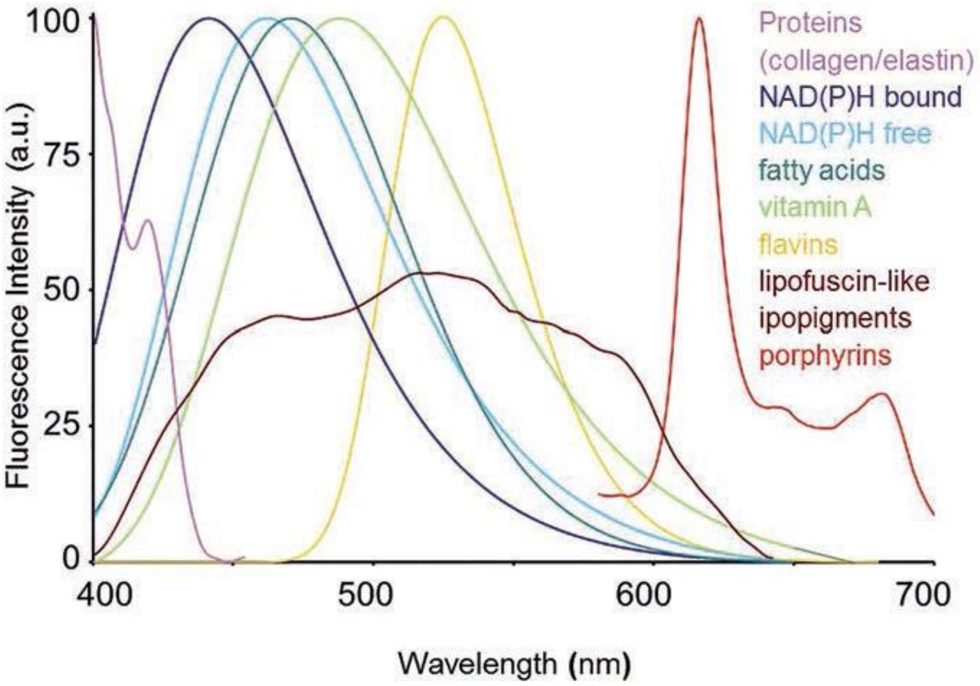

Figure 10 Emission profiles of the most common endogenous fluorophores under 366nm excitation (reproduced with permission under Creative Commons attribution non-commercial license, courtesy Croce et al.[180])

Included below (Fig. 11) is a cross section of bladder tissue showing major structural elements and the expected fluorophores at each level of tissue:

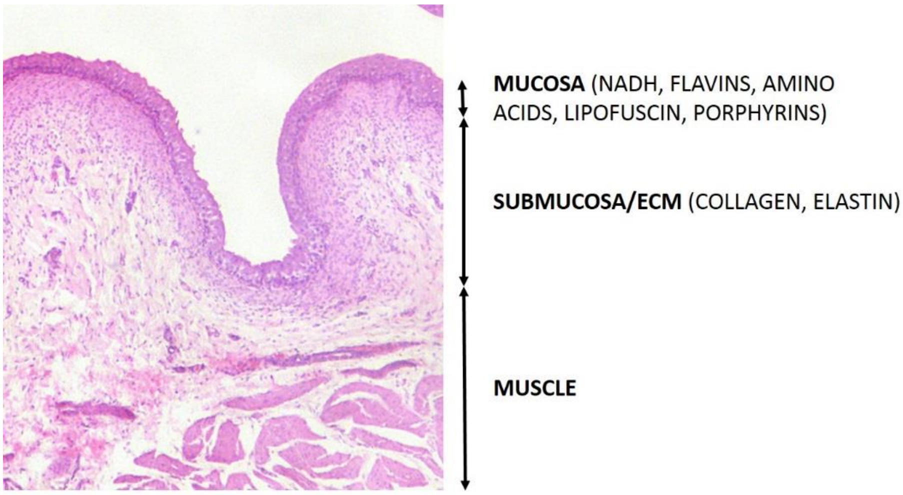

Figure 11 Cross section of the urinary bladder showing the main layers and related fluorophores (adapted from Wikiwand and included under a public domain license)

One of the advantages of autofluorescence spectroscopy, compared to WLC or NBI for instance, is that it has the potential to be applied across every step of diagnosis, including urine and shed cell analysis as well as tissue analysis during cystoscopy. At the cellular level, autofluorescence microscopy and related methodologies can be used to elucidate the metabolic processes occurring in cancer cells. Autofluorescence microscopy has recently contributed to the identification of specific cancer stem cell populations[181]. At the tissue level, the picture of autofluorescence becomes more complicated, with contributions from structural proteins such as collagen and elastin and the scattering of light by blood in tissue and, in some cases, melanin.

Urine autofluorescence also displays promise as a non-invasive clinical adjunct. Urine emits significant fluorescence under UV and blue light irradiation, possibly related to shed NADH, flavins and amino acids. Masilamani *et al.* suggest that the major contributors to urine fluorescence are flavoproteins and porphyrins[182]. Clinical relationships have been observed previously between urine autofluorescence and the presence of ovarian[183], colorectal[184] and lung cancer[185] as well as bacteriuria[186], however there is very little research in the field concerning the diagnostic worth of urine fluorescence spectroscopy for BCa.

To account for the variability in autofluorescence intensity between patients, a great deal of the current research in AS is in the development of diagnostic ratios to aid and improve sensitivity and specificity. The most frequently studied diagnostic ratio is the optical redox ratio (ORR), which gives a measure of the metabolic state of cells and tissues by ratioing fluorescence from NADH against fluorescence from flavins (equation 1):

$$\mathrm{ORR} = [\mathrm{NADH}]/[\mathrm{FAD}]$$

Equation 1 Calculation of the optical redox ratio (ORR)

The theoretical basis for the ORR lies with the Warburg effect[187], whereby it is hypothesised that as cells become malignant and change their functional machinery to promote an invasive and rapidly proliferating phenotype, they undergo a metabolic switch. Normal cells will tend to address their energy needs by producing adenosine triphosphate (ATP) by the process of aerobic respiration. To do this, glucose is catabolised and fed into the Krebs cycle, following which the metabolic intermediates NADH and FADH act as electron transporters to fuel ATP synthase in the mitochondria via oxidative phosphorylation, yielding NAD/FAD + H+. Cancer cells which have undergone metabolic modifications according to the Warburg effect no longer generate energy via oxidative phosphorylation, instead meeting their energy needs via accelerated glycolysis. As a result, NADH generated in the first steps of the respiratory process can no longer act as electron donors for oxidative phosphorylation, leading to an accumulation of NADH within cells. Crucially, it is only the reduced form of NADH (NADH) and the oxidised form of FAD (FAD) which fluoresce, therefore the ORR considering NADH and FAD levels can act as a marker of the increased rate of glycolysis compared to oxidative phosphorylation in a cell. The biochemical underpinning of the Warburg effect is detailed in Fig. 12.

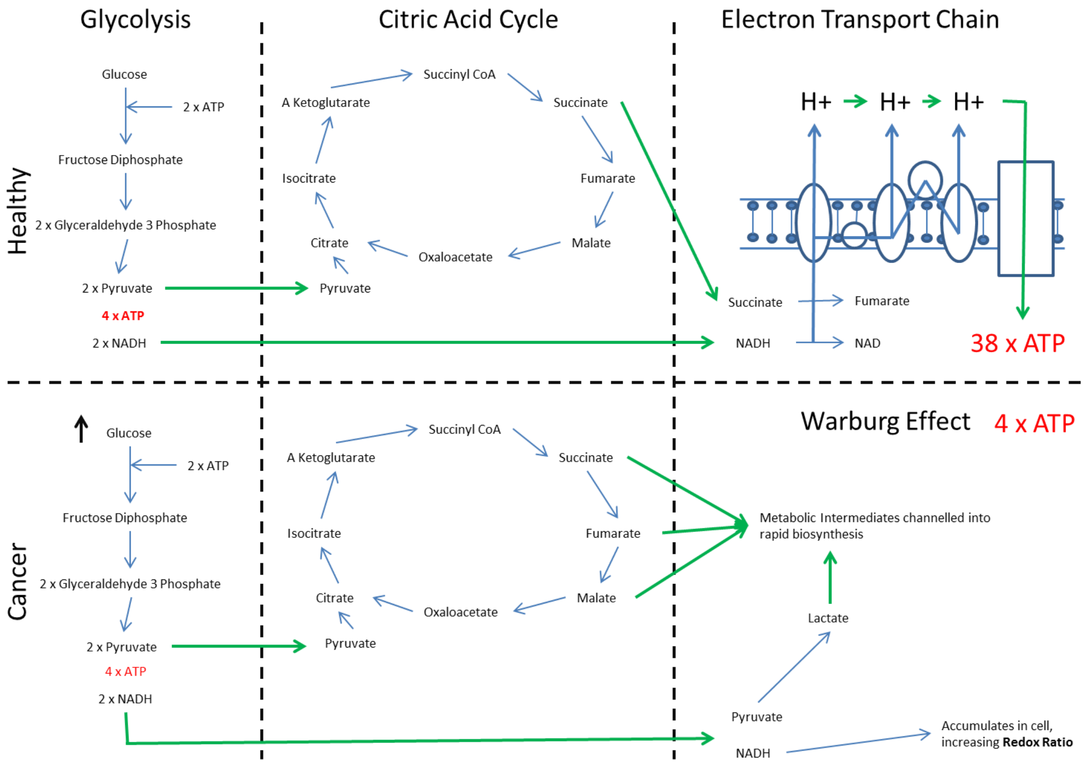

Figure 12 Molecular and cellular consequences of the Warburg Effect, adapted partially from text by Vander Heiden et al.[187] and text and figures by Chiarugi et al.[188]. Glycolytic switch in cancer cells causes a shutdown of the electron transport chain and an accumulation of NADH.

There exist various methods by which to calculate the redox ratio (e.g. NADH/FAD, FAD/NADH, FAD-NADH/FAD+NADH) but the crucial aspect of the ORR is that it reflects an increased relative NADH content in cancer cells (for instance ORR measured as NADH/FAD is higher in cancer cells than normal cells while ORR measured as FAD/NADH is lower in cancer cells than normal cells). ORR measurements have also been applied to the differentiation of healthy and pre-cancerous epithelia[189], identifying subtypes of breast cancer cell[190] and demarcating brain tumour margins[191]. Cicchi *et al.*

previously observed a statistically significant ORR between healthy bladder mucosa and CIS in a small sample study[98]. Other diagnostically relevant ratios include the tryptophan to NADH ratio[192] and collagen to NADH ratio[193]. The ability of the ORR in particular to identify pre-cancerous mucosa marks it as an attractive modality for the study of bladder cancer, potentially providing an opportunity with which to detect CIS, however ORR imaging has yet to be applied clinically.

In summary, BCa is a common disease associated with high morbidity and high recurrence and progression rates. Current gold standard detection techniques suffer from low sensitivity, especially for early stage cancers and the pre-malignant CIS. Steps have been taken to remedy the sensitivity issues encountered by gold standard techniques, namely with the development of PDD using PS and a wide range of urine diagnostic kits. These next generation techniques have suffered from low specificity, inter-user variability issues and increased cost compared to gold standards. Current research in the field aims to overcome the sensitivity/specificity dilemma of BCa diagnosis, however issues still remain: novel PS agents still suffer from low tissue penetration, nano-particles are shown to accumulate in tissue and contribute to systemic toxicity and the nascent field of autofluorescence spectroscopy, although promising, requires extensive validation and clinical testing before being considered a useful diagnostic adjunct. Similarly, PDT of BCa has been faced with similar issues, including non-specific toxicity and poor tissue penetration of dyes and activating light. Improved methodologies for the diagnosis and therapy of BCa which address some of these issues could allow the development of reliable clinical tools to reduce cost and increase patient quality of life.

1.1.9 Light-Oxygen Effect

A potential method for improving PDT is to do away with PS altogether. It has previously been suggested in the literature that direct irradiation of tissue in the near infrared at 1268nm can induce potent singlet oxygen generation, leading to cell death, the so-called light-oxygen effect (LOE). This is accomplished through the direct spin transition of molecular oxygen from triplet to singlet state through donation of energy by 1268nm light, rather than by the excitation of PS with subsequent release of singlet oxygen. This could prove beneficial for situations in which PDT is hampered by limited PS distribution, low light penetration into tissue containing deeper lying tumours and also in reducing non-specific toxicity. Furthermore, the application of LOE would remove the associated cost of PS, patient lay-up time and discomfort during PS administration.

Direct generation of singlet oxygen through spin transition following 1268nm irradiation was first observed by Matheson *et al.* in the 1970s[194]. Subsequently, much work has been done on the LOE in animal models and cell lines to characterise cellular and systemic effects[195]. The LOE has shown significant effects in both breast cancer and HeLa cell lines. The effects of LOE on HeLa cells were not reproduced in healthy HaCaT cells – this was attributed to the differential activation of Calcium channels and their respective effects on cell signalling[196]. Anquez *et al.* assessed the morphological effects of breast cancer cells exposed to 1268nm laser irradiation over time, demonstrating progressive morphological changes suggestive of apoptosis[197].

Crucially, LOE has not been demonstrated for bladder cancer, so we have no knowledge of its applicability to this disease. The validation of LOE in bladder cancer cells could allow for the development of a multi-functional laser system which detects (using AS) and eradicates bladder tumours (using LOE) without the need for administration of PS.

1.2 Light-tissue interactions

Human tissue can generally be considered as a non-uniform, turbid, light-scattering medium with contributions from various cellular and molecular components. Light entering tissue may encounter a wide range of different molecules which can either scatter or absorb the incident light. Occasionally, some light can also be entirely transmitted through tissue. The degree to which light is scattered, absorbed or transmitted through tissue depends greatly on the tissue type and thickness and can be influenced by the presence of blood, water and melanin. The physical underpinning of the optical properties of biological tissue has been comprehensively covered by Jacques *et al.*[198]. Detailed below are the possible fates of incident light when entering tissue (Fig. 13):

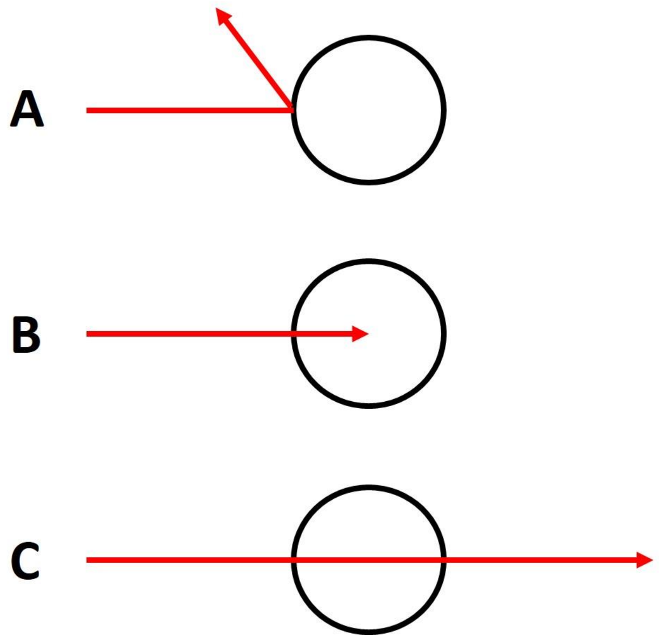

Figure 13 Fates of light entering tissue: light can either be scattered (A), for instance by cellular components such as nuclei; absorbed (B), for instance by hemoglobin, water and tissue fluorophores; or transmitted through full tissue (C)

The physical properties of tissue can have a significant bearing on how to measure the tissue autofluorescence. Briefly, in order to study tissue autofluorescence the following must be achieved: deliver sufficient light to be absorbed by the molecules of interest;

deliver the optimal excitation wavelength of light for the molecule of interest; detect the emitted fluorescence with high sensitivity. The scattering properties of tissue can affect both the first and third of these.

1.2.1 Scattering of light

Scattering of light occurs when a photon interacts elastically or inelastically with a molecule without being fully absorbed. Many components of mammalian cells are potent light scatterers, including the cell nucleus and mitochondria. The scattering properties of a tissue are denoted by its coefficient of scattering (μ_s). Within each cell, light will encounter dozens of scatterers. This must be considered when applying appropriate imaging methodologies. There are many forms of scattering which occur at a cell/tissue level, including Mie, Rayleigh and Raman scattering. Furthermore, the scattering properties of tissue are known to change as healthy tissue turns to cancer, in particular due to nuclear enlargement, tissue thickening and increased blood content due to inflammation and neovascularisation.

The wavelength of light can affect its inherent scattering properties – for instance, the short wavelength of UV light means it is more likely to encounter interactions with small molecular scatterers within cells and tissues than longer wavelength red light. Propagation of light through tissue also depends on the direction of scattering events (dictated by the physical nature of a tissue’s constituent molecules). Forward scattering of light by molecules serves to help light propagate further into tissue, while back-scattering of light by molecules impedes propagation resulting partly in diffuse reflectance. With regards to AS, scattering events which propagate light deeper into tissue may increase the fluorophores which light comes into contact with.

Another issue to consider when applying AS is how to measure the emitted fluorescence, especially in a highly absorbing and scattering environment. Both blood and melanin are known to strongly absorb UV and visible light. Increased blood and melanin content in tissue have been shown to correlate with reductions in the measured tissue NADH fluorescence [199].

1.2.2 Absorption of light

Absorption of light occurs when the relative energy of incident light is suitable to raise the energy profile of an absorber. This is known as “excitation” and is denoted as a transition from S0 to S1, as denoted in the Jablonski diagram below (Fig. 14):

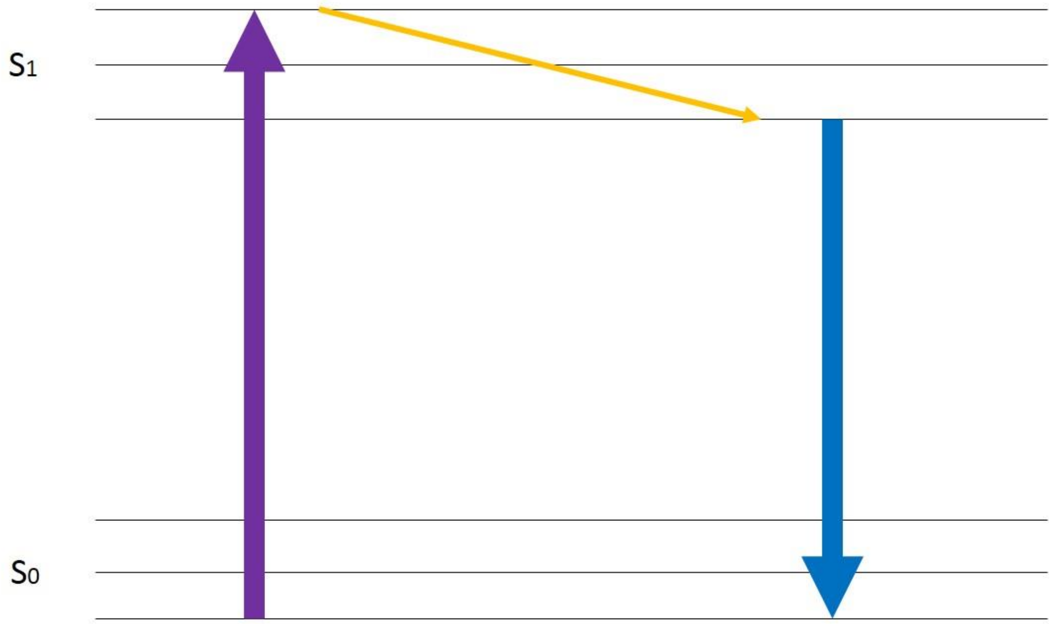

Figure 14 Jablonski diagram denoting the absorption of light by a molecule (purple arrow) and energy release (blue arrow)

Jablonski diagrams depict the discrete energy levels present in a specific molecule, at both the ground state and excited states. In this case, the purple arrow on the left represents the excitation of a molecule to singlet state through the absorption of a photon of light (purple arrow). Excitation of a molecule can be followed by vibrational relaxation (yellow arrow), often in the form of heat loss. Finally, during fluorescence, the remaining energy is released in the form of an emitted photon (blue arrow) returning the energy of the molecule to ground state. The absorption of light by a tissue will depend heavily on the “absorption maxima” of its constituent molecules and is defined by its coefficient of absorption (μ_a). Fig. 15 below details the absorption spectra of NADH and its oxidised form NAD, showing their absorption maxima at 260-270nm, with an additional strong absorption peak for NADH at 340nm. The absorption properties of these molecules can be applied to differentiate between them.

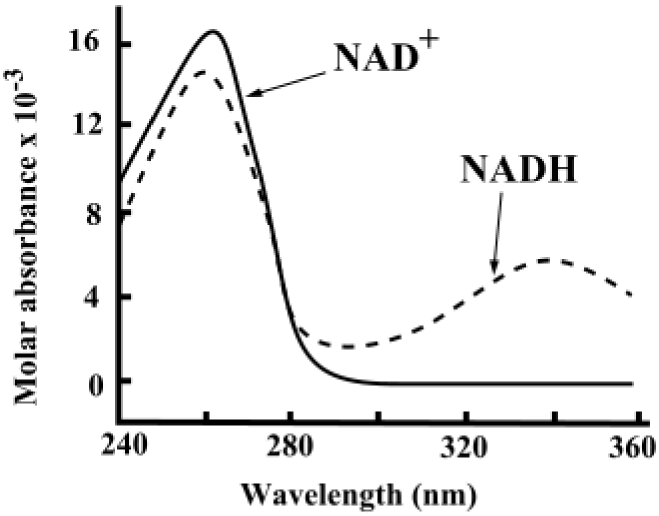

Figure 15 Absorption spectra of NAD+ (solid black line) and reduced counterpart NADH (dashed black line) between 240-360nm (courtesy Cronholm114 via Wikipedia.org, reproduced through public domain access (By Cronholm144 - Own work, Public Domain, https://commons.wikimedia.org/w/index.php?curid=3258108))

Most molecules in the human body will absorb light energy, but not all will fluoresce. The absorption maximum of a molecule relates to the amount of energy required to elevate it to its excited state. The donation of energy by light to molecules is heavily dependent on its wavelength, as shorter wavelength light (towards UV) contains higher relative energy per photon than longer wavelength light (towards IR). Fig. 16 shows the conventionally used wavelength range for AS applications within the electromagnetic spectrum.

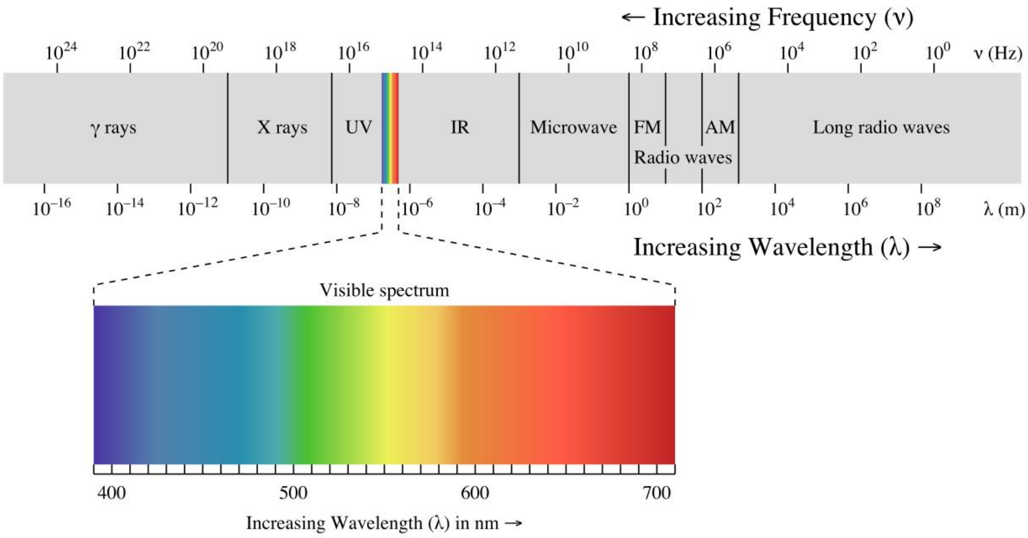

Figure 16 Electromagnetic spectrum showing the wavelengths of UV and visible light (reproduced freely under CC-BY license, courtesy Philip Ronan via commons.wikimedia.org (https://commons.wikimedia.org/wiki/File:EM_spectrum.svg))

Generally, most of the common endogenous fluorophores contain excitation/absorption maxima in the UV range, therefore illumination of tissue with UV light often causes simultaneous fluorescence from a range of molecules (demonstrated in Fig.10). Furthermore, light entering tissue can also be absorbed by both blood and by melanin. Much like scattering, the absorption of light by tissue is heavily dependent on the tissue type. In the bladder, we know from morphological studies that the main fluorophores in the top layers of mucosa will be the metabolic cofactors NADH and flavins, with possible contributions from lipofuscin and porphyrins. Therefore, the majority of UV light entering bladder tissue from the mucosal side will be absorbed by (and stimulate fluorescence from) these molecules. Although UV light is capable of exciting fluorescence from the structural proteins elastin and collagen in connective tissue, we may consider that the excitation of these molecules in intact bladder tissue will be impeded by light absorption and scattering from the mucosal layer. This is complicated somewhat by the higher quantum efficiency of structural proteins (defined as photons out/photons in) compared to NADH and flavins. Additionally, emitted fluorescence from these molecules may be strongly absorbed by NADH and flavins in the mucosal layer, impeding detection.

The effects of wavelength on tissue absorption and transmission can easily be demonstrated when holding a torch to human tissue. The reverse of the tissue appears red, not due to the illumination of blood vessels as once thought, but due to the complete transmission of red light through tissue, in contrast to shorter wavelength blue and green light.

One further concern when using UV illumination are the deleterious effects of UV exposure on human cells. UV irradiation of cells and tissues is known to be a potent carcinogen. With particular regards to cancer, therefore, we must be careful when employing UV AS that we do not induce new instances of cancer while diagnosing the old.

In recent years, multi-photon microscopy (MPM) has been enjoying increasing success for application to imaging biological systems. The basis of multi-photon microscopy is that the energy needs of a fluorophore can be met by the donation of energy by either 1 photon of high energy (short wavelength) or 2 photons of exactly half the energy (exactly double the wavelength). In theory, MPM allows imaging deeper into tissue and without the risk of deleterious effects of UV irradiation. A further benefit of MPM is that it can be used in conjunction with SHG to provide both structural and functional information on tissues. MPM is still yet to enjoy clinical application as laboratory setups for MPM devices are often bulky, requiring large high powered lasers and complex lensing systems.

An area of interest in biophotonics is in the “optical window” (Fig. 17), a range where absorption of light by blood and melanin (lower wavelengths) and water (higher wavelengths) are minimal. In this region, light penetration through tissue is at its greatest extent. In theory, this wavelength range should prove useful for the application of AS for the detection of deeper lying tumours and pre-cancerous tissue such as CIS, however the difficulty lies in finding a suitable fluorophore which is excited optimally at such long wavelengths. One suggestion is the excitation of endogenous porphyrins such as PpIX using 630nm light and recording the fluorescence emission at 710nm.

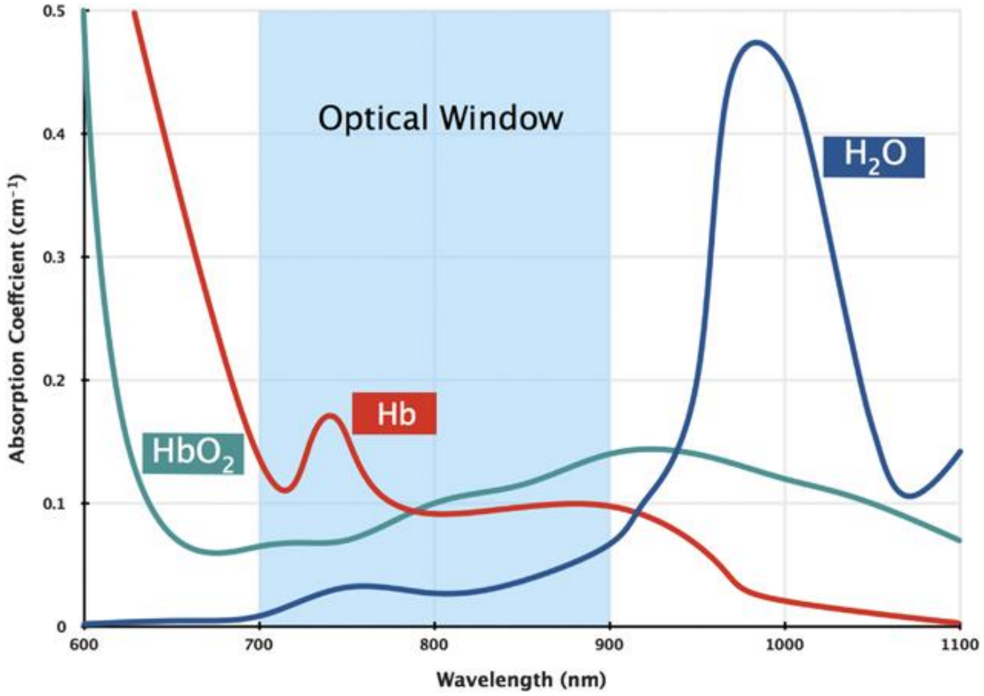

Figure 17 Diagram of the "Tissue Optical Window" displaying absorption of light by oxygenated blood (cyan line), deoxygenated blood (red line) and water (blue line) between the wavelength range of 600-1100nm (reproduced with permission from Nature Publishing Group, courtesy Phan & Bullen, 2010[200]

1.2.3 Energy release

Molecules in excited state are inherently unstable and release energy ("relaxation") through one of a few ways, including through thermal release, phosphorescence and fluorescence. The third, downward pointing arrow in the Jablonski diagram relates to the release of energy as a molecule relaxes. Often, molecules release energy in the form of heat, but some molecules (endogenous fluorophores) release energy in the form of an emitted photon. Owing to laws of energy conservation and the loss of a small amount of energy as heat (the second arrow in the Jablonski diagram), the emitted photon is always of a lower energy than the exciting photon. For instance, fluorophores excited using blue light will emit fluorescence in the green and yellow region, but never the UV region. The intensity with which a fluorophore fluoresces depends on the absorption cross-section of the molecules, its quantum efficiency and also the wavelength of excitation light. NADH, for instance, possesses an absorption maximum at 260-270nm (seen above), therefore it will fluoresce more intensely under illumination with this wavelength of light. NADH will cease to absorb light above approximately 400nm, therefore wavelengths of light longer than UV are inefficient for exciting NADH fluorescence.

Endogenous fluorophores each have a specific molecular fingerprint with regards to fluorescence. Generally, excited fluorophores emit photons within a narrow range of wavelengths, the full range of which can be seen when measuring a fluorescence spectrum. The emission profile of NADH, for instance, may span the wavelengths of 420-520nm with an emission maximum at 490nm. This means the most commonly emitted wavelength of photon by an excited NADH molecule is at 490nm. The emitted fluorescence spectrum of a given molecule will depend on the interactions between this molecule and others (for instance, bound NADH has slightly different optical properties from free NADH).

Non-specific heating of tissue should also be considered when applying AS. The absorption of light by water and blood will undoubtedly cause thermal effects in tissue, related to the optical power applied. Thermal effects on tissue can include the destruction of cellular DNA and protein denaturation. A balance must be struck in AS between extremely low power light with little damaging side effects at the expense of limited tissue fluorescence and extremely high powered light sources which excite significant tissue fluorescence at the expense of extensive tissue damage.

1.2.4 Second harmonic generation

In certain molecules with non-centrosymmetric surfaces (collagen being the best example), incident light can interact inelastically to produce forward propagating light of double the frequency through second harmonic generation (SHG). Crucially, in SHG the incident energy is entirely conserved, so there are no deleterious effects of energy absorption by tissue. Light in the NIR range (within the optical window) can thereby be used to study the presence, volume and spatial distribution of collagen in tissue non-invasively. The use of SHG to study collagen presents a few advantages over AS (optimal collagen autofluorescence is excited in the 200-300nm UV range): firstly, the longer wavelength of light used for SHG (generally around 800-900nm) can penetrate deeper into tissue as it exists in the “optical window” and is thus less readily absorbed by tissue. Secondly, the longer wavelength of light used causes fewer deleterious effects to tissue, especially when considering that SHG is an energy conserving process.

1.2.5 Modelling light tissue interactions

The clinical application of AS techniques may be enhanced through the use of computer simulations of tissues of interest. Computer modelling programmes such as TracePro allow users to create tissue models based on the optical properties (μ_a, μ_s) of the tissues of interest. Such models allow researchers to investigate the trajectory and interactions of incoming light of different wavelengths and intensities using Monte Carlo simulations for instance. Such simulations may inform the layout of optical probes, the choice of appropriate wavelengths of light for tissue diagnosis and therapy and the identification and monitoring of optical effects of tissue transformation. Monte Carlo modelling has previously been utilised to represent skin tissue across a range of wavelengths[201] and for the study of NIR properties in healthy and diseased breast tissue[202]. The development of an AS system for bladder cancer diagnosis with an accessory simulated tissue model could be of real clinical worth.

1.3 Multi-Functional Laser Based Non-Invasive Diagnostic Systems (MLNDS)

One class of medical technology receiving increased attention of late is that of multi-functional laser based non-invasive diagnostic systems (MLNDS). The term MLNDS covers a wide range of related systems, all with the broad function of diagnosis and therapy of disease non-invasively. Lasers are particularly suitable for application in non-invasive diagnosis as their wavelengths can be narrowly specified for fluorophores of interest. The setup of a laser is based around the stimulated emission of radiation of in phase light through a gain medium. The wavelength of laser light is tightly controlled by the choice of gain medium and the power can be controlled by setting the initial voltage. The advantages over broadband or white light illumination include increased specificity and efficiency of imaging processes along with the need for reduced optical powers. Most lasers used for medical spectroscopy nowadays possess optical powers in the range of milliwatts (mW) so as to avoid damaging effects on tissue through non-specific heating. The range of lasers commonly available nowadays (Fig. 18) are detailed below:

Gain media within the laser cavity are excited by the source (electrical or optical) to emit a photon (stimulated emission). Photons emitted by molecules within the gain media excite photon emission from further molecules, amplifying the initial photonic signal which is reflected by mirrors on each side of the cavity before exiting as a single beam. The uniform nature of the gain media ensures that emitted photons are in-phase and of the same direction and wavelength.

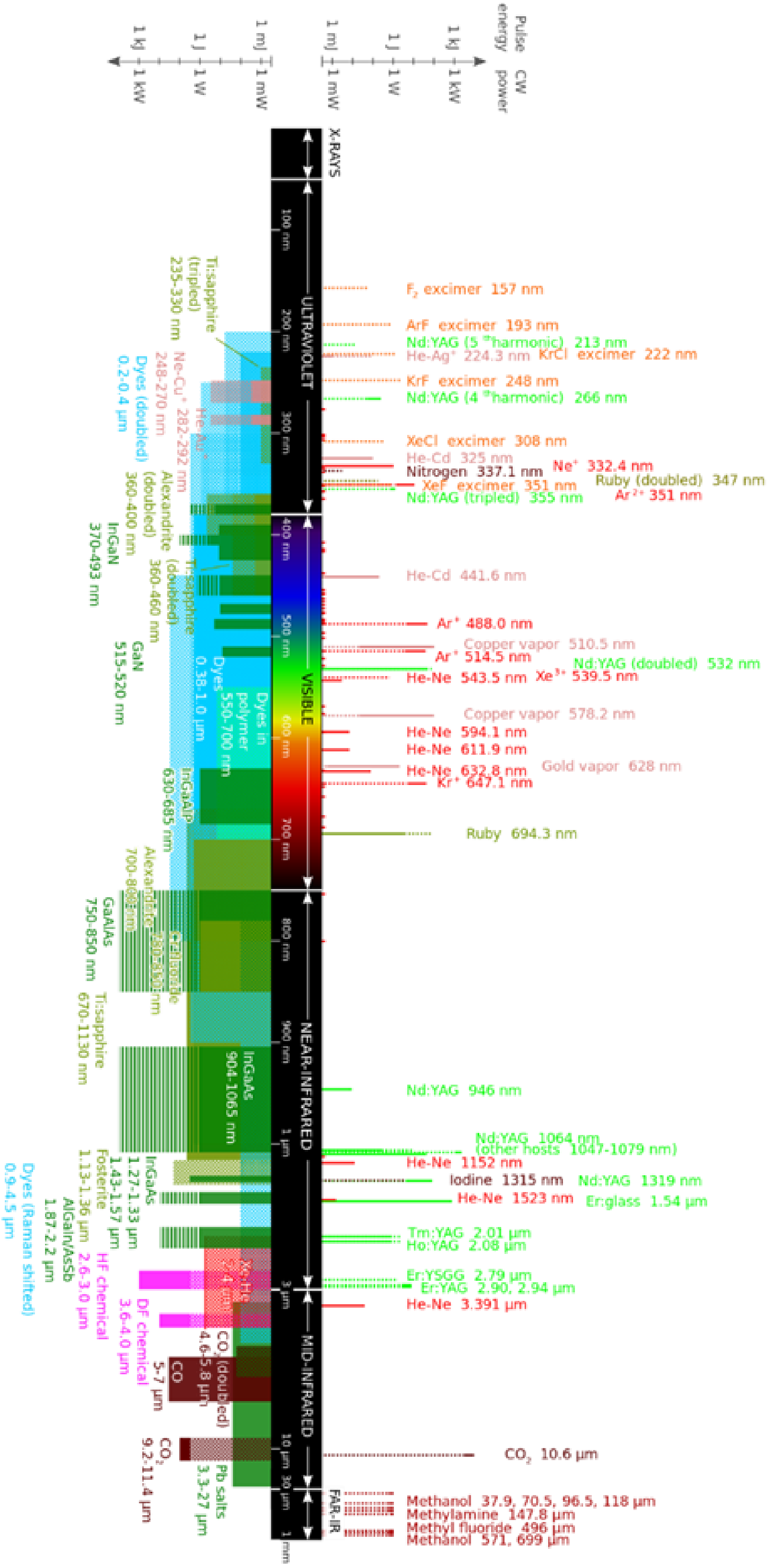

Figure 18 Range of commercially available lasers, reproduced freely under a CC-BY-SA license (original figure created by Danh, via Wikipedia.org: https://en.wikipedia.org/wiki/Laser#/media/File:Commercial_laser_lines.svg)

MLNDS are easily applicable to accessible tissue surfaces such as skin, oral mucosa and bladder mucosa. Among the MLNDS is the “LAKK-M” system, developed by SPE-LAZMA, Russia. This device contains within it light sources and channels for measuring tissue oxygenation, tissue blood flow and tissue autofluorescence, connected to an optical probe for in situ application. The experimental setup of the LAKK-M system is detailed below (Fig. 19):

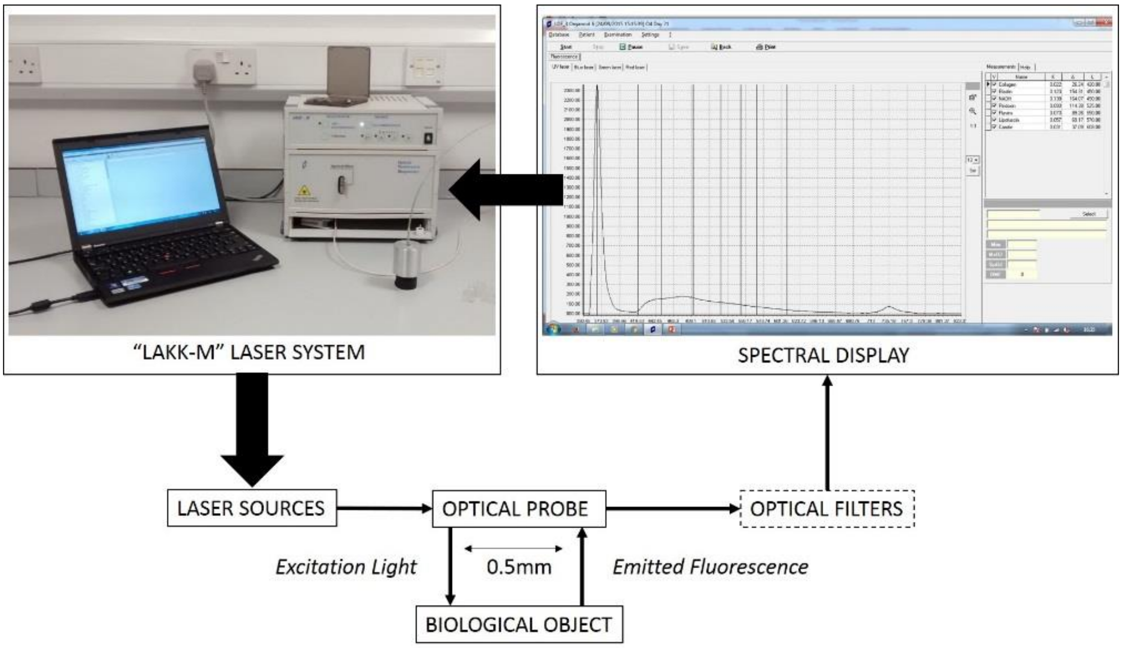

Figure 19 Experimental setup of the LAKK-M system

The functional unit of the LAKK-M (top left) contains the laser sources for AS, LDF and TRO. The sources for these channels are coupled to fibre optics which are delivered to the biological object (for instance tissue) by an optical probe with 2 mm diameter. The specific details of each laser source, including wavelength, function and optical power are included below (Table 4) alongside an illustration of the fibre layout within the optical probe (Fig. 20):

Table 4 Wavelength, source and optical power of the lasers used by the LAKK-M system

Wavelength	Function	Source	Filter	Power (mW)
UV (365nm)	AS	LED, continuous mode	Longpass, 370-2200nm	1.5
Blue (450nm)	AS	QD semiconductor laser, continuous mode	Longpass, 460-2200nm	3.5
Green (532nm)	AS TRO	Solid state laser, continuous mode Solid state laser, pulsed mode	Longpass, 540-2200nm	4.5 0.8
Red (635nm)	AS TRO	Semiconductor laser, continuous mode Semiconductor laser, pulsed mode	Longpass, 650-2200nm	5.5 0.5
NIR (1064nm)	LDF	QD semiconductor laser, continuous mode	-	1.2-1.5

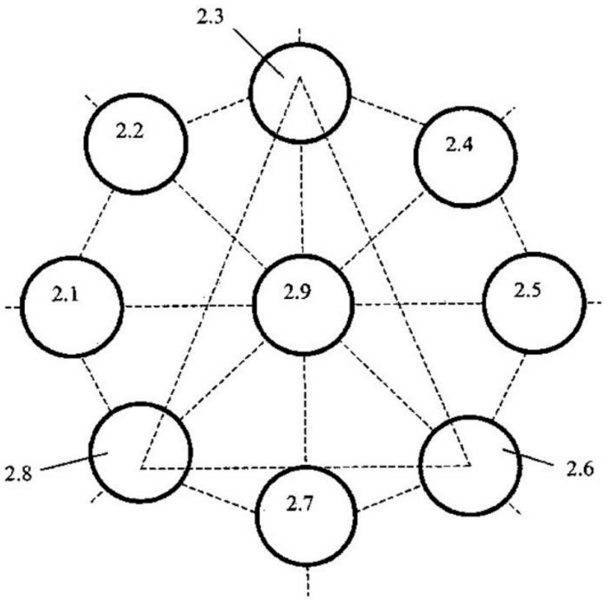

Figure 20 Layout of the LAKK-M optical probe including the source and detector fibres: (2.1) Green laser; (2.2) UV laser; (2.3) NIR laser; (2.4) Blue laser; (2.5) Red laser; (2.6) LDF detector; (2.7) TRO detector; (2.8) LDF detector; (2.9) AS detector. Separation distance between fibres = 1mm, diameter of each fibre = 100µm (120µm including cladding). NA for each fibre = 0.22.

The light is delivered to the biological object by gently touching the optical probe to the tissue surface. The light is transformed by tissue according to the parameter of interest and detected by detection channels in the optical probe. For AS, each excitation channel is separated from the detection channel by a distance of 1mm, measured centre-to-centre. The diameter of each fibre (excitation and detection) is 100µm (120µm including cladding) and each fibre has an NA = 0.22. For AS, the detected light is passed through a longpass filter to block the intensity of the back-scattered signal (the back-scattered intensity of incident laser light is often much more intense than that of fluorescence), following which the fluorescence is detected by a charge-coupled device (CCD) at 0.2nm increments between 350-823nm. Maximum transmission in the rejected region is 0.001%. Fluorescent light transmitted through the filter is dispersed in a polychromator, detected on a CCD and displayed in the analysis software as a complex fluorescence spectrum, normally with two peaks, the first of which represents back-scattered light of the same wavelength as the excitation light, and the second of which is the complex tissue fluorescence spectrum.

The AS laser sources included within the LAKK-M system are listed below alongside the endogenous fluorophores which they excite (Table 5)[203]:

Table 5 Excitation sources on the LAKK-M for AS

COLOUR	**WAVELENGTH**	**FLUOROPHORES**
UV	365nm	Collagen, Elastin, NADH, Flavins
Blue	450nm	Flavins
Green	532nm	Lipofuscin
Red	635nm	Porphyrins

From the complex fluorescence spectra recorded and displayed by the LAKK-M, it is possible to measure endogenous fluorophores of interest and calculate diagnostic ratios such as the ORR. An example spectrometer readout is included below with annotations (Fig. 21):

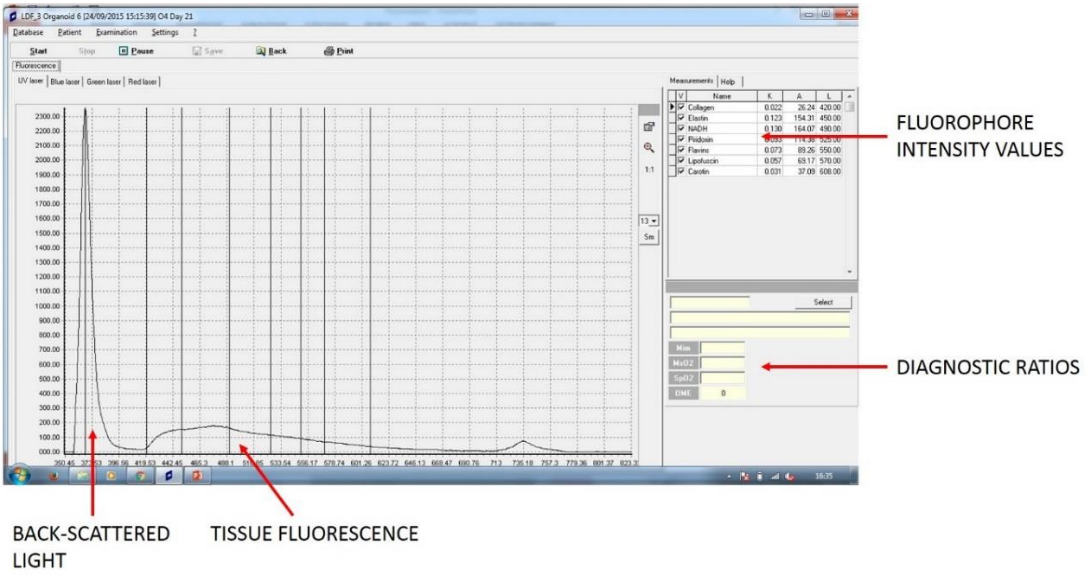
LDF_3 Organoid 6 [24/09/2015 15:15:39] O4 Day 21

	V	Name	K	A	L
▶	☑	Collagen	0.022	26.24	420.00
	☑	Elastin	0.123	154.31	450.00
	☑	NADH	0.130	164.07	490.00
	☑	Piridoxin	0.093	114.38	525.00
	☑	Flavins	0.073	89.26	550.00
	☑	Lipofuscin	0.057	69.17	570.00
	☑	Carotin	0.031	37.09	608.00

Mm
MsO2
SpO2
OME 0

Figure 21 Annotated screenshot of the LAKK-M spectrometer showing back-scattered laser light, fluorescence across 380-820nm and the measured parameters of fluorescence intensity for each fluorophore.

Fluorescence spectra measured using different excitation sources exhibit different fluorescence spectra, related to the varying contributions of endogenous fluorophores. Below are included example fluorescence spectra recorded from the skin of the finger using the four laser sources, annotated to include the wavelengths at which endogenous fluorophores of interest can be measured (Fig. 22-25). Wavelengths at which each fluorophore of interest are measured are selected in order to minimise spectral overlap between fluorophores, in keeping with previous work on tissue autofluorescence[180,204], including works utilising the LAKK-M system[179,199,205,206]: Comparison with measurements from fluorophores in solution are included in chapter 2.

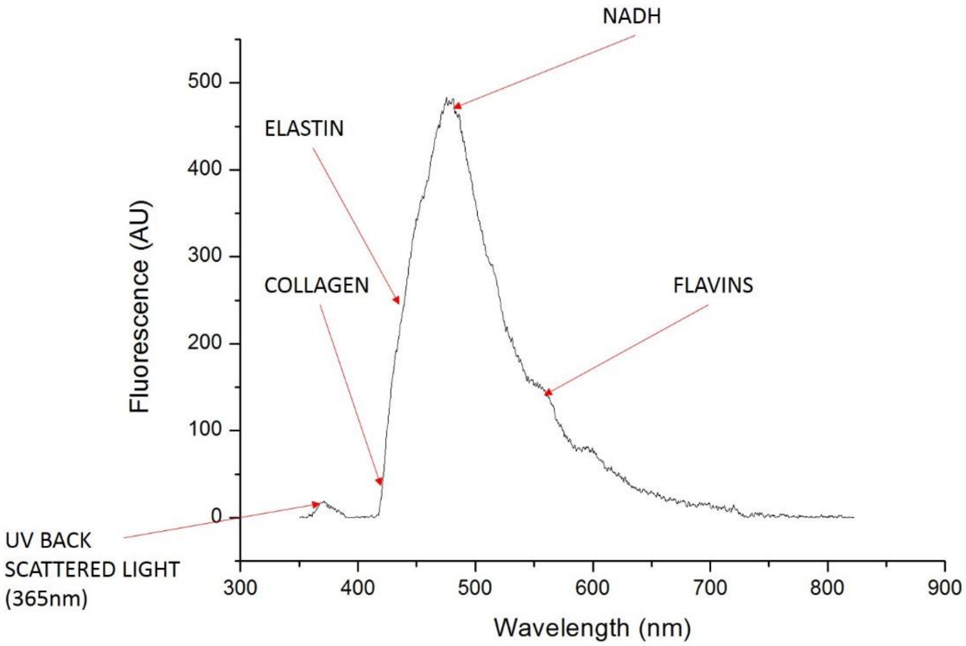

Figure 22 Example of a fluorescence spectrum recorded from the finger under UV excitation at 365nm

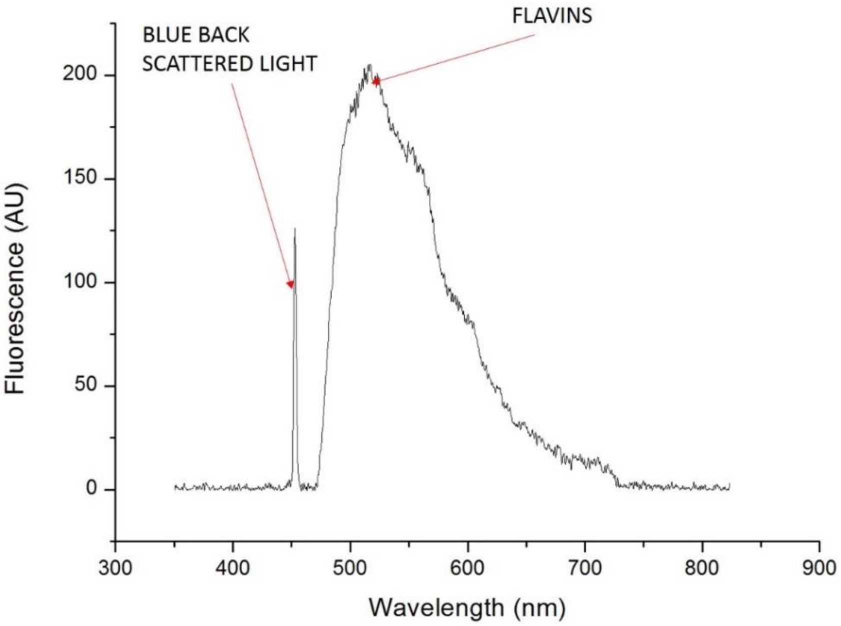

Figure 23 Example of a fluorescence spectrum recorded from the finger under blue excitation (450nm)

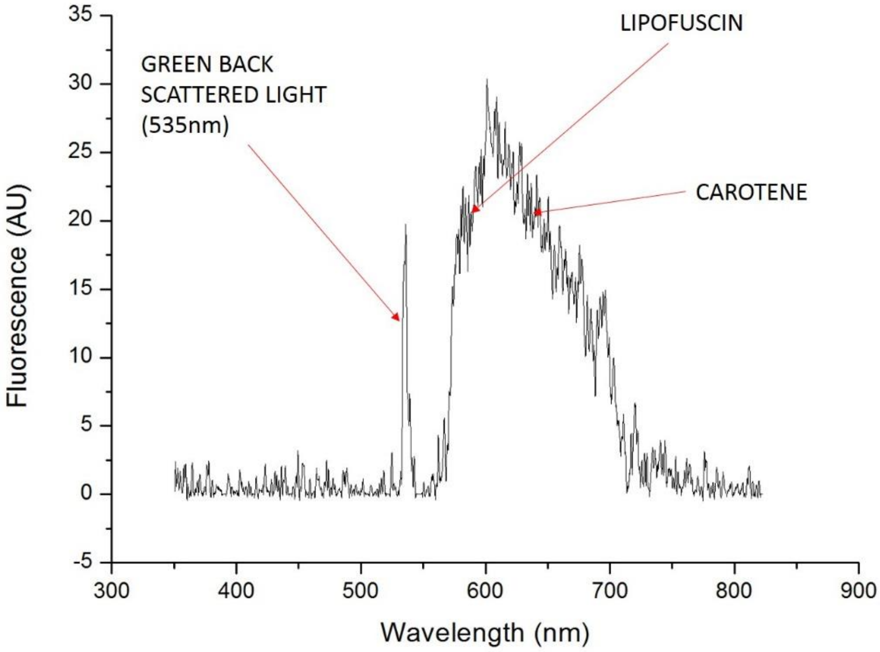

Figure 24 Fluorescence spectrum recorded from finger tissue excited using green light (535nm)

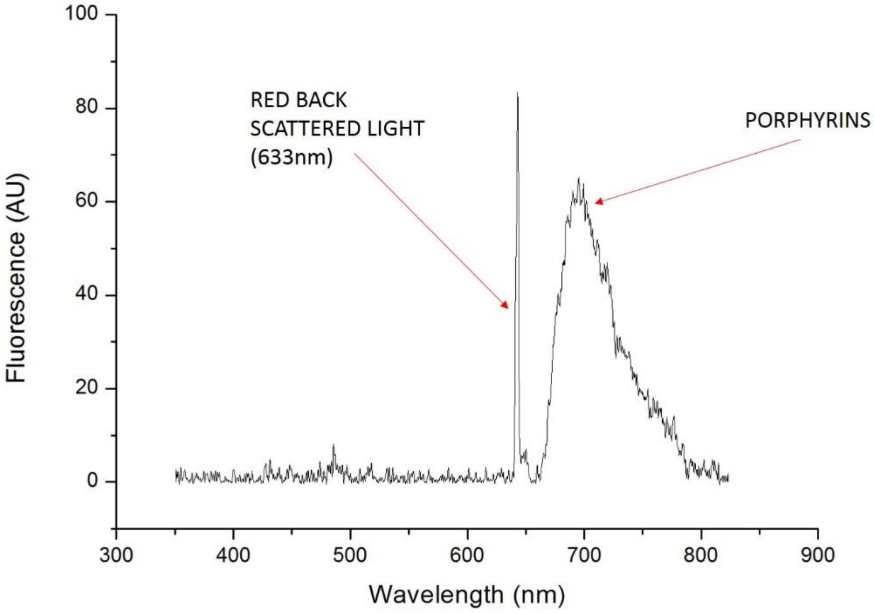

Figure 25 Fluorescence spectrum recorded from finger tissue excited using red light (633nm)

As seen in Fig. 22, UV excitation of tissue gives rise to a complex fluorescence spectrum with contribution from several endogenous fluorophores. Tissue excited using longer wavelengths of light (Fig. 23-25) gives rise to less complex fluorescence spectra as longer wavelengths of light outwith the UV range excite fewer fluorophores. Flavin fluorescence can be excited and recorded in both the UV and blue channels, as flavins are optimally excited around 450nm. The wavelength at which flavins are recorded changes between UV and blue spectra, due to the contribution to UV fluorescence from several other fluorophores (for instance, NADH).

Work is still ongoing to develop and apply the AS channel of the LAKK-M system clinically and diagnostically. Mayevsky *et al.* previously devised a similar system for multi-parametric measurements of NADH in brain tissue[207]. Recently, the LAKK-M was used to delineate differences in endogenous fluorophore levels such as NADH and flavins in a mouse model of cardiovascular disease[205]. Further work is also underway to optimise the technical performance of the device[208].

Our group previously reported the effects of various tissue parameters (such as blood volume and melanin content) on the measured parameters of fluorescence using the LAKK-M[199]. In this study, multi-parametric measurements were performed on volunteers with different skin colours and levels of nutritive blood flow. We measured the ORR values from different volunteers to better understand how this varies between healthy individuals. Melanin content was shown to inversely affect the measured parameters of UV fluorescence and the subsequent quantified levels of NADH, flavins, etc. Furthermore, nutritive blood flow was shown to significantly inversely effect the measured parameters of fluorescence from NADH and flavins. The fluorescence parameters of tissue in varying circumstance can therefore be probed successfully using the LAKK-M system. The physical properties of tissue (nutritive blood flow, melanin content, normal tissue variation, etc.) must also be taken into account when making measurements, although melanin content is of little consequence in bladder fluorescence analysis.

AS using the LAKK-M may be of worth to detect spectral differences between healthy and cancerous bladder tissue, however the worth of this device for the disease has not previously been studied. Work is required in the field to identify suitable biomarkers of bladder cancer which may be accurately monitored by the LAKK-M system, allowing its adaptation into a clinical device.

In addition to the AS channel, the LAKK-M system also possesses channels for measuring tissue blood flow parameters (using laser Doppler flowmetry (LDF)) and tissue oxygenation (using tissue reflectance oximetry (TRO)). Briefly, LDF works on the basis of Doppler shift of reflected NIR light by blood in tissue. NIR light directed to the capillaries via the optical probe is reflected by red blood cells. This reflected light is picked up by the LDF detector channel within the LAKK-M probe. Variations in blood flow velocity and red blood cell concentration are shown by variations in intensity of reflected light (proportional to Doppler shift of reflected light) which are recorded (as index of microcirculation (Im)) and can be used as the basis for medical diagnosis. Function and recent developments in LDF methodology have been reviewed elsewhere[209]. The effects of various physiological stimuli (exercise, occlusion tests, temperature, etc.) on the microcirculation can be evaluated using LDF. Furthermore, disorders and diseases can have an impact on tissue blood flow, affecting its regulation at several levels (neurogenic, myogenic, etc.), affecting the microcirculation within capillaries. LDF has been employed to study the blood flow and total blood volume of gastric cancer, in which blood flow was found to correlate with the presence of endothelial markers, particularly at the tumour periphery[210]. LDF can also be used to assess the efficacy of anti-angiogenic tumour treatment[211] LDF was first used to study bladder blood flow in 1996[212] and has previously been used for diagnosis of microvascular dysfunction in skin[213] and for the study of bladder cystitis[214]. TRO measurements are based on the preferential absorption of red and green light by oxygenated and deoxygenated haemoglobin in the blood, the proportions of which can change during the onset of disease. Index of microcirculation and values of tissue oxygenation (recorded as StO_2) combined can give values of tissue relative blood volume[215]. Our group have previously described the LDF and TRO channels of the LAKK-M device in greater detail, using the system to study the synchronisation of blood flow and oxygenation rhythms[215]. An annotated screenshot of LAKK-M readouts for index of microcirculation, tissue oxygenation and relative blood volume is included below (Fig. 26):

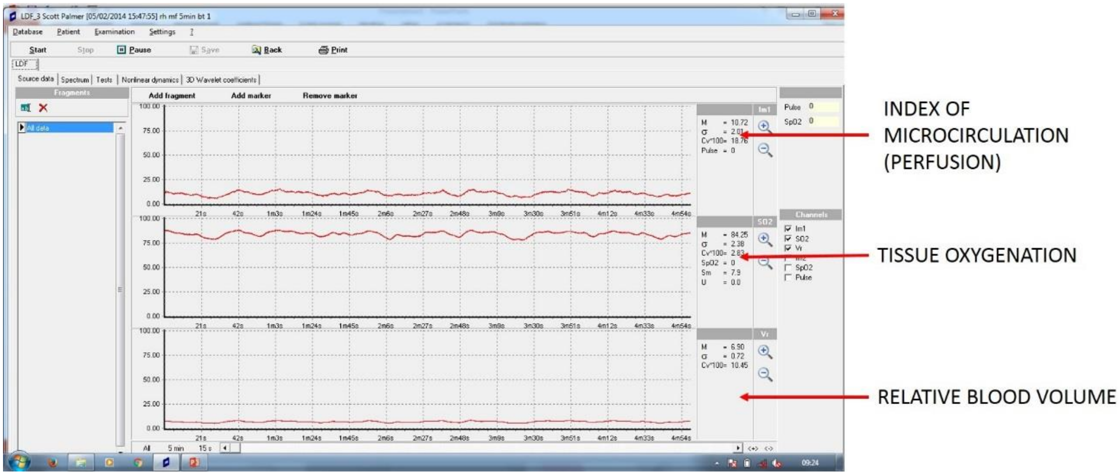

Pulse 0
SpO2 0

Im1
M = 10.72
σ = 2.01
Cv*100= 18.76
Pulse = 0

SO2
M = 84.25
σ = 2.38
Cv*100= 2.83
SpO2 = 0
Sm = 7.9
U = 0.0

Vr
M = 6.90
σ = 0.72
Cv*100= 10.45

Channels
☑ Im1
☑ SO2
☑ Vr
☐ Im2
☐ SpO2
☐ Pulse

Figure 26 Annotated screenshot of the LDF and TRO channel of the LAKK-M, including measured graphs and recorded values for index of microcirculation (perfusion), tissue oxygenation and relative blood volume

The roles of tissue oxygenation and blood flow in tumour development and progression are being widely studied in oncology. We know, for instance, that as tumours grow and develop, their interiors often become hypoxic[216], causing the need for angiogenesis which partially gives rise to the enhanced permeability and retention (EPR) effect, by which leaky, acidified tumours with high interstitial pressure take up and preferentially retain nanoparticles and some dyes. The effect of this is twofold: oxygenation of tumours relative to healthy tissue may decrease and the tumour may derive its blood supply from smaller, weaker blood vessels which are subject to alternative methods of regulation. Comprehensive simultaneous measurements of bladder tumours using the LAKK-M system (blood flow patterns, tissue oxygenation and biomarker quantification) may shed new light on the dynamic processes underpinning the disease.

Furthermore, with small adjustments to setup or measurement protocols, the LAKK-M could also serve to act as a spectrofluorimeter for fluorescence measurements of cell or molecular suspensions. Similarly, small modifications to the functional unit of the LAKK-M system could allow the addition of an extra channel for LOE. With particular reference to bladder cancer, the identification and validation of suitable biomarkers at the cellular and tissue level based on AS could pave the way for next-generation MLNDS for bladder cancer diagnosis.

1.4 Aims and objectives

The ultimate goal of the development of the LAKK-M system is a multi-functional medical device with the capacity to provide a wide range of diagnostic parameters to surgeons and clinicians through minimally invasive interaction with tissue of interest. Clinical application of the LAKK-M device as a spectroscopic probe for tumour detection relies heavily on technical substantiation. It is essential to identify reliable biomarkers with which to use the LAKK-M system to detect bladder cancer. Results of fluorescence analysis at the cellular and tissue level using the LAKK-M system will also hopefully help to corroborate earlier key studies in the field, including those by Koenig[113], Zheng[114], Aboumarzouk[112], Schafauer[116] and others.

The aim of this thesis is to explore the autofluorescence properties of bladder cancer across the range of cell to tissue with particular focus on diagnostic ratios such as the ORR. I also seek to address the applicability of the novel MLNDS system “LAKK-M” for diagnosis of bladder cancer at these levels. In conjunction with investigation into cell and tissue autofluorescence, lab grown bladder cancer organoids and computer tissue simulations with which to monitor and model endogenous fluorescence in developing bladder cancers are also explored. Finally, the applicability of the LOE using IR irradiation to bladder cancer cells is explored, discussing the therapeutic worth of this technique for the disease. The three main objectives, therefore, were:

1. Investigate the ORR in bladder cancer cell lines as a means to diagnose the disease from voided urine
2. Develop bladder cancer organoids with which to monitor changes in tissue fluorescence from metabolic and structural fluorophores over days and weeks.
3. Investigate the ORR in human bladder tissue using the LAKK-M system and identify other potential diagnostically relevant biomarkers

Primary hypotheses are that healthy bladder and bladder cancer at both the cell and tissue level would display significant differences in autofluorescence profiles - related to relative levels of structural proteins and metabolic cofactors – and the MLNDS system “LAKK-M” would be sensitive to these differences. In addition, I hypothesise that developing bladder cancer organoids will display progressive changes in fluorophore levels (both metabolic and structural fluorophores) as cancer grows over days and weeks. Finally, it is hypothesised that the IR treatment of bladder cancer cells will result in cell death through the pathway known as LOE.

The significant findings from this research were as follows:

1. Cancer cells display an elevated ORR (measured by flow cytometry as ex360em425-475/ex488em515-545) in comparison with healthy controls. This could potentially pave the way for novel non-invasive diagnostic techniques

2. Bladder cancer organoids grown in the lab show obvious changes in fluorescence profiles relative to control as tumours progress, specifically changes in the ORR (ex365em490/ex365em550), elastin to NADH ratio (ex365em450/ex365em490) and elastin/flavin ratio (ex365em450/ex365em550).
3. Bladder cancer tissue from human volunteers displays reduced ORR (ex365em490/ex365em550) and elevated porphyrin levels relative to healthy tissue. This finding could aid in the development of the LAKK-M system into a minimally invasive probe for the early detection of the disease

In addition, conclusions and future avenues of study for the application of second harmonic imaging of organoids, bladder tissue modelling using computer simulation and bladder cancer therapy using the light oxygen effect are discussed.

2. CELLULAR FLUORESCENCE ANALYSIS

2.1 Background

The aim of this work was to assess differences in autofluorescence between healthy bladder cells and bladder cancer cells. The ability to discriminate between healthy bladder and bladder cancer at the cellular level presents the opportunity to implement early diagnosis techniques for the disease non-invasively, analysing cells shed in the urine.

The perfect diagnostic technique for bladder cancer is sensitive, specific, quick and non-invasive. Urine analysis (urinalysis) is a completely non-invasive diagnostic technique, thereby causing no pain or discomfort to patients. Applications and limitations of bladder cancer screening have previously been discussed, being suggested as feasible but hampered by the lack of useful urinary biomarkers[217]. Urinalysis for diagnosis of bladder cancer has previously been explored extensively. Schmitz-Drager *et al.* among others have discussed the urgent need for novel urinary biomarkers for bladder cancer[218], while Karaoglu discusses the limitations to current urinary biomarkers, especially for non-muscle invasive disease[219]. Among the most common urinalysis techniques are NMP22, BTA STAT and Urovysion, which rely on antigens and cells shed in urine, however these techniques are hampered by limited sensitivity or specificity and require interpretation by skilled pathologists. Oge *et al.* demonstrated that BTA STAT detects bladder cancer with higher sensitivity than NMP22, however it was not sensitive enough to replace conventional cystoscopy[59]. Hosseini *et al.* also discuss the limited specificity of the NMP22 test[52]. It is clear, therefore, that advancements in the field of urinalysis for bladder cancer diagnosis are required to address the shortcomings of current modalities. Parker *et al.* have discussed some of the promising new modalities in urinalysis for bladder cancer detection[220].

Within cells, the main endogenous fluorophores of interest are the metabolic cofactors NADH and flavins. These fluorophores can be used to calculate the optical redox ratio (ORR), discussed in chapter 1, which is a measure of the metabolic activity of cells. Briefly, the Warburg effect occurring in cancer cells causes a glycolytic switch[187] which leads to relative increases in cellular NADH, increasing the ORR (calculated as NADH/flavins), therefore the ORR can be a useful tool for discriminating between healthy and cancer cells which have undergone a glycolytic switch. As the Warburg effect can occur in cells early in cancer development, in theory the ORR is capable of detecting early stage, low grade cancer cells. ORR differences between healthy and cancer cells have been previously reported for a wide range of cancers and pre-cancerous epithelia[189,221], alongside differentiating between different cancer subtypes[222]. ORR values for bladder cancer have not been extensively covered previously, therefore I intended to compare the ORR of healthy bladder and bladder cancer cell lines, with an aim to establish ORR analysis as an effective diagnostic technique for urothelial cells shed in urine.

Much is still unknown about how the autofluorescence properties of individual cells compare with that of complete tissues. Undoubtedly, there will be fluorophores contributing to tissue fluorescence which are not present in individual cells, especially in shed epithelial cells. The multi-functional laser system LAKK-M presents an opportunity to study and directly compare fluorescence of cells and tissues to discover similarities and differences.

Based on previous observations of other diseases, it is hypothesised that cancer cells will display an increased ORR compared to healthy cells. I propose that this difference will be detectable using the LAKK-M system, establishing it as a potential tool for voided urine cytology for bladder cancer diagnosis. Briefly, methodology involved: the design of cuvettes for use with the LAKK-M device (in matte black to minimise background noise); analysis of the fluorescence properties of NADH and flavins using this system; confirmation of mitochondrial origin of cellular autofluorescence; analysis of ORR discrepancies using a validated technique (flow cytometry) and finally the comparison of cells using the LAKK-M system.

2.2 Methods

2.2.1 LAKK-M System

LAKK-M multi-functional laser based non-invasive diagnostic system (MLNDS) was used for all fluorescence spectroscopy measurements. The LAKK-M contains sources for performing laser Doppler flowmetry (LDF), tissue reflectance oximetry (TRO) and autofluorescence spectroscopy (AS) and contains 5 laser sources for the various applications. The technical aspects of LAKK-M setup[208] and applications for skin tissue blood flow[215] and fluorescence analysis[199] have been covered previously. For fluorescence measurements, the following lasers are used: UV at 365nm; blue at 450nm; green at 530nm and red at 633nm. Laser sources are coupled to a fibre optic probe with diameter 2mm in which the source and detector are separated by a distance of approximately 1mm. Excitation light is supplied to tissue samples by gently but firmly touching the tip of the optical probe to the surface of the tissue of interest. Excitation light is supplied to the liquid solution or suspension samples by suspending the optical probe in the centre of the solution. This is made easier by the use of custom made cuvettes with lids to hold the optical probe in place. The subsequent fluorescence intensity from the object of interest is recorded in the detection channel of the optical probe, passed through the requisite filter and converted to an electronic signal via a CCD connected to an in-built spectrophotometer. The LAKK-M device is connected to a laptop with custom-made recording and analysis software “LDF” (version 3 of which was used for our work) created by SPE-LAZMA, Moscow, Russia, which displays the fluorescence intensities recorded by the inbuilt spectrophotometer in the form of a complex spectrum. Fluorescence measurements are performed in darkness to minimise interference and background noise from other light sources. To record spectra, “new experiment” is selected from the computer interface, the optical probe is put in the region of interest (ROI) and “start spectrometer setup” is selected, to calibrate the fluorescence channel. Upon receiving a green signal saying “spectrometer calibrated”, lasers can be switched on by pressing the corresponding button. Switching on the blue laser automatically switches off the UV laser, switching on the green laser automatically switches off the blue laser, and so on. The probe is held still for 30 seconds to ensure a stable signal, following which fluorescence spectra are recorded sequentially through UV, blue, green and red excitation sources. The optical probe is held perfectly in place for the duration of measurement. Spectra are recorded for each excitation source by selecting the button on the user interface saying “remember”, followed by “continue” to carry on study. Once all four spectra for a given sample are recorded, the study is stopped by selecting “stop” and “save” from the user interface. Excitation sources are associated with specific physical filters to block the intensity of back-scattered light (detailed in Table 4). These were changed accordingly as each measurement progressed from UV to red sources. The laser source must always be changed prior to the filter, to prevent aberrant results. From the database view, recorded spectra can be named and viewed to calculate fluorescence intensity parameters. From the spectrum view, data can be exported to excel spreadsheets in “csv” format by selecting from the user interface “export” -> “export data as”. The “csv” data contains 2 columns: wavelength (in nm) increasing in 0.2nm increments and corresponding amplitude of fluorescence in arbitrary units (AU). Figure 27 details the LAKK-M with accessory computer. The diagnostic probe of the LAKK-M is inserted into a cuvette for fluorophore measurements.

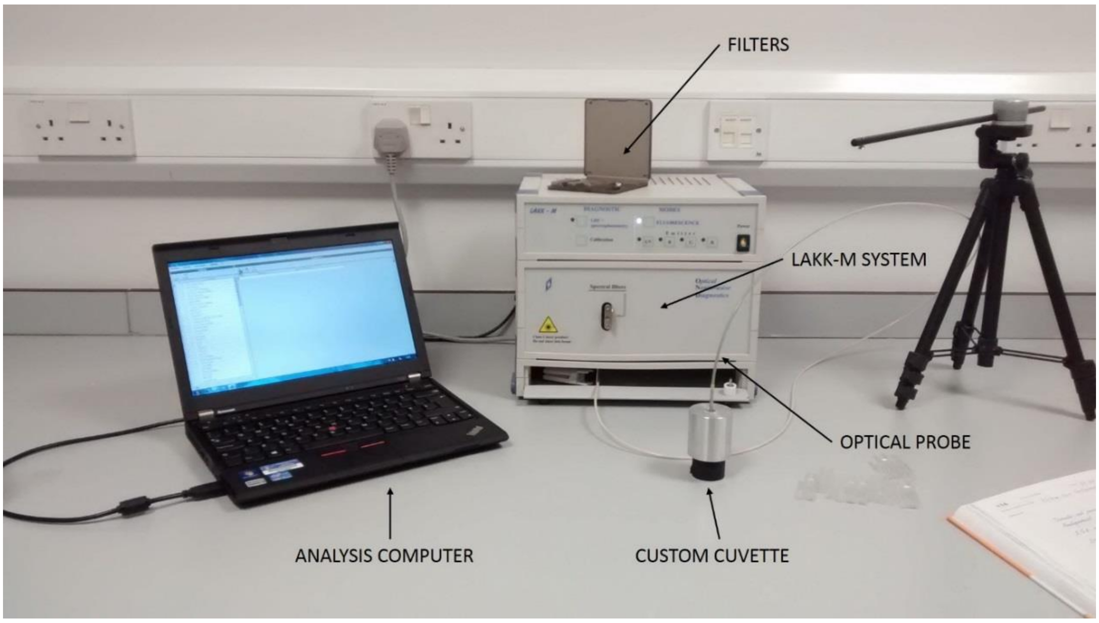

Figure 27 Experimental setup including LAKK-M system, attached laptop and cuvette

2.2.2 Cuvettes

For fluorophore and cell suspension fluorescence measurements, a cuvette (outer dimensions 10mm x 10mm x 30mm and inner dimensions 8mm x 8mm x 29mm) with a lid (dimensions 10mm x 10mm x 1mm, with a centred circular hole of diameter 2mm) was designed using 3D modelling software "123D" by Autodesk inventor, and printed in matte black plastic using a MakerBot 3D printer, Fulton Building, University of Dundee (Fig. 28B). The cuvette was designed to contain liquid solutions with a 2mm gap in the lid to allow addition of solutions, and to accurately hold the optical probe of the LAKK-M device in place. The development of cuvette informed further design of a more advanced custom cuvette in matte black plastic by SPE-LAZMA, Moscow, Russia (Fig. 28C). The custom built cuvette contained a matte black holding chamber with a stainless steel screw lid threaded to the exact dimensions of the chamber. The stainless steel lid contained a central holding reservoir for the LAKK-M optical probe (detailed below). Two similar types of custom matte black cuvette were designed, one with variable volume 100-300µl and one with variable volume 1-5ml.

The ability of custom made cuvettes to minimise background noise was tested by comparing them with a conventional clear plastic cuvette (Fig. 28A). All measurements were performed in the optics lab, Ninewells hospital, Dundee, in a dark room with the door closed to minimise background light. The LAKK-M system was switched on at least 30 minutes prior to use. First, the empty clear cuvette was placed beside the LAKK-M, with the optical probe held stably at a 2mm depth within the cuvette, with measurements being recorded across all 4 spectra. The 3D printed cuvette was then studied by attaching the lid and connecting the optical probe of LAKK-M through the holder to a depth of 2-3mm into the empty cuvette. Measurements were then recorded across all 4 spectra. Finally, the custom built cuvette was studied by screwing on the stainless steel lid and attaching the optical probe to the holder, holding the probe level with the top of the cuvette. Measurements were recorded across all 4 spectra. Measurements for all 3 cuvettes were repeated with the addition of 2ml PBS to each cuvette and recorded across all 4 spectra. Spectra were saved to the LDF analysis software, exported to excel files and graphed using Origin Pro 8 analysis software. A comparison of the background fluorescence across all 4 spectra from the 3 cuvette types is compared in the following section.

In addition, UV and blue fluorescence spectra were measured from a custom black cuvette positioned on a Gilson Labstir containing a magnetic stir bar, to determine the applicability of mechanical stirring to ORR measurements from cells. The setup of the custom cuvette on the LabStir, containing the stir bar, is included as Fig. 29 below.

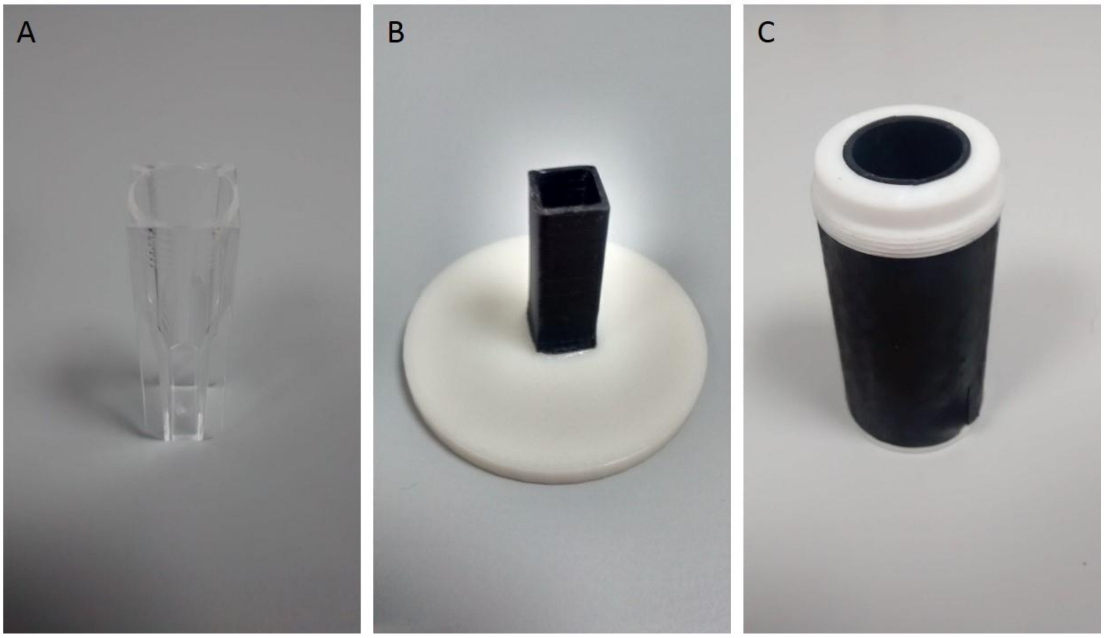

Figure 28 Cuvette types used for comparison: (a) conventional clear plastic cuvette; (b) 3D printed matte black cuvette; (c) custom made matte black cuvette

Figure 29 Setup of custom black cuvette on Gilson LabStir containing magnetic stir bar

2.2.3 Fluorophore Analysis

Reduced Nicotinamide Dinucleotide (NADH), Flavin Adenine Dinucleotide (FAD), Tyrosine, Tryptophan and Protoporphyrin IX powders were purchased from Sigma-Aldrich and prepared to serial dilutions starting at 1M in Phosphate Buffered Saline (PBS), purchased from Sigma-Aldrich. 300 µl of each fluorophore solution were added to the custom built matte black cuvette (SPE-LAZMA) (Fig. 30): the optical probe was attached following the previous protocol and fluorescence spectra of fluorophores were recorded across all four excitation wavelengths and archived to database for future reference. Additionally, a 1:1 mixture of NADH and FAD was studied across all 4 excitation wavelengths in the 300µl cuvette and compared to measurements of solutions of the pure fluorophores alone. 300µl Phosphate Buffered Saline (PBS) alone was added to matte black cuvette and analysed to determine background fluorescence. Serial mixtures of NADH and FAD were studied in the 5ml custom cuvette (Table 6) to assess accuracy of the computed optical redox ratio (ORR) parameters at the three suggested wavelengths (flavins measured at excitation 365nm emission 550; excitation 450 emission 510; excitation 450 emission 550):

Table 6 Relative NADH concentrations used to measure ORR using LAKK-M system

NADH Volume (ml)	**FAD Volume (ml)**	**Relative NADH (%)**
5	0	100
4	1	80
3	2	60
2.5	2.5	50

2	3	40
1	4	20
0	5	0

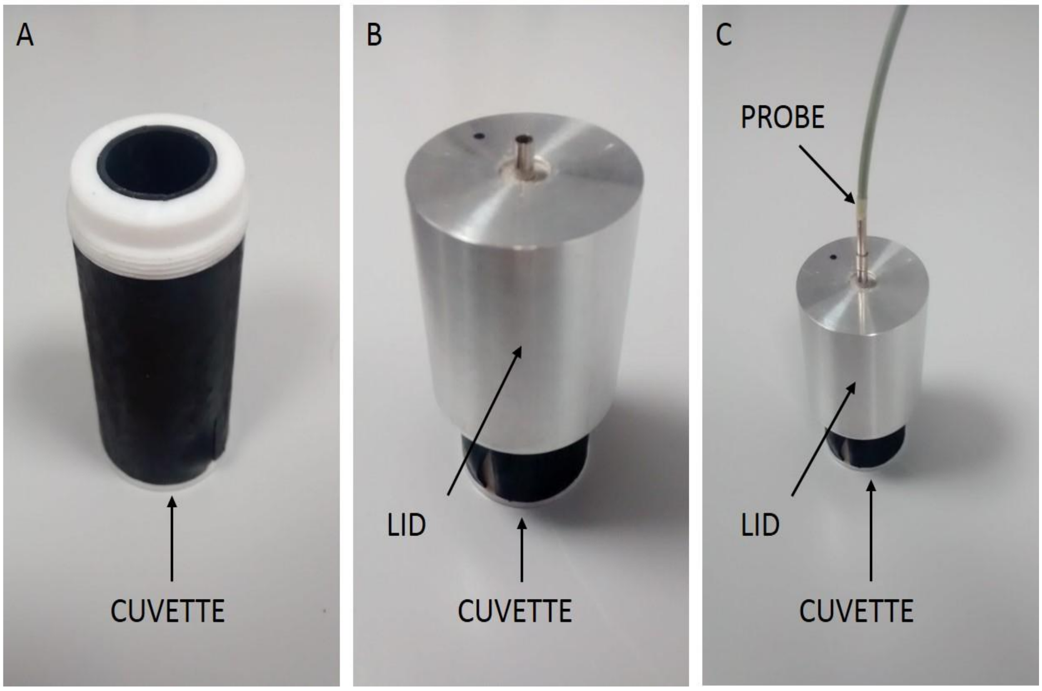

Figure 30 Cuvette setup for fluorophore and cell analysis: (a) solutions are pipetted into the top of the empty cuvette; (b) the stainless steel lid is screwed into place; (c) the optical probe of the LAKK-M device is placed into the holder in the lid

2.2.4 Cell Culture

Cells were seeded in sterile tissue culture hoods and grown in tissue culture incubators in the lab block of Ninewells Hospital and medical school, James Arrott Drive, Dundee, UK. The facilities used had no previous history of mycoplasma contamination and cells were certified mycoplasma-free upon delivery. Prior to all cell and tissue culture work, tissue culture hoods were opened, sprayed with 70% ethanol and cleaned thoroughly, then fans were switched on and left to run for at least 30 minutes prior to work being carried out.

The healthy bladder cell line “Human Urothelial Cell” (HUC), a weakly adherent cell line derived from human bladder urothelium, was purchased from ScienCell Research laboratories (Carlsbad, USA) and grown in 75cm^2 Corning culture flasks (Sigma-Aldrich) treated with Poly-L-Lysine solution (Sigma-Aldrich) to promote adherence. Culture flasks were treated with Poly-L-Lysine by adding 3ml Poly-L-Lysine solution per flask, rocking to thoroughly cover the growth surface and incubating flask for 15 minutes at 37^{o}C, 5% CO_2. Following incubation, the remaining solution was removed using a pipette and the growth surface was washed using PBS. Flasks were left for at least a day following polylysination before cell seeding. Cells were delivered on dry ice and rapidly thawed in a water bath set to 37^{o}C, mixed gently but thoroughly using a 1ml pipette and transferred to culture flask at a concentration of roughly 7500cells/cm^2 (cell concentration calculated using either a benchtop Coulter counter or haemocytometer). Cells were grown in complete Urothelial Cell Medium (UCM) (ScienCell Research laboratories) consisting of basal medium containing 1% Urothelial cell growth supplement (UCGS) and 1% Penicillin-Streptomycin. 15ml complete UCM was used per flask.

Human bladder grade II transitional cell carcinoma cell line “5637”, an adherent cell line with p53 mutation derived from a 68 year old Caucasian male, was purchased from American Type Culture Collection (ATCC) and grown in 75cm^2 Corning culture flasks in Dulbecco’s Modified Eagle Medium (DMEM) containing 10% Fetal Bovine Serum (FBS) and 1% Penicillin-Streptomycin using 15ml complete media per flask. Cells were delivered on dry ice to Ninewells hospital, thawed rapidly in a water bath set to 37^{o}C and gently but thoroughly re-suspended by pipetting.

Both cell types were maintained in a standard incubator set to 37^{o}C with 5% CO2 and media was replaced for both cell types every two days. Cells were split upon reaching 75% confluence to ensure normal growth was maintained. To do this, supernatant media was removed from flasks using a pipette. Cells were then washed in 2ml per flask 0.1% Trypsin-ethyldiaminetetraacetic acid (EDTA) to neutralise and remove remaining culture media. Following this, cells were incubated at 37^{o}C, 5% CO2 for 5-10 minutes in 3ml per flask 0.1% Trypsin-EDTA. After this period, cells were detached by gently nudging culture flasks. Cells were then re-suspended in 7ml complete DMEM to neutralise trypsin-EDTA solution. HUC cells were re-seeded at a concentration of 1:2 or 1:3 (cells from one flask used to reseed two or three new flasks), 5637 cells were re-seeded at concentration of 1:3 to 1:4.

To freeze, 1 x 10^6 cells detached by trypsinisation were spun at 1500RPM for 5 minutes in a benchtop centrifuge to form a cell pellet. Supernatant was removed and cells were re-suspended in complete DMEM containing 10% dimethyl sulfoxide (DMSO) an anti-crystallisation agent which enables cells to survive freeze/thaw. Frozen cells were maintained either in a -80^{o}C freezer or in liquid Nitrogen until further required.

2.2.5 Cell Fluorescence Analysis – Confocal Microscopy

5637 cells were grown to 75% confluence in #1.5 thickness coverslip bottom Petri dishes from Willcowells. Mitochondrial dye MitoTracker Red (Life Technologies) was prepared to a 1mM stock solution in DMSO and diluted to a 100nm solution in PBS (1% FBS). Prior to analysis, supernatant culture media was removed from cells in Petri dishes using a pipette, and cells were treated with 1ml/dish 100nM solution MitoTracker Red. Cells were incubated for 45 minutes with MitoTracker, after which solution was removed and 1ml PBS containing 10% FBS was added to Petri dish.

Stained cells in Petri dish were transported to the College of Life Sciences, main campus, University of Dundee for analysis in the light microscopy facility.

A Carl Zeiss 710 confocal microscope was used to observe cellular fluorescence using a 63x objective. NADH fluorescence was excited using a 60mW 355nm UV laser set to 100% power and recorded using a PMT across 401-462nm. Flavin fluorescence was excited using a 30mW 458nm blue laser set to 100% power and recorded using a PMT across 496-545nm. MitoTracker Red fluorescence was excited using a 30mW 543nm green laser set to 2% power and recorded using a PMT across 548-683nm. Optical powers were measured at sample. Images were saved to computer and transferred for visualisation and analysis using ImageJ image analysis software.

2.2.6 Cell Fluorescence Analysis – Flow Cytometry

5637 cells and HUC cells grown according to standard protocol to 75% confluence were trypsinised, neutralised and gently resuspended in PBS (1% FBS) using a 1ml pipette. Cell suspensions were filtered using a 30µl filter and kept on ice in FACS tubes until use. Samples were then transported in triplicate to flow cytometry core facility, College of Life Science, University of Dundee, Dundee for analysis.

A Becton Dickinson “Fortessa” flow cytometer was used. The flow cytometer was setup according to standard protocol, with forward scatter and signal width being examined by a blue laser of wavelength 488nm set to 162V. Following this, cellular NADH was excited using a 360nm laser set to 211V and recorded between 425-475nm and cellular FAD was excited using a 488nm laser set to 397V and recorded between 515-545nm. 10,000 cells were analysed from each sample (3 x HUC + 3 x 5637) with the results of forward scatter, side scatter and autofluorescence intensity saved in FCS files. The NADH value for each cell was calculated as a total intensity across excitation at 360nm, with emission at 425-475nm. The FAD value for each cell was calculated as a total intensity across excitation at 488nm, with emission at 515-545nm. FCS files were opened using "FCS Express" analysis software and dead cells were excluded from analysis using an elliptical inclusive gate between co-ordinates 3.8K, 68K and 113K, 154K, including 20,883 cancer cells and 19,564 healthy cells for analysis. Relative NADH and FAD contents were plotted on bivariate dot plots to create "redox overview" and NADH and FAD values for each cell were exported to excel spreadsheets. Taking the ORR value rather than absolute amplitudes meant calibration was not required. ORR values for each cell were calculated in excel by dividing NADH by FAD. ORR values for each cell were exported to SPSS for statistical analysis, cells being classified by cell type (1 = healthy, 2 = cancer). 19,564 healthy cells (taken from 3 flasks on the same day) were compared with 20,883 cancer cells (taken from 3 flasks on the same day) using ANOVA test in SPSS, with p value <0.05 being classed as statistically significant. Bar graphs charting average ORR and standard error of the mean (SEM) for each population were plotted using Origin Pro 8 analysis software.

2.2.7 Cell Fluorescence Analysis – LAKK-M

The LAKK-M system was switched on at least 30 minutes prior to use. Cells were freshly detached from culture flasks by trypsinisation, re-suspended in PBS to various concentrations and kept on ice until further use. Background fluorescence spectra across all four excitation wavelengths were recorded from empty matte black cuvette and cuvette containing 300µl PBS, following which spectra were recorded for 300µl cell suspensions. Amplitudes of fluorescence for fluorophores of interest were recorded as follows (Table 7), in keeping with previously recorded literature:

Table 7 Wavelengths at which metabolic fluorophores were studied (excitation and emission) using the LAKK-M

Fluorophore	Excitation (nm)	Emission (nm)
NADH	365	490
FAD	365	550
FAD Blue	450	510
FAD Blue	450	550

In addition, the optical redox ratio (ORR) was measured as: NADH (ex365 em490)/FAD (ex365 em550); NADH (ex365 em490/FAD Blue (ex450 em510) and NADH (ex365 em490/FAD Blue (ex450 em550).

These measurements were used to assess dose dependence of cellular autofluorescence, repeatability of measurements and to compare healthy and cancer cell lines.

2.2.8 Urine Fluorescence Analysis

To assess the ability of the LAKK-M to detect cellular fluorescence from voided urine, urine was collected across 3 days from a healthy volunteer and studied using the LAKK-M system. 20ml voided urine was collected per study in a 50ml Falcon tube, from which 5ml was removed and added to 5ml custom cuvette, to which the lid and optical probe were attached. 3 independent measurements were made each day, spectra of which were averaged and compared to each other using Origin Pro 8. Spectra were also compared to the pre-recorded fluorophore database to suggest potential contributing fluorophores.

To assess the individual components of urine, samples were spun at 1500RPM for 5 minutes to pellet voided urine cells. Presence of cells was confirmed by benchtop microscope observation. Pelleted cells were resuspended in PBS to concentration of approximately 1 x 10^4/ml. Fluorescence spectra of urine cells suspended in PBS was compared to PBS background, urine supernatant and complete urine spectra using Origin Pro 8.

2.3 Results

2.3.1 Comparison of Background Fluorescence in Cuvettes

Background fluorescence spectra of standard clear plastic cuvette, 3D printed matte black cuvette and custom built cuvette were compared across all 4 excitation channels using the LAKK-M system. This was to ensure there was no background fluorescence from the equipment affecting fluorophore and cell measurements. The fluorescence spectra of cuvettes were compared both when empty (Fig. 31) and when containing the non-fluorescent chemical buffer phosphate buffered saline (PBS) (Fig. 32). Both the 3D printed cuvette and custom built cuvette display a marked reduction in background fluorescence compared to clear, standard cuvettes. There is a slight increase in the background fluorescence from custom built cuvettes under red excitation, which may be the result of material properties of the cuvette. This background fluorescence is far weaker than that observed in the clear cuvette under UV or blue excitation. As UV and blue excitation are considered the optimal wavelengths for measuring the ORR from cell suspensions, custom cuvettes were considered preferable despite this increased background red fluorescence. Custom cuvettes were selected for all future experiments due to their adjustable volume and attachable lid.

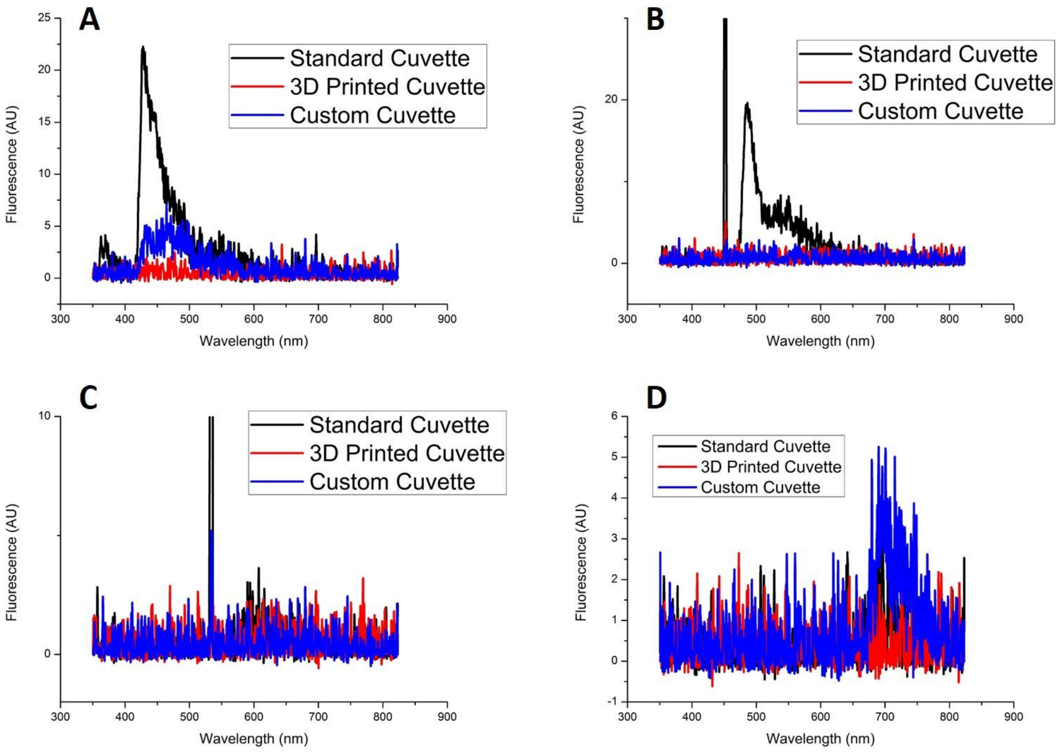

Figure 31 Background fluorescence recorded from standard plastic cuvette (black line), 3D printed cuvette (red line) and custom built cuvette (blue line) under UV (a), blue (b), green (c) and red excitation (d).

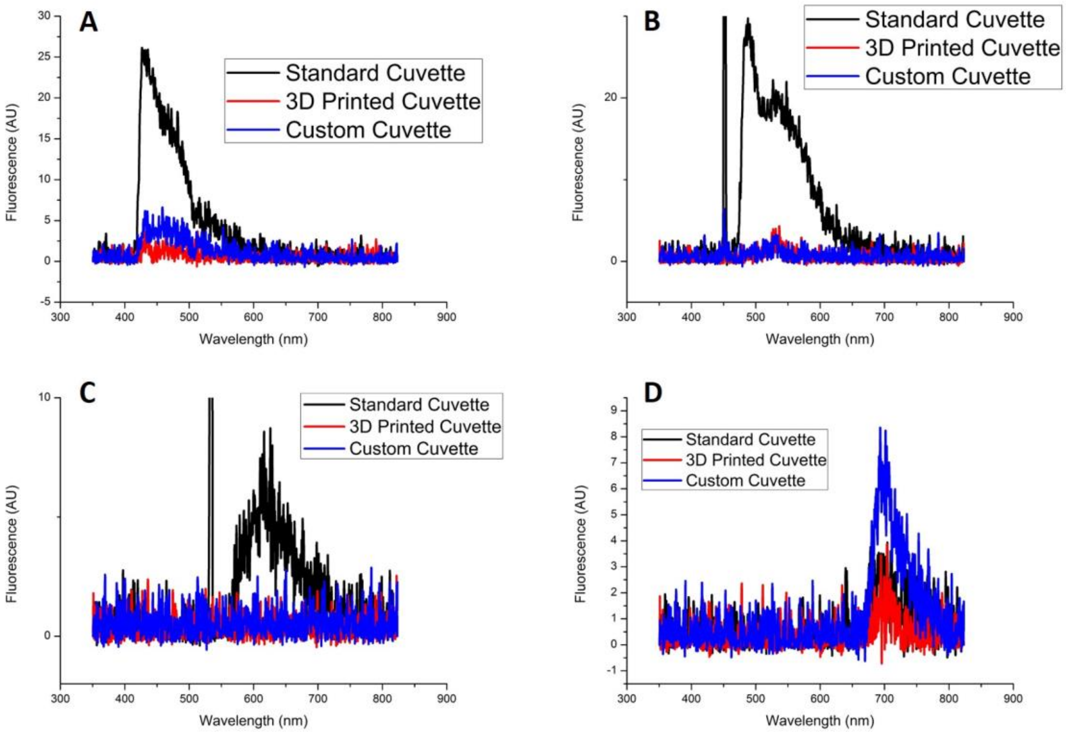

Figure 32 PBS fluorescence measured in standard plastic cuvette (black line), 3D printed cuvette (red line) and custom built cuvette (blue line) under UV (a), blue (b), green (c) and red (d) excitation.

From this data, we can clearly demonstrate that both the 3D printed and custom made matte black cuvettes provide a significant reduction in both background and PBS induced fluorescence across the desired UV and blue wavelength ranges. 3D printed cuvette was slightly better at reducing background fluorescence than the custom cuvette across all 4 wavelengths, however the custom cuvette was selected for use due to its flexibility.

To determine whether a magnetic stir bar could be used to maintain cells in suspension, the background fluorescence of an empty custom cuvette was compared with that of a cuvette containing a white magnetic stir bar. From Figure 33, an increase in the background fluorescence measured using UV and blue excitation (wavelengths used to measure ORR) when including stir bar can be seen. Furthermore, magnetism between LabStor base and stir bar was disrupted by the thickness of the cuvette. For these reasons, stir bar is not recommended when measuring cell or fluorophore fluorescence in custom cuvettes.

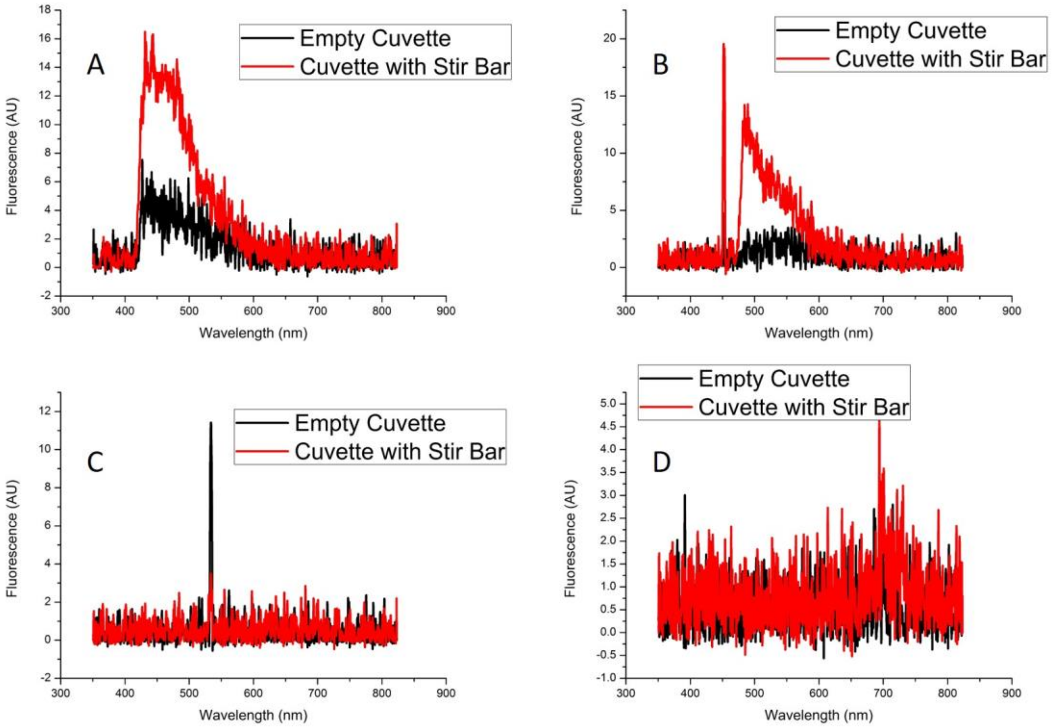

Figure 33 Figure 34 Background fluorescence measured from empty cuvette (black line) and cuvette containing magnetic stir bar (red line) under UV (a), blue (b), green (c) and red (d) excitation

2.3.2 Fluorophore Fluorescence Spectroscopy

Fluorescence spectra of common cellular fluorophores NADH, flavins, tryptophan, tyrosine and Protoporphyrin IX were recorded on the LAKK-M system to assess fluorescence maxima. Spectra of fluorophores are detailed below (Fig. 34 – 36):

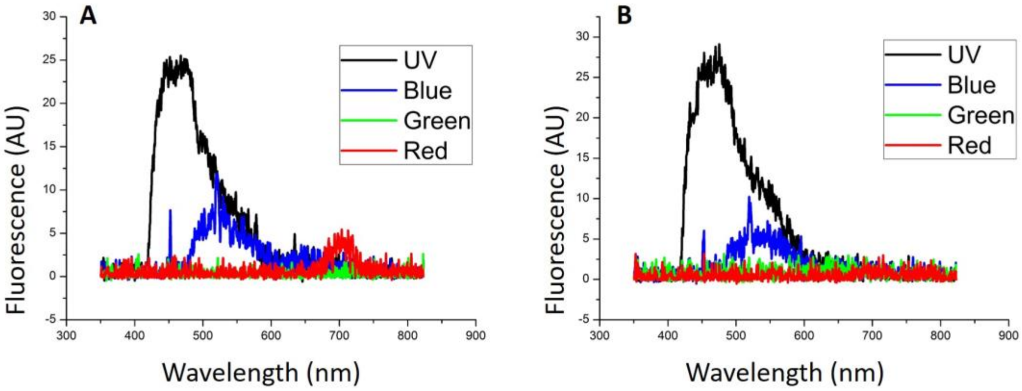

Figure 34 Fluorescence intensity of 1M solutions of tryptophan (a) and 1M tyrosine (B) in PBS measured under UV excitation (black line), blue excitation (blue line), green excitation (green line) and red excitation (red line).

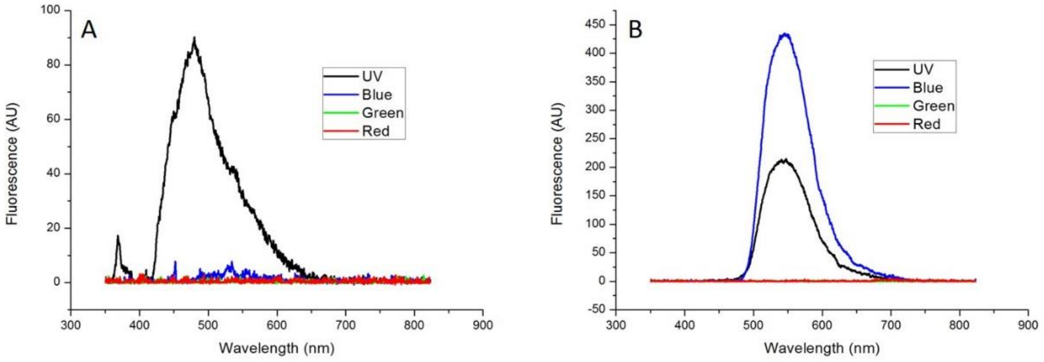

Figure 35 Fluorescence spectra of 1M NADH (a) and 1M flavin (b) under UV (black line); blue (blue line); green (green line) and red excitation (red line)

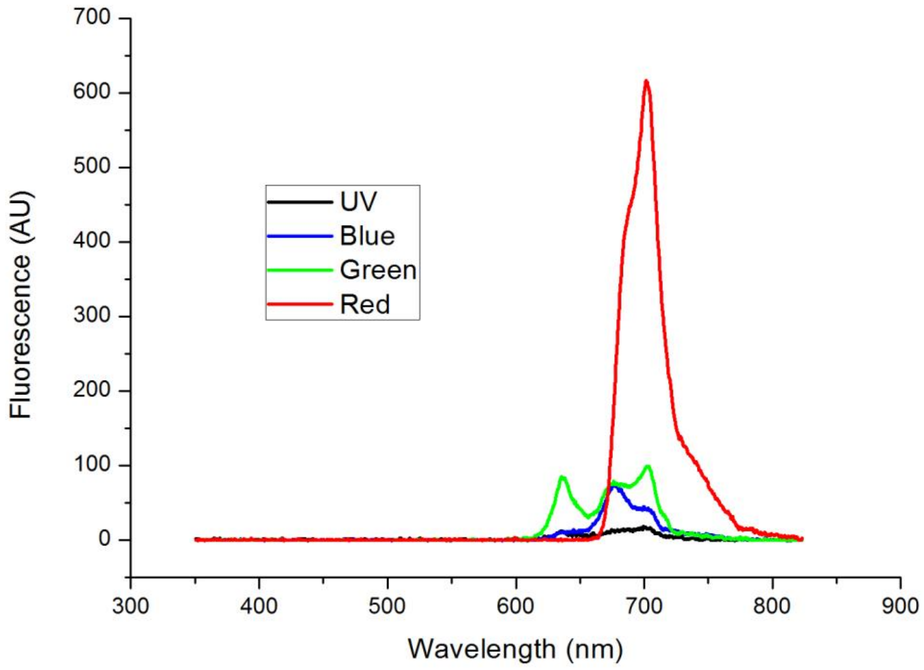

Figure 36 1M PpIX fluorescence under UV (black line); blue (blue line); green (green line) and red (red line) excitation

From these figures we can clearly see that the fluorophores responding most strongly to UV irradiation are the metabolic cofactors NADH and flavins. NADH spectrum shows some artefacts and the spectral line is not completely smooth. As the concentration of NADH solution was quite high (1M), this may be due to an incomplete mix of the solution resulting in powder clumping. More likely, this may be due to the “inner filter effect” whereby light entering solution is entirely absorbed close to the light source, impeding light delivery to the rest of the solution and reducing fluorescence intensity measured by the detector. The LAKK-M spectrometer auto-calibrates before each measurement by measuring background noise prior to laser sources being switched on. Therefore, because spectra of other fluorophores (for instance flavins and PpIX) displayed expected fluorescence, the artefacts observed in NADH spectra are probably not due to calibration errors. The LAKK-M can also be recalibrated following hardware modifications against plastic reference equipment of known optical properties, however this was not carried out prior to NADH analysis. Future analysis of NADH solutions at lower concentrations would be of worth to minimise the inner filter effect and remove spectral artefacts. Tryptophan and tyrosine were found to fluoresce modestly under UV excitation (maxima 450-500nm), however this wavelength is likely above the optimal wavelength for exciting fluorescence from the amino acids. As tryptophan and tyrosine residues are major contributors to collagen and elastin fluorescence, it can be considered that the UV excitation wavelength is sub-optimal to excite these fluorophores too. PpIX, a possible cellular component, was found to fluoresce strongly, but limited to the red region of the spectrum (maximum around 710nm), therefore not interfering with ORR measurements. NADH was found to fluoresce solely under UV excitation (maximum around 470-490nm), while flavins fluoresced under both UV and blue excitation (maxima around 530-550nm). Flavin fluorescence was found to be stronger under blue excitation than UV excitation. It is concluded, therefore, that the major components contributing to cellular fluorescence at the wavelengths of interest for calculating ORR are NADH and flavins. As powers varied slightly between light sources (1.5mW for UV, 3.5mW for blue, 4.5mW for green and 5.5mW for red), spectral intensity variations may be influenced slightly by optical powers. I further explored how the LAKK-M responds to increasing doses of fluorophores, using flavins as an example (Fig. 37):

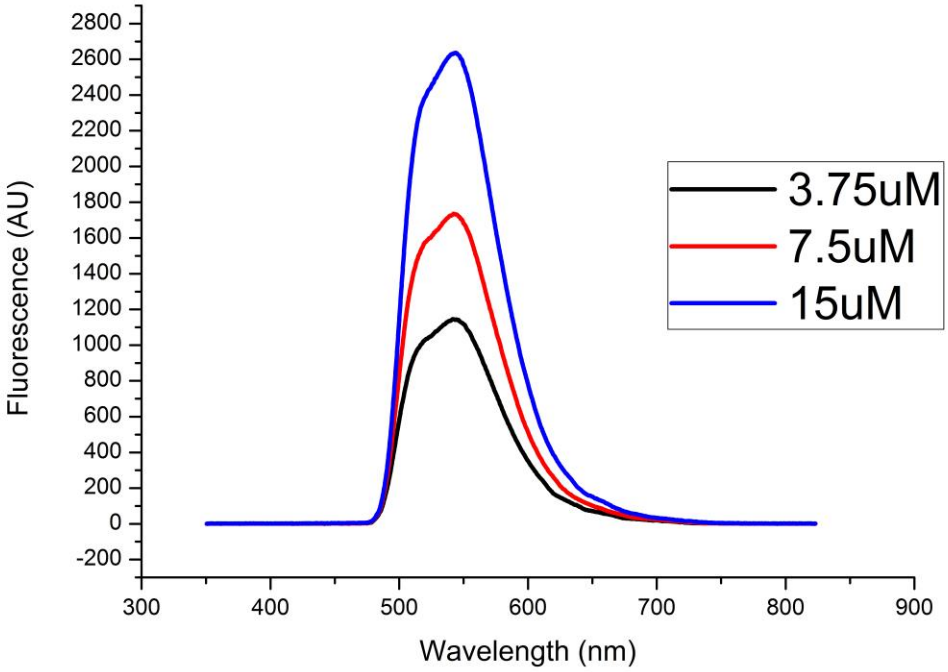

Figure 37 Fluorescence measured from flavin solutions under blue (450nm) excitation. Black line depicts a 3.75uM solution, red line depicts a 7.5uM solution and blue line depicts a 15uM solution.

From this it can be concluded that the LAKK-M can approximately represent increasing fluorophore concentrations. I then sought to assess in greater detail the relationship between NADH and flavins by comparing the fluorescence spectra of each to that of a mixed solution of both fluorophores (Fig. 38):

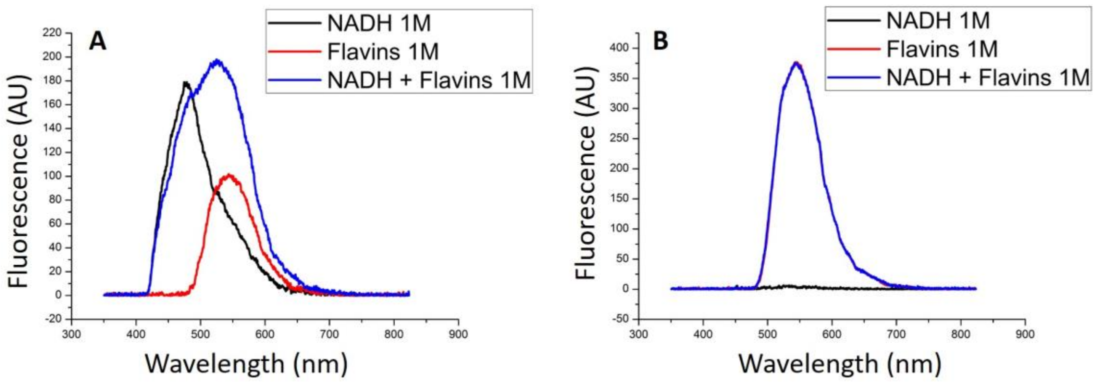

Figure 38 Fluorescence spectra of 1M NADH (black line), 1M flavins (red line) and a 50:50 mix of NADH and flavins (blue line) under uv (a) and blue (b) excitation.

It can be seen from Fig.38 that a combination of NADH and flavins under UV excitation (a) gives rise to a complex spectrum involving contributions from both fluorophores. There may also be some synergistic effect of combining both fluorophores. Blue excitation (b) gives rise to a spectrum which is identical to that of flavins, confirming that NADH contributes no fluorescence at this wavelength. As there is considerable overlap between NADH and flavin spectra under UV excitation, blue spectra may be more useful for studying flavins. Finally, I sought to assess the accuracy of the three suggested methods for measuring optical redox ratio (ORR), by measuring ORR values at increasing concentrations of NADH (Fig. 39):

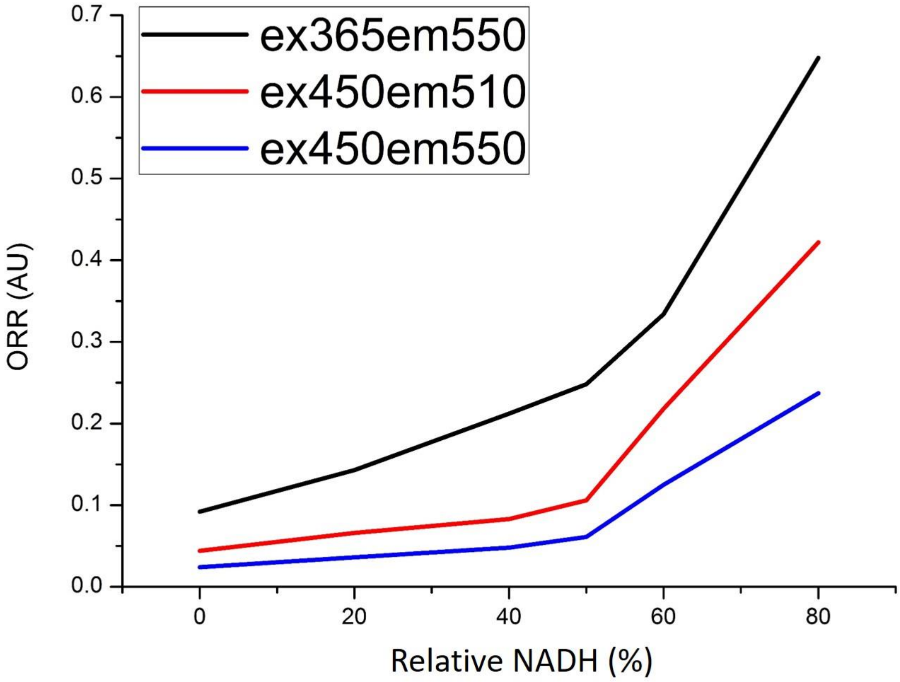

Figure 39 Chart of ORR values measured at increasing NADH (ex365em490): Flavin ratios with flavins measured at ex365em550 (black line), ex450em510 (red line) and ex450em550 (blue line)

It can be seen from Fig.39 that all 3 measurements of ORR reflect relative increases in NADH, although predicted ORR responses should be linear. This could be caused by incomplete mixing of solutions, however every care was taken to ensure solutions were well mixed prior to measurement. This may also be partially caused by an "inner filter effect" – discussed earlier – occurring at high NADH concentrations. It was shown earlier that there is a small amount of spectral overlap between NADH and flavins which may also account for the nonlinear nature of the response. Similarly, combination of fluorophores seems to cause a synergistic effect regarding fluorescence intensity which may contribute to the observed results. Due to the non-linear response of the LAKK-M to increasing NADH concentrations, care must be taken in future when interpreting ORR measurements.

2.3.3 Confocal Analysis of Cell Fluorescence

Bladder cancer cell line "5637" was studied using confocal microscopy to understand and confirm the origin of the Autofluorescence at wavelengths of interest for calculating the ORR. Fig.40 (below) suggests that fluorescence excited and recorded across UV and blue spectra may be mitochondrial in origin and occurs from NADH and flavins respectively due to co-localisation with mitochondria-specific dye "MitoTracker". More work using higher resolution microscopy and overlaying fluorophores will help to better elucidate this.

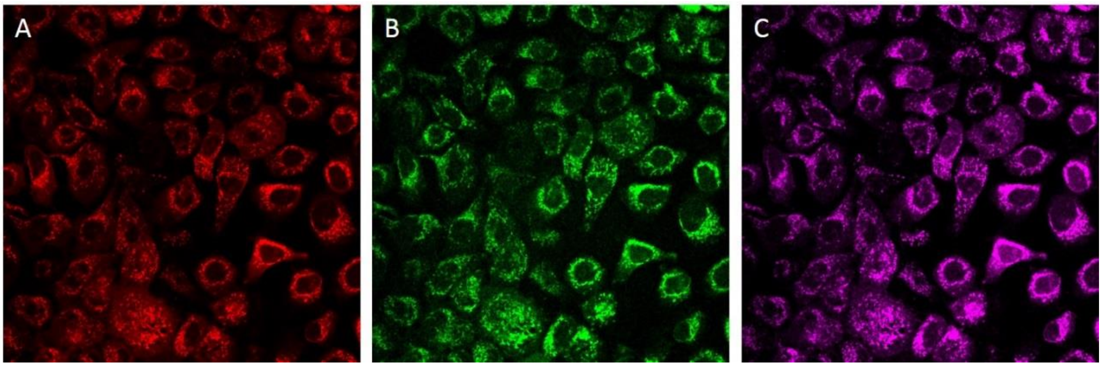

Figure 40 Confocal Microscopy images from bladder cancer cells showing localisation of (a) MitoTracker Red, (b) NADH and (c) flavins

2.3.4 Flow Cytometric Analysis of ORR

To compare ORR values prior to LAKK-M analysis, healthy bladder and bladder cancer cells were analysed using a conventional flow cytometer with UV and blue laser sources to excite NADH and flavins, respectively. Relative NADH and flavin contents of all cells for healthy and cancer populations were plotted on bivariate dot plots (Fig.41) and population means were also compared for statistically significant differences in SPSS using ANOVA (Fig.42). Fig.41 shows that healthy and cancer bladder cells possess different population distributions with respect to NADH (x-axis) and flavins (y-axis).

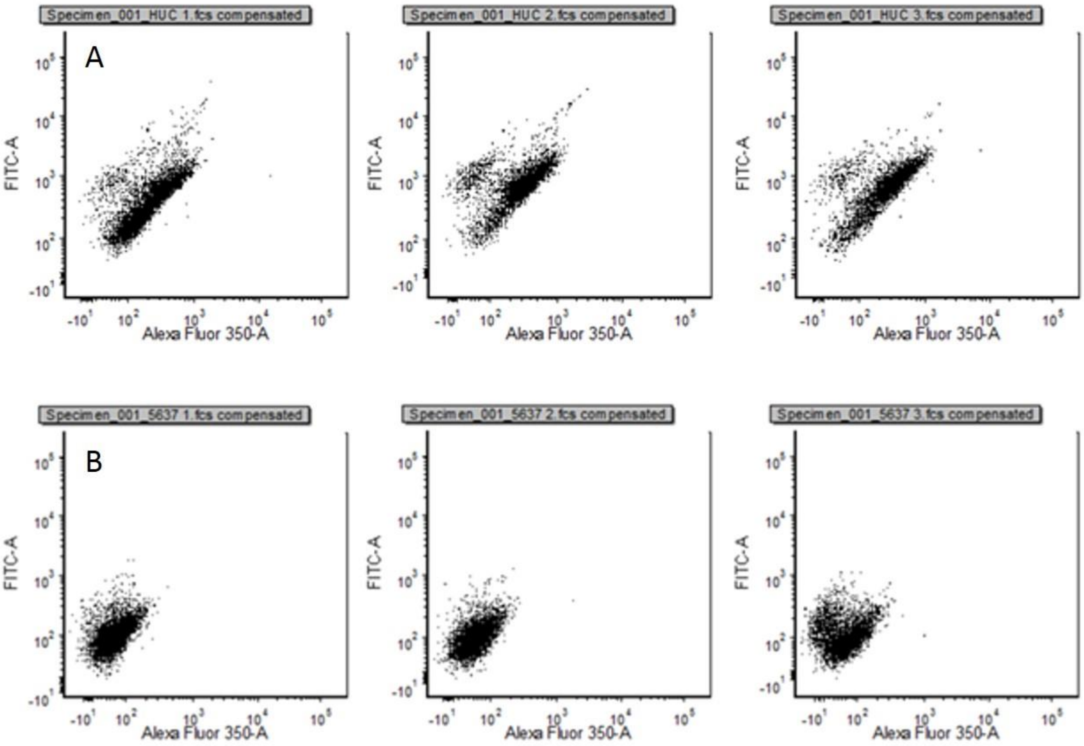

Figure 41 Bivariate dot plots of (A, top row) healthy bladder and (B, bottom row) bladder cancer cells measured in triplicate, charting cellular content of NADH (x-axis) and flavins (y-axis) showing differences between population distributions

Fig.42, comparing the mean ORR values of each cell type, demonstrates an increased mean ORR (measured as ex360em425-475/ex488em515-545) in bladder cancer cells (dark shaded) compared to healthy control (light shaded). This difference was found to be statistically significant ($p = 2 \times 10^{-16}$). This extremely low p value may be due to the lack of independence of measurements. Although cells from 3 separate flasks (3 x healthy flasks and 3 x cancer flasks), measurements were performed on the same day so are not technically independent. More work in future, particularly repeat experiments, will help to elucidate the true significance of this difference.

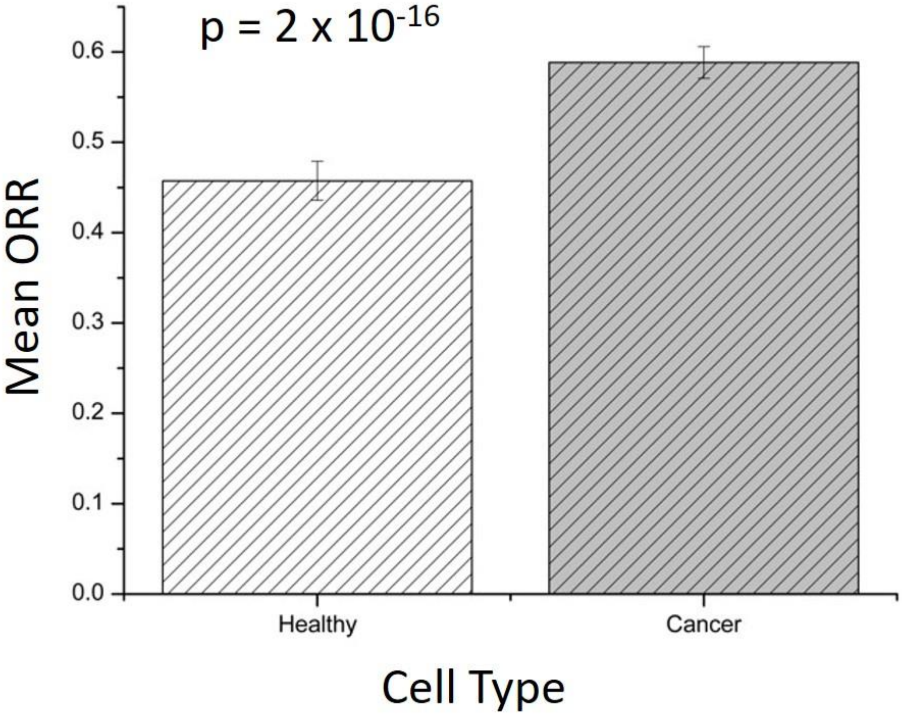

Figure 42 Comparison of ORR mean +/- SEM for healthy bladder cells (pale shaded) and bladder cancer cells (dark shaded). ORR measured as ex360em425-475/ex488em515-545.

2.3.5 LAKK-M Cell Autofluorescence Analysis

Having determined a statistically significant increase in the ORR of bladder cancer cells compared to healthy bladder cells, the next aim was to determine whether this difference could be detected by the LAKK-M system. Both the stability of ORR measurements in cancer cells day to day and dose dependent changes in fluorophore levels were studied, alongside differences in ORR between bladder cancer cells and healthy control. Fig.43 below, charting cellular fluorescence spectra across all 4 spectra averaged from 5 datasets of bladder cancer cells, shows that cells fluorescence under UV and blue excitation, but not green or red excitation. Furthermore, comparing cell fluorescence under UV excitation (maximum 470-490nm) to fluorophore spectra suggests that cells contain a combination of both NADH and flavins with some possible small contribution from tryptophan/tyrosine. Cell fluorescence under blue excitation (maximum 530-550nm) seems to arise solely from flavins:

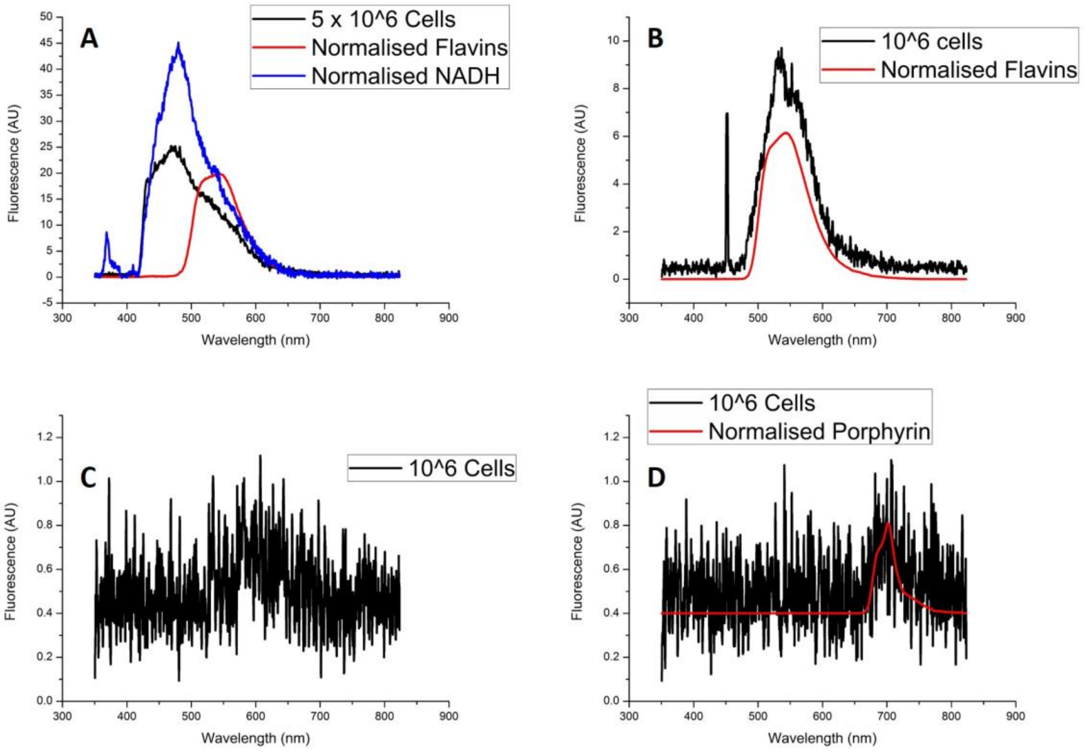

Figure 43 Cell fluorescence averaged from 5 measurements of 10^6 cells: cells (black line) under UV excitation (a) overlaid with NADH (blue line) and flavins (red line); cells under blue excitation (b) overlaid with flavins (red line); cells under green excitation (c); cells under red excitation (d) overlaid with porphyrins (red line).

Stability measurements of cells (Fig.44 & 45) demonstrate that cell fluorescence under UV and blue excitation shows similar patterns but varies considerably. Each sample was measured after identical preparation. As cells were transported on ice, approximately 10 minutes was allowed in each instance to stabilise to room temperature in a temperature controlled room. Small variations in acclimatisation period may account for variations in observed fluorescence. In particular, UV spectra show considerable variability in what look to be NADH and flavin contributions to cellular fluorescence, which would drastically skew the ORR if measured purely using UV values. Blue fluorescence spectra also show some variability, but are more stable than UV spectra:

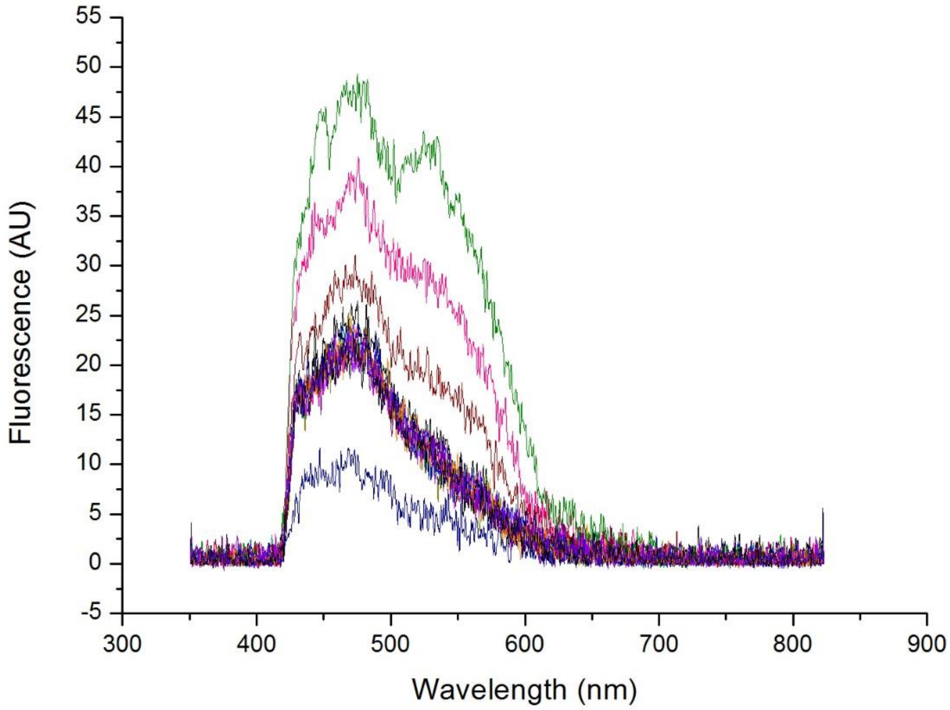

Figure 44 Fluorescence spectra of 15 separate measurements of cellular fluorescence from individually prepared bladder cancer cells under UV excitation, showing signal variability

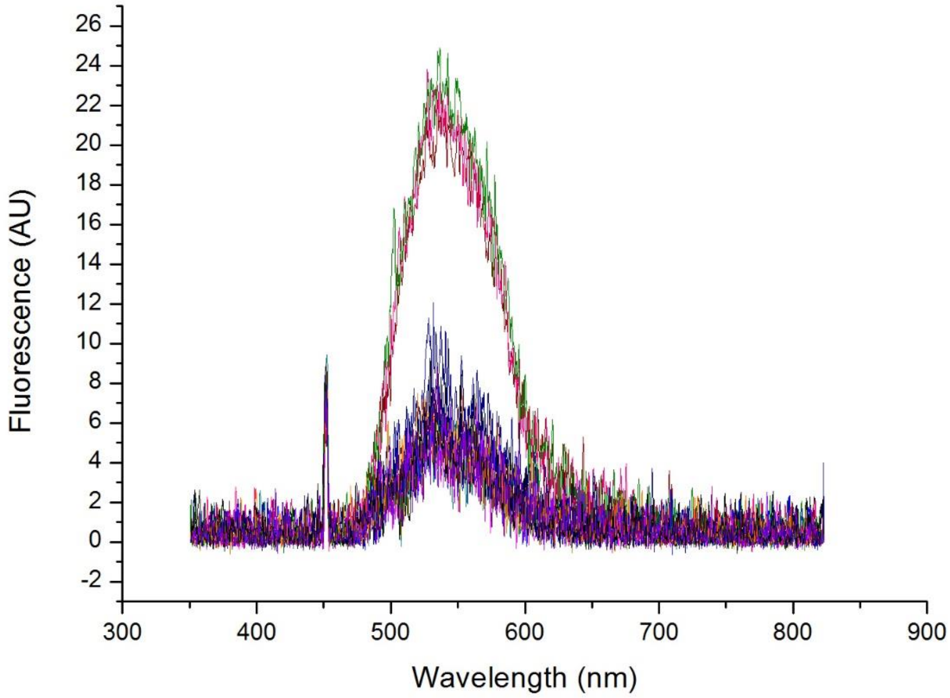

Figure 45 Fluorescence spectra of 15 separate measurements of cellular fluorescence under blue excitation showing signal variability

Dose dependence measurements of cells under UV and blue excitation (Fig.46) demonstrate that fluorescence arises exclusively from cells and is dose dependent, however:

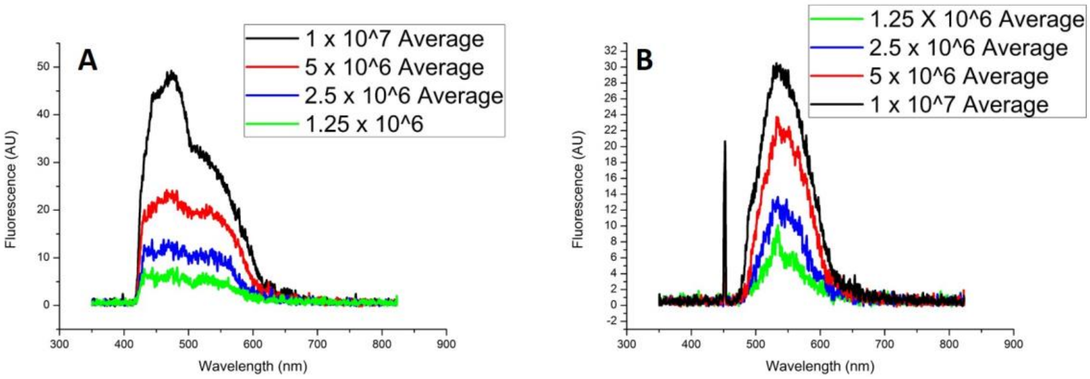

Figure 46 Dose dependence of bladder cancer cell spectra using UV (a) and blue (b) excitation at concentrations ranging from 1.25 x 10^6 to 1 x 10^7 cells/ml in PBS

Comparison of ORR from healthy (dark shaded) and cancer (pale shaded) measured using LAKK-M (NADH ex365em490/flavin ex365 em550) show no significant difference (Fig.47):

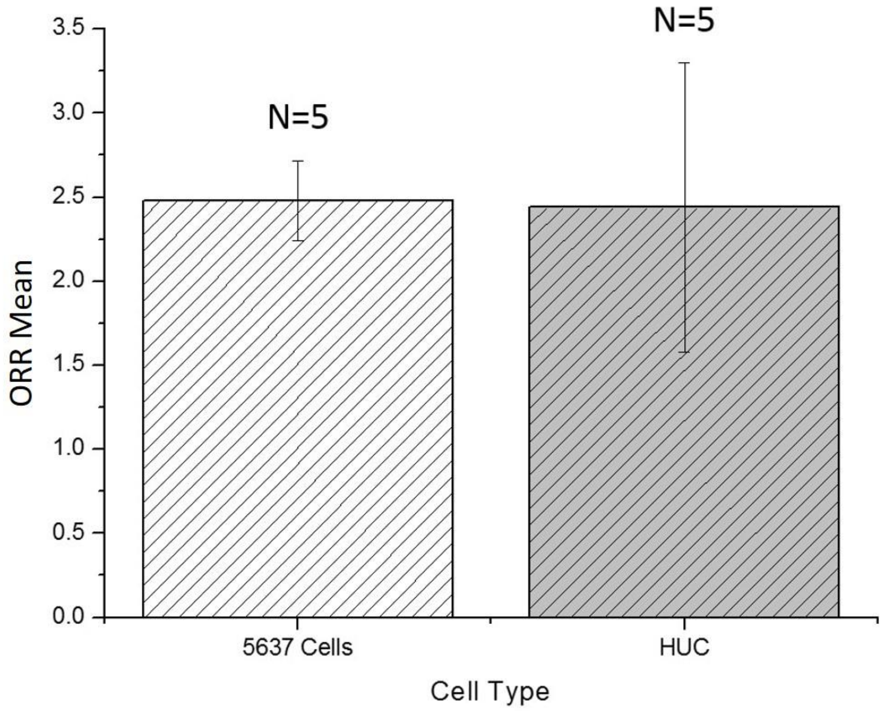

Figure 47 ORR mean +/- SEM values measured from bladder cancer (pale shaded, 5 measurements) and healthy bladder (dark shaded, 5 measurements) cells. ORR measured as ex365em490/ex450em550

Furthermore, analysis of ORR values from repeat measurements of bladder cancer cells shows large variability between samples (Fig.48). Again, each sample was prepared identically and measured following transport on ice and a 10 minute acclimatisation period to room temperature. In particular, the largest variability was found when exciting flavins at 450nm and recording them at 510nm. The lowest variability was recorded when exciting flavins at 365nm and recording at 550nm:

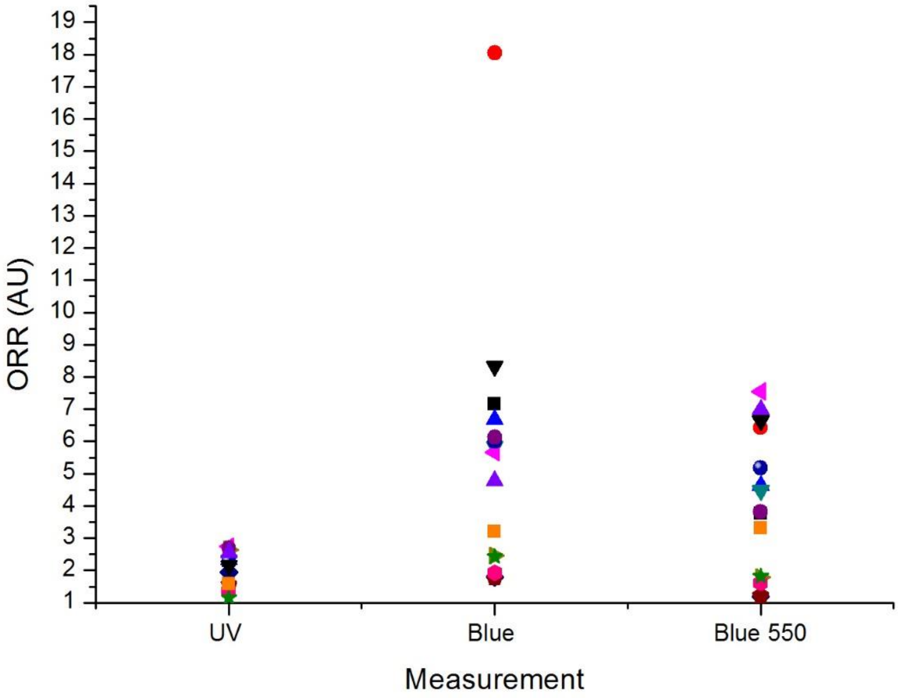

Figure 48 Scatter diagram charting ORR values of repeated measures from bladder cancer cells calculated in 3 ways (ex365em490/ex365em550 ("UV"); ex365em490/ex450em510 ("Blue"); ex365em490/ex450em550 ("Blue 550"))

It was also observed that time on bench has an effect on cell ORR measured using the LAKK-M (Fig.49). ORR drops significantly up to 15 minutes after initial measurement then plateaus after around 20 minutes. This suggests the need to compare cells of both type immediately after preparation. Reduced ORR may be a physical effect of cells settling in suspension or may more likely be suggestive of cell death on bench. Increased flavins and decreased NADH levels have been observed previously in Doxorubicin induced cell death, which would obviously skew the ORR[223].

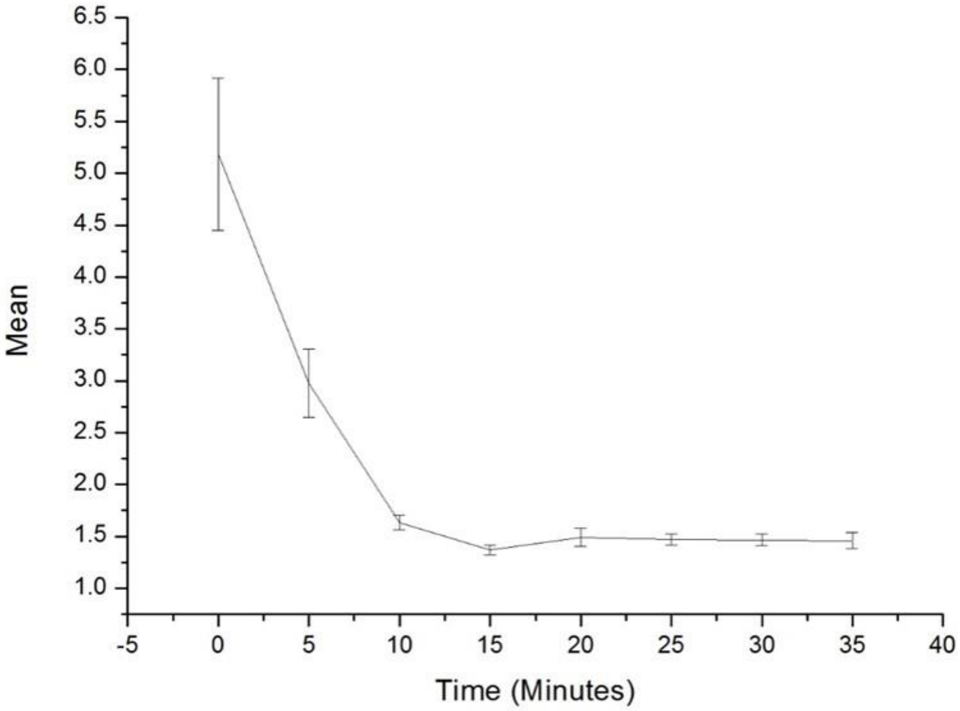

Figure 49 Average +/- SEM ORR values of bladder cancer cells measured at 5 minute intervals up to 35 minutes following initial measurement (ORR measured as ex365em490/ex365em550).

2.3.6 Urine Fluorescence Analysis

Fluorescence analysis of urine samples shows fluorescence spectra which vary in intensity from day-to-day, but which show similar spectral shapes (Fig.50):

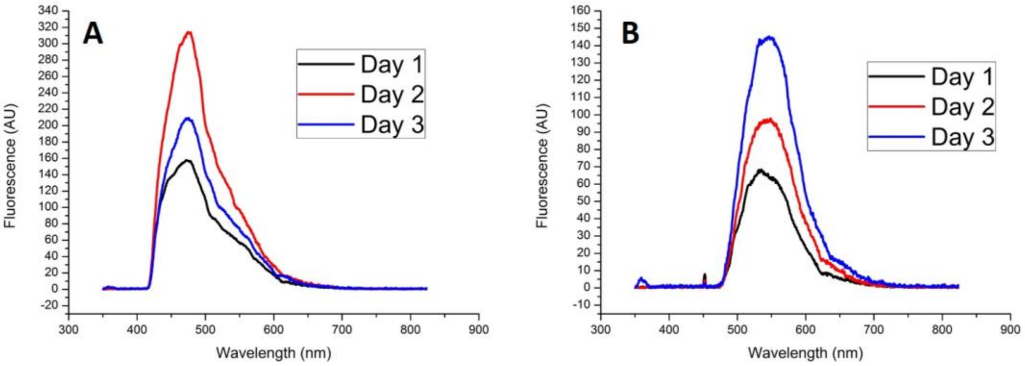

Figure 50 Spectra recorded from urine on days 1, 2 and 3 (black, red and blue lines) measured using UV (a) and blue excitation (b)

Comparing urine fluorescence spectra with pre-recorded fluorophore analysis suggests the presence of large volumes of NADH and flavins in voided urine, although this requires further investigation as fluorescence may equally arise from excreted amino acids or dietary vitamins such as vitamin B. Crucially, the inherent fluorescence from urine supernatant contributes almost all of the total urine fluorescence (Fig.51), fluorescence of urine cells suspended in PBS shows very little signal compared to background PBS:

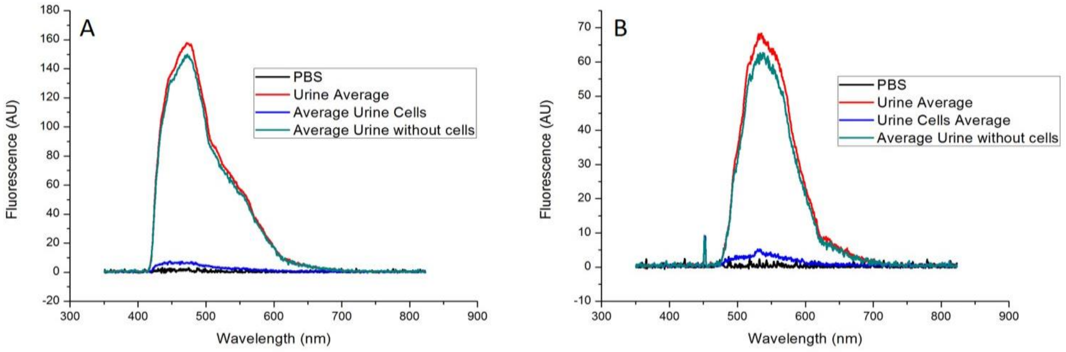

Figure 51 comparison of the UV (a) and blue fluorescence (b) of PBS (black line); total urine fluorescence average (red line); urine cells in PBS (blue line) and average urine without cells (green line)

Finally, dose response measurements of urine supernatant combined with PBS confirms that fluorescence arises almost exclusively from urine (Fig.52):

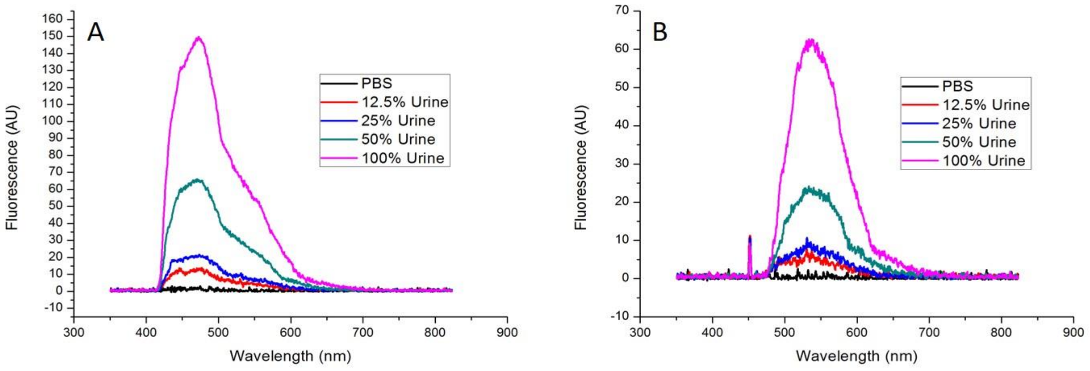

Figure 52 Fluorescence under UV (a) and blue excitation (b) arising from PBS (black line); 12.5% urine in PBS (red line); 25% urine in PBS (blue line); 50% urine in PBS (green line) and 100% urine (magenta line)

2.4 Discussion

Spectroscopic analysis of the fluorophores NADH and flavins was used, alongside previous relevant literature, to calculate the optimum wavelengths at which to study the fluorophores of interest and calculate the ORR, a measure of cell metabolic activity. Spectra in figure 34 clearly show UV excitation at 365nm can excite fluorescence from both solutions of NADH and flavins, whereas excitation using blue light at 450nm excites only fluorescence from flavins. These measurements were made in cuvettes specifically designed to minimise background fluorescence noise both from material and the environment. Optimal wavelengths at which to calculate the ORR using the LAKK-M were investigated by measuring varying ratios of NADH and flavins and charting linear or non-linear responses of ratios. The LAKK-M, with the use of custom built cuvettes to minimise background noise, is therefore capable of stably measuring fluorophores of interest and calculating relevant ratios including the ORR. Although measuring flavins at ex450em550 appears the optimal method to delineate this fluorophore from others in solution, lower variability in ORR values from cells when measuring flavins at ex365em550 compared to ex450em550 suggests that this is a more stable wavelength for making measurements diagnostically. Analysis of the ORR from organoids (chapter 3) and human tissue (chapter 4) therefore use the ORR defined as NADH(ex365em490)/flavins(ex365em550)

Confocal microscopy setup was prepared as closely to these parameters as possible, limited by the available equipment. From studies using the mitochondrial dye MitoTracker a strong association can be seen between MitoTracker fluorescence and that hypothesised to arise from cellular NADH and flavins. Elucidation of contributing cell fluorophores at the chosen wavelengths could be improved by obtaining higher resolution images and also by overlapping images obtained from MitoTracker and autofluorescence. There is a small amount of autofluorescence observed using confocal microscopy which does not associate with the mitochondria. It is possible that this fluorescence is arising from either bound or unbound non-mitochondrial (cytoplasmic) NADH/FAD or from fluorescent amino acids such as tyrosine and tryptophan. In my experience, and in previous literature[224], the excitation wavelength used was out-with the optimal excitation wavelength for these amino acids however, as UV fluorescence spectroscopy of tryptophan and tyrosine solutions yielded far lower fluorescence intensity than from NADH and flavins. One concern to the use of such strong laser powers for confocal microscopy (up to 60mW) was the unwanted effects of irradiation on cells. Irradiation using a 355nm laser at 60mW may reduce cell viability over time. Future studies using similar setups should be careful therefore that similar laser powers do not affect the viability of sample cells.

Data from flow cytometric analysis indicates that bladder cancer cells possess a statistically significantly increased ORR (ex360em425-475/ex488em515-545) compared to healthy cells ($p = 2 \times 10^{-16}$)[225]. This is in keeping with knowledge of the ORR in other models of cancer and pre-cancer, including breast cancer[222]. For this analysis, 10,000 cells were measured each, in triplicate, from healthy and cancer bladder cells. Optimal parameters were again limited by the availability of physical equipment, meaning excitation and emission parameters differed up to 40nm either way from the setup used with the LAKK-M system or confocal microscopy. I believe, according to previous similar research in the field, that this will not cause significant analysis issues, as the use of flow cytometry to measure autofluorescence was previously suggested by Thorell in the 1980s[226]. The use of techniques to minimise background autofluorescence for conventional flow cytometry measurements suggests that autofluorescence signals are worth studying in their own right[227]. Results from this analysis suggest that flow cytometric analysis of ORR may be a worthwhile diagnostic technique to assess the metabolic parameters of urothelial cells shed in voided urine. In theory, the ability to measure both NADH and flavin levels in the same cell, allowing the construction of "redox overview" could prove a useful diagnostic tool. This setup has been demonstrated to be capable of measuring mitochondrial NADH and flavin levels on a cell-by-cell basis, while further equipment modifications may allow for the assessment of more endogenous fluorophores (for instance, an excitation wavelength closer to 300nm could allow for the analysis of cellular tryptophan or tyrosine levels). The calculation of cell redox ratios means that compensation for cell size is not required, considerably simplifying the setup. In order to further progress this technique, it would be useful to simultaneously calculate cell viability using a dye such as To-PRO iodide. Cell viability was measured following this experiment and estimated to be around 95%, however this was using the less sensitive trypan blue dye exclusion analysis on a haemocytometer. Furthermore, in theory the 5% dead cells included in analysis may be unfairly skewing values. Additionally, a small secondary population of healthy cells with increased flavin content can be observed from the redox plots. It would be interesting in future to assess what contributes to this difference and how this population contributes to overall ORR measurements. It may be that the secondary population of cells with increased flavin content corresponds to the 5% dead cells measured using

Trypan Blue exclusion analysis. Further investigation into the autofluorescence profiles of dead and dying cell populations will help to better understand this. Flow cytometric analysis was hampered by slow turnover rate of primary "HUC" cells, therefore it is suggested that the use of a robust, immortalised healthy cell line, such as "SV-HUC" would be beneficial for establishing future results. SV-HUC cells have been used as healthy controls in many areas of contemporary urology research, however an initial concern was that the immortalisation of these cells may have caused metabolic alterations which skew the ORR towards a cancer phenotype.

Speaking clinically, the use of ORR flow cytometry could prove an attractive technique as it is fast, completely non-invasive and detects a cellular defect which often occurs early in development of cancer. Conventional flow cytometry[228] and DNA image cytometry[229] have enjoyed application in bladder cancer detection previously, paving the way for potential application of ORR flow analysis. Furthermore, the visualisation of redox overviews allows for the observation of the redox profile of each cell in populations upwards of 10,000, therefore allowing the identification of very rare cells with potentially aberrant metabolism. As only cell lines were used, clinical implementation of this technique would likely require more thorough investigation of the phenomenon of increased ORR in cancer cells across a wide range of cell lines of varying grades and stages. This study was limited by time and financial constraints to the study of the "5637" cell line, therefore the study of a wide range of bladder cancer cell lines as a future avenue of study is suggested to move towards potential clinical applications. I hypothesise that cancer cell lines of higher stages and grades will demonstrate progressively increased ORR values compared to healthy control cells.

Having confirmed the hypothesis that bladder cancer cells would possess an increased ORR relative to healthy bladder cells, I sought to investigate whether this phenomenon could be accurately identified using the LAKK-M system. Healthy and cancer cell line fluorescence in the UV and blue spectra was found to broadly follow that of NADH and flavin solutions, indicating again that these are the major contributing fluorophores. Results indicate that, although there is a noticeable dose dependence in cellular autofluorescence measured by the LAKK-M, there is very low overall fluorescence. Furthermore, there was found to be noticeable day to day variations in ORR even within the same cell lines. It was found that in the region of 2-5 x 10^6 cells/ml minimum were required to receive adequate signals above the PBS background signal, which is far greater than the concentration of urothelial cells normally shed in urine. Due to the slow turnover rate and relatively low yield of healthy bladder cell line “HUC”, it was difficult to yield adequate cell concentrations for meaningful analysis. The existing measurements comparing healthy and bladder cancer cell lines show no statistically significant difference in the ORR. At present, therefore, the LAKK-M system is not suitable for measuring fluorescence from cell suspensions.

The low fluorescence signal recorded from cell suspensions may be due to the low relative power of the laser sources in the LAKK-M system itself. The inherent power of the UV and blue lasers in the LAKK-M, measured using an optical power meter (ThorLabs) is in the region of 1-2mW. Considering that confocal microscopy measurements required 100% laser power in sources with 30mW (blue laser) and 60mW (UV laser) optical power to elicit cellular fluorescence, it can be suggested that an increased laser power in the LAKK-M system would be of use for this application. Increasing laser power in the LAKK-M would bring new issues with its use on living tissue, as high power UV irradiation is known to be mutagenic[230]. It is suggested that the low fluorescence signal and high day to day variability from cell suspensions may also arise due to uneven distribution of cells in solution, leading to high levels of light scattering, discussed by Mourant *et al.*[231]. Previous studies using spectrophotometry and spectrofluorimetry to analyse cell suspensions have employed magnetic stir bars to ensure even suspensions of cells in solution. I attempted to incorporate a magnetic stir bar (Gilson LabStir) into cell spectroscopy measurements (Fig. 29), however the thickness of the custom cuvette obscured the magnetism. It is suggested based on these findings that a new custom cuvette with a thinner base may allow for more even cell suspensions in solution and more accurate fluorescence measurements.

A concern of using a magnetic stir bar for LAKK-M fluorescence measurements comes from the inherent fluorescence of the stir bar itself. The background fluorescence of an empty cuvette was compared with the fluorescence from a cuvette containing a stir bar, finding fluorescence in UV and blue spectra arising from the stir bar (Fig.33).

Spectrofluorimetry measurements of cell suspensions generally employ a laser passing from one side of the cuvette to the other, entering the detector on the far side and bypassing the stir bar. As the LAKK-M contains both excitation source and detector in the same fibre, light travelling down into the cuvette and back will interact with the stir bar (Fig.53). Modifications to the cuvette, allowing the attachment of the optical probe to the side, or a custom design matte black stir bar may allow for measurements using this method.

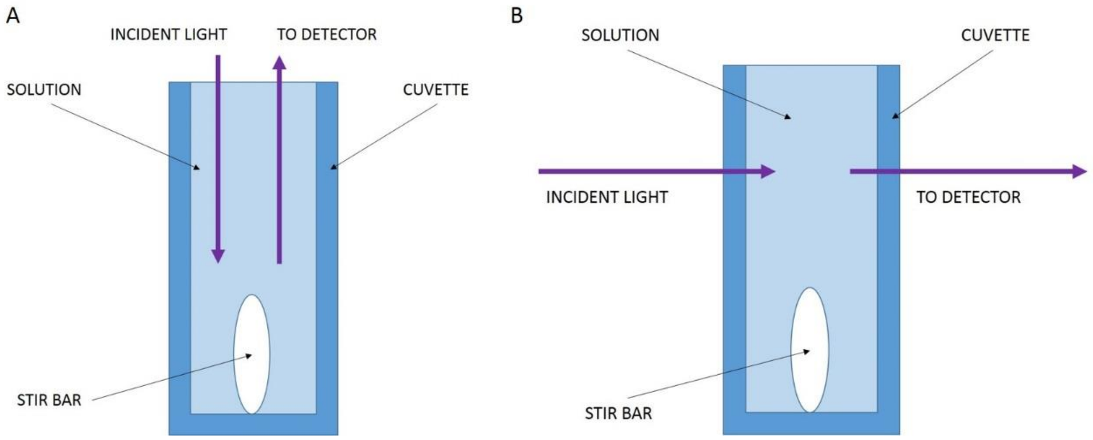

Figure 53 Diagrams of fluorescence spectroscopy using the LAKK-M system (a) and conventional spectrofluorimetry (b)

A potential future avenue of interest for urinalysis would be the comparison of autofluorescence of urine samples from healthy controls and patients with bladder cancer. It has been demonstrated that the majority of fluorescence from urine comes from the supernatant itself, with very little coming from the voided urine cells. Fluorescence analysis of voided urine has previously shown the ability to detect bacteriuria[186], cervical cancer[232] and ovarian cancer[183], however there is no published research covering fluorescence analysis of urine in bladder cancer. It is suggested from fluorescence spectra that the main fluorophores in voided urine are NADH and flavins therefore the ORR could potentially be used to account for fluorescence amplitude variations between samples and day-to-day. It may also be feasible to study other fluorophores such as endogenous voided porphyrins. Based on this preliminary data, an application is underway to carry out a pilot study comparing autofluorescence from urine of bladder cancer patients with healthy control using the LAKK-M system.

2.5 Conclusion

To conclude, it has been demonstrated that the major contributing fluorophores to cellular autofluorescence at the wavelengths of interest are likely the mitochondrial NADH and flavins. There exists a statistically significant difference ($p = 2 \times 10^{-16}$) in the ORR (ex360em425-475/ex488em515-545) between healthy and bladder cells, determined using a customised flow cytometry setup. Further study in the field of autofluorescence flow cytometry, particularly using the ORR, could lead to novel clinical breakthroughs. The LAKK-M, although capable of making spectroscopic measurements, is not suitable at present for assessing ORR values from cell suspensions owing to low fluorescence yield and high incidence of scattering events. Increasing laser power of the LAKK-M system and modifying custom cuvettes to allow the addition of magnetic stir bars may serve to rectify these issues, providing the opportunity to use this system for voided urine cytology. Analysis of urine supernatant autofluorescence from healthy and bladder cancer patients may provide novel insights into avenues for non-invasive disease diagnosis and monitoring.

3. ORGANOID DEVELOPMENT

3.1 Introduction

One of the main challenges facing autofluorescence spectroscopy for medical application is a poor understanding of individual fluorophore properties, particularly regarding changes as tumours progress through stages (CIS to non-invasive to muscle invasive). In chapter 2, early detection of bladder cancer by studying autofluorescence properties at a cellular level was discussed. The ability to analyse an autofluorescence model of bladder cancer which grows and progresses over time could allow new insights into the structural and metabolic processes occurring in developing tumours. This would allow researchers to more reliably identify biomarkers of interest, potentially leading to the application of autofluorescence spectroscopy to bladder cancer detection and diagnosis. Among the most applicable and attractive methods with which to study developing tumours is the use of organoids. Organoids are small, organotypic reconstructions of human tissues which can be grown or maintained *In vitro.* Organoid models have previously been demonstrated for a range of tissue and disease types, such as colon[233] and prostate cancer[234]. Organoids are generally split into 2 categories: those grown from small clusters of cancer cells and those which depend on a tissue scaffold for growth (developed from synthetic chemicals such as Matrigel, or from excised animal or human tissue). Bladder organoids have previously been developed using rat[134,235], pig[137] and human explant tissue[136]. Human bladder cancer cells have previously been shown to adhere to rat and porcine mucosal tissue, allowing research groups to better investigate how bladder cancer invasion, progression and recurrence occurs alongside assessing therapeutic options for disease *In Vitro*. Huygens *et al.* developed a bladder cancer organoid model from urothelial cells to study the penetration of the PS agent Hypericin into tissue[236]. Additionally, autofluorescence imaging has been applied to the study of the optical redox ratio in breast cancer organoids in response to drug therapy[237]. Despite this increasing focus on cancer organoids in disease research, there exists no literature covering autofluorescence profiles in developing bladder cancer organoids. Second harmonic imaging of organoids is likewise poorly covered in the literature, however this technique may reveal progressive changes in collagen in the underlying connective tissue. SHG imaging has previously been used to identify hallmark collagen patterns in malignant breast tissue and ovarian tissue[93], therefore it may also be of worth for bladder cancer. As urothelial thickening often obscures collagen autofluorescence signals in bladder cancer, combined use of autofluorescence and SHG imaging of tissue will be a useful tool to better assess the relationship between collagen and NADH/FAD profiles in disease. Combined MPM/SHG imaging has been used to assess morphology of mouse bladder tissue[96] and to discern between healthy and cancerous bladder tissue in a small sample size[98]. The focus of this chapter, therefore, is the development of an organoid model of muscle invasive human transitional cell carcinoma of the bladder using porcine bladder tissue and a human bladder cancer cell line. This work was informed by previous work by Varley *et al.* in which human bladder mucosa was successfully reconstructed using urothelial cell lines[136], and work by Janssen *et al.* to develop a straightforward bladder organoid model using porcine bladder biopsy[135]. Within this model, bladder cancer cells were found to adhere to tissue scaffold by day 2 of the study, culminating in invasion and an invasive TCC phenotype by day 12. My hypothesis was that application of autofluorescence spectroscopy to the developing organoids would reveal progressive changes in the optical properties of tissue, related to fluorescence intensity and fluorescence ratios such as the optical redox ratio. Furthermore, I hypothesised that second harmonic generation imaging of tissue sections would reveal differences in collagen volume and orientation around the infiltrating cancer cells, in keeping with previous work on breast cancer.

Autofluorescence spectroscopy of the developing organoids revealed significant changes in the optical properties (spectral shape and ORR values) compared to control samples. Furthermore, SHG of the tissue slides revealed significant differences in the collagen volume and texture surrounding cancer cells. It is hoped that these newly recognised factors can help to apply non-invasive medical imaging to human tissue, with a better understanding of potential diagnostically relevant biomarkers.

3.2 Methods

3.2.1 Porcine bladder scaffold

Porcine bladders from freshly slaughtered pigs were purchased from Medical Meat Supplies Ltd. The tissue was halved to reveal the urothelial surface of the bladder. From one half of the bladder, a 20 cm^2 (4cm x 5cm) section was cut with a scalpel. From this, the mucosa and a small section of muscle were cut away from the remaining muscle layer, to give a tissue scaffold with a remaining thickness of roughly 2-3mm. The mucosa/muscle layer was kept and the remaining muscle was discarded. Following this, the tissue scaffold was cut into 20 identical sections of $1cm^2$, washed x 3 in Phosphate Buffered Saline (PBS) (Sigma Aldrich) to remove leftover urine or contaminants, sterilised in 10,000 Units Penicillin- 10mg Streptomycin solution (Sigma Aldrich) and transferred to 0.25% Trypsin – EDTA solution (Sigma Aldrich) and incubated for 15 minutes to disrupt urothelium, following which they were again washed in PBS x 3 and placed in individual wells of a Corning Costar 12 well plate (Sigma Aldrich). It is important to note that the scaffold was not acellular. A cross section of the tissue scaffold (54a) and an image of the optical probe in contact with the tissue (54b) are included in Fig.54. Tissue fluorescence measured in a plastic 12 well plate was compared with tissue fluorescence in custom matte-black cuvette, ensuring that background plastic fluorescence did not interfere with measurements.

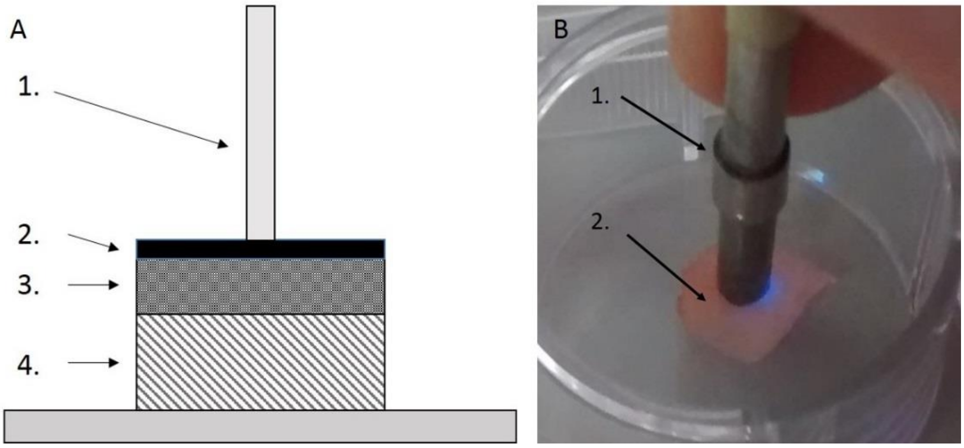

Figure 54 Experimental setup of organoid measurement showing cross-section (A) and top-down view (B) of optical probe (1) touched to urothelial surface (2) overlaying connective tissue (3) and muscle layer (4)

3.2.2 Cell culture

Bladder cancer cell line “5637” was purchased from American Type Culture Collection and grown for several passages in Dulbecco’s Modified Eagle Medium (DMEM) (Sigma Aldrich) supplemented with 10% Fetal Bovine Serum (FBS) (Sigma Aldrich) and 1% Penicillin-Streptomycin (Sigma Aldrich) in 75cm^2 cell culture flasks (Corning). At 70% confluence, cells from one flask were detached by conventional trypsinisation, re-suspended in DMEM, split into ten 15ml Falcon tubes (BD Biosciences) and spun at 1500RPM for 10 minutes to form pellets. Pellets of approximately 10^6 cells were applied to ten of twenty bladder scaffolds, leaving ten scaffolds as a control. The scaffolds and cell pellets were each resuspended in 1ml DMEM (10% FBS, 1% penicillin-streptomycin, 1% Fungizone) and incubated overnight.

3.2.3 Fluorescence spectroscopy

Fluorescence spectroscopy was performed using multi-functional laser based non-invasive diagnostic system “LAKK-M”, described in greater detail in Chapter 1. The system was initiated 30 minutes prior to study then transferred to the cell culture lab. Measurements were performed at the same time on all samples in the afternoon of each day on days 0, 1, 4, 7, 11, 14, 18 and 21 of study by gently bringing into contact, without pressing down, the probe of the “LAKK-M” to the exact centre of the mucosal (upward facing) surface of tissue each time. On day 0, tissue was measured prior to seeding of cancer cells to ensure all tissues displayed similar fluorescence. Fluorescence measurements were performed in the dark to prevent interference from background noise. Measurements were performed sequentially for each wavelength. Spectra recorded from tissue was visualised on accompanying laptop using custom-made software (LDF 3 v3.1.1.403, SPE “LAZMA” Ltd, Russia).

3.2.4 Confirmation of invasion

A pilot study was run using the steps described, but for two and twelve days, after which the samples were fixed in formalin and submitted to the Tayside Tissue Bank, Ninewells Hospital, Dundee, for sectioning and staining of tissue slides with Haematoxylin and Eosin (H & E). Attachment of cancer cells to scaffold in organoids by day two, and T1 transitional cell carcinoma phenotype by day 12, were confirmed by an experienced pathologist. Slides were imaged at 200x magnification using a Nikon Eclipse E600 microscope. H & E stained slides of control (55A), attachment (55B) and invasion (55C) are included below (Fig.55):

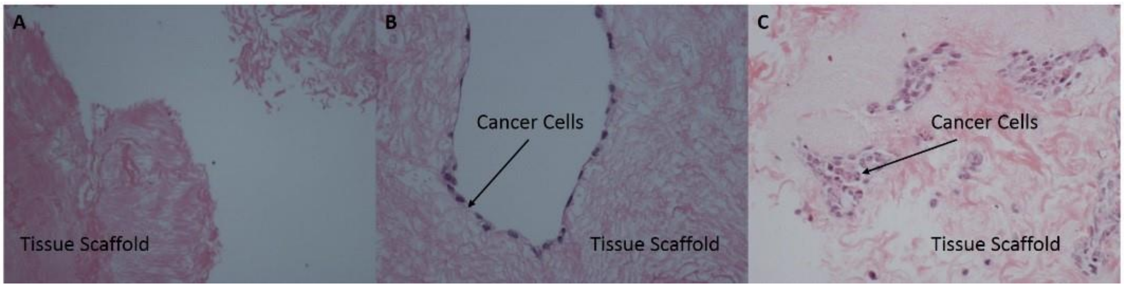

Figure 55 H & E stained sections of control (A), attachment of cancer cells (B) and invasion of cells into tissue (C) with tissue scaffold and cancer cell labelled as appropriate

To compare tissue with human equivalent, H & E stains of human tissue were requested from Tayside tissue bank, photographed using the same setup and included below. Organoid and control sections stained with H & E are depicted below (Fig. 56).

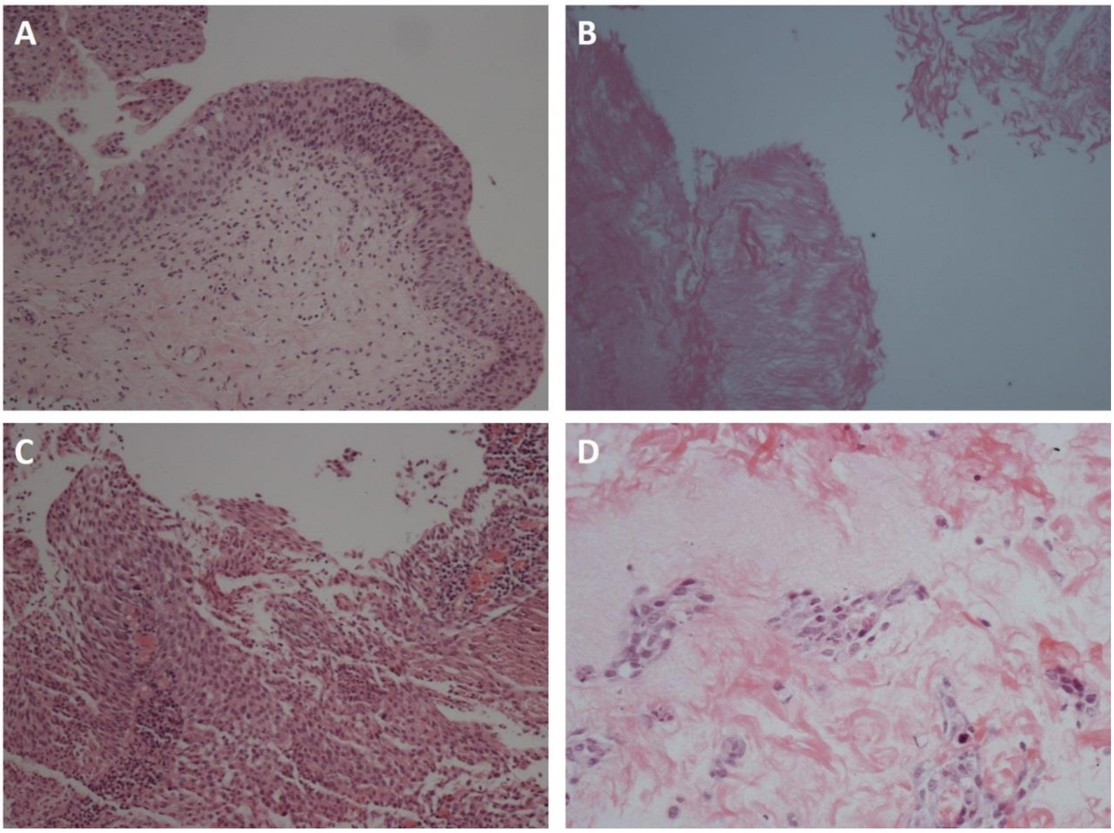

Figure 56 Comparison of H & E stained human healthy tissue (A) with organoid control (B) and human TCC (C) with cancer organoid (D)

3.2.5 Data analysis

Data was analysed using custom made analysis software LDF 3 v3.1.1.403 (SPE "LAZMA" Ltd). The software calculates and records the amplitude of fluorescence (Af) at distinct pre-set wavelengths in accordance with previously published literature. The fluorophores of interest and their excitation and emission values were as follows (Table 8)[199]:

Table 8 Common tissue fluorophores measured using the LAKK-M system

Fluorophore	**Excitation (nm)**	**Emission (nm)**
Collagen	365	420
Elastin	365	450
NADH	365	490
Flavin	365	550
Flavin (450 ex.)	450	510
Lipofuscin	532	570
Carotene	532	608
Porphyrin	633	710

Optical redox ratio was calculated for each sample on each day as NADH (ex365 em490)/Flavin (ex365 em550) as this was determined the most stable measurement in chapter 2. Additionally, the following ratios were also calculated: Elastin/NADH; NADH/Collagen and Elastin/Flavin. Elastin/NADH, elastin/flavin and NADH/collagen ratios were selected to address structural rather than metabolic changes in tissue and to best reflect spectral differences between control and organoid samples by day 21. Average and ratio values were compared by plotting mean + SEM (Standard Error of the Mean) for control versus organoid over the 21 days of study. One control sample was removed from study on day 4 owing to fungal contamination. Two further control samples were removed on day 18 due to fungal contamination. Collected data were analysed and plotted as graphs using Origin Pro 8 (OriginLab). Data were compared and assessed for statistically significant differences at each time point using AOV (ANOVA) test in R Studio (leverage of residuals and Q-Q plots were assessed to ensure applicability of analysis) for p value with $p < 0.05$ considered statistically significant. Data from each day were compared and analysed separately for statistical significance to account for the removal of contaminated specimens on days 4 and 18.

Based on this data, ROC curves were generated, charting sensitivity (y-axis) versus 1 – specificity (x axis). ROC curves were generated for ORR (NADH/FAD) and elastin/NADH on day 21 only using MATLAB and were qualified based on their calculated area under the curve (AUC) value. AUC values indicate the diagnostic worth of a test, ranging from 0.5 – 1.0 with 0.5 = useless and 1.0 = ideal.

3.2.6 Second harmonic generation imaging

Microscope slides containing 5µm thick H & E stained sections of control (n = 2) and organoid (n = 5) tissue were assessed using a Leica TCS SP8 confocal microscope with 20x objective fitted with tunable IR for MPM and SHG (Fig. 57). SHG was excited from samples at 880nm and detected in the forward direction (below samples) using a photomultiplier tube (PMT) with a 440/20 band-pass filter to detect and report full signal between 430-450nm and discard all <430nm and >450nm. Cancer cell outlines were detected by transmitted light at 488nm detected above the sample by a transmitted light sensor. Individual and merged images were saved and opened in Leica "LASX" microscope image analysis programme. Channel 1 (transmitted light) was not modified in the programme. Channel 2 (SHG signal) was compressed to a setting of 790/4095 for each image to improve contrast. Snapshots were taken of merged images, saved as JPEGs and exported for further analysis. From the JPEGs of dimension 420 x 420 pixels, individual frames of 60 x 60 pixels were cut for study using Photoshop 6.0 from the area of connective tissue, displaying the strongest SHG intensity. In total, 24 frames were taken from 2 slides of control tissue and 29 frames were taken from 5 slides of organoid tissue. Selection of regions of interest from full scans are shown in Figure 58. Tissue sections were analysed in MATLAB using grey level co-occurrence matrix (GLCM) texture analysis. GLCM represents an estimate of the separation of adjacent grey levels in the matrix “i” and “j”. From the GLCM, energy, entropy, correlation, contrast and inverse different moment can be derived. The parameters, their derivations and what they represent are denoted in Table 9. Alongside GLCM analysis, average and maximum pixel intensity was calculated for each frame.

Table 9 Parameters derived from GLCM

Parameter	**Formula**	**Information**
Energy	$ASM=\sum_{i=1}^{k}\sum_{j=1}^{k}(G(i,j))^2$	Uniformity of pixel information
Entropy	$ENT=-\sum_{i=1}^{k}\sum_{j=1}^{k}G(i,j)\log G(i,j)$	Randomness of texture
Contrast	$CON=\sum_{n=0}^{k-1}n^2\{\sum_{\lvert i-j\rvert=n}G(i,j)\}$	Local variations in GLCM
Inverse Different Moment	$IDM=\sum_{i=1}^{k}\sum_{j=1}^{k}\frac{G(i,j)}{1+(i-j)^2}$	Local correlation of pixels

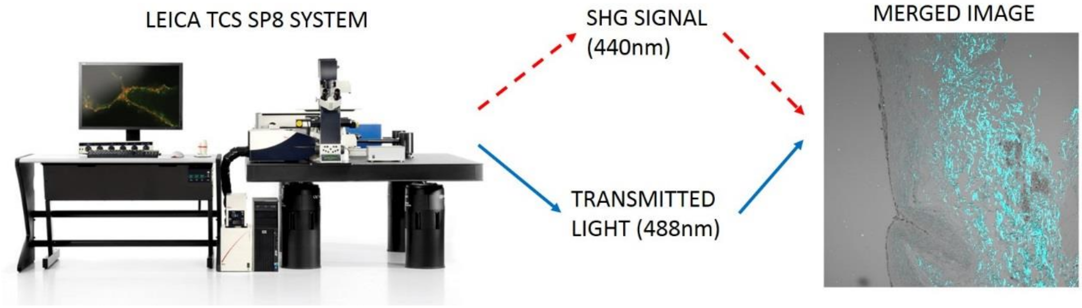

Figure 57 General setup of confocal imaging system used to generate SHG images, showing combination of SHG signal at 440nm with transmitted light at 488nm.

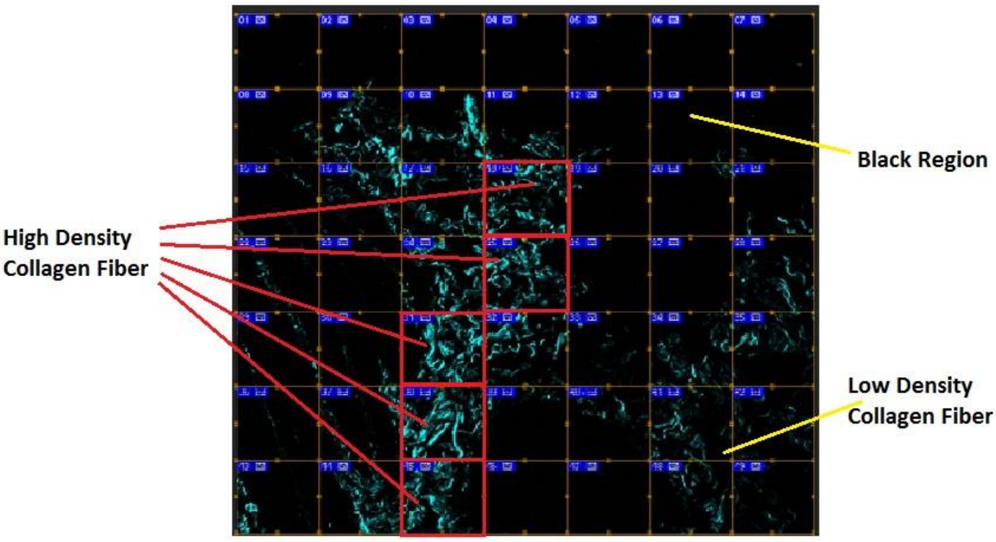

Figure 58 Sectioning of SHG image to remove background signal and include areas of strong SHG signal for analysis (image generated as montage of fields of view from one healthy sample)

3.2.7 Classification algorithms

Classification algorithms were developed using MATLAB data processing software. For autofluorescence spectroscopy, the algorithm analyses a CSV file containing spectral fluorescence intensity data, calculating the area under the curve (AUC), ratio of 450/490nm (elastin/NADH) and the ratio of 490/550nm (NADH/flavins), using pre-set diagnostic threshold to determine healthy from cancer. In each instance, a parameter of interest was selected, either NADH/flavin or elastin/NADH, following which the measured value for the sample in question was compared against a threshold. For ORR values, the threshold was 2 (>2 = healthy, <2 = cancer) and for elastin/NADH the threshold was 1.1 (>1.1 = healthy, <1.1 = cancer). The programme then provides the spectral chart, alongside the opinion as to whether tissue is healthy or cancer. For SHG, the algorithm analyses the GLCM parameters from Table 9. The programme then provides a classification output based on a calculated parameter as to whether the tissue is healthy or cancerous, with diagnostic thresholds as follows: energy (<0.1 = cancer); entropy (>3.5 = cancer); contrast (>7.5 = cancer); correlation (<0.05 = cancer); average brightness (>60 = cancer); pixel/pixel ratio (>1 = cancer).

3.3 Results

3.3.1 Fluorescence spectra

The average UV fluorescence spectra for both control and organoid samples were compiled and plotted at the beginning (Day 0) and end (Day 21) of experimental time course. Average fluorescence spectra on day 0 are similar (Fig.59a), however fluorescence spectra on day 21 (Fig.59b) show differences in line shape suggestive of altered levels of contributing fluorophores.

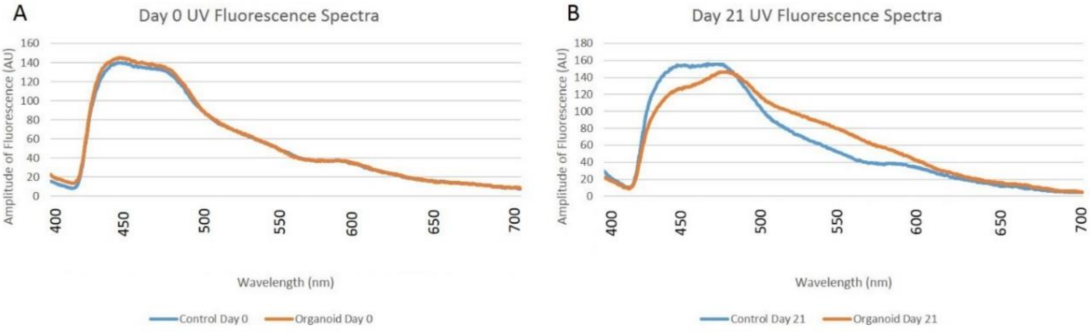

Figure 59 Average UV spectra of control (orange line) and organoid (blue line) on days 0 (A) and 21 (B). Orange and blue lines on A represent n = 10; orange line on B represents n = 7; blue line on B represents n = 10.

3.3.2 Optical redox ratio

Data on each day was handled and analysed separately to account for the removal of contaminated specimens. Measurements of individual fluorophores over time (Fig. 60-62) showed no consistent significant changes, with the exception of flavins, which show a general trend of increasing in organoids. Optical redox ratio (ORR) values (measured as NADH (ex365em490)/flavins (ex365em550)) show a sharp decrease in organoids, from equitable levels to control at day 0 to progressive decreases across day 1-21 (Fig.63), which may be partially caused by the changes observed in flavins. Data at day 0, before addition of cancer cells, were found to not be statistically significantly different ($p = 0.334$), however data on each subsequent day were found to be statistically significantly different (day 1, $p = 0.0118$; day 4, $p = 0.000977$; day 7, $p = 1 \times 10^{-6}$; day 11, $p = 9 \times 10^{-10}$; day 14, $p = 3.5 \times 10^{-8}$, day 18, $p = 7.8 \times 10^{-7}$; day 21, $p = 5.15 \times 10^{-6}$). Day to day variations in environment and instrumentation are accounted for by control. ORR calculated using flavins measured under blue excitation (ex450em510) showed no significant difference over the course of the experiment (day 0, $p = 0.918$; day 1, $p = 0.335$; day 4, $p = 0.712$; day 7, $p = 0.636$; day 11, $p = 0.232$; day 14, $p = 0.204$; day 18, $p = 0.9$; day 21, $p = 0.483$). The cause of this remains to be determined by future investigation.

3.3.3 Elastin relative to metabolic cofactors

Taking the ratio of elastin fluorescence (ex365em450) against that from both the metabolic cofactors NADH (ex365em490) (Fig.62) and flavins (ex365em550) (Fig.64) also shows significant decreases in the relative elastin levels compared to these fluorophores in organoids across the 21 day period. For elastin/NADH measurements, data at day 0 and day 1 were not statistically significant ($p = 0.668$ and $p = 0.146$, respectively), however differences in data from each subsequent day was statistically significant (day 4, p = 0.00236; day 7, p = 5.3 x 10^{-7}; day 11, p = 6.9 x 10^{-5}; day 14, p = 0.000102; day 18, p = 0.00282; day 21, p = 0.000146). Data from elastin/flavin measurements on day 0 were not statistically significant (p = 0.598), however differences in data were statistically significant on each subsequent day (day 1, p = 0.0282; day 4, p = 0.000588, day 7, p = 2.14 x 10^{-7}; day 11, p = 1.81 x 10^{-8}; day 14, p = 1.1 x 10^{-7}; day 18, p = 1.27 x 10^{-5}; day 21, p = 3.07 x 10^{-6}), which again may be partially caused by the increased flavin values in organoids over time. Data from NADH/collagen showed no consistent statistically significant changes across the experimental period. Furthermore, data for this ratio on day 0 prior to addition of cancer cells was statistically significant (p = 0.0182). This is possibly due to very low relative fluorescence of collagen recorded at ex365em420 making it susceptible to background noise interference.

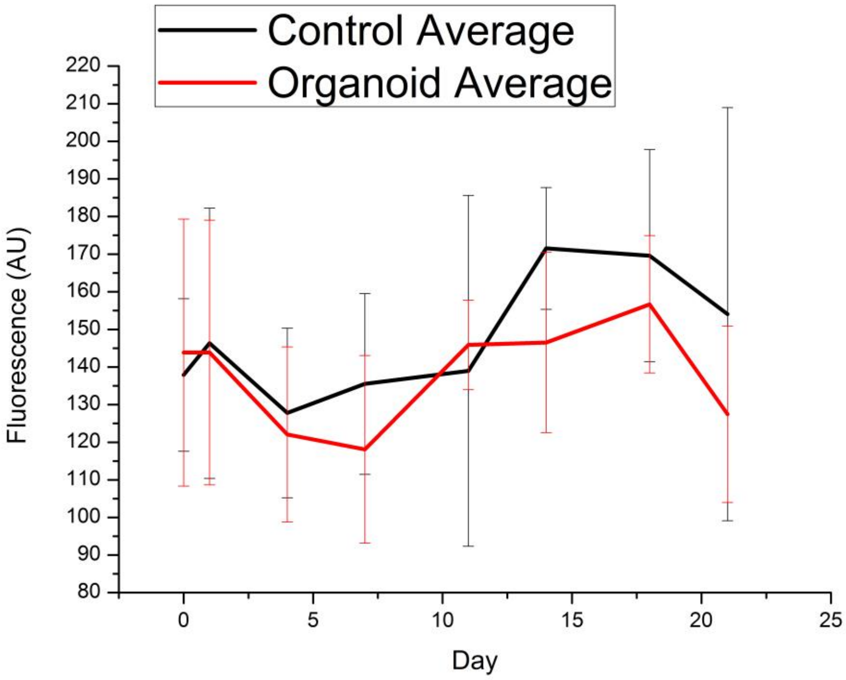

Figure 60 Day to day variations in elastin fluorescence measured from samples at ex365em450. Black line depicts control average (n = 10 on days 0 &1, n = 9 on days 4, 7, 11 & 14, n = 7 on days 18 & 21), red line depicts organoid average (n = 10 on each day). Error bars depict standard error of the mean (SEM)

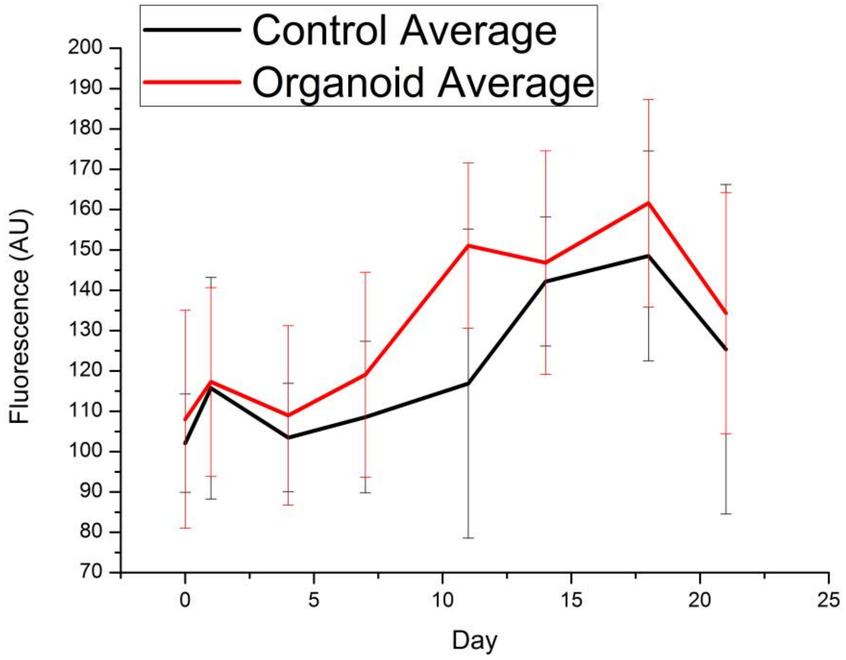

Figure 61 Day to day variations in NADH fluorescence measured from samples at ex365em490. Black line depicts control average (n = 10 on days 0 &1, n = 9 on days 4, 7, 11 & 14, n = 7 on days 18 & 21), red line depicts organoid average (n = 10 on each day). Error bars depict standard error of the mean (SEM)

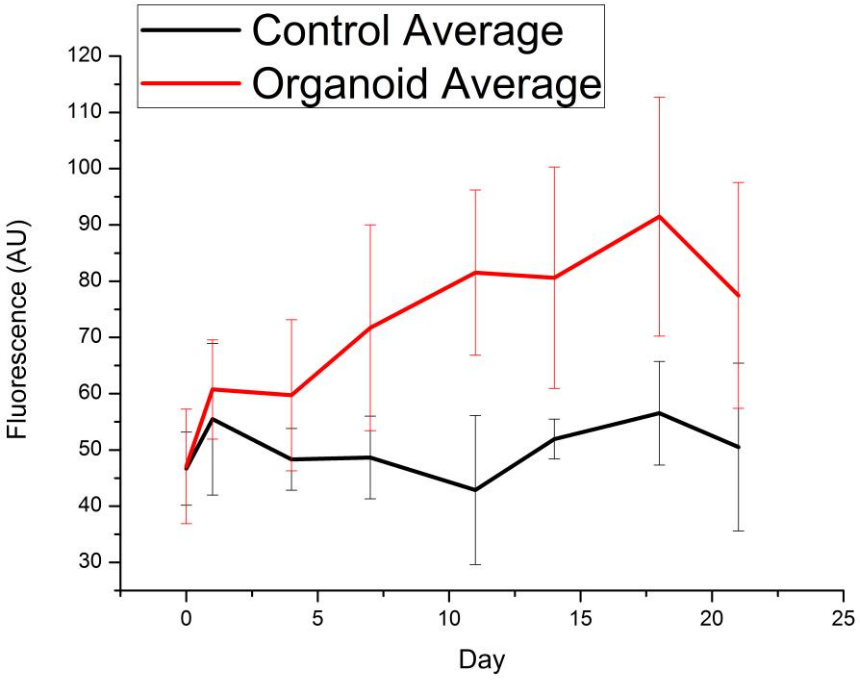

Figure 62 Day to day variation in flavin fluorescence measured from samples at ex365em550. Black line depicts control average (n = 10 on days 0 &1, n = 9 on days 4, 7, 11 & 14, n = 7 on days 18 & 21), red line depicts organoid average (n = 10 on each day). Error bars depict standard error of the mean (SEM)

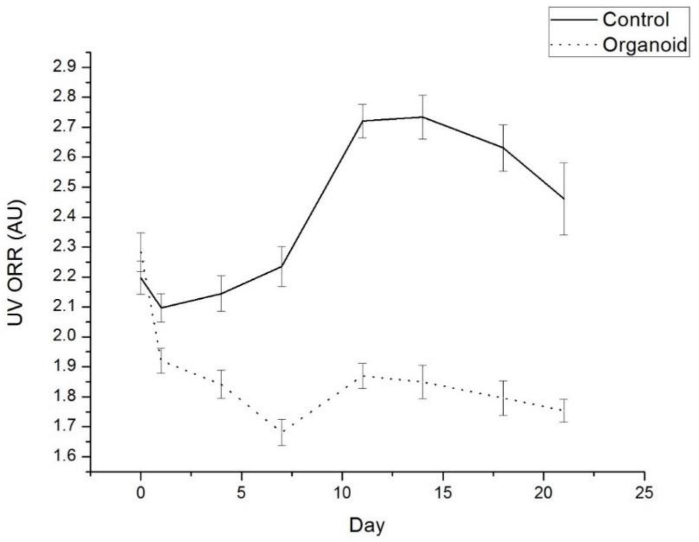

Figure 63 Average ORR values for control (solid line) and bladder cancer organoid (dashed line) across the 21 day measurement period (+/- SEM). Organoid n = 10 on each day. Control n = 10 on days 0 & 1, n = 9 on days 4, 7, 11 & 14 and n = 7 on days 18 & 21.

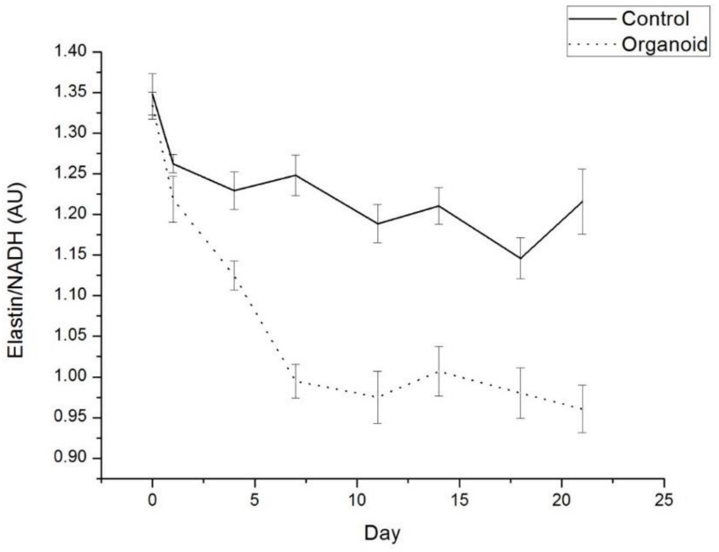

Figure 64 Average elastin/NADH ratios for control (solid line) and cancer organoids (dashed line) across the 21 day study (+/- SEM). Organoid n = 10 on each day. Control n = 10 on days 0 & 1, n = 9 on days 4, 7, 11 & 14 and n = 7 on days 18 & 21.

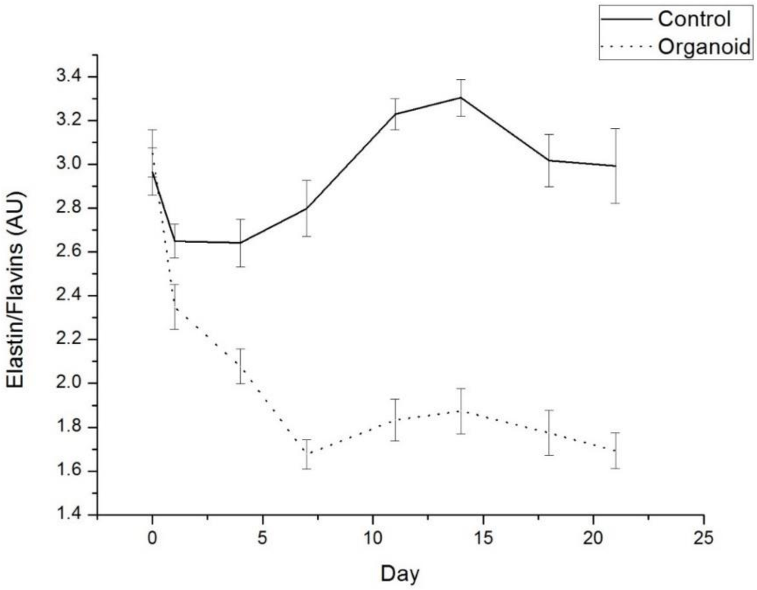

Figure 65 Average elastin/flavins ratios for control (solid line) and cancer organoids (dashed line) across the 21 day measurement period (+/- SEM). Organoid n = 10 on each day. Control n = 10 on days 0 & 1, n = 9 on days 4, 7, 11 & 14 and n = 7 on days 18 & 21.

3.3.4 Development of Diagnostic Algorithm

The significant results for the ratios covered previously led to assessment of their worth as diagnostic criteria to classify control and organoid samples. It can clearly be seen based on the organoid data that the UV ORR (NADH/Flavins) is a good candidate with which to classify both control and organoid samples, with an ROC AUC value of 1 (Fig. 66a). Elastin/NADH ROC analysis similarly delivered an AUC value of 0.99, indicating diagnostic promise (Fig. 66b). It would be of interest to determine how well these ratios apply to human biopsy data, therefore this was attempted in chapter 4. Below, Figure 67 displays the diagnostic interface developed in MATLAB to provide diagnostic opinion based on automated analysis of ORR and elastin/NADH parameters, alongside spectral readout and fluorescence AUC value. Based on a small sample size, this programme was capable of cancer organoid detection with 100% sensitivity and 100% specificity.

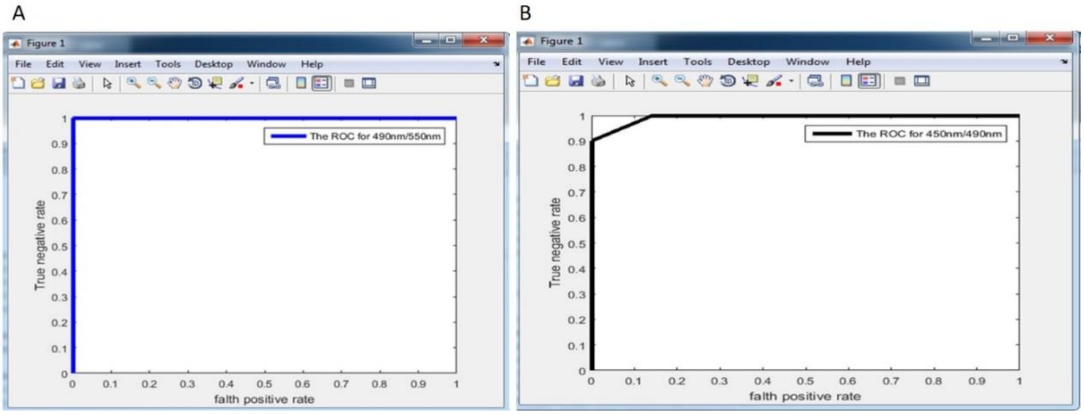

Figure 66 ROC curves for ORR (A) and elastin/NADH (B) values

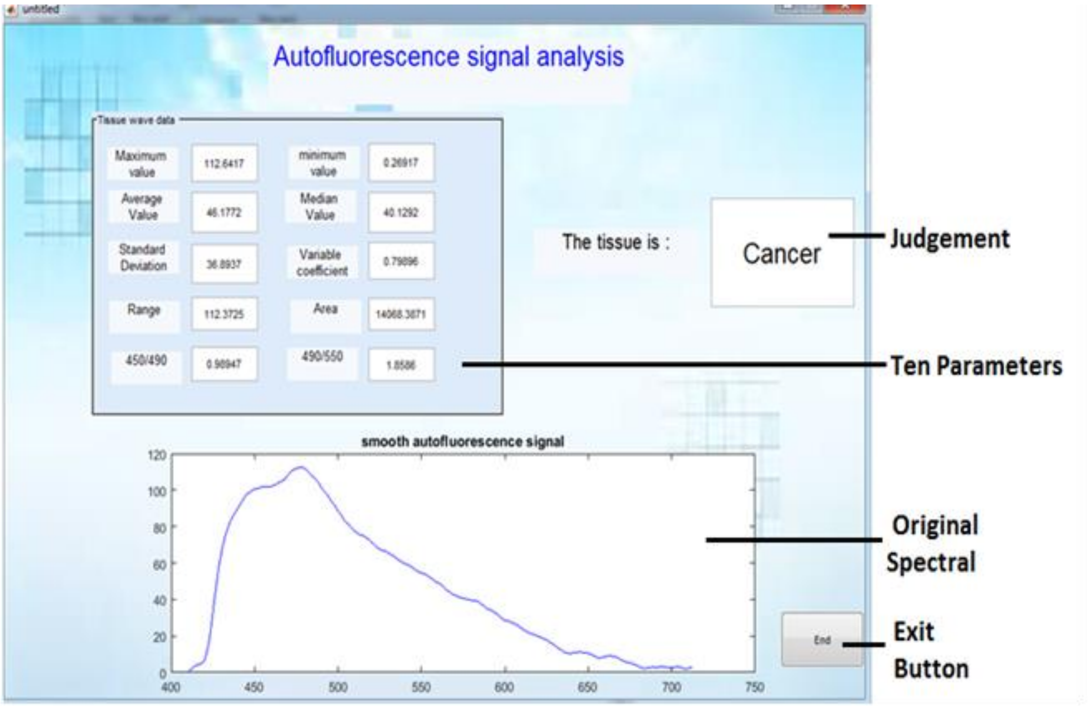

Autofluorescence signal analysis

Tissue wave data

Maximum value: 112.6417
minimum value: 0.26917
Average Value: 46.1772
Median Value: 40.1292
Standard Deviation: 36.8937
Variable coefficient: 0.79896
Range: 112.3725
Area: 14068.3871
450/490: 0.98947
490/550: 1.8586

The tissue is : Cancer

Figure 67 Screenshot of diagnostic interface showing measured parameters of AUC, ORR and elastin/NADH along with tissue classification

3.3.5 Second Harmonic Imaging

From the images of control and organoid acquired using SHG microscopy, the different layers of tissue can clearly be seen (labelled, Fig. 68 & 69) demarcated by their varying levels of collagen (light blue). In the urothelial layer there is moderate SHG from the collagen underlying the epithelial cells, in the connective tissue zone there is a higher signal from collagen and in the underlying muscular region there is almost no noticeable SHG. The difference in SHG signal between urothelial and connective tissue layers can clearly be seen in Fig.68, while the difference between connective tissue and muscular layers can clearly be seen in Fig.69. This is in keeping with previous understanding of collagen distribution in the bladder. Furthermore, from SHG scans of the organoid tissue (Fig. 70) the presence of the bladder cancer cells attaching to the urothelium and invading into the connective tissue, forming “collagen nests” which generate a higher SHG signal.

Mathematical assessment in MATLAB of individual frames of connective tissue from control and cancer organoid revealed a number of differences between the two tissue types which could be of diagnostic worth. Statistically significant differences were found between populations for energy ($p = 2 \times 10^{-16}$), entropy ($p = 2 \times 10^{-16}$), contrast ($p = 2 \times 10^{-16}$), correlation ($p = 2 \times 10^{-16}$), average brightness ($p = 2 \times 10^{-16}$) and pixel ratio number ($p = 2 \times 10^{-16}$). These differences indicate that connective tissue from cancer organoid samples is modified by invading cancer cells. This manifests as cancer organoids possessing increased averaged collagen content, more complex and less uniform textural information and increased contrast between regions, depicted in Figure 70. Figure 71 displays bar charts (+/- SEM) for each of the measured SHG parameters from organoids, while Fig. 72 depicts a screenshot of the diagnostic interface showing tissue classification as either healthy or cancer.

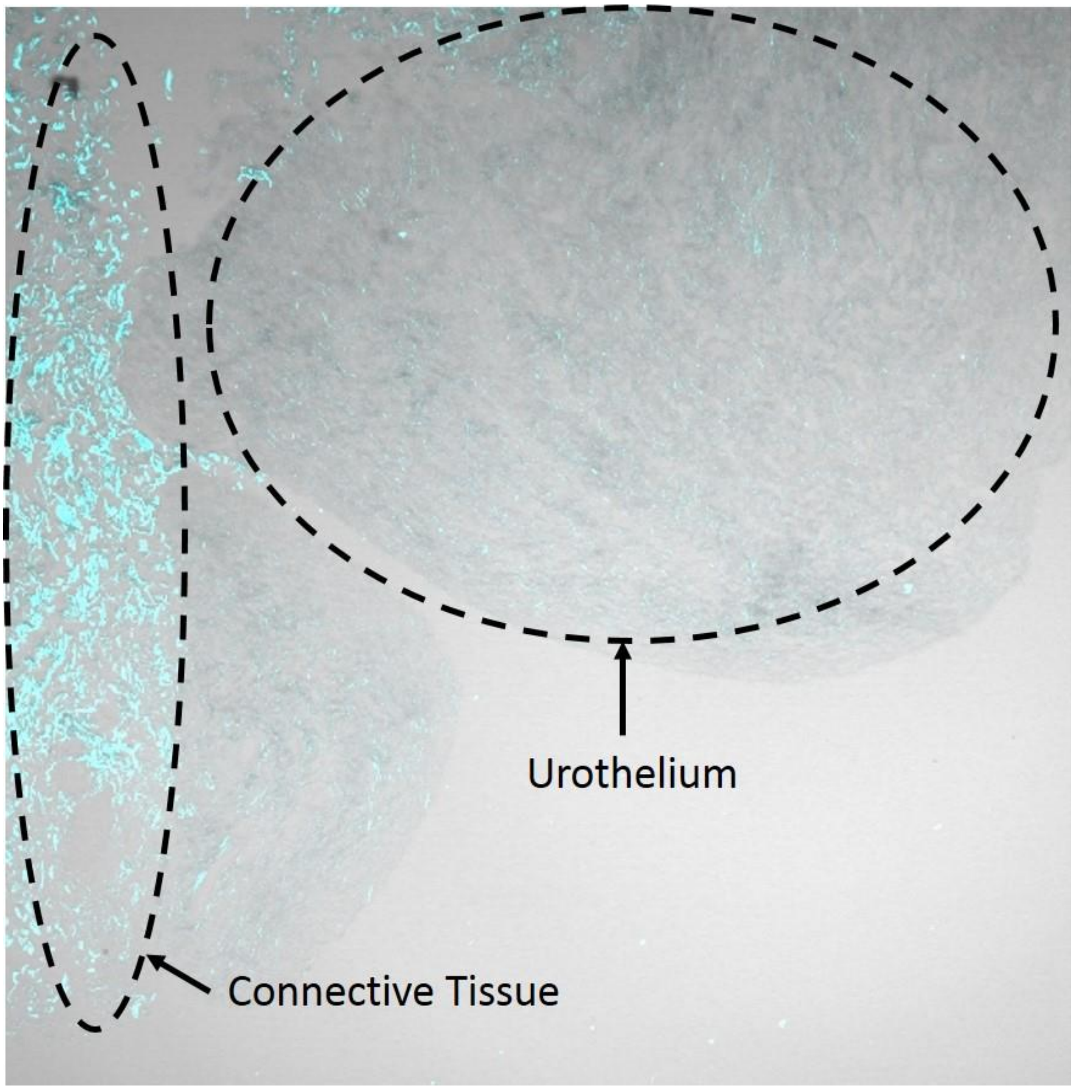

Figure 68 Merged SHG + transmitted light of control sample slide showing connective tissue and urothelium

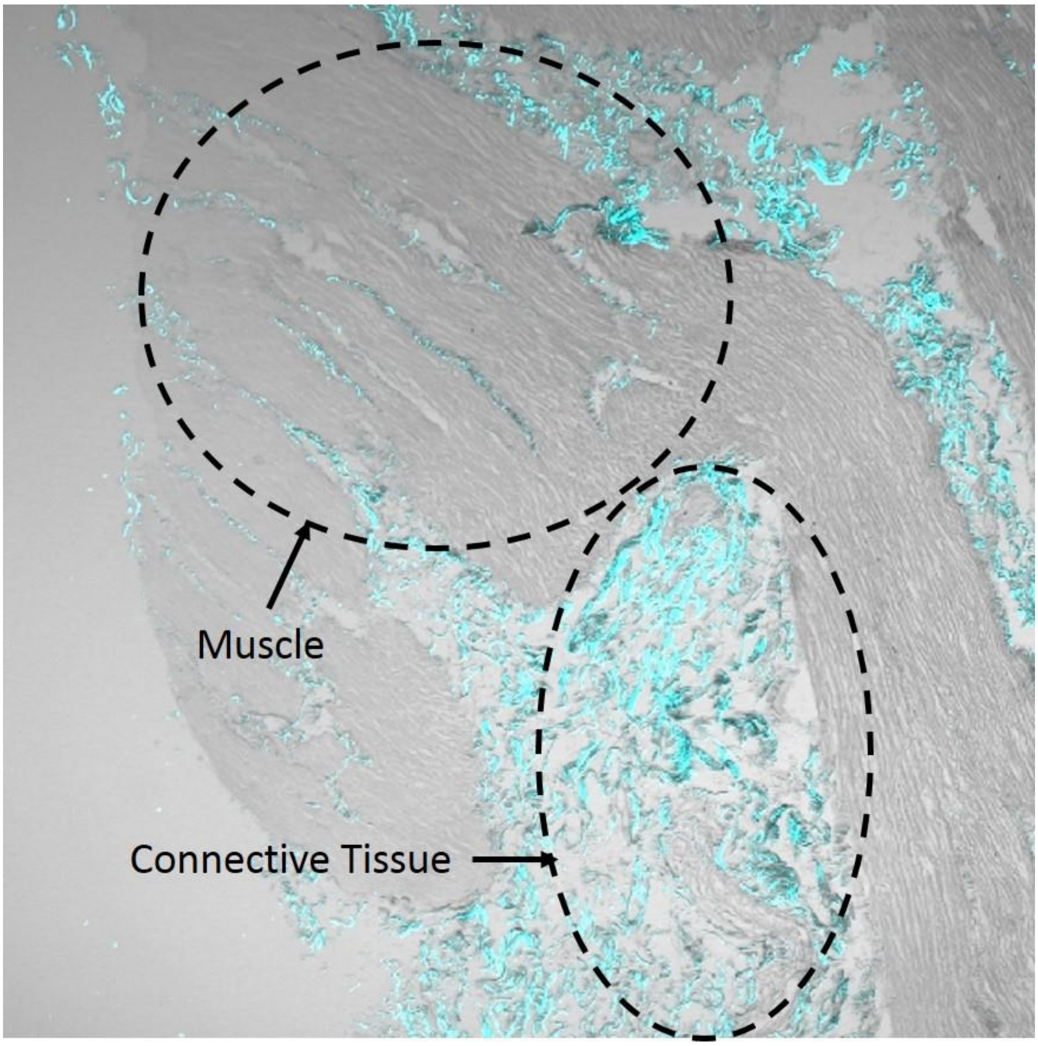

Figure 69 Combined SHG + Transmitted light image of control sample slide showing connective tissue and muscle

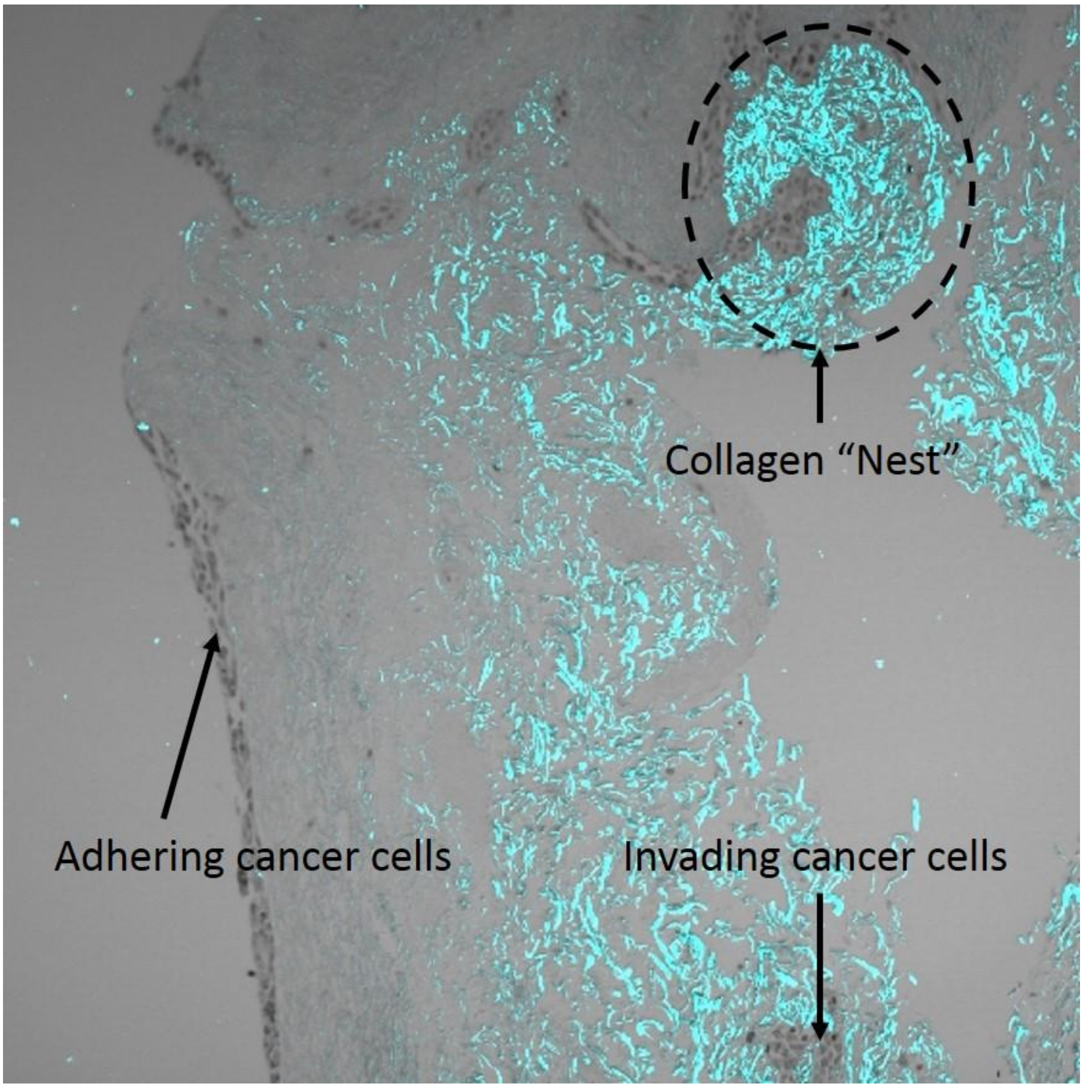

Figure 70 Combined SHG + Transmitted light image of cancer organoid slide showing bladder cancer cells adhering and invading into tissue scaffold

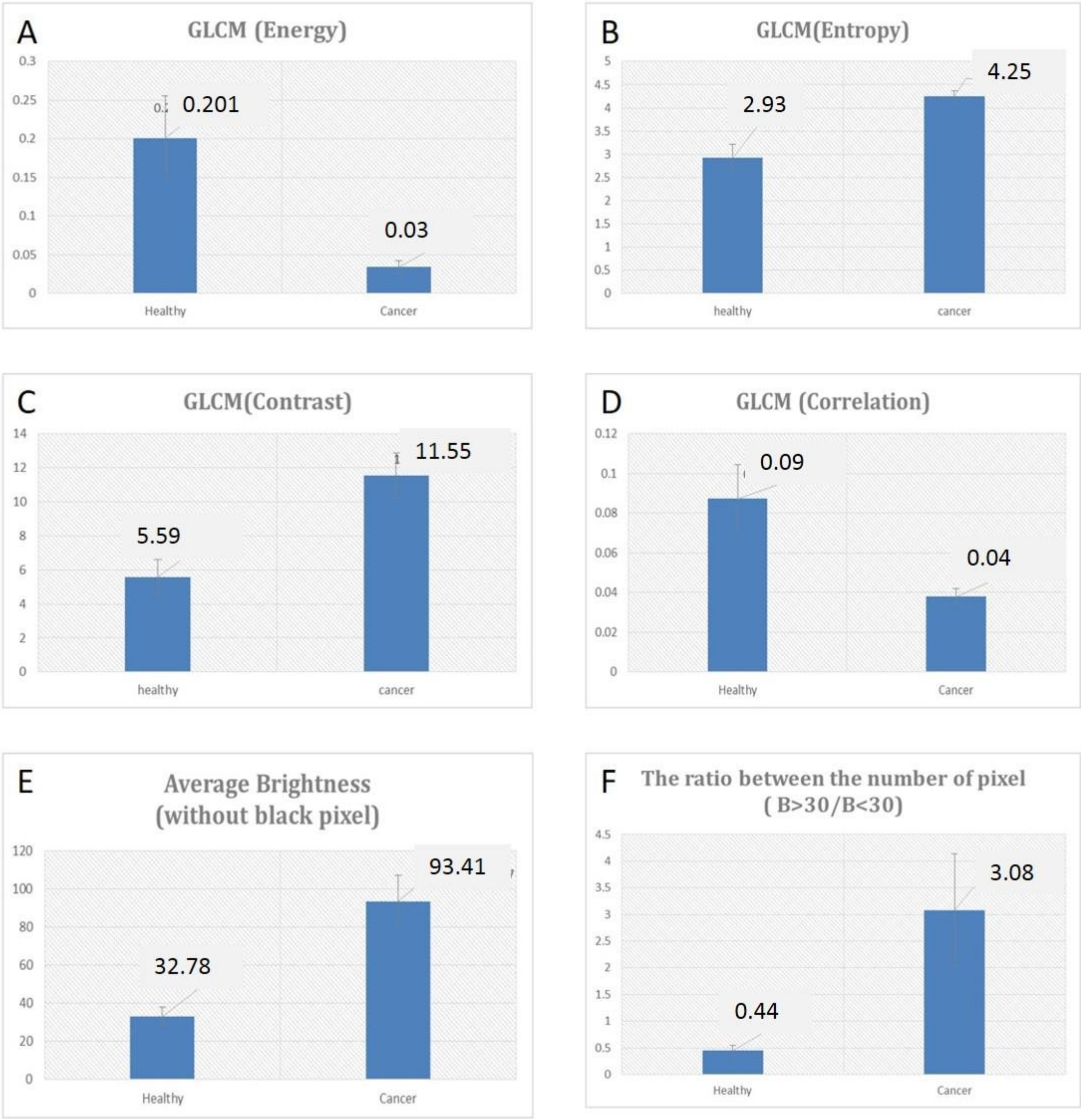

Figure 71 Bar charts depicting mean +/- SEM for energy (A), entropy (B), contrast (C), correlation (D), average brightness (E) and pixel ratio (F) comparing control with organoid (in each case, healthy n = 24, cancer n = 29)

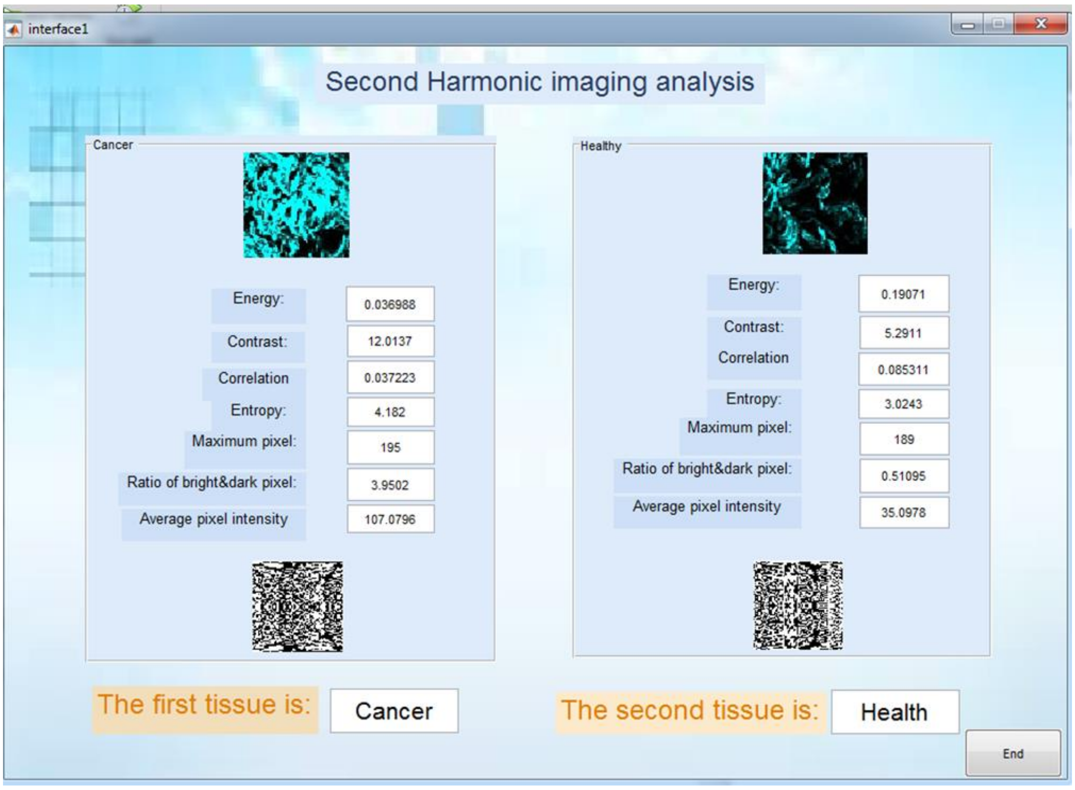

Cancer
Energy: 0.036988
Contrast: 12.0137
Correlation 0.037223
Entropy: 4.182
Maximum pixel: 195
Ratio of bright&dark pixel: 3.9502
Average pixel intensity 107.0796

Healthy
Energy: 0.19071
Contrast: 5.2911
Correlation 0.085311
Entropy: 3.0243
Maximum pixel: 189
Ratio of bright&dark pixel: 0.51095
Average pixel intensity 35.0978

The first tissue is: Cancer
The second tissue is: Health

Figure 72 Screenshot of MATLAB diagnostic interface designed to classify images based on measured GLCM parameters

3.4 Discussion

From the data presented in this chapter, patterns of fluorescence emerge as tissue scaffold is adhered to and invaded by the cancer cells. Fluorescence has been assessed from distinct endogenous tissue fluorophores using the “LAKK-M” diagnostic system and based on analysis techniques previously followed by Dunaev *et al.*[199] and Akbar *et al.*[205] Previous studies generating bladder organoids from porcine bladders have demonstrated viability of cells within tissue scaffolds up to 3 weeks after induction. From this it was concluded that 3 weeks would be a suitable time frame for this fluorescence study. This work has shown that the UV spectrum of organoids changes relative to control across the experimental period. To investigate why this occurred, the properties of several endogenous fluorophores across the study period were assessed. The study of individual fluorophores is not well suited to this type of spectroscopy, as day to day variations in both laser power and tissue condition can affect amplitudes of fluorescence. Therefore no consistent patterns of fluorescence were observed from individual fluorophores. Instead, we looked at ratios of particular fluorophores relative to one another. The measurement of ratios, as used previously by Georgakoudi[193], Ostrander[190] and ourselves[225], among others, provides a much more robust measurement of fluorescence parameters. In particular, I focussed on the metabolic cofactors NADH and flavins, and the structural protein elastin, all known to fluoresce under UV excitation. As the source of NADH and flavins is primarily cellular, the conclusion is that the progressive decrease in ratios of elastin/NADH and elastin/flavins may reflect adherence, epithelialisation and invasion of tissue by cancer cells. Furthermore, it may also directly reflect the progressive destruction of the structural protein elastin in the surrounding connective tissue of the mucosa, lamina propria and muscular layers as cancer cells attach and begin to secrete digestive enzymes such as matrix metalloproteinases to promote invasion. It is known from previous studies that the urothelium (2-3 cells thick) contributes significantly to the NADH and flavin signals present in bladder tissue. In optical biopsies obtained by multi-photon microscopy, intense autofluorescence can be observed on the top layers of urothelium with strong second harmonic generation (SHG) signal from collagen observed below. It is considered that the main fluorophores contributing to organoid fluorescence may be NADH and flavins from the new tumour urothelium, while control fluorescence may contain a higher contribution from the underlying collagen and elastin matrix of the lamina propria and extra-cellular matrix (ECM) with NADH and flavin signals arising from the remaining mucosa. Comparisons between H & E stained samples from control slides with healthy human tissue indicate that although a certain amount of mucosa/urothelium is present in control sample, future studies would benefit from more thorough reconstitution of the urothelium through use of healthy urothelial cell lines.

This was not attempted as this work represented a first step pilot study. Comparisons between cancer organoid slides and human bladder TCC slides indicate morphological similarities, namely the infiltration of cancer cells deep into tissue and the formation of irregular tissue patterns.

Previous studies have suggested increased optical redox ratios (increased NADH relative to flavins) in cancer cells and tumours compared to healthy controls. The opposite of this was observed – a reduced optical redox ratio (measured as ex365em490/ex365em450) in the tumour organoid. This could be a result of changes in structural proteins, rather than changes in metabolism. As the excitation and emission profiles of elastin overlap somewhat with that of NADH, the complex fluorescence spectrum arising from UV excited tissue likely contains an NADH signal at 490nm with underlying contribution from elastin. Research by Croce *et al.* suggests that this overlap should be minimal past 450nm[180], however it is possible that there is some contribution. The epithelialisation of organoids results in increased cellular fluorophores, therefore the reduced ORR seen in organoids may be a function of the increased Flavin to elastin ratio we observe rather than a reduced NADH – flavin couple. It is suggested from this research that studying the relative changes in elastin and collagen compared to NADH and flavins may serve as a useful tool for monitoring bladder tumour development. Furthermore, the high sensitivity and specificity of the diagnostic ratios for fluorescence spectra obtained from bladder cancer organoids suggests that these ratios merit application to human bladder samples to assess diagnostic worth (covered in the subsequent chapter).

SHG imaging of tissue slides reveals a number of potentially useful parameters for discriminating between healthy and cancerous bladder tissue. Analysis focussed solely on connective tissue of the extracellular matrix as this possessed the strongest SHG signal and because the ECM is known to contribute significantly to bladder pathology[148] in which collagen is known to contribute directly to both pro- and anti-cancer effects[143]. Increases in average pixel intensity in organoid sample slides indicate that implanted cancer cells are stimulating the production of new collagen fibrils in tissue, potentially to facilitate the production of cancer cell nests. The initial hypothesis was that the addition of cancer cells to tissue scaffold may have resulted in a decreased relative collagen content as cancer cells secreted MMPs to facilitate further invasion[139], however this has been disproved by these findings. Future studies would benefit from investigating average pixel intensity values in larger population sizes and with varying grades of cancer cell. Furthermore, GLCM analysis reveals that cancer organoid slides possess greater textural variation, reflected in greater contrast and entropy values than control, combined with reduced correlation values. These findings can be accounted for by studying H & E stained slides of both organoid and human cancer samples. In both human cancer and organoid, regular tissue structure is disrupted by the invasion of bladder cancer cells. It can be concluded that the cancer cells are extensively modifying their environment to facilitate tissue invasion, causing changes in textural correlation in surrounding tissue (particularly ECM) compared to control samples which still possess a uniform anatomical structure. Unlike previous work in breast cancer, no obvious changes were observed in patterns of collagen distribution, denoted earlier by "TACS"[94]. This may be a result of comparing organoid studies with human biopsy analysis, or may simply be a result of different tissues of interest. Nevertheless, TACS and associated diagnostic patterns are a useful tool to further understanding and the clinical application of SHG imaging. GLCM application to intact organoids may allow us to better understand the collagen remodelling process as it happens, and identify suitable collagen patterns as diagnostic indicators, similar to work on TACS.

In this chapter, a method has been demonstrated for studying the day-to-day changes in fluorophore levels during colonisation and invasion of bladder tissue by tumour cells.

That cells were still viable by day 21 of the study suggests this model could be further used for evaluation of fluorescent responses to drug and treatment regimens such as Mitomycin C, akin to microscopy work done by Walsh *et al.* for breast cancer[237]. Moving forward, it would also be interesting to study the fluorescence properties of colonisation of scaffolds by cell lines representing different grades of urinary bladder cancer. Finally, researchers may benefit from the development of organoids derived from human explant tissue to account for any structural differences between porcine and human bladder tissue. Critical time points could then be identified where fluorescence differs, giving a clinical insight into spectral cues for malignancy and invasion in bladder cancer. The application of SHG imaging to slides taken from organoids clearly allows the demarcation of tissue layers by relative collagen content and identification of adherence and invasion by bladder cancer cells. From a small sample size, a number of potential diagnostic factors has been identified for the detection of bladder cancer which display statistically significant differences between control and cancer and which display extremely high levels of sensitivity and specificity for cancer. It would be of great value to study a much larger number of samples to give a clearer understanding of collagen profiles. At present, the current SHG microscopy setup is not well suited to the study of developing organoids due to the risk of contamination. Modifications to the SHG setup to allow its use under culture conditions, along with characterising the optical properties of full thickness organoid tissue (rather than microscope sections) would allow application of SHG imaging in a similar way to the autofluorescence study. This would allow the assessment of collagen profiles day by day. The use of SHG directly addresses one of the shortcomings of our autofluorescence study using the LAKK-M – the relatively low fluorescence yield of collagen under 365nm fluorescence excitation and detection at 420nm. A better understanding of collagen roles in developing tumours may help to put proposed changes into context and directly address the issue of tissue thickening as a cause of autofluorescence variation in bladder cancer. Combined autofluorescence and SHG imaging of developing organoids could give a wealth of structural and metabolic imaging, leading to the identification of relevant diagnostic biomarkers. Studies of this type may benefit from the use of multi-photon microscopy to elicit autofluorescence, rather than autofluorescence spectroscopy, as this modality is easily combined with SHG and can give image characteristics of tissue, noted in previous research in the field[96,98]. Furthermore, MPM utilises longer wavelength light, so may be better suited to the study of deeper lying tissues during the carcinogenesis process by exploiting the tissue optical window.

3.5 Conclusion

Autofluorescence spectroscopy of the bladder cancer organoid models developed reveals progressive changes in spectra as cancer cells attach and invade into tissue. This is seen by progressive decreases in organoid ORR values (measured as ex365em490/ex365em550), alongside changes in the ratio of the structural protein elastin to metabolic cofactors NADH and flavins. These findings suggest the introduction of cancer cells to bladder cancer induce both structural and metabolic changes, both of which could improve our understanding of bladder cancer as a disease and allow us to develop new diagnostic techniques and therapies. Similarly, SHG imaging of tissue slides has identified significant differences in collagen volume and distribution in organoid tissue, suggestive of modifications by cancer cells. Combined autofluorescence/SHG imaging of developing organoids will allow a much greater understanding of the structural and metabolic alterations occurring as tissue transitions from health to muscle invasive disease.

4. ANALYSIS OF HUMAN TISSUE

4.1 Introduction

As discussed previously, BCa is the 4th most common cancer in men and the 9th most common cancer overall in the UK, accounting for 5200 deaths each year[1]. Unfortunately, white light cystoscopy (WLC) and voided urine cytology (VUC) suffer from low sensitivity, especially for low stage cancers such as flat NMIBC and pre-cancerous lesions like CIS[13]. VUC sensitivity for TCC is considered to be between 25-50%[14,15], while WLC sensitivity for TCC ranges between 60-70%[16,17] (but can be as low as 4% for CIS cases[18]). The result of this low sensitivity is a high rate of tumour progression and recurrence, which puts a large burden on health services each year. Furthermore, bladder cancers which progress to MIBC stage can often only be adequately dealt with by radical cystectomy[12]. Photosensitisers accumulate preferentially in tumour tissue due to the enhanced permeability and retention effect[238], and vividly fluoresce under laser illumination through the promotion of endogenous porphyrin generation. PDD using common PS agents such as hexaminolaevulinate (HAL)[21] and 5-aminolaevulinic acid (5-ALA)[27] are shown to greatly improve the sensitivity of cytoscopic detection of bladder cancer compared to WLC[23] – reducing NMIBC recurrence rates[24] - but at the cost of greatly reduced specificity due to uptake by inflamed previously treated by surgery or chemotherapy[17,29]. According to meta-analysis, sensitivity of PDD ranges from 80-100%, while specificity ranges from 36-79%[17]). The result of reduced specificity is a greater number of false positives and an increase in unnecessary biopsy. There is a great deal of focus on addressing the sensitivity-specificity disparity in BCa detection, with many suggested solutions.

Many of the molecules present in human tissue naturally fluoresce, including structural proteins (collagen[145] and elastin[152]), metabolic cofactors (NADH[165] and flavins[167]) and blood precursors (porphyrins[175]). Metabolic perturbations in cancerous cells and tissues, along with the structural effects of tissue remodelling and tumour invasion, can lead to changes in the autofluorescence profile of tissue. Tissue remodelling by tumours has previously been shown to significantly reduce local collagen levels to promote invasion and metastasis[138]. Furthermore, metabolic disparity between healthy and cancerous tissue has been extensively explained by the Warburg effect[187], which postulates that cancer cells preferentially generate energy by aerobic glycolysis at the expense of oxidative phosphorylation. Thus, electron carriers including NADH accumulate in cancer cells, skewing the ratio of reduced metabolic cofactors relative to oxidised counterparts such as flavins. The optical redox ratio (ORR) takes into account the accumulation of NADH in cancer cells by ratioing NADH content by flavin content to give a measure of the extent of the Warburg effect. The ORR has previously been used to good effect to discriminate between healthy and cancerous cells of a number of tissue types[189-191], including by ourselves in bladder cancer[225]. The worth of autofluorescence spectroscopy for cancer diagnosis in a wide range of tissues has previously been covered comprehensively[100]. Early research in the field identified UV fluorescence spectroscopy as a useful tool for detecting breast and lung cancers[102]. Furthermore, compared with PDD, autofluorescence spectroscopy has been shown to improve bladder tumour margin demarcation[115]. Spectral differences between healthy and neoplastic bladder tissue have previously been identified using autofluorescence spectroscopy[111,112,114,116].

Fluorescence spectroscopy of bladder cancer has generally relied on the use of UV light, which is known to excite a wide range of endogenous tissue fluorophores, therefore giving rise to complex multi-component fluorescence spectra. A major limitation to understanding and application of autofluorescence spectroscopy for bladder cancer detection is an inability to detect and identify individual fluorophores of interest within complex spectra, however some groups are seeking to overcome this by delineating individual fluorophores[146,147]. D'Hallewin *et al.* have extensively covered the use of autofluorescence spectroscopy for bladder cancer[118], concluding that changes in autofluorescence spectra of bladder cancer tissue is largely a result of epithelial thickening obscuring signals from underlying fluorophores, in keeping with previous findings from prostate cancer[146] and Barrett's oesophagus[193]. Previously, in chapter 3, the use of combined autofluorescence/SHG imaging was discussed as a means to overcome the issue of tissue thickening in bladder cancer. It has been suggested therefore that AS is of little worth for CIS detection as this flat dysplasia does not cause tissue thickening. CIS nevertheless possesses considerable malignant potential, therefore early detection is of utmost importance. This issue has been addressed by Anidjar *et al.*, recording diagnostic worth of urothelial tryptophan fluorescence for CIS diagnosis[121].

In chapter 2, the application of ORR measurements to bladder cancer diagnosis at the cellular level was studied, identifying some promising early results from flow cytometry, reflected in an increased ORR in bladder cancer cells compared to healthy control (measured as ex360em425-475/ex488em515-545). In chapter 3 progressive changes were identified in the optical redox ratio of bladder cancer organoids as they progressed from cancer cell attachment to muscle invasion[203]. In this chapter the direct assessment of human tissue is performed to apply knowledge from cells and organoids to clinical diagnosis of bladder cancer. I sought to use the multi-functional laser diagnostic device "LAKK-M" to investigate whether the decreased ORR seen in progressing bladder cancer organoids would be corroborated in human bladder tissue.

One final limitation of bladder cancer diagnosis is the short wavelength of light used (generally UV or blue). Short wavelength light is scattered and absorbed much more readily by tissue, impeding its penetration deeper into tissue. As a result, it may be less applicable to detect deeper lying tumours including CIS and flat lesions using short wavelength light. Longer wavelength of light (for instance, green and red) could provide diagnostic worth from deeper lying tissue through the analysis of endogenous porphyrins. There is current interest in the study of tissue optical properties at longer wavelengths, into the tissue optical window (650-950nm)[239]. The secondary objective, therefore, was to use longer wavelength light (635nm) to investigate whether endogenous porphyrins can be used as a diagnostic marker of bladder cancer). The majority of research into the relationship between porphyrin levels and bladder cancer relates to their accumulation following the addition of PS agents, therefore researchers do not understand in great detail the properties of endogenous porphyrin in non-sensitised tissue. Previously, however, porphyrins have been shown to accumulate in oral cancer[173] and in the blood[175] and tissue[176] of mice bearing renal cell carcinoma. It was therefore considered that endogenous porphyrins may likewise accumulate in non-sensitised human bladder tissue. Finally, tying together both avenues of research, I sought to corroborate previous findings by Aboumarzouk *et al.*[112] of a statistically significant difference in the ratio of NADH/porphyrins. My main hypotheses, based on our previous findings and on contemporary research, were: bladder cancer tissue will possess a reduced ORR, an increased endogenous porphyrin concentration and a reduced NADH/porphyrin ratio relative to healthy tissue. Research findings confirm these hypotheses: firstly, the ORR of human bladder cancer samples (measured as ex365em490/ex365em550) was found to be statistically significantly lower than healthy tissue, in keeping with previous findings in organoids; secondly, endogenous porphyrin levels were found to statistically significantly increase in cancer samples compared to healthy. Finally, the NADH/porphyrin ratio was statistically significantly reduced in cancer samples in keeping with previous findings by Aboumarzouk *et al.* These findings may better inform understanding of autofluorescence analysis of bladder cancer through the corroboration of human fluorescence by a lab-based organoid model (ORR values) and through the identification of a suitable cancer biomarker at a longer wavelength (endogenous porphyrins).

4.2 Methods

4.2.1 "LAKK-M" Setup

"LAKK-M" setup for this experiment was identical to that used in chapter 3. The same system was used under the same operating protocol. For further information, please read section 3.2.1.

4.2.2 Fluorophore Fluorescence Spectroscopy

Fluorophores of interest (NADH, FAD and Protoporphyrin IX (PpIX)) were purchased as powders from Sigma-Aldrich (Gillingham, Dorset, UK) and prepared to 1M solutions in phosphate buffered saline (PBS). The LAKK-M MLNDS device was used to measure the fluorescence of the solutions in matte black cuvettes. NADH and FAD were excited at 365nm and measured across 400-823nm and PpIX was excited at 635nm and measured across 650-823nm. ASCII files containing fluorescence spectra of fluorophores were exported to Origin Pro 8 analysis software and used to generate line graphs.

4.2.3 Patient Recruitment

Ethical approval was sought and obtained from NRES London Central Ethics Committee for a research project named "ABLADE: Diagnosis of bladder cancer using multifunctional laser" (REC reference 14/LO/1076, approved 17.06.14) with sponsorship from TASC (University of Dundee/NHS Tayside). The ethical approval granted 12 months for the recruitment of 20 patients to the study under informed consent. In total, 20 patients were recruited to the study. Patient number for recruitment was based on predicted number of samples obtained (approximately 100), scale of predicted differences between healthy and cancerous tissue and desired p value for statistical significance ($p<0.05$). The inclusion criteria were: patients between the ages of 16-90 with suspected bladder tumour undergoing cystoscopic examination solely by WLC, with transurethral resection of bladder tumour (TURBT) at Ninewells Hospital, Dundee. Potential participants were identified and approached solely by the research team. Participants were given a participant information sheet (PIS) and asked to provide informed consent by signing and initialling a consent form.

4.2.4 Tissue Fluorescence Spectroscopy

Tissue obtained from patients undergoing TURBT at Ninewells Hospital, Dundee was delivered by surgical staff to the research team prior to fixation. TURBT was carried out on patients exclusively using WLC, therefore there was no addition of PS agents to tissue. The LAKK-M system was switched on 30 minutes prior to study and the study was performed in darkness, either in the workroom adjacent to the urology theatre (in Ninewells Hospital, Dundee), or in the microscopy laboratory (within the Division of Imaging and Technology, University of Dundee, Ninewells Hospital, Dundee). Tissue was placed mucosal side face up where possible (some tissue was obscured by crush and cautery artefacts) in a matte black cuvette. The optical probe of the LAKK-M system was brought into contact with the tissue surface and held for 10 seconds to steady, following which fluorescence spectra were taken from tissue at each of the 4 wavelengths (UV, blue, green and red). One measurement was taken for each spectrum from each sample, however there were often multiple samples from the same site, which were recorded and analysed individually. A schematic of the tissue measurement is presented in Fig.73. The fluorescence spectra were saved in the “LDF 3.1” inbuilt database, denoted by patient ID (Participant 1 = "ABLADE 1", etc.) and by tissue location and sample number from that location (the 3rd sample studied from the right bladder wall would be "RBW3", etc.). Prior to fluorescence spectroscopy of the tissue, reference spectra for each of the 4 excitation wavelengths (UV, blue, green and red) were recorded from the matte black cuvette to ensure the background fluorescence was minimal. The pathology opinion of the tissue was not known to the research team at the time of analysis. Immediately after analysis, the biopsy samples were delivered to the pathology lab (in Ninewells Hospital, Dundee) by a member of the research team. In total, the process of receiving samples, measuring and returning to the pathology lab took no longer than 2 hours in each instance.

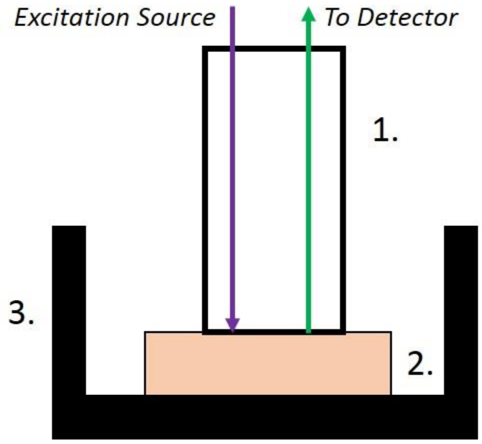

Figure 73 Cross section of tissue fluorescence measurement showing optical probe (1) containing individual excitation and detection fibres, in contact with the mucosal surface of biopsy tissue (2) held in matte black cuvette (3)

4.2.5 Histopathology as reference standard

All pathology analyses were independently provided by an experienced, qualified NHS pathologist with no involvement in the research team and no knowledge of the spectroscopy results. In total, from 20 participants, 122 samples were received. Of the 122 samples, 33 were confirmed healthy and 89 were diagnosed as bladder cancer. Of the 33 healthy samples, 10 were normal (non-inflamed) and 23 were inflamed (including cystitis cystica). Within the 89 bladder cancer samples, 6 were CIS, 7 were squamous cell carcinoma (SCC) and the remaining 76 were transitional cell carcinoma (TCC). The TCC samples were further broken down by stage: 30 samples were Ta (tumour is contained entirely within the urothelium/transitional epithelium); 20 samples were T1 (tumour extends into connective tissue without invading muscle); 26 samples were T2 (tumour invades into underlying muscle). All 7 of the SCC samples were stage T2.

4.2.6 Data Analysis

Sample spectra were exported as ASCII files and combined, plotted and visualised using Origin Pro 8 analysis software. One blue spectrum and one green spectrum were disregarded due to instrumental error. Area under the curve (AUC) values for tissue fluorescence spectra were recorded as follows (sum values were divided by 5 to account for the 0.2nm increment step in spectrometer measurements, thus giving results in standard units (nm)): UV (Σ400-823nm); Blue (Σ470-823nm); Green(Σ550-823nm); Red(Σ650-823nm). From the custom-made LDF3.1 software, amplitudes of fluorescence for specific fluorophores of interest were recorded, in keeping with previous work by Dunaev et al[199], Akbar et al.[205] and Smirnova et al.[206]. The excitation and emission wavelengths for the endogenous fluorophores of interest were identical to chapter 3.

Amplitudes of fluorescence for each fluorophore for each tissue were calculated at the listed parameters and included in a study master file. Additionally, the ORR for each sample was calculated as (NADH/FAD) in accordance with chapters 2 & 3 (ex365em490/ex365em550). To ensure that porphyrin amplitude of fluorescence was not being affected by measurement angle, tissue turbidity or refractive index, the coefficient of fluorescent contrast (Kf) of porphyrin was also calculated according to previous methods[179].

Biomarker amplitude values, ORR and NADH/porphyrin value and AUC values for each sample were collated in a master file spreadsheet using Microsoft Excel, alongside tissue opinion (1 = healthy, 2 = cancer). The study master file was imported to the analysis programme R Studio for statistical analysis. As populations were not normally distributed (this commonly occurs in tissue fluorescence spectroscopy), populations were compared using the analysis of variance (ANOVA) function in R Studio. Statistical analyses were performed to calculate the p value in every instance, with $p<0.05$ considered statistically significant. Non-inflamed and inflamed healthy tissue were compared by ANOVA for each parameter. No statistically significant differences were found between populations, therefore they were considered as a single population (healthy) for the purpose of this study. Data were log transformed during analysis to ensure better fit within Q-Q and residuals versus leverage plots. For factors with statistically significant differences between populations, bar charts were generated in Origin Pro 8 depicting the population mean +/- the standard error of the mean (SEM) for opinion (healthy vs cancer). In addition, for statistically significant factors, receiver operating characteristic (ROC) curves were generated using Origin Pro 8 analysis software to evaluate the diagnostic worth of each factor by comparing the sensitivity/specificity trade-off of a diagnostic parameter at different diagnostic thresholds. For ROC curves, AUC and asymptotic probability were calculated automatically, with AUC values ranging from 0.5 (worthless) to 1 (ideal).

4.3 Results

4.3.1 Analysis of fluorophore contribution to tissue fluorescence

To assess the contribution of distinct tissue fluorophores to the overall fluorescence spectra received from tissue, 1M solutions of NADH, FAD and PpIX were studied using the LAKK-M system and superimposed over average fluorescence spectra from healthy and cancerous tissue. Fluorescence spectra from 1M solutions of NADH and FAD, excited at 365nm, were superimposed over the tissue fluorescence spectra received at 365nm excitation (Fig. 74A). Fluorescence spectrum received from 1M solution of PpIX excited at 635nm was superimposed over tissue fluorescence spectra received at 635nm (Fig. 74B). Additionally, the blue fluorescence spectra were corroborated to arise from FAD fluorescence by fluorophore spectroscopy, however no significant differences were observed between the populations ($p = 0.465$, data not shown). Integrated green fluorescence spectra showed statistically significant differences between population types, but could not be corroborated by any of the studied fluorophores, so require further investigation. From Fig.74A it can clearly be seen that the spectral shape of tissue under 365nm excitation suggests a significant contribution from NADH (main tissue peak at 490nm) and FAD (shoulder peak at 550nm), while fluorescence spectra of tissue under 635nm excitation (Fig.74B) suggests a significant contribution from porphyrins (main tissue peak 700-710nm). Slight differences in full width at half maximum between tissue and PpIX fluorescence may be explained by overlapping fluorescence from different forms of porphyrin in tissue. This observation may enable a better understanding of the contribution of individual fluorophores to the complex fluorescence spectra received from bladder tissue. It can be seen from Fig. 74A that the average fluorescence spectral intensity from healthy tissue is higher than that of cancer tissue, in keeping with previous findings (however, ANOVA analysis of UV AUC was not statistically significant). Differences in line shape of the UV spectra suggested possible differences in ORR values between populations. Furthermore, it can be seen from the average red fluorescence spectra that the intensity of fluorescence from cancer samples is almost double that of healthy tissue. AUC analysis confirms that this difference is extremely statistically significant. Cancer samples were further separated into CIS (n=6), SCC (n=7) and TCC (n=76) and averages plotted alongside healthy and cancer average spectra for both 365nm excitation (Fig. 75A) and 635nm excitation (Fig. 75B). From these figures it can clearly be seen that cancer average spectra are largely dictated by TCC cases in both instances. CIS samples were found to display the lowest average intensity AUC values under 365nm excitation, while SCC samples displayed the highest. Further observation indicates that the ORR was lowest in CIS samples.

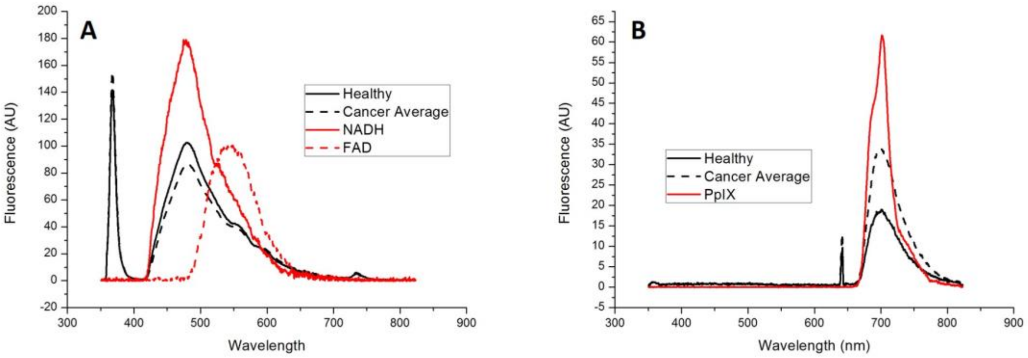

Figure 74 Comparison between healthy average (solid black line, n = 33) and cancer average (dashed black line, n = 89) under UV excitation (a) and red excitation (b). Figure 74a overlaid with spectra from 1M NADH (solid red line) and 1M FAD (dotted red line). Figure 74b overlaid with 1M protoporphyrin IX (solid red line)

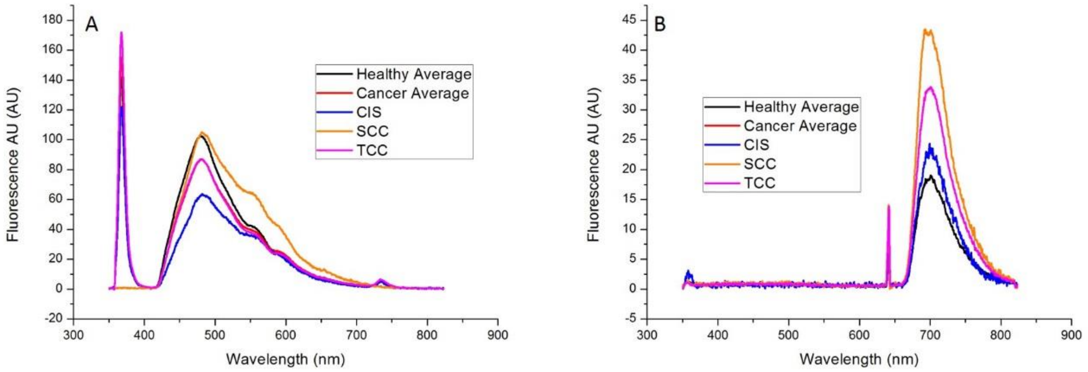

Figure 75 Comparison of healthy tissue fluorescence spectra (black line, n = 33) compared to cancer average (red line, n = 89) and cancer samples broken down into CIS (blue line, n = 6), TCC (magenta line, n = 76) and SCC (orange line, n = 7)

Figure 76 depicts the standard deviation values of healthy and cancerous tissue under UV (76a) and red excitation (76b). From these figures, it can be seen that there was a large deviation is fluorescence between samples. This has been accounted for when applying analysis.

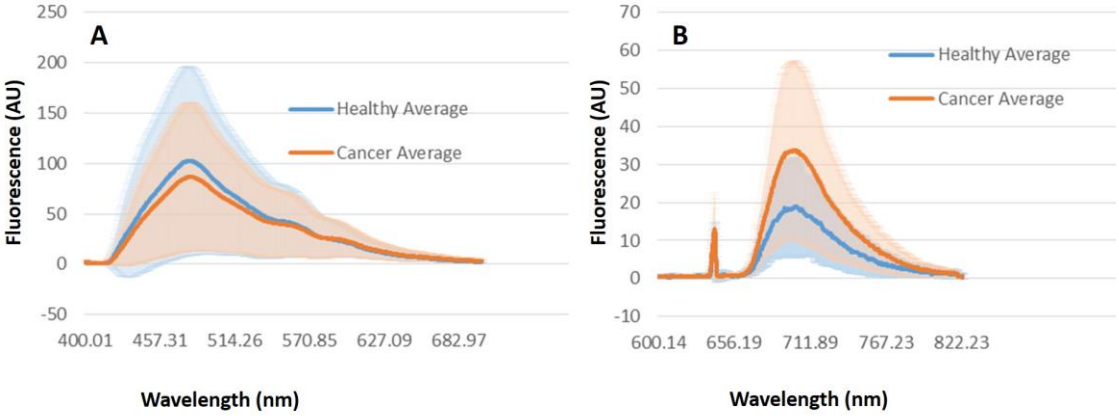

Figure 76 Average spectra +/- SD for healthy tissue (blue line +/- blue shading, n = 33) and cancer tissue (orange line +/- orange shading, n = 89) under UV (a) and red excitation (b)

Figure 77 depicts the average fluorescence spectra of healthy and cancerous tissue under green (532nm) excitation, from which it can be seen that cancerous samples display increased fluorescence compared to healthy samples. From Figure 78, depicting the standard deviation values of green fluorescence of healthy and cancerous tissues, it can be seen that green fluorescence displays considerable deviation between samples.

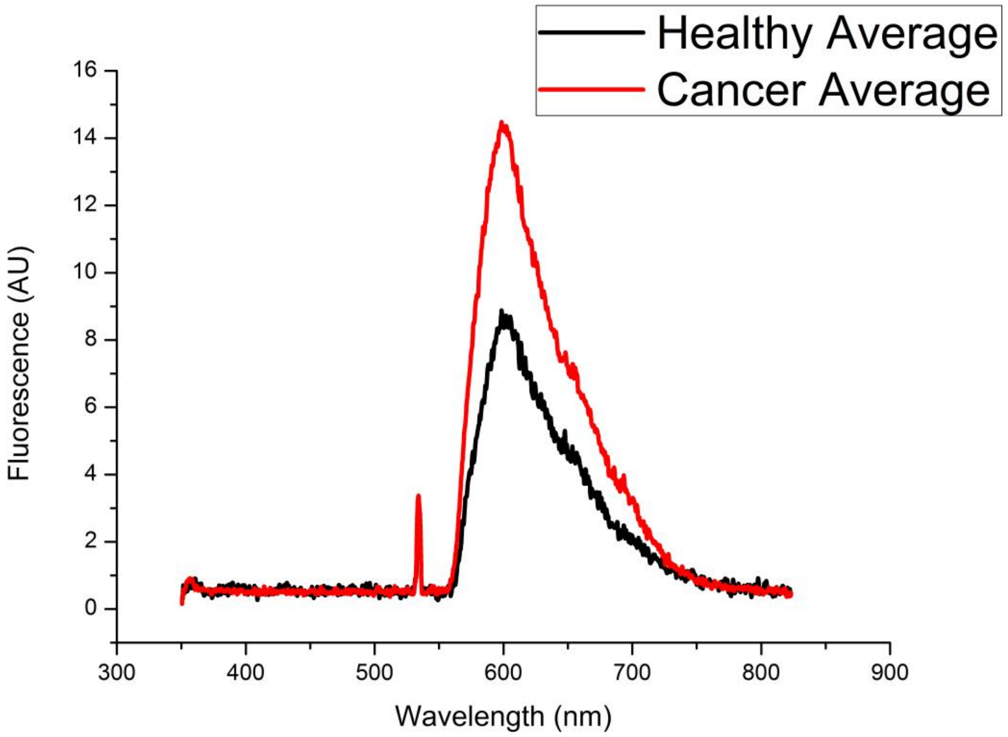

Figure 77 Average fluorescence spectra of healthy bladder tissue (black line, n = 32) and bladder cancer tissue (red line, n = 89) excited using green (532nm) laser.

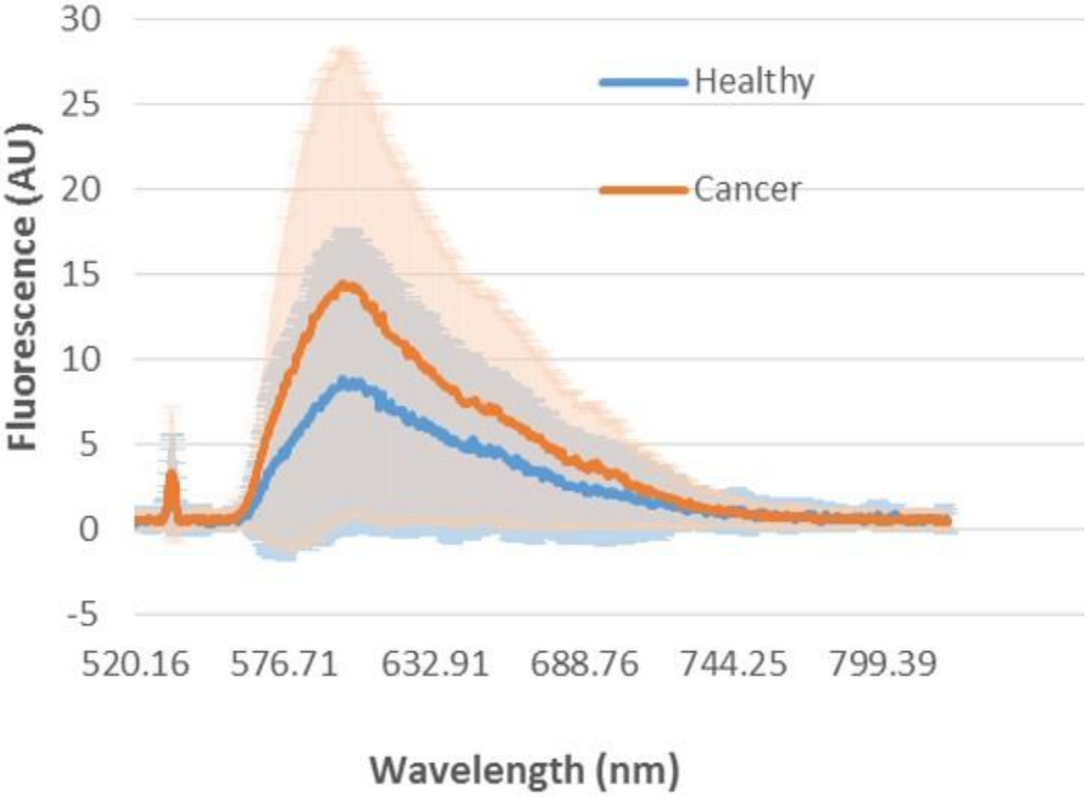

Figure 78 Average fluorescence spectra +/- SD values for healthy (blue line +/- blue shading, n = 32) and cancer (orange line +/- orange shading, n = 89) under green excitation.

4.3.2 Fluorophore analysis

Optical redox ratio (ORR) values for each sample were calculated and compared for statistically significant differences. The mean +/- SEM values for healthy and cancerous bladder tissue are depicted below (Fig. 79). No significant differences were found between populations for collagen, elastin, NADH or flavin intensities. A statistically significant difference in the ORR (ex365em490/ex365em550) can be seen between healthy and cancer tissue (p = 0.00891). This result is in keeping with previous finding of progressive reductions in the ORR of bladder cancer organoids in the lab as cancer grows and develops. The amplitude of fluorescence of porphyrins was recorded and analysed for statistically significant differences. The mean +/- SEM values for porphyrin fluorescence amplitude in healthy and cancer tissue are depicted below (Fig. 79B). It can be seen from this data that porphyrin levels in cancer samples are greatly increased compared to healthy samples. This difference was found to be statistically significant (p=0.00241). Calculation of Kf values from endogenous porphyrins also revealed a statistically significant difference of 0.0144 (data not shown), corroborating fluorescence intensity findings. Endogenous porphyrin levels may therefore present a useful biomarker for cancerous bladder tissue. From Fig.79C the average +/- SEM values for the NADH/porphyrin ratios for healthy and cancer samples can be seen. The difference between samples was also found to be extremely statistically significant (p=0.00624).

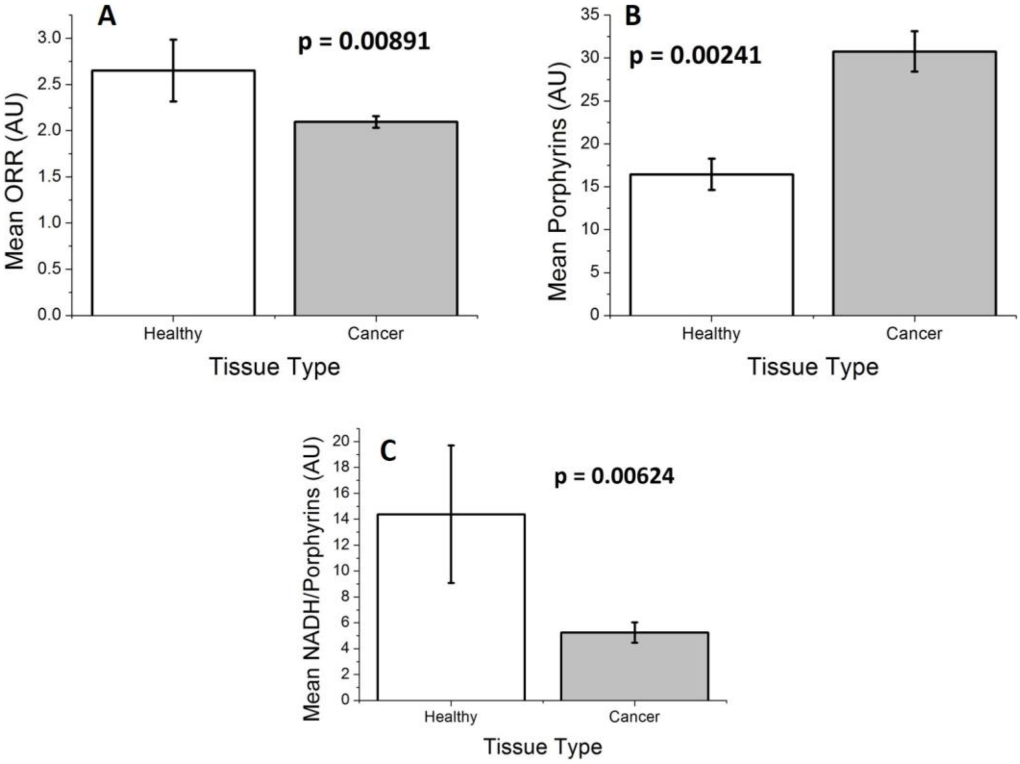

Figure 79 Bar charts depicting mean +/- SEM for UV ORR (a); porphyrin amplitude of fluorescence (b) and NADH/porphyrin ratio (c) for healthy (white bars, n = 33) and cancer (light grey bars, n = 89).

Furthermore, from figure 80, a statistically significant difference (p = 0.0392) can be seen in the integrated fluorescence intensity of healthy and cancerous tissue excited at 532nm.

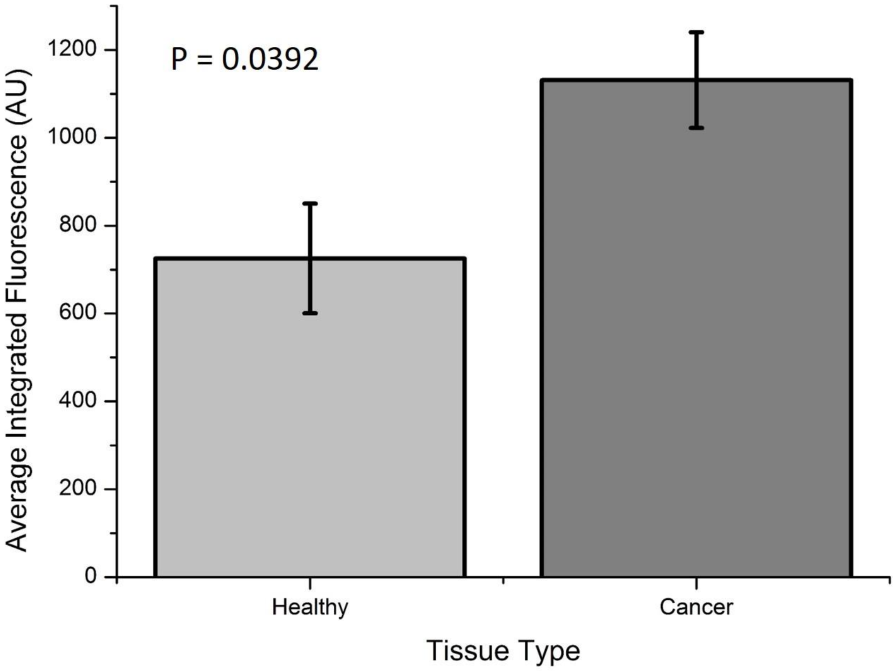

Figure 80 Mean +/- SEM values for integrated fluorescence intensity under green (532nm) excitation for healthy tissue (pale grey, n = 32) and bladder cancer tissue (dark grey, n = 89)

4.3.3 ROC calculations

ROC curves were generated for both UV ORR and endogenous porphyrin amplitude values to determine the diagnostic worth of these biomarkers for bladder cancer detection. Fig.81 below details these ROC curves. From Fig. 81A it can be seen that UV ORR (ex365em490/ex365em550) displays fair diagnostic worth for the detection of bladder cancer (AUC value = 0.64), however when comparing healthy samples to CIS samples alone (Fig. 81B), the AUC value increases to 0.83, indicating a much more promising diagnostic test. The accuracy of the CIS analysis is limited somewhat by small sample size (n = 6) so future studies would benefit from seeking to corroborate this finding. Considering porphyrins (Fig. 81C) the AUC value suggests a test with greater diagnostic worth than ORR for all bladder cancers (AUC = 0.71), at the expense of a reduced performance against CIS (AUC = 0.63). Finally, the ROC based on the ratio of NADH to porphyrins (Fig.81D) was found to have an AUC of 0.64. The AUC value for NADH/porphyrin detection of CIS was 0.69.

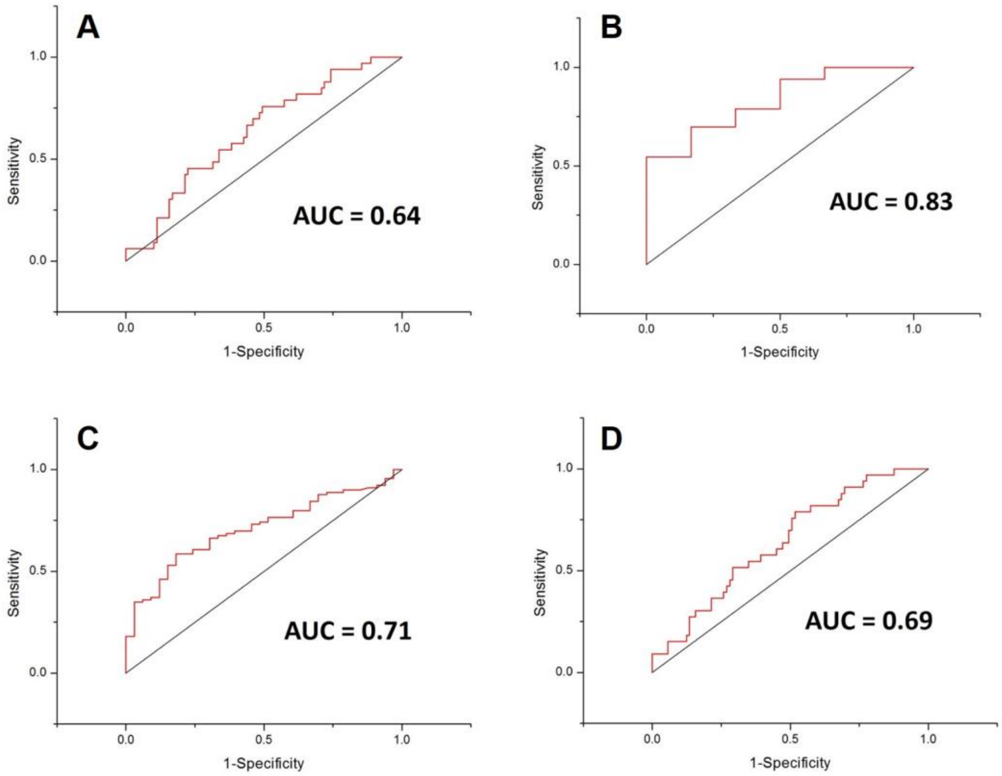

Figure 81 ROC curves for UV ORR (a), UV ORR healthy vs CIS (b), porphyrin (c) and NADH/porphyrin ratio (d), including AUC values.

4.4 Discussion

The hypothesis at the onset of this research based on previous findings in organoid models (chapter 3) was that bladder cancer tissue would exhibit a reduced ORR compared to healthy tissue. Furthermore, owing to malfunctions in the heme biosynthetic pathway of cancer cells (the basis of PDD) and previous work by Aboumarzouk *et al.*[112], it was hypothesised that it would be possible to detect an elevated level of endogenous porphyrins and a reduced NADH/porphyrin ratio in cancer tissue compared to healthy control. Results confirm these hypotheses. Firstly, it was demonstrated that tumours exhibit a reduced ORR (measured as ex365em490/ex365em550) compared to healthy tissue. This finding is in keeping with previous findings in an organoid model of bladder cancer in chapter 3[203], but in contrast with findings from cell lines alone in chapter 2. Most contemporary focus on the ORR suggests that the metabolic alterations which occur during cancer development skew the degree to which cancer cells use their electron transport chain, thus causing accumulation of the primary electron donor NADH in cancer cells. We ourselves have previously confirmed this finding in bladder cancer cell lines[225], however the ORR has not been extensively covered regarding human bladder tissue. At the tissue level it may be considered that other fluorophores may contribute to the complex fluorescence spectrum obtained under UV illumination, such as the structural proteins collagen and elastin, however the spectral overlap of these proteins past 450nm has been shown to be minimal[180]. Previously, Mayevsky *et al.* used a similar system to the LAKK-M to study tissue NADH fluorescence up to 480nm[207] so it is considered that this is the major contributing tissue fluorophore at 490nm. Comparisons between average tissue fluorescence under UV illumination and the endogenous fluorophores NADH and FAD seem to robustly confirm that these are the major contributing fluorophores to tissue fluorescence at this wavelength, however underlying contributions from collagen and elastin may account for the differences between healthy and cancerous tissue. No significant differences were found between populations for elastin/NADH or elastin/FAD (as were found in organoids), suggesting that this observation is largely a metabolic result. Previously, the potential of tissue remodelling and the catabolism of elastin and collagen in developing cancer was discussed as an underlying factor in the reduced ORR values seen in bladder cancer organoids compared with healthy controls[203]. It is possible that this phenomenon is also occurring in human bladder cancer tissue. Equally, the observed differences may be a result of altered metabolism in a variety of cell types, including not also cancer cells but also surrounding healthy urothelium and underlying fibroblasts. Previous research by Cicchi *et al.* using the ORR observed an increased relative NADH content in bladder CIS in a small sample size. The difference between observations may stem from the equipment used (Cicchi *et al.* relied on fluorescence microscopy, while our system relies on spectroscopy) or may be a result of variations between patients. ROC curve analysis of the ORR suggests it displays some potential as a diagnostic tool, but is particularly effective at detecting CIS (based on a small sample number). CIS is commonly missed during WLC and displays malignant potential to progress into muscle invasive disease, therefore new techniques for its detection are crucial. Future studies should therefore seek to corroborate our findings regarding the ORR, with a particular focus on an increased population of CIS samples.

Regarding porphyrin levels, the statistically significant increase in porphyrin levels in cancer tissue suggests a selective accumulation similar to that which is witnessed in PDD but without any need for PS administration. Furthermore, ROC calculations suggest that this biomarker possesses potential for diagnosis. One of the largest limitations to PDD is its reduced specificity. In particular, inflamed benign tissue is often recorded as cancer under PDD, owing to the leaky vasculature of previously treated tissue. This results in increased false positive rates and a large number of unnecessary invasive biopsies. That a statistically significant difference was observed in endogenous porphyrin levels between healthy (including inflamed tissue) and cancer suggests in future it may be possible to quantify porphyrin levels in non-sensitised tissue with the ability to discern between inflamed and cancer tissue. Increased endogenous porphyrin levels have previously been observed in renal cell carcinoma[176]. Similarly, iron levels (involved in the porphyrin biosynthetic pathway) have been shown to preferentially accumulate in mouse mammary tumours[240] where they have been suggested to play a role in tumour cell survival and progression. Endogenous porphyrin fluorescence has previously been described in non-sensitised oral mucosa, even in healthy tissue[241]. Oral mucosa possesses similar structure to that of the bladder, therefore it is considered that non-sensitised healthy bladder would likewise present some endogenous porphyrin fluorescence. In order to better exploit the tissue optical window and avoid fluorescence contributions from other fluorophores at lower wavelength (for instance, FAD and lipofuscin at 405nm), the secondary porphyrin peak at 635nm excitation/710nm emission was studied. This is in keeping with previous work in PDD of bladder TCC[178] and in oral mucosa – in which identical measurement parameters observed increased endogenous porphyrin fluorescence in tumour tissue with small fluorescence signal from healthy tissue[179]. Average porphyrin fluorescence from both tumour and healthy tissue in this study was low compared with tissue fluorescence under UV excitation. In addition to intensity of porphyrin fluorescence, statistically significant differences in coefficient of fluorescent contrast (Kf) between healthy and cancer were observed, indicating that differences are due to porphyrin level itself rather than other factors such as tissue turbidity or refractive index. Previously, chronic hypoxia has been suggested as an underlying factor of increased porphyrin levels in oral mucosa[179], therefore elevated porphyrin levels and reduced NADH/porphyrin ratio may reflect an effect of tissue hypoxia on the reduction of cell metabolic activity.

One concern for the application of this technique is its low applicability to CIS detection. Similar to UV ORR measurements, expanding this pilot study to a larger study with a focus on larger CIS populations may allow us to better delineate porphyrin profiles in the disease. Theoretically, the use of longer wavelengths of light to investigate tissue should allow deeper penetration into tissue and the detection of a greater number of deeper lying tumours (for instance, CIS), therefore it may be that the metabolic perturbations resulting in increased porphyrin levels in obvious bladder cancer are not at play in pre-cancerous lesions. Finally, NADH/porphyrin levels were observed to be decreased in cancer samples, in keeping with previous research findings[112].

In keeping with previous research in the field, average integrated UV fluorescence was greater in healthy tissue than in cancer, however this was not statistically significant. This could be due to the effects of tissue thickness on amplitude of fluorescence (which ranged from 2-15mm) and also angle and firmness of application of the diagnostic probe to tissue. Diagnostic ratios such as the ORR and NADH/Porphyrin ratio are less affected by these factors and are therefore more robust measurements for diagnosis. Therefore, in this study previous findings by ourselves[203] and others[112] have been corroborated and findings from other forms of cancer[176] have been applied to the identification of a novel biomarker for bladder cancer (endogenous porphyrins).

Green fluorescence displayed a statistically significant increase in cancerous tissue compared to healthy, therefore this may be a worthwhile avenue for future research. As it could not be corroborated with the fluorescence of any known fluorophore, green fluorescence was instead measured solely as integrated fluorescence intensity. Future work with a wider range of fluorophores may serve to better elucidate the contributing factors to tissue fluorescence excited using green light.

As this was a pilot study of 20 participants, it would be of worth to expand this study with particular focus on diagnostic ratios such as ORR and NADH/porphyrins with particular focus on their applicability to CIS and early stage tumours. The LAKK-M system has not previously been used for the study of bladder cancer tissue, however understanding of the autofluorescence properties of bladder cancer[113,114] and development of the LAKK-M for the study of individual fluorophore variability in healthy volunteers[199] and its application to the diagnosis of cardiovascular disease[205] suggests its worth as a diagnostic tool. Furthermore, efforts are ongoing to better understand the tissue fluorescence by using tissue fluorescence simulation models[242,243]. The LAKK-M system also contains sources for LDF and TRO which have previously been assessed from a diagnostic perspective[215]. LDF has previously been used to identify and characterise interstitial cystitis[214] while tumour hypoxia is a much-studied subject[216], suggesting that identification and substantiation of suitable biomarkers of bladder cancer using the autofluorescence spectroscopy channel may allow the LAKK-M system to be developed into an effective multi-functional diagnostic tool for bladder cancer.

4.5 Conclusion

In conclusion, this chapter has detailed a pilot study into the autofluorescence spectra across four different excitation wavelengths of healthy and cancerous human bladder tissue using the LAKK-M, identifying three main parameters with which to identify bladder cancer. These findings improve understanding of the contribution of several endogenous fluorophores to bladder cancer fluorescence spectra, identifying potential novel biomarkers with which to detect the disease. The LAKK-M system had not previously been used to study bladder cancer, however these findings present promise for the system to be developed into a multi-functional minimally invasive system for the diagnosis of the disease. The findings presented in this pilot study would benefit from corroboration in a large scale study, with particular focus on the discrimination of CIS.

5. LIGHT-OXYGEN EFFECT

5.1 Introduction

One of the benefits to the use of PDD for bladder cancer is that the areas in which PS agents are sequestered can also be killed via the generation of reactive oxygen species. This is known as photodynamic therapy (PDT) and where PDD relies on excited PS relaxing to ground state through fluorescence, PDT relies on the generation of reactive intermediates (Type I reactions) and singlet oxygen (Type II reactions) following excitation of PS agents to kill cancer cells. Sequestration of PS agents is caused by the enhanced permeability and retention effect due to leaky vasculature and hydrophobicity of tumour tissue[238] while protoporphyrin IX accumulation is due to modifications to the heme biosynthetic pathway in cancer cells[244]. PDT is a useful therapeutic technique for surgical follow-up, especially in Mitomycin C and BCG refractive patients. Considering that the alternative for refractive patients is often radical cystectomy, PDT is an attractive alternative. Bladder anatomy is unique in that it can be assessed (and PS applied) using minimally invasive trans-urethral probes and catheters. Other, deeper lying tissues (such as kidney) often require surgery/laparoscopy to uncover. Conversely, skin cancer can be targeted completely non-invasively by topical application of PS[43]. Therefore, consideration must go into the design of imaging probes and irradiation sources for bladder cancer, defined by the strict dimensions of the urethra. The choice of PS agent defines the optimal administration route: PDT using 5-ALA and HAL can be achieved by oral administration (at the expense of potential systemic effects of PpIX), while hypericin can be instilled directly into the bladder, with selective tumour uptake occurring 15 minutes after instillation[67]. Type I reactions occur when excited PS agents rapidly transfer energy to molecular intermediates, which themselves generate ROS such as superoxide anion. ROS play a number of roles in the day-to-day function of cells, ranging from homeostasis to immune defence. Normally they are counteracted at high levels by cellular anti-oxidants[245], while low level ROS generation has been shown to play a role in cancer cell survival, promoting expression of pre-metabolic and pro-angiogenic genes[35]. Type II reactions occur when excited PS agents interact with molecular oxygen, generating potently reactive singlet oxygen. Due to its inherent instability, singlet oxygen readily reacts with many electron-rich molecules, including fatty acids[36], aromatic amino acids[38] and the phosphate backbone of DNA[37]. Singlet oxygen was previously thought to have a very short half-life (40ns) and therefore a very short diffusion distance (20nm). Although this has recently been challenged[246,247], it is generally considered that the cellular organelles in the location of singlet oxygen generation are its primary targets. The perfect PS agent is defined as having: high purity (to prevent adverse systemic effects); minimal dark toxicity (activation only in the presence of exciting light); preferential retention in tumours (to prevent damage to healthy tissue); low systemic toxicity together with swift pharmacokinetics (i.e. no accumulation in liver to cause systemic toxicity); high quantum yield and a strong absorption profile (to maximise photon efficiency and therapeutic efficacy). Dark toxicity can be expanded to include “non-specific toxicity”, that is, PS activation by light out-with therapeutic confines (such as sunlight). The development of PS agents with different desirable qualities has been a long running process over a number of years[32]. As discussed in previous chapters, clinical implementation of PDD has been hampered by its low specificity when compared to WLC[17], the same is therefore also true for PDT. Lack of specificity of this therapeutic regime may cause damage and destruction of healthy tissue, contributing to patient morbidity. This issue has been tackled by developments in active targeting of tumours[248], either via antibody tagging of PS agents against EGFR[249] or p185[250].

Delivery of PS agents to tumour cells has also been shown to be improved by the use of liposomes[251] and modified nano-particles[252], while quantum dots also show therapeutic and theranostic potential[253,254], however concerns still remain about the systemic toxicity of these targeting and delivery agents.

The activation wavelength of PS dye is another of the most crucial decisions to be made in PDT as it dictates tissue penetration and quantum efficiency of reactions. Conventional first generation PS agents such as 5-ALA have absorption maxima around 400nm so are generally excited with blue light. Blue light has a number of advantages, including high relative energy compared to higher wavelength light, meaning a shorter irradiation period to obtain photosensitisation. Blue light unfortunately possesses comparatively low tissue penetration depths and high levels of scattering compared to light of higher wavelengths. The recently developed PS agent Hypericin has remedied this issue slightly, with absorption maxima at 540 and 590nm allowing excitation with longer wavelength green light[67]. To overcome the problems of limited tissue penetration and high scattering of low wavelength light in the blue and green regions, there has been considerable focus in recent years on two photon activated PS dyes (2P PDT). Activation of PS with two photons of infrared light at 700-800nm rather than one photon of UV/blue light at 350-400nm presented the opportunity of increased tissue penetration with less scattering and non-specific tissue damage. Unfortunately, early attempts at 2P PDT suffered from very low optical cross sections of absorbers, meaning a low efficiency for converting input photons to singlet oxygen generation. The consequence of this was a requirement of 6300J/cm^2 over the course of a 4 hour irradiation period to kill 50% cancer cells in the study[255]. Recent work in the field has improved the optical cross section and thus efficiency of their absorbers almost ten-fold, presenting 2P PDT as a viable regime[255].

Another issue of concern in PDT is the limited solubility of many PS agents. Tumours possess a number of physiological features which enhance their uptake and retention of PS compared to healthy tissue. The major issue is how to promote PS distribution through the bloodstream in the first place. First generation PS such as 5-ALA and HAL were known to suffer from low penetration owing to their low solubility, lipophilicity and tissue specificity. One of the largest groups of PS, phthalocyanines, suffers from severely limited solubility owing to the presence of phenyl groups in their chemical makeup. Hypericin has sought to offer improved tissue penetration compared with first generation PS but still requires chemical additives to heighten absorption, penetration and solubility. In particular, n-methyl pyrrolidone has been demonstrated as a useful adduct to PS agents to improve tissue penetration, even at concentrations of 0.05%[256].

Another possible solution to the issues of limited PS solubility and laser irradiation into tissue is the use of the light-oxygen effect, whereby infrared light at 1270nm is used to generate singlet oxygen in the absence of PS agents. Direct generation of singlet oxygen from 1270nm light irradiation was first demonstrated in the 1970s[194]. In the intervening years, it has been employed to assess effects on cells in aqueous solution[257] and to directly target cancer cells. Recently, the light oxygen effect was discovered to induce cell death in the breast cancer cell line MCF-7[197] independent of temperature effects. The absorption cross section of molecular oxygen was found to be 5 orders of magnitude weaker than conventional PS (suggesting a hugely energy inefficient process), however the threshold intensity of oxygen (4.6mM) required to induce cell death was in keeping with results using PS. Clinical implementation of light oxygen effect is still hampered by our limited understanding of the molecular mechanisms leading to cell death. This question has been partially answered using the cervical cancer cell line HeLa[196], which was found to selectively accumulate ROS following 1270nm irradiation compared to healthy control cells. This was hypothesised to be caused by an impaired anti-oxidant machinery in the cancer cells. Patch clamp analysis on HeLa cells also revealed a differential calcium influx response to 1270nm compared to healthy cells, which may partially explain the differences in ROS accumulation due to the known feedback pathways between Calcium signalling and ROS. The application of light oxygen effect to bladder cancer therapy may be of use by improving on the low penetration of PS agents and activating light, however the dynamics of the process are still not fully understood.

The aim of the research being undertaken in this chapter was to better elucidate the generation of singlet oxygen within bladder cancer cells, possible pathways of cell death and the effects of dose and fluence on cell viability. Preliminary results confirm the generation of singlet oxygen in aqueous media following irradiation with a 1270nm laser. Cell death analysis suggests, however, that any death observed in irradiated cancer cells is predominantly due to heating effects of the laser rather than the generation of singlet oxygen.

5.2 Methods

5.2.1 Cell culture

The human bladder cancer cell line “5637” was purchased from ATCC and grown to 75% confluence either in 12 well culture plates (VWR) or in #1.5 coverslip thickness bottomed petri dishes (Mattek) in Phenol red-free Dulbeccos’ Modified Eagle Medium (DMEM) (Life Technologies) containing 10% fetal bovine serum (FBS) (Life Technologies) and 1% penicillin-streptomycin (Sigma-Aldrich). Cells were grown in an incubator set to 37^{o}C and 5% CO2. Prior to experiments, complete media was removed and replaced with serum free DMEM.

5.2.2 Laser Setup

A fibre coupled InGaAs/InAs quantum dot 1268nm infrared diode laser (Innolume GmbH) was used. An optical fibre delivered the beam to the optics scaffold (lens, focus, filter disc) which was positioned 15cm above the irradiation platform. The maximum power output of the laser was 400mW and could be controlled by altering the drive current. The optical power was measured using an optical power meter (ThorLabs). The beam width was set to 2cm for all experiments. Cells in 12 well plates were irradiated for 1-30 minutes at irradiances of 100-400mW/cm2, yielding doses of 1.9J/cm2 to 228J/cm2. Heating effects of laser were measured using a thermocouple implanted in media in one well of a 12 well plate during irradiation with doses ranging from 1.9J/cm2 to 228J/cm2. Heating effects were also measured in a tissue mimic (pig bladder) using identical beam diameter and irradiation regimes. The setup was housed in a custom built platform and optical power was modified using a neutral density filter housed by the lensing apparatus. The laser setup is included below (Fig.82) and depicted in a schematic (Fig. 83) showing the lensing and filtering apparatus:

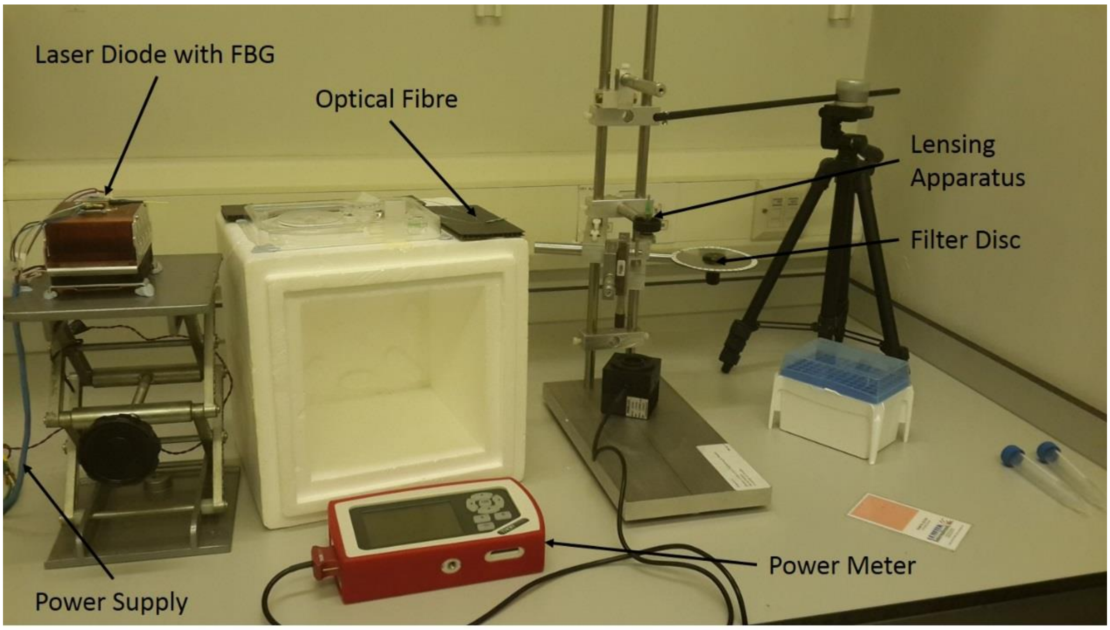

Figure 82 Basic experimental setup of laser showing laser diode connected to lensing apparatus via optical fibre

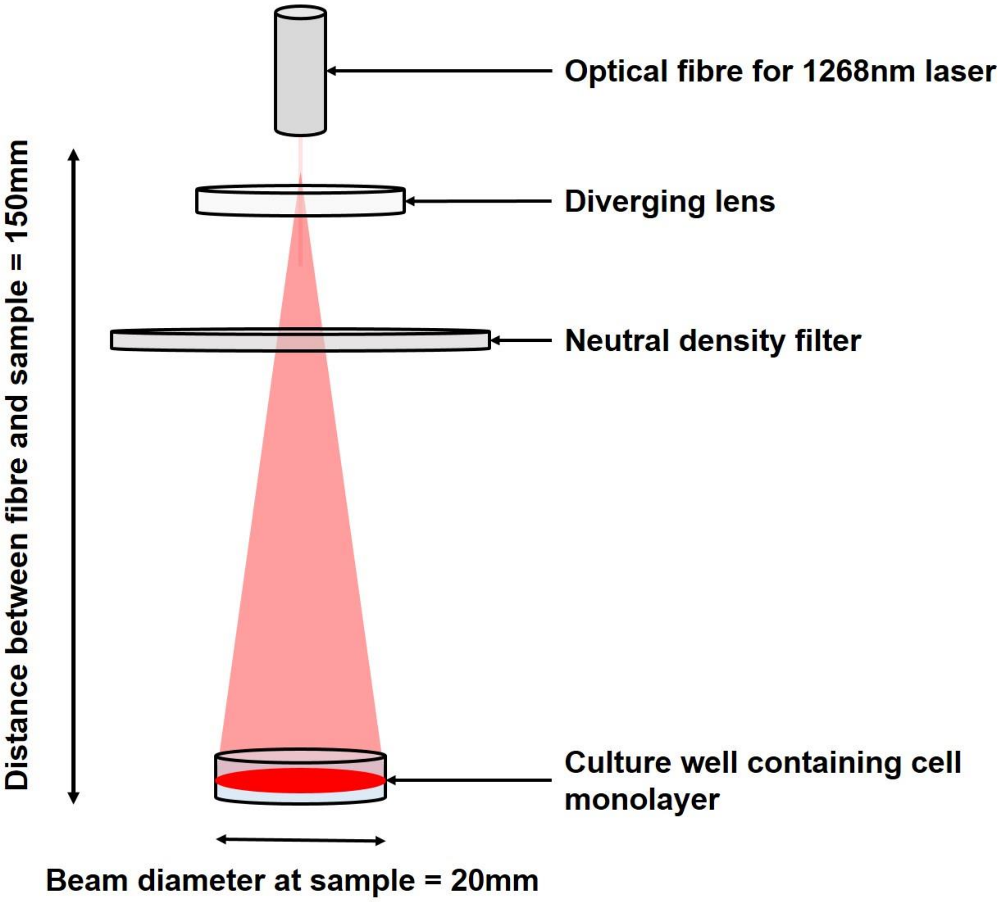

Figure 83 Laser schematic showing optical fibre, diverging lens and neutral density filter. Approximate beam diameter at sample = 20mm

5.2.3 Irradiation of singlet oxygen sensor and cancer cells

Dose was calculated, in J/cm^2, as a function of optical power and exposure time as follows (equation 2):

$$\textbf{Dose (J/cm}^{2}\textbf{) = (Optical power (W) x Irradiation period (seconds))/Area (cm}^{2}\textbf{)}$$

Equation 2 Calculation of dose applied to sample

Therefore a beam of diameter 2cm covered circular area of 3.14cm^2. Examples of doses achieved with a set beam width with varying optical powers and irradiation periods is included below (Table 10).

Table 10 Examples of effects of optical power and irradiation period on delivered dose

Optical power (W)	**Irradiation period (s)**	**Dose (J/cm^2)**
0.1	60	1.9
0.1	120	3.9
0.1	180	5.7
0.4	600	76.4
0.4	1200	152.9
0.4	1800	229.2

Singlet oxygen sensing dye anthracene 9-10 dipropionic acid (ADPA) was purchased from Abcam (Cambridge, UK) and prepared to a 10µM concentration (henceforth ADPA solution) in phosphate buffered saline (PBS) (Sigma-Aldrich).

The fluorescence spectrum of non-irradiated ADPA solution was recorded by adding 1ml solution to a matte black cuvette. ADPA fluorescence was excited using the UV

(365nm) laser source of the laser spectroscopy system LAKK-M (SPE-LAZMA, Moscow, Russia). 1ml solutions of ADPA were irradiated with 400mW optical power for between 5-60 minutes, yielding irradiation doses between 38-458J/cm^2, after which they were added to matte black cuvette and UV excited fluorescence recorded between 400-500nm (covering ADPA standard peaks). 1ml solutions of ADPA (1µM) were also measured following 5-60 minutes on the bench without irradiation, to determine background quenching of ADPA fluorescence. For apoptosis measurements, bladder cancer cell line 5637 was grown to 75% confluence in petri dishes as described above in serum free media and irradiated using 400mW optical power for 0, 10, 20 and 30 minutes, yielding irradiation doses of 76, 153 & 229J/cm^2, respectively. For trypan blue exclusion measurements, 5637 cells grown to 75% confluence in petri dishes as described above in serum free media were irradiated for 10 minutes at optical powers of 100, 200, 300 & 400mW, yielding irradiation doses of 19, 38, 57 & 76J/cm^2, respectively. For trypan blue measurements, serum free media was replaced with complete media following irradiation. In both cases, following irradiation, cells were returned to the incubator immediately following irradiation.

To determine heating effects of laser, the sensor of a conventional thermocouple was attached to the inside of a well containing 1ml media. Media was irradiated for 4 minutes using each optical power (100, 200, 300 and 400mW) in triplicate, using a new well for each measurement. The average measurement for each optical power was charted and used to calculate approximate appropriate temperatures for performing future temperature controls.

5.2.4 Detecting apoptosis

Five hours post-irradiation, serum free media was removed from irradiated cells and control. Cells were stained with 1nm solutions of Annexin V-Allophycocyanin (APC) conjugate (Molecular Probes) and MitoTracker Green (Molecular Probes) in PBS and imaged using a Carl Zeiss 710 confocal microscope (Zeiss) using a 40x objective lens. MitoTracker fluorescence (green) was excited using a 488nm laser set to 50% power and recorded across 510-560nm using a photomultiplier tube (PMT). APC fluorescence (red) was excited using a 633nm laser set to 50% power and recorded across 660-700nm using a PMT. The images were transferred to ImageJ for analysis and APC intensities from 50 cells from each sample were quantified for comparison.

5.2.5 Detecting necrosis

24 hours post-irradiation, media was removed from cells and cells were detached from wells using trypsin-EDTA solution (Sigma-Aldrich) and spun with cells in supernatant at 1500 RPM for 5 minutes. Cells were re-suspended in PBS to which live cell exclusion dye Trypan Blue (Sigma-Aldrich) was added in a 50:50 ratio. 10µl cell/trypan blue solution was injected under the coverslip of a VWR haemocytometer. 100 cells from each sample (4 irradiation regimes, each in triplicate) were counted by following conventional haemocytometer protocol and expressed as % viability. To account for heating effects of laser, cells grown following identical protocol were immersed for 10 minutes in a water bath at 42^{o}C, incubated, and assessed after 24 hours following an identical trypan blue staining protocol.

5.3 Results

5.3.1 Singlet oxygen generation in aqueous media

ADPA kept on the bench for 1 hour without irradiation was found to have no effect on fluorescence at 365nm excitation (Figure 84). 1 hour irradiation of a 10mM solution of ADPA in PBS was found to induce a 4-fold reduction in fluorescence amplitude measured under 365nm excitation (Fig. 85), indicating production of singlet oxygen in aqueous media during irradiation with the 1268nm laser. Progressive reduction in ADPA fluorescence with increasing irradiation periods suggests a dose-dependent effect of irradiation on singlet oxygen generation in aqueous media (PBS).

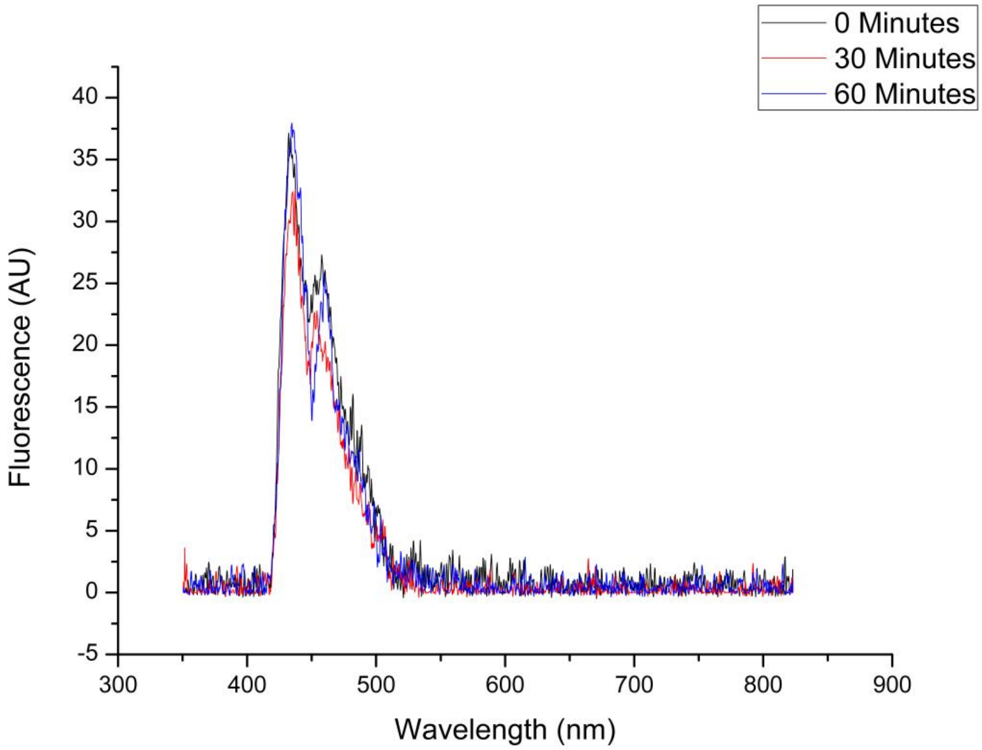

Figure 84 Fluorescence spectra of 1uM solution of ADPA measured using UV excitation following preparation (black line) and following 30 minutes (red line) and 60 minutes on bench without irradiation (blue line)

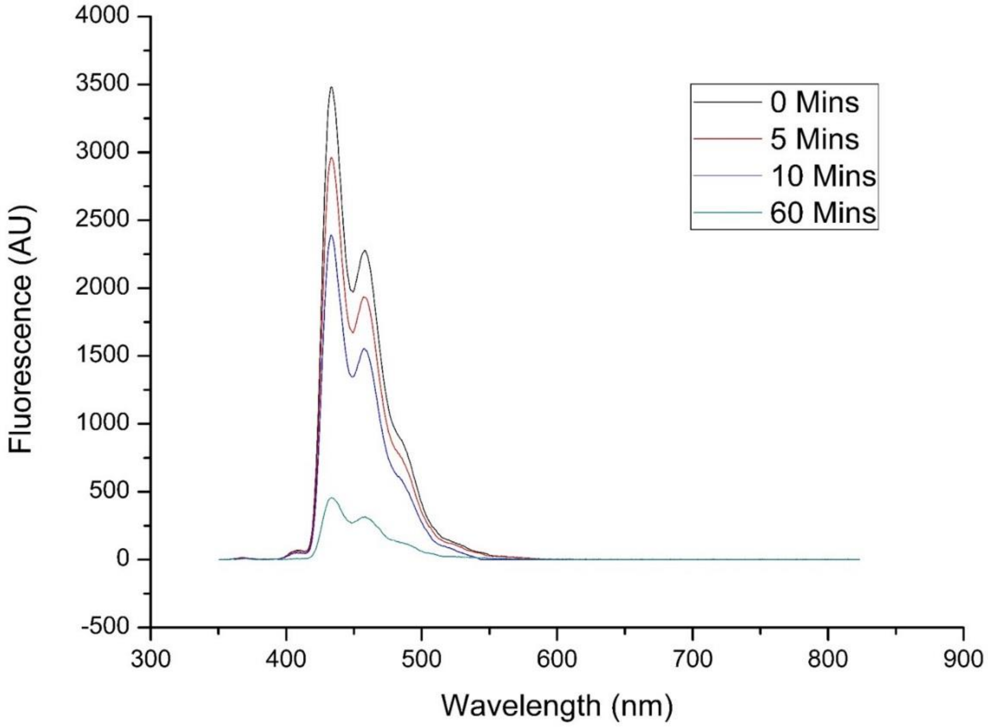

Figure 85 ADPA fluorescence recorded at 365nm excitation for 1ml ADPA solution irradiated for increasing periods

5.3.2 Cell death analysis by Annexin-V expression

To assess the effects of irradiation on apoptosis induction, Annexin-V was used to detect phosphatidylserine expression on cell membrane in non-irradiated (Fig. 86A), cells irradiated for 10 (Fig. 86B), 20 (Fig. 86C) and 30 (Fig. 86D) minutes with 400mW of optical power, imaged using a confocal microscope. Results indicate that irradiation does not induce any additional apoptosis compared to control sample (APC fluorescence was actually slightly elevated in control sample). Mitochondrial specific dye MitoTracker was used to stain cell mitochondria for imaging (green) and annexin-V was used to stain outer membrane (red). Future studies should utilise a positive control for apoptotic cell death, for instance a photosensitising dye.

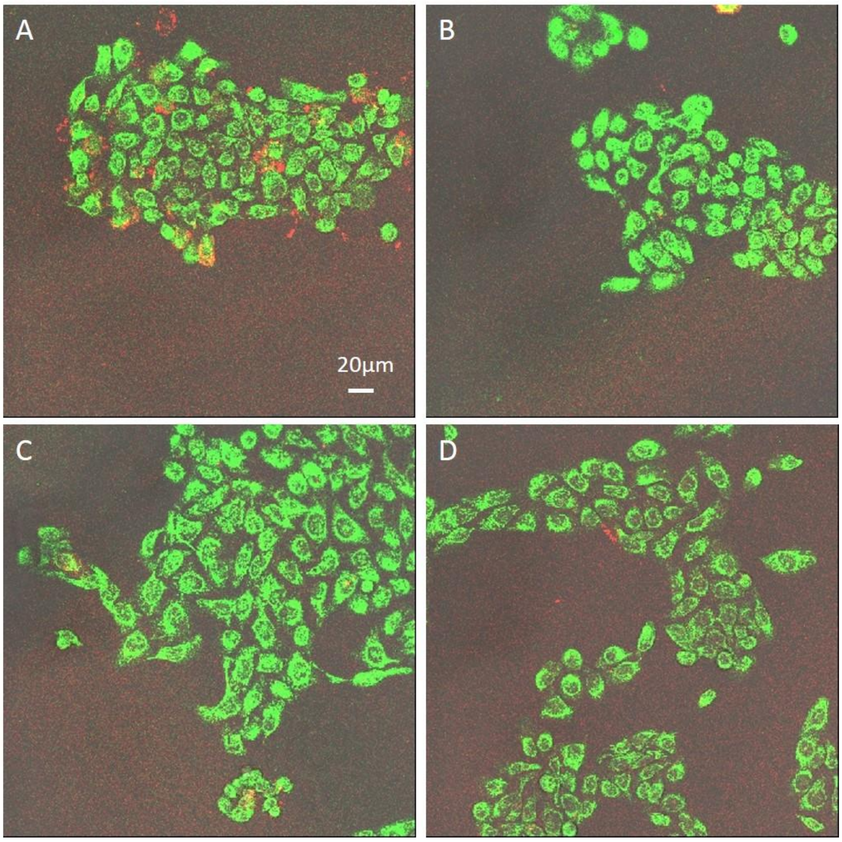

Figure 86 Confocal microscopy of cells stained with MitoTracker Green (green) and Annexin V-APC (red): (A) non-irradiated control; (B) sample irradiated for 10 minutes; (C) sample irradiated for 20 minutes; (D) sample irradiated for 30 minutes

5.3.3 Cell death analysis by Trypan blue exclusion dye

To assess cell death at a later time point, cells were detached from culture wells and incubated with the dead cell dye trypan blue. Results indicate that increased optical power (100-400mW) with a set irradiation period (10 minutes) induces progressive cell death in bladder cancer cells (Fig. 87), however irradiation of cells for 4 minutes with 400mW optical power causes a temperature increase of around 2.4^{o}C, equalling roughly a 5^{o}C temperature increase when extrapolated over 10 minutes (Fig.88). Comparison between cells irradiated at for 10 minutes with 400mW of optical power and a temperature control (heated water bath) reveals that the cell killing effects may be temperature dependent (Fig. 89).

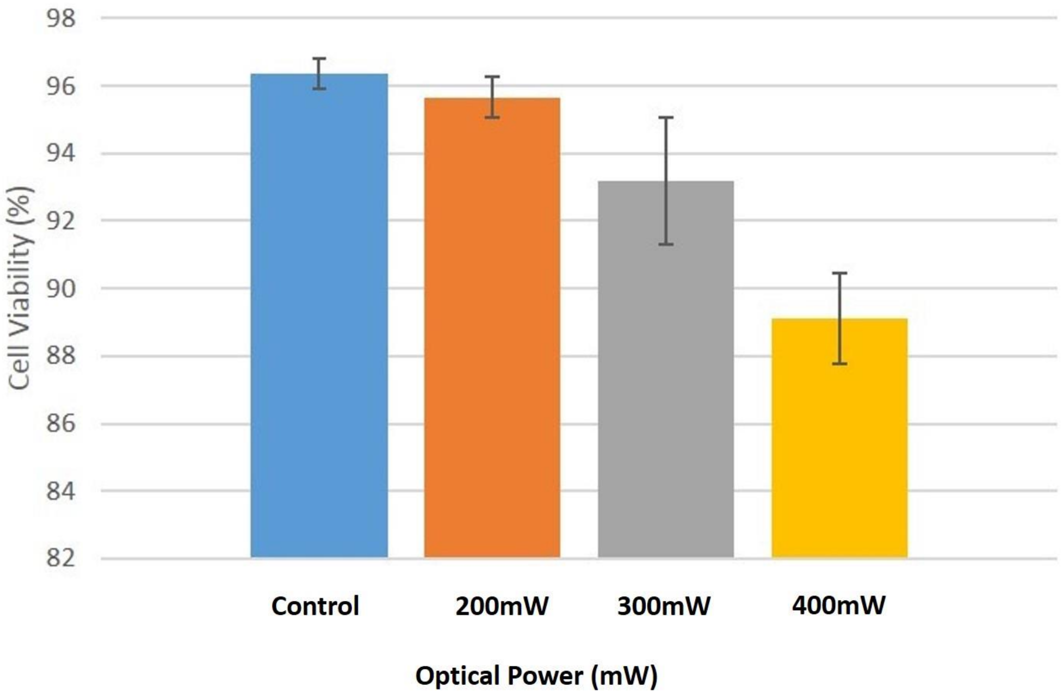

Figure 87 Average +/- Standard deviation values for 3 measurements each of cell viability in control (blue) and following 10 minute irradiation at 200mW optical power (orange), 300mW optical power (grey) and 400mW optical power (yellow)

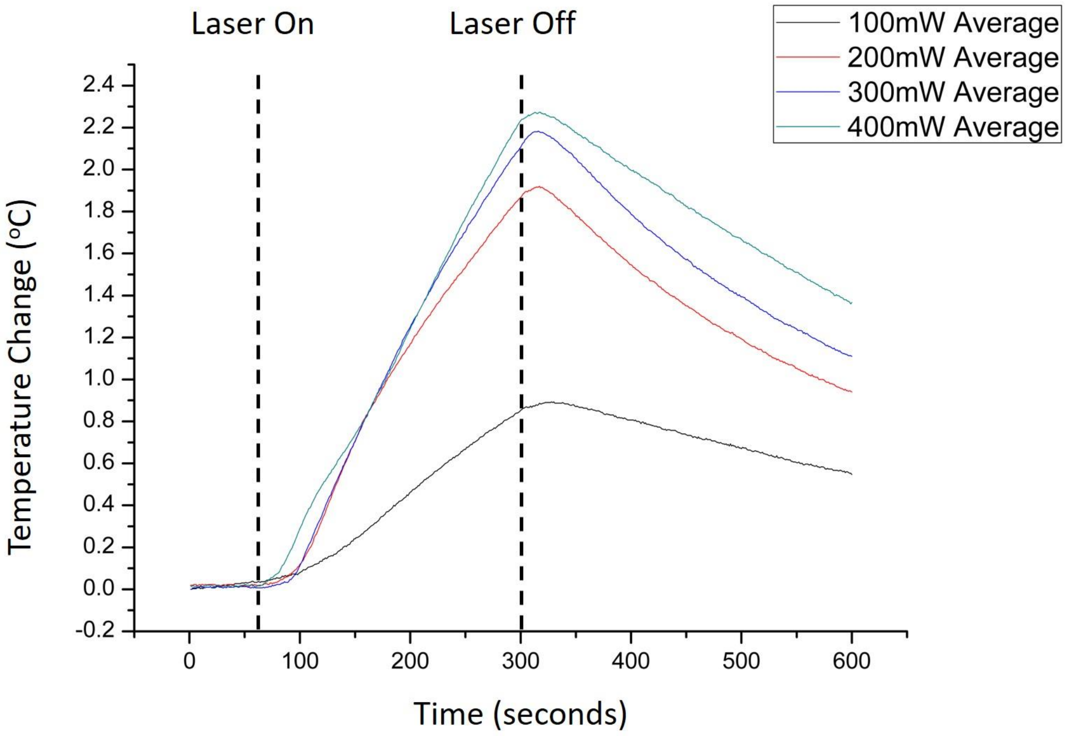

Figure 88 Temperature increase in media irradiated for 4 minutes using 1268nm laser with set optical power of 100mW (black line), 200mW (red line), 300mW (blue line) and 400mW (green line). Lines represent average of 3 measurements each.

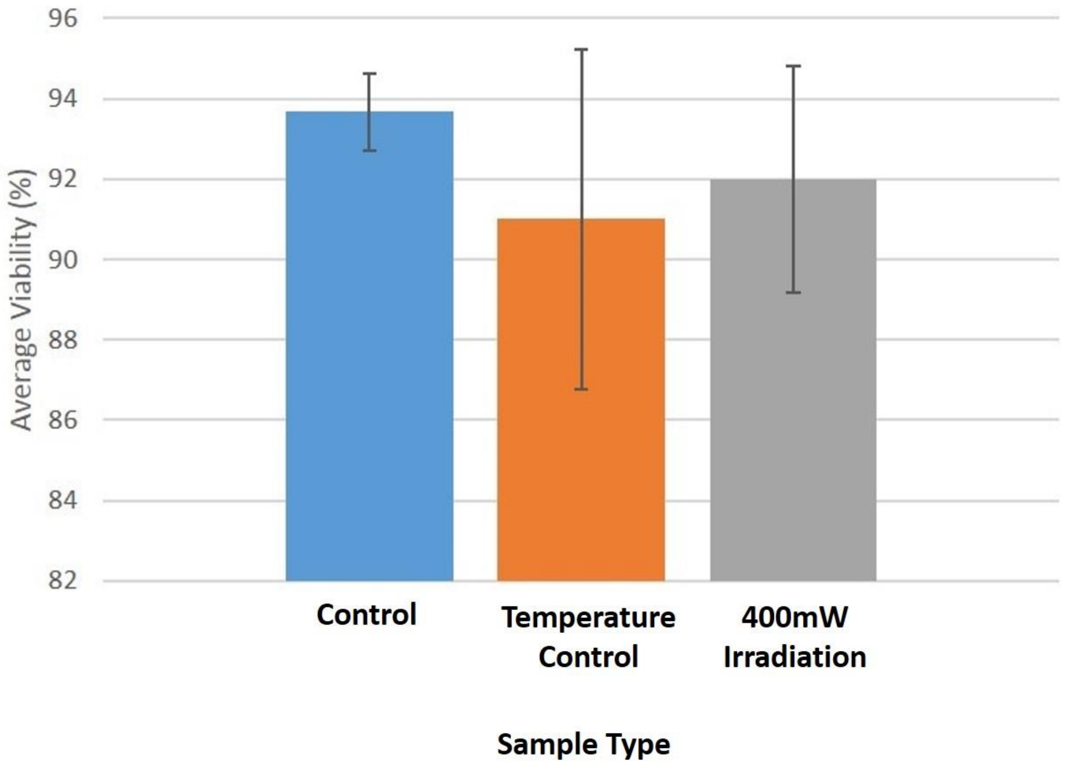

Figure 89 Average +/- standard deviation values of 3 measurements each of cell viability for control (blue), for cells submerged for 10 minutes in a 42oC water bath (orange) and for cells irradiated for 10 minutes using 400mW optical power (grey)

5.4 Discussion

From the results presented in this chapter, it appears that 1268nm laser irradiation induces singlet oxygen generation in aqueous media. Analysis of ADPA fluorescence across increasing irradiation periods shows ADPA quenching suggestive of singlet oxygen generation in media. Control (non-irradiated) samples showed no observable decrease in ADPA fluorescence over time, although differences in ADPA concentration may cause slight discrepancies. Future studies should seek to corroborate these findings using identical ADPA concentrations, potentially measuring over longer time frames and with a greater number of time points to better elucidate the relationships between irradiation and singlet oxygen generation in media. Irradiation of bladder cancer cells was sufficient to cause limited cell death through necrosis, although this is likely attributable to the heating effects of the laser. This may be the result of an inherent inability in the cell line used to undergo apoptosis, as depicted by Annexin V analysis. Future analysis would benefit from the use of a positive control for apoptosis when studying and measuring Annexin V – APC fluorescence. This could be achieved through an alternative singlet oxygen inducer such as a PS agent. The cell cycle regulator p53 (mutated in 5637 cells) is central to the regulation of cell growth and division. Intrinsic or extrinsic signals in malignant or infected cells are often enough to induce apoptosis, a tightly regulated process of cell death[258], however many cancers are known to possess mutations in the tumour suppressor gene p53[259]. The escape from cell cycle checkpoints in bladder cancer, leading to invasive disease, is associated with p53 mutation[260]. Previous work has demonstrated that 1268nm irradiation causes considerable increases in ROS levels and aberrations in calcium signalling within cancer cells. The high levels of ROS witnessed in cancer cells as an effect of 1268nm irradiation seem to be central to their death. The intracellular physiological modifications, together with the timing of cell death are suggestive of apoptotic cell death, although more work must be done to elucidate the distinct effects.

The bladder cancer cell line 5637 is known to contain a p53 mutation (which results in its aberrant metabolic profile, as seen in chapter 2), therefore apoptotic signals may have no effect in this cell line. One other possibility for the negative results from apoptosis measurements could be dead and dying cells detaching from culture plates during or post-irradiation. As confocal microscopy analysis focussed solely on attached cells undergoing apoptosis, it is possible that a population of cells which had previously been killed were missed. In future, this may be remedied by developing a more elegant method for detecting and quantifying apoptosis, for instance using flow cytometry.

In contrast to apoptosis, necrosis is considered to be an uncontrolled pathway of cell death suggestive of tissue destruction. Necrosis is caused by sudden disruption of the plasma membrane or lysosomes[261]. Cell death and therapeutic response suggest a role for necrosis in tumour control post-PDT[262]. Necrosis causes immune infiltration by attracting immune cells and promoting their activation, however inflammation can be a double edged sword for cancer. Products of immune effector cells have previously been shown to promote malignant transformation of bystander cells[263] along with cell growth and proliferation[264]. There is evidence of identical irradiation regimes with 5-ALA promoting apoptosis in some cell lines and necrosis in others[42]. Results from trypan blue dead cell dye analysis suggest that laser irradiation and the LOE induces a small decrease in cell viability, which may be attributable to necrotic cell death. An advantage to trypan blue inclusion analysis was the inclusion of cells in the culture supernatant. The result of this was that cells which had previously died and detached from culture wells were also accounted for during analysis. It is considered that cells killed by the temperature control would have died via necrosis as opposed to apoptosis, therefore the therapeutic ability of the LOE may be solely due to its effects on temperature of the culture media. Similarly to apoptosis measurements, trypan blue analysis would benefit from a positive control, for instance PS agents, to determine the efficacy of each regime. Calculations from irradiation measurements using a thermocouple indicate that 10 minute irradiation of 1ml aqueous media with an optical power of 400mW would result in a local temperature increase in the region of 5^{o}C, therefore a water bath at 42^{o}C (5^{o}C above body/incubator temperature) is a suitable temperature control. As expected, exposure to optical powers of 400mW causes greater heating of media than exposure to 100, 200 and 300mW optical powers. Analysis of temperature changes indicates that this response is not dose dependent, however, therefore future investigation is required to determine the full heating effects of the laser on both media and tissue. To calculate the expected temperature increase after 10 minutes, results from measurements made over 4 minutes were approximately extrapolated, however response may not be entirely linear. This means temperature increase in media may be slightly more or slightly less than 5^{o}C. Future analysis should also better seek to account for acclimatisation periods on the bench, as the temperature control utilised in this study was considered as 5^{o}C above incubator temperature (37^{o}C). The mutagenic potential of necrotic environments suggests that the mode of cell killing (apoptosis vs necrosis) should be carefully balanced to avoid undesirable therapeutic results.

In many instances, PDT may directly kill only a small proportion of tumour cells. A major driving force behind tumour clearance following PDT is its stimulating effects on the immune system[265]. Furthermore, PDT can induce rapid antigen specific responses on secondary insult[266]. Therefore, although only an approximately 5% cell kill was observed using LOE, it may be that the death of these cells would be sufficient to instigate a strong and long lasting anti-tumour immune response.

Treatment regimens which maintain oxygen levels are generally demonstrated to lead to greater degrees of cancer cell death and tumour control[267]. Research by Anquez *et al.*[197] has demonstrated that low level but long period irradiation is suitable to induce morphological changes in breast cancer cells suggestive of cell death, possibly due to the oxygen sparing nature of this regime. It is possible that the fluences and fluence rates employed in this study were sufficient to generate singlet oxygen but also served to rapidly deplete oxygen levels in culture, therefore future studies may benefit from exploring the effects of irradiation regime on singlet oxygen generation. Low fluence, long exposure irradiation regimes are not directly applicable to bladder cancer therapy as the results would be substantial patient lay-up time. A balance must be struck, therefore, between fluences and fluence rates which are clinically feasible but also therapeutically effective. It would be of future interest to integrate a 1268nm irradiation source with a cell culture incubator, as done by Anquez *et al.*, to determine the effects of long term exposure on oxygen levels and morphological response in cells.

There are a few additional experiments which may serve to improve the validity of these findings and to improve understanding of the effects of irradiation on cell death. The first, as already stated, is to utilise positive controls for apoptosis and necrosis experiments. This would allow assessment of the worth of the detection techniques utilised here.

Secondly, as shown by thermocouple measurements, laser irradiation of media causes temperature increases which may cause non-specific killing of cells. In order to assess the wavelength dependence of irradiation on singlet oxygen generation and cell death, a control laser line could be employed. This may be achieved by directly irradiating ADPA and cells with a laser of similar wavelength which is outside the range to induce an oxygen spin transition (e.g. 1000-1100nm wavelength) at identical optical powers. Theoretically, irradiation of ADPA with a 1000nm laser using an identical setup should induce a similar temperature change without singlet oxygen generation, allowing observation of the effects of temperature on ADPA fluorescence (this could also be achieved with a water bath). Similarly, irradiation of cells with a control wavelength between 1000-1100nm would allow clear observation of the relative contributions of both temperature changes and singlet oxygen on cell death.

Finally, to corroborate conclusively whether 1268nm irradiation acts via singlet oxygen, experiments should be performed in O_2 free media, or in the presence of $^1O_2$ quenchers. Quenching could be achieved through the use of bovine serum albumin in media, for example. Both Anquez and Sokolovski proved the effects of laser irradiation in their experiments were cancelled out by the addition of singlet oxygen quenchers. Conversely, the effects of irradiation could also be observed in O_2 enriched media. In the case of ADPA measurements, reductions in ADPA fluorescence following irradiation in the absence of O_2 would suggest an unaccounted for effect to be considered in future experiments. Similarly, comparable cell death in the absence of O_2

would suggest the role of irradiation induced singlet oxygen in cell death is minimal. This would point towards thermal effects as the significant contributor to cell death, which would be of limited worth therapeutically.

As stated earlier, the application of tumour therapy must be specific to avoid unwanted destruction of healthy tissue. LOE has shown promise for the targeted ablation of tumour tissue through the generation of singlet oxygen, however care must be taken when applying this technique that the specific, singlet oxygen dependent effects of irradiation are separated from any non-specific destructive thermal effects.

5.5 Conclusion

To conclude, LOE has shown promise in previous studies for its ability to selectively kill cancer cells without the need for photosenstising dyes. The mode of action of therapy and its applicability to bladder cancer are still not known, however it could provide benefit for disease therapy in BCG/Mitomycin C refractive patients. Results included in this chapter indicate the following: 1268nm laser irradiation of aqueous solutions is suitable to induce dose dependent singlet oxygen generation; irradiation of cells is not sufficient to induce apoptosis; irradiation of cells may be sufficient to induce necrosis, however this is likely a result of the heating effects of the laser. Although early effects such as calcium signalling can be seen within minutes of irradiation, the cell death witnessed by Anquez *et al.*[197] occurred only after up to 24 hours of continuous irradiation. The low optical cross section and quantum efficiency of singlet oxygen generation by the light oxygen effect suggests that in current form this is not a strategy which would lend itself well to bladder cancer therapy, owing to the time frames which would be needed for effective treatment. The benefits of the light oxygen effect are obvious: this would negate all issues regarding PS solubility, cost and patient lay-up time. The use of infrared lasers as excitation sources, as covered earlier, can theoretically double tissue penetration depth, greatly increasing the therapeutic potential of PDT. Complementarily, the design of small scale infrared diode lasers such as Nd-YAG diodes and Ga-Al-As quantum well diodes now means that this could be achieved with compact, mobile irradiation sources. A major concern with the employment of the light-oxygen effect is an inability to selectively localise doses to, for instance, mitochondria or plasma membrane, meaning it may be difficult to specify pathways of cell death. As discussed, PS localisation and irradiation regime have profound effects on the expression of transcription factors and the expression of inflammatory molecules, which in turn effects the method of cell death. Much more work is needed therefore in how to selectively localise and optimise the administration of light and generation of singlet oxygen. It is suggested that future analysis of the light oxygen effect with regards to bladder cancer should focus on the following: the comparison of apoptotic processes in bladder cancer cells with and without p53 mutations; the effects of long-term (>24 hour) exposure at low fluence rates and finally immune responses to LOE in representative animal models of bladder cancer.

6. TISSUE COMPUTER MODELLING

6.1 Introduction

One of the major limitations in the clinical application of autofluorescence spectroscopy to the detection of bladder cancer is an inability to reliably delineate the contributions of individual fluorophores to the complex fluorescence spectra obtained, especially under UV illumination. It is known that several integral tissue fluorophores possess similar fluorescence excitation and emission profiles (for instance collagen, elastin and NADH)[180]. The interference between the fluorescence profiles of elastin and NADH has previously been discussed as a potential underlying factor of the reduced optical redox ratio seen in bladder cancer organoids (chapter 3) and biopsy tissue (chapter 4). A system with which to determine the individual contribution of fluorophores to complex fluorescence spectra would therefore improve our knowledge of bladder cancer at the tissue and molecular level. In recent years, focus has turned to the creation of computational tissue simulation models based on measured optical properties of tissues and fluorophores of interest[268-270]. As the endogenous tissue fluorophores collagen, elastin, NADH and FAD possess known optical properties (optical cross section, quantum yield, absorption and fluorescence properties) and the layers of bladder tissue (mucosal and muscular) are easily measurable to obtain optical properties, theoretically there is potential to generate a computer model to delineate the contribution of each of these fluorophores to tissue fluorescence. The optical properties of human and animal tissue have previously been extensively reviewed, thereby providing data repositories for the design of such computer simulations[198,271,272]. This chapter details efforts to develop a computational model of light transport and autofluorescence in bladder tissue using TracePro software and the Monte-Carlo method. Results from theoretical modelling of fluorescence based on contributions from collagen and NADH show strong similarity to measured experimental results, indicating that this methodology may be useful in future to further understanding of fluorophore properties in bladder tissue.

6.2 Materials and Methods

6.2.1 Literature Search

Relevant medical literature was searched in PubMed to determine the optical properties of bladder tissue across a wavelength range of 360-1100nm. The parameters of interest for the research were the following: coefficient of scattering; coefficient of absorption; anisotropy factor. Results from literature search were used to approximate the physical properties of bladder tissue for simulation and modelling.

6.2.2 Creation of tissue simulation

TracePro optical modelling software (Lambda software) was used to generate a 2-layered object (bladder simulation). The separate layers (mucosa and muscle) were endowed with their respective absorption and scattering properties recorded from literature search of optical properties of porcine bladder tissue (detailed in Table 13). The thickness of the mucosal layer was selected as 200µm, while the thickness of the muscle layer was selected as 2000µm. Tissue layers were populated with the fluorophores NADH (mucosal layer) and collagen (submucosal/muscle layer) at approximate concentrations recorded in measured tissue. The optical properties of collagen and NADH (absorption cross-section, absorption and emission maxima, quantum yield) were recorded from the relevant literature[273-276]. The Beer-Lambert law is used to calculate absorption of light by each layer of tissue (equation 3):

$$\Phi = \Phi_0 \exp(-\mu_a t)$$

Equation 3 Calculation of tissue absorption of light using Beer-Lambert law

Where Φ is the transmitted flux, Φ_0 is the incident flux, μ_a is the coefficient of absorption and t is the sample thickness.

Additionally, Fresnel’s law was used to account for the refractive index mismatch at the interface of the two tissue layers. The Henyey-Greenstein function was used as the scattering phase function (equation 4):

$$\text{SDF} = p(\theta) = 1 - g^2/4\pi(1 + g^2 - 2g \operatorname{Cos} \theta)$$

Equation 4 Scattering phase function using Henyey-Greenstein function

Where g is the anisotropy factor and θ is the angle of scatter.

When the beam encounters a scattering medium it is spread to a random distance (x), defined by the probability distribution (equation 5):

$$P(x)dx = \exp(-\mu_s x)dx$$

Equation 5 Probability distribution

Where μ_s is the coefficient of scattering and x is a random value between 0 and 1.

Fluorescence is modelled in TracePro by entering the parameters of relative absorption $ab(\lambda)$ and relative extinction $ex(\lambda)$ normalised to the molar extinction coefficient K_{peak} and the relative emission $em(\lambda)$. The concentration of fluorescent material in each tissue layer is set by entering the molar concentration C_{molar} for each fluorophore, defined in previous literature[273-276]. Additionally, the coefficient of fluorophore absorption in media is determined by equation 6:

$$\mu_a(\lambda) = ab(\lambda)K_{peak}C_{molar}$$

Equation 6 Coefficient of absorption

The path length before absorption is calculated as:

$$d(\lambda) = -\log10(x)/\mu_s(\lambda)$$

Equation 7 Path length before absorption

The computer simulation model of bladder tissue constructed in TracePro was used as the medium for a Monte-Carlo light transport investigation. A source and detector were placed on the tissue surface replicating the dimensions of the LAKK-M system (source and detector diameters and source/detector separation distances). Fibre diameters (source and detector) were set at 100µm, with NA values of 0.22 each. The separation distance between source and detector was 1mm. A wavelength of 365nm was chosen for the incident light to closely approximate the dimensions of the UV source of the LAKK-M system.

6.2.3 Experimental Comparison

Pig bladder from freshly slaughtered pig was purchased from Medical Meat Supplies, Ltd. Tissue was dissected transversely to reveal the interior (mucosal surface) and rinsed with phosphate buffered saline (PBS). The probe of the LAKK-M was gently brought into contact with the mucosal surface of the tissue, after which the UV source was activated, spectrum was given 5 seconds to stabilise and was then recorded in the optics lab in darkness. In total, UV fluorescence spectra were recorded and averaged from 16 sites of the bladder across a wavelength range of 300-800nm at 0.2nm increments, recorded in custom built “LDF 3.1” software and exported. The average measured fluorescence spectrum was imported to Origin Pro 8 software and plotted alongside the theoretical fluorescence spectrum received from Monte-Carlo modelling.

6.3 Results

6.3.1 Literature Review

Optical properties of bladder tissue were found through a PubMed literature search, concerning light at wavelengths of 532nm, 633nm and 1064nm. Additionally, optical properties of pig tissue were found at a range of wavelengths during the literature search. The optical properties of tissue recorded from literature are included in Tables 11 & 12, below. The values used for the final TracePro model are included in Table 13.

Table 11 Optical properties of human bladder tissue

Tissue	**Wavelength (nm)**	**Absorption μ_a (cm^{-1})**	**Scattering μ_s (cm^{-1})**	**Reference**
Whole	532	0.27-0.71	1.28-3.3	[277]
Whole	633	0.28-0.76	2.5-6.37	[277]
Submucosa	633	1.4	88	[271]
Submucosa	1064	0.4	116	[278]
Mucous	1064	0.7	75	[278]
Wall	1064	0.9	543	[278]

Table 12 Optical properties of porcine bladder tissue

Tissue	**Wavelength (nm)**	**Absorption μ_a (cm^{-1})**	**Scattering μ_s (cm^{-1})**	**Reference**
Whole	458	1.3	255	[279]
	488	1.4	248	
	514	1.8	240	
	532	3.5	277	
	630	0.57	214	
	630	0.99	258	

Table 13 Parameters used for the generation of each layer in the Monte Carlo model, including thickness, coefficient of absorption, coefficient of scattering, anisotropy, fluorophore type, coefficient of fluorophore absorption, fluorophore optical cross section and molar extinction coefficient,

Layer	**Thicknesses, µm**	**n**	**μ_a, cm^{-1}**		**μ_s, cm^{-1}**		**g**	**Fluorophore**	**μ_s, cm^{-1}**	**ϕ_f**	**ε_f, M^{-1}cm^{-1}**
Mucosa	200	1.55	458 nm	1.3	458 nm	255	0.9	NADH	3.15	0.05	6220
			488 nm	1.4	488 nm	248					
			514 nm	1.8	514 nm	240					
			532 nm	3.5	532 nm	277					
			630 nm	0.57	630 nm	214					
Muscle	2000	1.55	458 nm	1.3	458 nm	255	0.9	Collagen	0.9	0.3	52940
			488 nm	1.4	488 nm	248					
			514 nm	1.8	514 nm	240					
			532 nm	3.5	532 nm	277					
			630 nm	0.57	630 nm	214					

6.3.2 Monte-Carlo Modelling of photon transport in tissue

Figure 90 below depicts results from Monte-Carlo modelling simulation of the transport of individual photons of UV light (365nm) through the mucosal and muscular layers of tissue. Photons entering tissue can either be reflected by tissue surface, transmitted through the full tissue thickness or be absorbed by the tissue constituent molecules. Fig. 90a depicts a cross-section of tissue, while Fig. 90b gives a 3D view. From this simulation the maximum and median penetration depth of photons into tissue can be seen clearly.

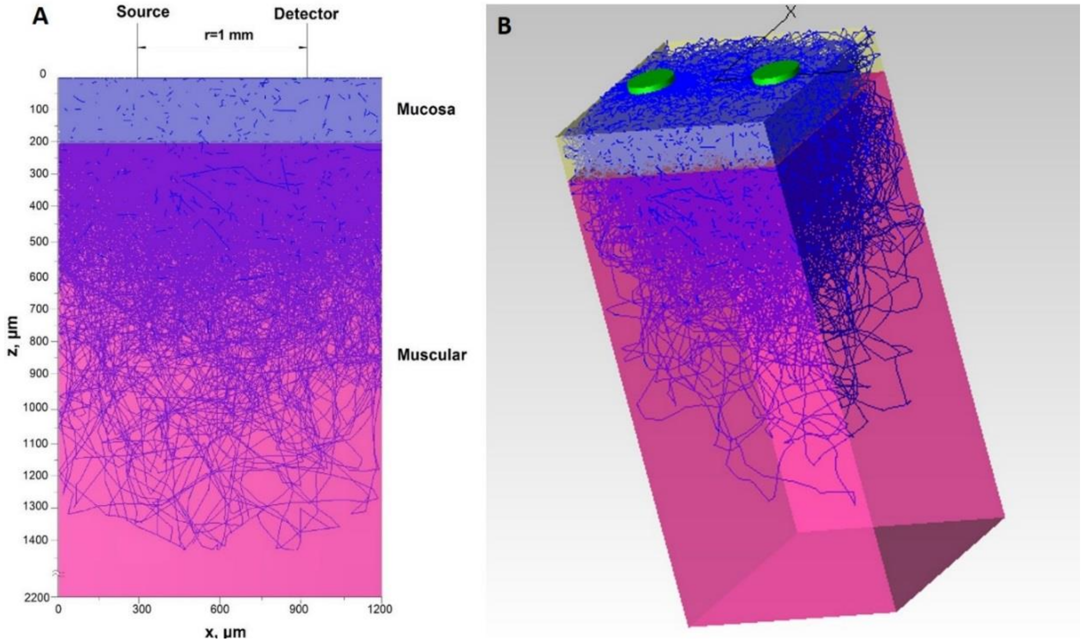

Figure 90 Optical model of bladder tissue generated in TracePro: (a) cross section of tissue; (b) 3D simulation

6.3.3 Comparison with measured fluorescence

The predicted tissue fluorescence calculated at 365nm excitation from the TracePro model was plotted alongside the experimental tissue fluorescence measurement (Figure 91). From Figure 91 similar features can be seen between the spectra, indicating a good fit of the theoretical model for bladder fluorescence.

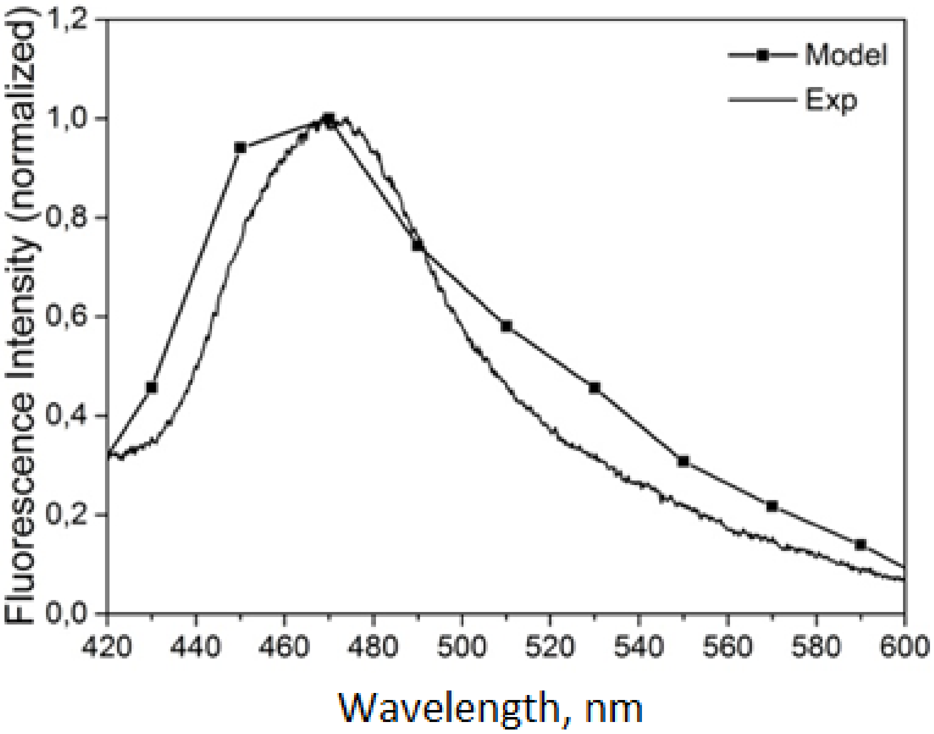

Figure 91 Comparison of the measured UV fluorescence (black line) with theoretical fluorescence simulated from TracePro model (dotted black line)

6.4 Discussion

From the results presented in this chapter, it is shown that it is possible to computationally simulate a model of bladder tissue with similar optical properties to physical tissue. The use of this model allows the calculation of the maximum penetration depth of photons into tissue alongside the propensity for incident photons from the laser source to be scattered, reflected and absorbed by the individual layers of bladder tissue. In this work, only the average values for mucosal and muscle layers of bladder tissue have been studied. A common cause of disagreement in the field of autofluorescence spectroscopy is the effect of tissue thickening on recorded fluorescence[118,280]. Often, flat lesions can cause proliferation of urothelial cells. The result of this may be two-fold: a thickened urothelium may contain increased contribution from the metabolic cofactors NADH and flavins while simultaneously dampening fluorescence signals from underlying structural proteins[121]. As demonstrated in this chapter, the maximum penetration depth of UV light in healthy tissue is approximately 1.4mm, therefore thickening of the urothelium in bladder cancer may further reduce the penetration of light deeper into tissue. It may be that urothelial thickening contributes significantly to the measured reduction in bladder cancer autofluorescence seen by many groups (ourselves included). Furthermore, urothelial keratinisation has been observed in bladder disease[281], which may interfere with NADH and flavin fluorescence measurements[282]. The observations previously reported in organoid (chapter 3) and human biopsy tissue (chapter 4) still leave a number of questions which may be addressed through the use of tissue simulation models. Due to the complex nature of UV fluorescence spectra[180], it is difficult to say whether the phenomena observed (reduced ORR in cancer organoids(ex365em490/ex365em550)) are a result of metabolic or structural modifications.

Key to the application of this Monte Carlo model is the validation of code against simple geometries and phantoms of known optical properties. Due to unknown optical properties within tissue and also inhomogeneity of fluorophores, it is difficult to definitively state the applicability of a model. Before proceeding to further modifications, it is crucial to know whether the code and model employed for the Monte Carlo method is accurate. For diffuse reflectance measurements, human tissue mimicking phantoms can be generated using varying concentrations of haemoglobin embedded with polystyrene beads which scatter incoming light[283]. Similarly, fluorescence measurements could be performed on a phantom set with known, uniform concentrations of NADH or collagen. This would allow a direct assessment of the ability of the method to accurately report on increasing fluorophore concentrations. Multiple layer phantoms containing distinct NADH and collagen layers could then also be compared against relevant code. Validation is a crucial step of Monte Carlo modelling, therefore this must be performed as a priority before moving forward with further testing.

There are a number of additional adjustments which may serve to improve the accuracy and applicability of the model in the future. The first is to replace porcine tissue with human. Implementation of suitable equipment and methodology, including spectrophotometers and integrating spheres, would allow the measurement of tissue optical properties at wavelengths exactly matching the specifications of the LAKK-M system. Previously, the calculation of tissue optical properties from measured values has been described by using the inverse adding-doubling method[284]. Work is currently ongoing to optimise the use of TracePro simulations of bladder tissue[243].

Secondly, during slaughter tissue is exsanguinated. We have previously published on the absorptive and scattering effects of tissue blood supply[199], observing a reduced autofluorescence signal in tissues rich in blood. Simulation of tissue vasculature in computer models may therefore allow a better insight into realistic light transport. Similarly, our model would benefit from the addition of additional fluorophores (such as elastin and flavins) to their respective tissue regions, and the addition of an extra tissue layer to reflect the region of connective tissue (rich in collagen) which lies between the mucosal and muscle layers. Finally, the LAKK-M system contains 4 sources (UV, blue, green and red). The present model only accounts for UV light at a wavelength of 365nm, therefore the simulation and inclusion of light transport at the other wavelengths would be of value. It is extensively reported that longer wavelength light penetrates further into tissue owing to fewer scattering and absorption events[44].

In summary, the computational method described in this chapter is a useful technique for simulating the optical properties of tissue and studying parameters such as tissue autofluorescence, however this model must be validated.

6.5 Conclusion

In this chapter, ongoing efforts to develop tissue mimicking computer simulations were discussed for the study of light penetration in bladder tissue to aid in the development of diagnostic and therapeutic techniques for bladder disease. A cross-sectional model using TracePro has been developed in this chapter which is capable of use for Monte-Carlo simulations of photon transport through tissue. Comparison of the theoretical fluorescence spectrum from our model shows a good fit with experimental measurements from fresh pig bladder, indicating that this is a useful model for future studies. Validation and development of this modelling technique, in conjunction with organoid development and larger scale biopsy analysis, may allow researchers to better understand the contributing fluorophores to healthy and diseased fluorescence spectra, improving clinical application of diagnostic ratios such as the ORR.

7. CONCLUSION AND FUTURE PERSPECTIVES

The aim of this thesis was to explore new techniques for bladder cancer diagnosis and therapy, addressing current concerns with gold standard techniques. Bladder cancer is among the most common cancers in the UK, causing significant morbidity to sufferers and in the region of 5000 deaths per year[1]. WLC and VUC suffer from low sensitivity, particularly for the flat dysplasia CIS[17]. Efforts to improve sensitivity using PDD suffer themselves from reduced specificity, particularly for tissue previously treated by chemotherapy or surgery[29]. Autofluorescence spectroscopy of tissue has been suggested as a suitable technique to address the sensitivity-specificity disparity between these techniques ever since first being applied in the 1980s[102]. Autofluorescence spectroscopy and imaging has been covered for a wide range of diseases[100], including bladder[118], and has been shown to increase accuracy of surgical margin demarcation[115]. Despite over 30 years of development, clinical application of autofluorescence imaging is still yet to occur. Reduced autofluorescence of tissue under UV excitation has been demonstrated by a number of research groups[112,118], however this has largely been attributed as an effect of urothelial thickening. The roles of individual fluorophores of interest (collagen, NADH, flavins, porphyrins) in bladder cancer is still relatively unknown and presents a considerable gap in understanding in autofluorescence spectroscopy.

In order to address this, I considered that the optical redox ratio (ORR) may be a useful technique with which to study bladder cancer and detect early cellular abnormalities, based on previous work in the field[190,222]. ORR imaging generally relates to metabolic abnormalities, rather than structural effects of bladder cancer such as tissue thickening - although this may be complicated slightly by spectral overlap from collagen and elastin - therefore it was hypothesised that it may provide increased accuracy for CIS detection.

The majority of this research has focused on the use of the multi-functional laser system "LAKK-M", which contains a central functional unit for autofluorescence spectroscopy alongside sources for monitoring blood flow and tissue oxygenation. The LAKK-M system has previously been used to measure the effects of tissue properties on fluorescence[199] and fluorescence parameters in cardiovascular disease[205] therefore it could be of worth for bladder cancer. A strength of this system is the ability to measure multiple parameters simultaneously (for instance the effects of tissue blood flow on measured fluorescence parameters[199]), furthermore these measurements can be made non- or minimally-invasively. The LAKK-M system has not previously been applied to the study of bladder tissue, therefore a necessary first step in the clinical validation of this system was the study of bladder tissue across the cell to tissue level.

In chapter 2, the LAKK-M system was demonstrated as suitable for the study of common endogenous fluorophores. ORR measurements from the LAKK-M (ex365em490/ex450em510, ex365em490/ex450em510 and ex365em490/ex365em550) approximately represent increasing relative levels of NADH, although more work is necessary to understand the non-linear response of the ORR. Autofluorescence measurements from the finger ensured that tissue fluorescence was achievable using the LAKK-M setup, making it applicable to bladder tissue for biopsy study. Findings from confocal microscopy and flow cytometry analysis on the ORR suggested that NADH and flavins were the major contributing fluorophores to cellular fluorescence, while a statistically significant difference ($p = 2 \times 10^{-16}$) in the ORR (measured as ex360em425-475/ex488em515-545) existed between cell types, with cancer cells exhibiting an increased ORR relative to healthy bladder cells. In accordance with previous literature in other cancer types, bladder cancer cells were found to possess an increased ORR relative to healthy control. Unfortunately, this finding could not be replicated using the LAKK-M system. There are a few factors which may underlie this result: fluorescence yield from cultured cells using the LAKK-M was very low, even using concentrations far above those hypothetically present in voided urine, therefore significant differences may have been lost as noise. Additionally, cells in solution showed significant variability in ORR values over time (both day-to-day and over 5-30 minute time spans). From variability measurements, it is concluded that the most stable ORR measurement using the LAKK-M system is NADH(ex365em490)/flavins(ex365em550). This may help to inform future studies of the ORR in tissue using the LAKK-M system. It is suggested that the use of increased laser powers (>30mW) and design of cuvettes which incorporate magnetic stir bars may overcome the limitations encountered in our research by increasing fluorescence yield from cells and providing uniform solutions for analysis.

Preliminary analysis of human urine from a healthy volunteer indicates that the urine supernatant itself is responsible for the majority of fluorescence, as opposed to voided urothelial cells, therefore future studies may benefit from comparing the fluorescence parameters (including ORR) of voided urine from healthy participants and patients with bladder cancer.

Flow cytometric analysis of ORR values may present some clinical worth itself. Statistically significant differences between cell types were observed based on a comparison of 30,000 cells each[225]. This figure is more in keeping with the normal concentration of shed urothelial cells. Furthermore, the generation of the redox overview allows for the identification of individual abnormal cells from large populations. The Warburg effect postulates that metabolic abnormalities in cancer cells occur early during cancer development, therefore this may be a technique with which to identify bladder cancer cells at an early stage. The flow cytometry setup is relatively straightforward and the use of diagnostic ratios means that system compensation is not required. Furthermore, measurements could feasibly be performed directly on shed urine, leading to a completely non-invasive technique. As only a single bladder cancer cell type was compared with healthy control, future studies would benefit from applying similar measurement parameters to a wide range of bladder cancer cell lines of different stages and grades, to determine whether this phenomenon is universal. Following this, flow analysis of cells shed in human urine samples may allow the assessment of clinical implementation of the technique.

A key step to the understanding of bladder cancer fluorescence is the ability to observe parameters as tumours grow and develop. For this reason, bladder cancer organoids were developed which were grown *In vitro.* Using these organoids, progressive changes were observed in the ORR (measured as ex365em490/ex365em550) and elastin/NADH and elastin/flavin ratios as organoids developed, compared to control samples. These findings may shed new light on how autofluorescence changes as bladder cancer develops. The findings of reduced ORR in cancer organoid are in contrast with findings from ORR analysis of cell lines in chapter 2. It is considered that this may be caused by a more complex network of cells (as scaffolds were not acellular) and the contribution of additional fluorophores such as collagen and elastin to tissue fluorescence spectra. Organoids were nonetheless useful for allowing the observation of progressive changes in fluorescence. Development of diagnostic algorithms in MATLAB revealed that ORR and elastin/NADH ratios both show considerable worth for discriminating bladder cancer organoid from healthy control tissue, therefore these ratios were explored further using human tissue. Human tissue biopsy analysis identified a significant increase in porphyrin levels in tumour tissue compared to healthy, therefore organoid data was revisited to assess if this was also the case. Unfortunately, no significant differences in porphyrin levels between control and organoid were observed. This may be a result of the lack of blood flow in the organoid experiments.

SHG analysis of organoid sections revealed significant changes in collagen volume and alignment in the extra-cellular matrix surrounding cancer cells. This may be attributed to cancer cells modifying surrounding collagen to facilitate invasion and to generate collagen nests to protect themselves from immune attack. The diagnostic user interface developed in MATLAB may be of use for surgical teams as it provides fast automated tissue classification based either on autofluorescence spectral features or collagen alignment features. This could be further developed for application to human tissue data. Combined autofluorescence/SHG imaging has previously been carried out in bladder[96,98] and may allow us to better address the issue of urothelial thickening as a factor of autofluorescence discrepancies. Alongside the LAKK-M, it would be useful in future to apply an MPM system capable of autofluorescence and SHG measurements simultaneously to developing organoids to develop a better understanding of the spatial distribution of fluorophores of interest.

This promising work would benefit from being corroborated using organoids comprising bladder cancer cells of various stages and grades. Comparison of organoid samples with human bladder samples also suggests that a method to improve the accuracy of the study would be a more thorough recapitulation of the urothelium in control samples as this would give a more life-like tissue representation. Equally, porcine bladder scaffolds may be replaced in future with excised human biopsy tissue as a more appropriate tissue mimic. Finally, organoid samples were exsanguinated therefore possessing no blood supply. This likely affected porphyrin measurements but may also have affected fluorescence amplitudes as average UV organoid fluorescence was found to be greater than that of average human tissue. As was previously discussed, tissue blood supply has an effect on measured fluorescence parameters[199], possibly presenting a contributing factor to this fluorescence discrepancy. Future studies may therefore benefit from replicating tissue blood supply if at all possible.

Based on findings from organoid analysis, it was hypothesised that human bladder cancer tissue would possess a reduced ORR (measured as ex365em490/ex365em550) relative to healthy tissue. Results confirm this ($p = 0.00891$). In particular, the ORR displayed strong worth for the discrimination of CIS cases. ORR may therefore represent a useful novel biomarker of bladder cancer which is irrespective of tissue thickening. Again, this finding was in contrast to previous findings in cell lines. Similarly to organoid findings, the reduced ORR in cancer samples may reflect changes to a range of cell types, such as surrounding healthy cells and fibroblasts. Porphyrin levels were also found to be statistically significantly different in bladder cancer tissue ($p = 0.00241$). The increase in porphyrins in cancer tissue is suggestive of a selective accumulation similar to which occurs in PDD but without the need for PS. If true, this technique could provide a boost to bladder cancer detection by applying PDD methodology without the associated cost and patient lay-up time. Furthermore, the study of porphyrins at longer wavelengths into the tissue optical window may provide a technique with which to detect bladder cancer deeper in tissue. One concern with the application of porphyrin spectroscopy was its low accuracy for CIS. As this was a pilot study of 20 participants, it is recommended that a larger scale study will corroborate these findings, with particular focus on a larger sample size of CIS cases. SHG imaging of human biopsy tissue in future may also be a useful tool for understanding the complex role of collagen in developing bladder tumours and the effects of tissue thickening on fluorescence yield. In chapter 3, significant changes in the volume and distribution of collagen in bladder cancer organoids were identified ($p = 2 \times 10^{-16}$). SHG imaging of human tissue may allow a better understanding of this phenomenon and to identify whether findings in organoids can be replicated as reliable biomarkers in human tissue.

In parallel to autofluorescence diagnosis of bladder cancer, in chapter 5 the light oxygen effect was explored, following promising results published by other groups in breast[197] and cervical cancer[196]. The application of the LOE to bladder cancer would overcome current limitations to tissue penetration by PS agents and also activating light, by instead relying on the spin transition of molecular oxygen by 1268nm laser irradiation. Preliminary results show that 1268nm laser irradiation is capable of inducing singlet oxygen generation in aqueous media, however the effect of irradiation on bladder cancer cells is unconvincing. The results observed indicate that irradiation of cells induces a small amount of cell death through necrosis, although this is possibly attributable to the heating effects of the laser. Future analysis may benefit from focussing on analysis techniques which measure apoptosis and necrosis simultaneously (such as flow cytometry) to achieve a better understanding of the processes of cell death occurring post-irradiation. Previously it was discussed that limited cell death post-irradiation may be a result of p53 mutations in the bladder cancer cell line used in the study. It would be useful to explore additional cell lines in future to determine whether this is the limiting factor. In chapter 5 the effects of PDT on immune priming and surrounding non-cancerous cells were discussed. It may be, therefore, that the small percentage of cells killed in our study may be sufficient to instigate a large scale immune response. Application of LOE in organoids, similar to those developed in chapter 3, may also provide some clues on the wide-scale effects of tissue irradiation. If heating effects are solely responsible for the cell death observed in this study, this technique may not be well suited to clinical application due to non-specific effects on surrounding tissue. Thermal ablation of bladder tumours has previously been explored, but has been ignored in recent years in favour of PDT.

Many of the questions still surrounding autofluorescence spectroscopy of bladder cancer may be addressed by using tissue simulations such as that which was developed in chapter 6. The model created in TracePro using relevant data from the literature demonstrated similar fluorescence parameters to fluorescence measured experimentally from fresh bladder tissue. This finding indicated some worth of the developed tissue simulation, although further validation is required. The crucial step to be taken before advancing any Monte-Carlo modelling studies is the validation of code against tissue phantoms of known optical properties and simple geometries (for instance, single layered phantoms with flat surfaces). Without this validation, modelling is speculative and provides little scientific and diagnostic worth, therefore this is recommended as a future avenue of work. Monte-Carlo modelling of tissue indicates that UV light at 365nm travels significantly deeper into the bladder past the mucosa, suggesting that UV fluorescence is partly composed of fluorescence from structural proteins in the connective tissue. Modelling various tissue layers (mucosa, muscle, etc.) and simulating the presence of fluorophores such as NADH and collagen directly addresses the issues of tissue thickening in bladder cancer, leading to a better understanding of the contribution of individual fluorophores to complex fluorescence spectra. Accounting for measured values from organoid (chapter 3) and human biopsy tissue (chapter 4) will allow better understanding of the contributing fluorophores to these observations. Techniques such as the inverse adding-doubling method allow the calculation of coefficients of attenuation and scattering. Future biopsy studies would therefore benefit from simultaneous measurements of light absorption and transmission by tissue along a wide wavelength range in addition to fluorescence. This would allow generation of suitable patient specific tissue models. Similarly, tissue modelling may also allow a better understanding of the processes underpinning LOE at the tissue scale, giving a better understanding of the penetration of 1268nm light into bladder tissue, and the necessary optical powers to induce cell death at various depths of tissue.

Taken together these results contribute to a better understanding of bladder cancer at the cell and tissue level and will allow development of the LAKK-M system further towards clinical implementation. The ideal system for bladder cancer diagnosis would be sensitive, specific and non-invasive to overcome current limitations to WLC, PDD and tissue biopsy. Ideally, the system would also contain a therapeutic option. The LAKK-M system, with modification, could be a useful tool for minimally invasive, multi-parametric analysis of bladder cancer. The optical probe of the system could be easily modified to fit the dimensions of the urethra, while the multiple channels in the functional unit could provide simultaneous information about tissue autofluorescence, blood flow and oxygenation. In this thesis I have identified novel biomarkers for bladder cancer diagnosis (ORR and endogenous porphyrins) through organoid development and human tissue analysis. Crucially, these may represent potential for the diagnosis of CIS. Further analysis of more advanced bladder cancer organoids and in larger populations of human volunteers will help to corroborate and further understanding of these diagnostic biomarkers, while the use of tissue simulations may help to better explore the contributions from individual fluorophores to complex fluorescence spectra. Our results indicate that the LAKK-M at present is not suitable for cellular analysis, however modifications to cuvette design or laser power may make this a more feasible option. Further analysis of the ORR in bladder cancer cell lines using flow cytometry or fluorescence microscopy should provide a better understanding of autofluorescence at the cellular level. Urine autofluorescence analysis using the LAKK-M may however provide useful information for future non-invasive diagnostic testing of suspected bladder cancer.

One limitation to the LAKK-M system is an inability to provide tissue imaging. This would undoubtedly improve understanding of the individual fluorophores in bladder cancer. It is not unreasonable to envision in future a combined imaging and spectroscopy system for fluorescence diagnosis of bladder cancer which provides an indication of whether fluorescence is cellular or extracellular and simultaneously calculates diagnostic ratios such as the ORR. Previously, MPM has been used to good effect in the study of bladder morphology and bladder cancer[96,98] therefore it might be of worth to employ an MPM setup or similar in future iterations of the LAKK-M. MPM would provide image analysis of tissue fluorescence alongside SHG, which could be applied both to developing organoids and human biopsy tissue. Furthermore, the use of MPM exploits the tissue optical window, leading to deeper tissue penetration by excitation light. Finally, corroboration of cell killing effects of the LOE in bladder cancer could see the addition of a 1268nm laser source to the LAKK-M, resulting in a system which can both diagnose and treat bladder cancer with high sensitivity and specificity.

In summary, bladder cancer is a common cancer in the UK which requires new diagnostic and therapeutic techniques to overcome the limitations of current gold standards. In this thesis I have explored the application of non-invasive diagnosis of bladder cancer across the cell to tissue level, identifying the following:

1. A statistically significant increase ($p = 2 \times 10^{-16}$) in optical redox ratio (measured as ex360em425-475/ex488em515-545) in bladder cancer cell line (5637 cells) compared to healthy control cell line (HUC cells)
2. Progressive changes in the autofluorescence properties of developing bladder cancer organoids, including reductions in the ORR (measured as ex365em490/ex365em550), elastin/NADH (ex365em450/ex365em490) and elastin/flavin ratios (ex365em450/ex365em550) of bladder cancer organoid relative to control.

3. Significant differences in the ORR, measured as ex365em490/ex365em550 (decreased in cancer) and endogenous porphyrin levels (increased in cancer) between healthy bladder tissue and bladder cancer from human volunteers

These findings will hopefully contribute to the development of new techniques with which to diagnose the disease at an earlier stage, reducing the rates of disease recurrence, progression and cancer deaths. With some modification, the multi-functional laser system “LAKK-M” could prove useful for the non-invasive diagnosis of disease.

REFERENCES

1. CRUK. Bladder cancer statistics. 2016; http://www.cancerresearchuk.org/health-professional/cancer-statistics/statistics-by-cancer-type/bladder-cancer. Accessed 21.04.16, 2016.

2. A. A. Shokeir, "Squamous cell carcinoma of the bladder: pathology, diagnosis and treatment", BJU Int. **93**(2), 216-20 (2004)

3. D. J. Grignon, J. Y. Ro, A. G. Ayala, D. E. Johnson & N. G. Ordonez, "Primary adenocarcinoma of the urinary bladder: a clinicopathological analysis of 72 cases", Cancer **67**(8), 2165-72 (1991)

4. Y. Zhang, "Understanding the gender disparity in bladder cancer risk: the impact of sex hormones and liver on bladder susceptibility to carcinogens", J. Environ. Sci. Health C Environ. Carcinog. Ecotoxicol. Rev. **31**(4), 287-304 (2013)

5. H. Anton-Culver, A. Lee-Feldstein & T. H. Taylor, "The association of bladder cancer risk with ethnicity, gender, and smoking", Ann. Epidemiol. **3**(4), 429-33 (1993)

6. J. D. Figueroa et al., "Genome-wide interaction study of smoking and bladder cancer risk", Carcinogenesis **35**(8), 1737-44 (2014)

7. K. Simonis, S. F. Shariat & M. Rink, "Smoking and smoking cessation effects on oncological outcomes in nonmuscle invasive bladder cancer", **24**(5), 492-9 (2014)

8. A. Cassidy, W. Wang, X. Wu & J. Lin, "Risk of urinary bladder cancer: a case-control analysis of industry and occupation", BMC Cancer **15**(9), 443 (2009)

9. S. Bonassi, F. Merlo, N. Pearce & R. Puntoni, "Bladder cancer and occupational exposure to polycyclic aromatic hydrocarbons", Int. J. Cancer **44**(4), 648-51 (1989)

10. Z. Zhu, X. Wang, Z. Shen, Y. Lu, S. Zhong & C. Xu, "Risk of bladder cancer in patients with diabetes mellitus: an updated meta-analysis of 36 observational studies", BMC Cancer **26**(13), 310 (2013)

11. P. S. Sullivan, J. B. Chan, M. R. Levin & J. Rao, "Urine cytology and adjunct markers for detection and surveillance of bladder cancer", Am. J. Transl. Res. **2**(4), 412-40 (2010)

12. D. J. Parekh, B. H. Bochner & G. Dalbagni, "Superficial and muscle-invasive bladder cancer: principles of management for outcomes assessments", J. Clin. Oncol. **24**(35), 5519-27 (2006)

13. P. A. Humphrey, "Urothelial carcinoma in situ of the bladder", J. Urol. **187**(3), 1057-8 (2012)

14. R Talwar et al., "Voided urinary cytology in bladder cancer: is it time to review the indications?", Urology **70**(2), 267-71 (2007)

15. F. A. Yafi, F. Brimo, J. Steinberg, A. G. Aprikian, S. Tanguay & W. Kassouf, "Prospective analysis of sensitivity and specificity of urinary cytology and other urinary biomarkers for bladder cancer", Urol. Oncol. **33**(2), 25-31 (2015)

16. B. L. Isfoss, "The sensitivity of fluorescent-light cystoscopy for the detection of carcinoma in situ (CIS) of the bladder: a meta-analysis with comments on gold standard", BJU Int. **108**(11), 1703-7 (2011)

17. G. Mowatt et al., "Photodynamic diagnosis of bladder cancer compared with white light cystoscopy: Systematic review and meta-analysis", Int. J. Technol. Assess. Health Care **27**(1), 3-10 (2011)

18. H. Ren, K. C. Park, R. Pan, W. C. Waltzer, K. R. Shroyer & Y. Pan, "Early detection of carcinoma in situ of the bladder: a comparative study of white light cystoscopy, narrow band imaging, 5-ALA fluorescence cystoscopy and 3-dimensional optical coherence tomography", J. Urol. **187**(3), 1063-70 (2012)

19. G. Mowatt et al., "Systematic review of the clinical effectiveness and cost-effectiveness of photodynamic diagnosis and urine biomarkers (FISH, ImmunoCyt, NMP22) and cytology for the detection and follow-up of bladder cancer", Health Technol. Assess. **14**(4), 1-331 (2010)

20. T. Jager et al., "The prognostic value of cadherin switch in bladder cancer", Oncol. Rep. **23**(4), 1125-32 (2010)

21. J. E. Frampton & G. L. Plosker, "Hexyl aminolaevulinate: in the detection of bladder cancer", Drugs **66**(4), 579-80 (2006)

22. J. C. Kennedy, R. H. Pottier & D. C. Pross, "Photodynamic therapy with endogenous protoporphyrin IX: basic principles and present clinical experience", J. Photochem. Photobiol. B **6**(1-2)**,** 143-8 (1990)

23. M. Burger et al., "Photodynamic diagnosis of non-muscle-invasive bladder cancer with hexaminolaevulinate cystoscopy: a meta-analysis of detection and recurrence based on raw data", Eur. Urol. **64**(5), 846-54 (2013)

24. A. Stenzl et al., "Hexaminolevulinate guided fluorescence cystoscopy reduces recurrence in patients with nonmuscle invasive bladder cancer", J. Urol. **184**(5), 1907-13 (2010)

25. J. Schmidbauer et al., "Improved detection of urothelial carcinoma in situ with hexaminolevulinate fluorescence cystoscopy", J. Urol. **171**(1), 135-8 (2004)

26. S.Daneshmand et al., "Hexaminolevulinate blue-light cystoscopy in non-muscle-invasive bladder cancer: review of the clinical evidence and consensus statement on appropriate use in the USA", Nat. Rev. Urol. **11**(10), 589-96 (2014)

27. K. Inoue et al., "Porphyrins as urinary biomarkers for bladder cancer after 5-aminolaevulinic acid (ALA) administration: the potential of photodynamic screening for tumors", Photodiagnosis Photodyn. Ther. **10**(4), 484-9 (2013)

28. M. Miyake et al., "Diagnostic approach for cancer cells in urine sediments by 5-aminolevulinic acid-based photodynamic detection of bladder cancer", Cancer Sci. **105**(5), 616-22 (2014)

29. M. C. Grimbergen, C. F. van Swol, T. G. Jonges, T. A. Boon & R. J. van Moorselaar, "Reduced specificity of 5-ALA induced fluorescence in photodynamic diagnosis of transitional cell carcinoma after previous intravesical therapy", Eur. Urol. **44**(1), 51-6 (2003)

30. E. R. Cordeiro, A. Anastasiadis, M. T. Bus, G. Alivizatos, J. J. de la Rosette & T. M. de Reijke, "Is photodynamic diagnosis ready for introduction in urological clinical practice?", Expert Rev. Anticancer Ther. **13**(6), 669-80 (2013)

31. M. Rink et al., "Hexyl aminolevulinate-guided fluorescence cystoscopy in the diagnosis and follow-up of patients with non-muscle-invasive bladder cancer: a critical review of the current literature", Eur. Urol. **64**(4), 624-38 (2013)

32. A. P. Castano, T. N. Demidova & M. R. Hamblin, "Mechanisms in photodynamic therapy: part one-photosensitizers, photochemistry and cellular localization", Photodiagnosis Photodyn. Ther. **1**(4), 279-93 (2004)

33. C. C. Cauberg Evelyne, J. J. de la Rosette & T. M. de Reijke, "Emerging optical techniques in advanced cystoscopy for bladder cancer diagnosis: A review of the current literature", Indian J. Urol. **27**(2), 245-51 (2011)

34. B. W. Henderson & T. J. Dougherty, "How does photodynamic therapy work?", Photochem. Photobiol. **55**(1), 145-57 (1992)

35. K. R. Martin & J. C. Barrett, "Reactive oxygen species as double-edged swords in cellular processes: low-dose cell signaling versus high-dose toxicity", Hum. Exp. Toxicol. **21**(2), 71-5 (2002)

36. S. Matsushita & J. Terao, Chapter "Singlet oxygen-initiated photooxidation of unsaturated fatty acid esters and inhibitory effects of tocopherols and β-carotene" in "Autooxidation in food and biological systems" by M. G. Simic & M. Karel, 27-44 (1980)

37. L. F. Agnez-Lima et al., "DNA damage by singlet oxygen and cellular protective mechanisms", Mutat. Res. **751**(1), 15-28 (2012)

38. A. Michaeli & J. Feitelson, "Reactivity of singlet xoygen toward amino acids and peptides", Photochem. Photobiol. **59**(3), 284-9 (1994)

39. D. Kessel, M. Castelli & J. Reiners, "Mechanism of PDT-induced mitochondrial photodamage", Proc. SPIE **4248** (2001)

40. D. Kessel & Y. Luo, "Mitochondrial photodamage and PDT-induced apoptosis", J. Photochem. Photobiol. B **42**(2), 89-95 (1998)

41. A. P. Castano, T. N. Demidova & M. R. Hamblin, "Mechanisms in photodynamic therapy: part two-cellular signaling, cell metabolism and modes of cell death", Photodiagnosis Photodyn. Ther. **2**(1), 1-23 (2005)

42. B. B. Noodt, K. Berg, T. Stokke, Q. Peng & J. M. Nesland, "Apoptosis and necrosis induced with light and 5-aminolaevulinic acid-derived protoporphyrin IX", Br. J. Cancer **74**(1), 22-9 (1996)

43. M. B. Ericson, A. M. Wennberg & O. Larko, "Review of photodynamic therapy in actinic keratosis and basal cell carcinoma", Ther. Clin. Risk Manag. **4**(1), 1-9 (2008)

44. D. C. Shackley et al., "Light penetration in bladder tissue: implications for the intravesical photodynamic therapy of bladder tumours", BJU Int. **86**(6), 638-43 (2000)

45. J. Y. Lee et al., "Efficacy and safety of photodynamic therapy for recurrent, high grade nonmuscle invasive bladder cancer refractory or intolerant to bacille Calmette-Guerin immunotherapy", J. Urol. **190**(4), 1192-9 (2013)

46. A. Francois et al., "How to avoid local side effects of bladder photodynamic therapy: impact of the fluence rate", J. Urol. **190**(2), 731-6 (2013)

47. F. A. Stewart, Y. Oussoren, J. A. le Poele, S. Horenblas & W. J. Mooi, "Functional and histological damage in the mouse bladder after photodynamic therapy", Br. J. Cancer **65**(6), 884-90 (1992)

48. B. Onal, U. Han, S. Yilmaz, F. Koybasioglu & U. Altug, "The use of urinary nuclear matrix protein 22 (NMP22) as a diagnostic adjunct to urine cytology for monitoring of recurrent bladder cancer - institutional experience and review", Diagn. Cytopathol. **43**(4), 307-14 (2015)

49. K. C. Halling & B. R. Kipp, "Bladder cancer detection using FISH (UroVysion assay)", Adv. Anat. Pathol. **15**(5), 279-86 (2008)

50. J. F. Nasuti, L. G. Gomella, M. Ismial & M. Bibbo, "Utility of the BTA stat test kit for bladder cancer screening", Diagn. Cytopathol. **21**(1), 27-9 (1999)

51. A. Schlake, P. L. Crispen, A. P. Cap, T. Atkinson, D. Davenport & D. M. Preston, "NMP-22, urinary cytology, and cystoscopy: a 1 year comparison study", Can. J. Urol. **19**(4), 6345-50 (2012)

52. J. Hosseini et al., "Detection of recurrent bladder cancer: NMP22 test or urine cytology?", Urol. J. **9**(1), 367-72 (2012)

53. M. Jovanovic et al., "Diagnostic value of the nuclear matrix protein 22 test and urine cytology in upper tract urothelial tumours", Urol. Int. **87**(2), 134-7 (2011)

54. S. Huber et al., "Nuclear matrix protein-22: a prospective evaluation in a population at risk for bladder cancer. Results from the UroScreen study", BJU Int. **110**(5), 699-708 (2012)

55. T. Behrens, A. Stenzl & T. Bruning, "Factors influencing false-positive results for nuclear matrix protein 22", Eur. Urol. **66**(5), 970-2 (2014)

56. H. Boman, H. Hedelin & S. Holmang, "Four bladder tumor markers have a disappointingly low sensitivity for small size and low grade recurrence", J. Urol. **167**(1), 80-3 (2002)

57. D. Hanahan & R. A. Weinberg, "The hallmarks of cancer", Cell **100**(1), 57-70 (2000)

58. D. Hanahan & R. A. Weinberg, "Hallmarks of cancer: the next generation", Cell **144**(5), 646-74 (2011)

59. O. Oge, N. Atsu, A. Sahin & H. Ozen, "Comparison of BTA stat and NMP22 tests in the detection of bladder cancer", Scand. J. Urol. Nephrol. **34**(6), 349-51 (2000)

60. S. Basu et al., "Cellular expression of cyclooxygenase, aromatase, adipokines, inflammation and cell proliferation markers in breast cancer specimen", PLoS One **10**(10) (2015)

61. J. Ose et al., "Inflammatory markers and risk of epithelial ovarian cancer by tumor subtypes: the EPIC cohort", Cancer Epidemiol. Biomarkers Prev. **24**(6), 951-61 (2015)
62. K. Echizen, O. Hirose, Y. Maeda & M. Oshima, "Inflammation in gastric cancer: Interplay of the COX-2/prostaglandin E2 and Toll-like receptor/MyD88 pathways", Cancer Sci. **107**(4), 391-7 (2016)
63. H. Zuo et al., "Interferon-y-induced inflammatory markers and the risk of cancer: the Hordaland health study", Cancer **120**(21), 3370-7 (2014)
64. G. Gakis, "The role of inflammation in bladder cancer", Adv. Exp. Med. Biol. **816**, 183-96 (2014)
65. A. Masson-Lecomte et al., "Inflammatory biomarkers and bladder cancer prognosis: a systematic review", Eur. Urol. **66**(6), 1078-91 (2014)
66. K. Saito & K. Kihara, "Rose of C-reactive protein in urological cancers: a useful biomarker for predicting outcomes", Int. J. Urol. **20**(2), 161-71 (2013)
67. M. Olivo, C. Y. Fu, V. Raghavan & W. K. Lau, "New frontier in hypericin-mediated diagnosis of cancer with current optical technologies", Ann. Biomed. Eng. **40**(2), 460-73 (2012)
68. M. Olivo, S. S. Lucky, J. F. Kent Mancer & W. K. Lau, "Altered expression of cell adhesion molecules leads to differential uptake of hypericin in urothelial cancer", Urol. Oncol. **30**(5), 624-34 (2012)
69. M. A. D'Hallewin, P. A. De Witte, E. Waelkens & L. Baert, "Fluorescence detection of flat bladder carcinoma in situ after intravesical instillation of hypericin", J. Urol. **164**(2), 349-51 (2000)
70. A. R. Wielgus et al., "Phototoxicity in human retinal pigment epithelial cells promoted by hypericin, a component of St. John's wort", Photochem. Photobiol. **83**(3), 706-13 (2007)
71. A. Kubin, H. G. Loew, U. Burner, G. Jessner, H. Kolbabek & F. Wierrani, "How to make hypericin water-soluble", Pharmazie **63**(4), 263-9 (2008)
72. A. Wirz, B. Meier & O. Sticher, "Solubility of hypericin in methanol and methanol-pyridine", Pharmazie **57**(8), 543-5 (2002)
73. A. Valizadeh et al., "Quantum dots: synthesis, bioapplications, and toxicity", Nanoscale Res. Lett. **7**(1), 480 (2012)
74. S. J. Rosenthal, J. C. Chang, O. Kovtun, J. R. McBride & I. D. Tomlinson, "Biocompatible quantum dots for biological applications", Chem. Biol. **18**(1), 10-24 (2011)
75. J. J. Liu, M. J. Droller & J. C. Liao, "New optical imaging technologies for bladder cancer: considerations and perspectives", J. Urol. **188**(2), 361-8 (2012)
76. S. Palmer, S. G. Sokolovski, E. Rafailov & G. Nabi, "Technologic developments in the field of photonics for the detection of urinary bladder cancer", Clin. Genitourin. Cancer **11**(4), 390-6 (2013)
77. Z. Ye et al., "A comparison of NBI and WLI cystoscopy in detecting non-muscle-invasive bladder cancer: A prospective, randomized and multi-center study", Sci. Rep. **5**, 10905 (2015)
78. M. Jecu et al., "NBI cystoscopy in routine urological practice - from better vision to improve therapeutic management", J. Med. Life **7**(2), 282-6 (2014)
79. E. Altobelli, D. V. Zlatev & J. C. Liao, "Role of narrow band imaging in management of urothelial carcinoma", Curr. Urol. Rep. **16**(8), 58 (2015)
80. J. Y. Lee et al., "A network meta-analysis of therapeutic outcomes after new image technology-assisted transurethral resection for non-muscle invasive bladder cancer: 5-aminolaevulinic acid fluorescence vs hexylaminolevulinate fluorescence vs narrow band imaging", BMC Cancer **15**, 566 (2015)
81. F. M. Lyng, D. Traynor, I. R. Ramos, F. Bonnier & H. J. Byrne, "Raman spectroscopy for screening and diagnosis of cervical cancer", Anal. Bioanal. Chem. **407**(27), 8279-89 (2015)

82. P. Kumar, T. Bhattacharjee, A. Ingle, G. Mary & C. M. Krishna, "Raman spectroscopy of experimental oral carcinogenesis: study on sequential cancer progression in hamster buccal pouch model", Technol. Cancer Res. Treat. (2015)

83. J. Zhao, H. Lui, S. Kalia & H. Zeng, "Real-time Raman spectroscopy for automatic in vivo skin cancer detection: an independent validation", Anal. Bioanal. Chem. **407**(27), 8373-9 (2015)

84. J. Desroches et al., "Characterization of a Raman spectroscopy probe system for intraoperative brain tissue classification", Biomed. Opt. Express **6**(7), 2380-97 (2015)

85. R. O. Draga et al., "In vivo bladder cancer diagnosis by high volume Raman spectroscopy", Anal. Chem. **82**(14), 5993-9 (2010)

86. B. W. de Jong et al., "Discrimination between nontumor bladder tissue and tumor by Raman spectroscopy", Anal. Chem. **78**(22), 7761-9 (2006)

87. A. Shapiro, O. N. Gofrit, G. Pizov, J. K. Cohen & J. Maier, "Raman molecular imaging: a novel spectroscopic technique for diagnosis of bladder cancer in urine specimens", Eur. Urol. **59**(1), 106-12 (2011)

88. E. Canetta et al., "Modulated Raman spectroscopy for enhanced identification of bladder tumor cells in urine samples", J. Biomed. Opt. **16**(3) (2011)

89. P. Crow, J. S. Uff, J. A. Farmer, M. P. Wright & N. Stone, "The use of Raman spectroscopy to identify and characterize transitional cell carcinoma in vitro", BJU Int. **93**(9), 1232-6 (2004)

90. I. Barman, N. C. Dingari, G. P. Singh, R. Kumar, S. Lang & G. Nabi, "Selective sampling using confocal Raman spectroscopy provides enhanced specificity for urinary bladder cancer diagnosis", Anal. Bioanal. Chem. **404**(10), 3091-9 (2012)

91. X. Chen, O. Nadiarynkh, S. Plotnikov & P. J. Campagnola, "Second harmonic generation microscopy for quantitative analysis of collagen fibrillar structure", Nat. Protoc. **7**(4), 654-69 (2012)

92. A. J. Walsh, R. S. Cook, J. H. Lee, C. L. Arteaga & M. C. Skala, "Collagen density and alignments in responsive and resistant trastuzumab-treated breast cancer xenografts", J. Biomed. Opt. **20**(2) (2015)

93. K. Tilbury & P. J. Campagnola, "Applications of second-harmonic generation imaging microscopy in ovarian and breast cancer", Perspect. Medicin. Chem. **7**, 21-32 (2015)

94. M. W. Conklin et al., "Aligned collagen is a prognostic signature for survival in human breast carcinoma", Am. J. Pathol. **178**(3), 1221-32 (2011)

95. J. Qiu et al., "Monitoring changes of tumor microenvironment in colorectal submucosa using multiphoton microscopy", Scanning **37**(1), 17-22 (2015)

96. A. Schueth, M. A. van Zandvoort, W. A. Buurman & G. A. van Koeveringe, "Murine bladder imaging by 2-photon microscopy: an experimental study of morphology", J. Urol. **192**(3), 973-80 (2014)

97. S. Mukherjee et al., "Human bladder cancer diagnosis using multiphoton microscopy", Proc. SPIE Int. Soc. Opt. Eng. **7161** (2009)

98. R. Cicchi et al., "Time- and spectral-resolved two-photon imaging of healthy bladder mucosa and carcinoma in situ", Opt. Express **18**(4), 3840-9 (2010)

99. G. Thomas, J. van Voskuilen, H. C. Gerritsen & H. J. Sterenborg, "Advances and challenges in label-free nonlinear optical imaging using two-photon excitation fluorescence and second harmonic generation for cancer research", J. Photochem. Photobiol. B **141**, 128-38 (2014)

100. N. Ramanujam, "Fluorescence spectroscopy of neoplastic and non-neoplastic tissues", Neoplasia **2**(1-2), 89-117 (2000)

101. E. N. Harvey, "Bioluminescence and fluorescence in the living world", Am. J. Physiol. **77**(3), 555-61 (1926)

102. R. R. Alfano, B. B. Das, J. Cleary, R. Prudente & E. J. Celmer, "Light sheds light on cancer - distinguishing malignant tumours from benign tissues and tumours", Bull N Y Acad. Med. **67**(2), 143-50 (1991)

103. K. Moriichi et al., "Quantification of autofluorescence imaging can accurately and objectively assess the severity of ulcerative colitis", Int. J. Colorectal Dis. **30**(12), 1639-43 (2015)

104. Y. H. Krul-Poel et al., "Vitamin D status is associated with skin autofluorescence in patients with type 2 diabetes mellitus: a preliminary report", Cardiovasc. Diabetol. **14**, 89 (2015)

105. F. Batioglu, S. Demirel & E. Ozmert, "Fundus autofluorescence imaging in age-related macular degeneration", Semin. Ophthalmol. **30**(1), 65-73 (2015)

106. M. Scheer et al., "Autofluorescence imaging in recurrent oral squamous cell carcinoma", Oral Maxillofac. Surg. **20**(1), 27-33 (2016)

107. A. Almeida, S. Kaliki & C. L. Shields, "Autofluorescence of intraocular tumours", Curr. Opin. Ophthalmol. **24**(3), 222-32 (2013)

108. G. Succo et al., "Direct autofluorescence during CO2 laser surgery of the larynx: can it really help the surgeon?", Acta Otorhinolaryngol. Ital. **34**(3), 174-83 (2014)

109. Q. He et al., "Value of autofluorescence imaging videobronchoscopy in detecting lung cancers and precancerous lesions: a review", Respir. Care **58**(12), 2150-9 (2013)

110. K. H. Awan, P. R. Morgan & S. Warnakulasuriva, "Assessing the accuracy of autofluorescence, chemiluminescence and toluidine blue as diagnostic tools for oral potentially malignant disorders - a clinicopathological evaluation", Clin. Oral Investig. **19**(9), 2267-72 (2015)

111. M. A. D'Hallewin, L. Baert & H. Vanherzeele, "In vivo fluorescence detection of human bladder carcinoma without sensitizing agents", J. Am. Paraplegia Soc. **17**(4), 161-4 (1994)

112. O. Aboumarzouk et al., "Laser-induced autofluorescence spectroscopy: can it be of importance in detection of bladder lesions?", Photodiagnosis Photodyn. Ther. **12**(1), 76-83 (2015)

113. F. Koenig, F. J. McGovern, A. F. Althauen, T. F. Deutsch & K. T. Schomacker, "Laser induced autofluorescence diagnosis of bladder cancer", J. Urol. **156**(5), 1597-601 (1996)

114. W. Zheng, W. Lau, C. Cheng, K. C. Soo & M. Olivo, "Optimal excitation-emission wavelengths for autofluorescence diagnosis of bladder tumours", Int. J. Cancer **104**(4), 477-81 (2003)

115. I. Rokahr et al., "Optical detection of human urinary bladder carcinoma utilising tissue autofluorescence and protoporphyrin IX-induced fluorescence following low dose ALA instillation", Proc. SPIE **2627** (1995)

116. C. Schafauer et al., "Detection of bladder urothelial carcinoma using in vivo noncontact, ultraviolet excited autofluorescence measurements converted into simple color coded images: a feasibility study", J. Urol. **190**(1), 271-7 (2013)

117. M. Anidjar et al., "Laser induced autofluorescence diagnosis of bladder tumors: dependence on the excitation wavelength", J. Urol. **156**(5), 1590-6 (1996)

118. M. A. D'Hallewin, L. Bezdetnaya & F. Guillemin, "Fluorescence detection of bladder cancer: a review", Eur. Urol. **42**(5), 417-25 (2002)

119. D. Zaak et al., "Ultraviolet-excited (308 nm) autofluorescence for bladder cancer detection", Urology **60**(6), 1029-33 (2002)

120. M. Szygula et al., "Fluorescent diagnosis of urinary bladder cancer-a comparison of two diagnostic modalities", Photodiagnosis Photodyn. Ther. **1**(1), 23-6 (2004)

121. M. Anidjar et al., "Laer-induced autofluorescence of normal and tumor bladder cells and tissues", 241-247 of volume 286 of "Analytical use of fluorescent probes in oncology" published by Springer (1996)

122. J. R. Albani, "Origin of tryptophan fluorescence lifetimes part 1. Fluorescence lifetimes origin of tryptophan free in solution", J. Fluoresc. **24**(1), 93-104 (2014)

123. M. S. Islam, M. Honma, T. Nakabayashi, M. Kinjo & N. Ohta, "pH dependence of the fluorescence lifetime of FAD in solution and in cells", Int. J. Mol. Sci. **14**(1), 1952-63 (2013)

124. J. R. Lakowicz, H. Szmacinski, K. Nowaczyk & M. L. Johnson, "Fluorescence lifetime imaging of free and protein-bound NADH", Proc. Natl. Acad. Sci. U. S. A. **89**(4), 1271-5 (1992)

125. L. Marcu, "Fluorescence lifetime techniques in medical applications", Ann. Biomed. Eng. **40**(2), 304-31 (2012)

126. R. Cicchi & F. S. Pavone, Non-linear fluorescence lifetime imaging of biological tissues", Anal. Bioanal. Chem. **400**(9), 2687-97 (2011)

127. W. Becker, "Fluorescence lifetime imaging - techniques and applications", J. Microsc. **247**(2), 119-36 (2012)

128. G. T. Kennedy et al., "A fluorescence lifetime imaging scanning confocal endomicroscope", J. Biophotonics **3**(1-2), 103-7 (2010)

129. S. Coda et al. "Fluorescence lifetime spectroscopy of tissue autofluorescence in normal and diseased colon measured ex vivo using a fibre-optic probe", Biomed. Opt. Express **5**(2), 515-38 (2014)

130. Y. Sun et al., "Fluorescence lifetime imaging microscopy: in vivo application to diagnosis of oral carcinoma", Opt. Lett. **34**(13), 2081-3 (2009)

131. A. J. Bower et al., "Label-free in vivo cellular-level detection and imaging of apoptosis", J. Biophotonics **10.1002** (2016)

132. T. Nakajima et al., "Fluorescence-lifetime molecular imaging can detect invisible peritoneal ovarian tumours in bloody ascites", Cancer Sci. **105**(3), 308-14 (2014)

133. S. Dochow et al., "Combined fiber probe for fluorescence lifetime and Raman spectroscopy", Anal. Bioanal. Chem. **407**(27), 8291-301 (2015)

134. C. Fujiyama et al., "Human bladder cancer invasion model using rat bladder in vitro and its use to test mechanisms and therapeutic inhibitors of invasion", Br. J. Cancer **84**(4), 558-64 (2001)

135. D. A. Janssen et al., "A new straightforward ex vivo organoid bladder mucosal model for preclinical research", J. Urol. **190**(1), 341-9 (2013)

136. C. L. Varley & J. Southgate, "Organotypic and 3D reconstructed cultures of the human bladder and urinary tract", Methods Mol. Biol. **695,** 197-211 (2011)

137. K. Nakamura, C. Fujiyama, Y. Tokuda, H. Sugihara & Z. Masaki, "Bladder cancer cell implantation in reconstructed bladder in vitro: a model of tumour recurrence", BJU Int. **89**(1), 119-25 (2002)

138. H. Sato & T. Takino, "Coordinate action of membrane-type matrix metalloproteinase-a (MT1-MMP) and MMP-2 enhances pericellular proteolysis and invasion", Cancer Sci. **101**(4), 843-7 (2010)

139. G. B. Fields, "Interstitial collagen catabolism", J. Biol. Chem. **288**(13), 8785-93 (2013)

140. E. Wieczorek, W. Wasowicz, J. Gromadzinska & E. Reszka, "Functional polymorphisms in the matrix metalloproteinase genes and their association with bladder cancer risk and recurrence: a mini-review", Int. J. Urol. **21**(8), 744-52 (2014)

141. C. A. Fernandez et al., "A novel approach to using matrix metalloproteinases for bladder cancer", J. Urol. **182**(5), 2188-94 (2009)

142. T. Szarvas et al., "Urinary matrix metalloproteinase-7 level is associated with the presence of metastasis in bladder cancer", BJU Int. **107**(7), 1069-73 (2011)

143. M. Fang, J. Yuan, C. Peng & Y. Li, "Collagen as a double-edged sword in tumor progression", Tumour Biol. **35**(4), 2871-82 (2014)

144. E. Karousou et al., "Collagen VI and hyaluronan:the common role in breast cancer", Biomed Res. Int. **2014** (2014)

145. V. Prabhu et al., "Objective assessment of endogenous collagen in vivo during tissue repair by laser induced fluorescence", PLoS One **9**(5) (2014)

146. Y. Pu, W. Wang, G. Tang & R. R. Alfano, "Changes of collagen and nicotinamide adenine dinucleotide in human cancerous and normal prostate tissues studied using native fluorescence spectroscopy with selective excitation wavelength", J. Biomed. Opt. **15**(4) (2010)

147. R. Drezek et al., "Understanding the contributions of NADH and collagen to cervical tissue fluorescence spectra: modeling, measurements, and implications", J. Biomed. Opt. **6**(4), 385-96 (2001)

148. K. J. Aitken & D. J. Bagli, "The bladder extracellular matrix. Part I: architecture, development and disease", Nat. Rev. Urol. **6**(11), 596-611 (2009)

149. J. N. Iuliano et al., "Metastatic bladder cancer cells distinctively sense and respond to physical cues of collagen fibril-mimetic nanotopography", Exp. Biol. Med. (Maywood) **240**(5), 601-10 (2015)

150. X. Jiang, I. Luttrell, D. Y. Li, C. C. Yang & K. Chitaley, "Altered bladder function in elastin-deficient mice at baseline and in response to partial bladder outlet obstruction", BJU Int. **110**(3), 413-9 (2012)

151. J. Z. Cui et al., "Quantification of aortic and cutaneous elastin and collagen morphology in Marfan syndrome by multiphoton microscopy", J. Struct. Biol. **187**(3), 242-53 (2014)

152. P. L. Tong et al., "A quantitative approach to histopathological dissection of elastin-related disorders using multiphoton microscopy", Br. J. Dermatol. **169**(4), 869-79 (2013)

153. A. Hansch et al., "Autofluorescence spectroscopy in whole organs with a mobile detector system", Acad. Radiol. **11**(11), 1229-36 (2004)

154. L. Zhang et al., "Tryptophan as the fingerprint for distinguishing aggressiveness among breast cancer cell lines using native fluorescence spectroscopy", J. Biomed. Opt. **19**(3) (2014)

155. L. A. Sordillo, P. P. Sordillo, Y. Budansky, Y. Pu & R. R. Alfano, "Differences in fluorescence profiles from breast cancer tissues due to changes in relative tryptophan content via energy transfer: tryptophan content correlates with histologic grade and tumor size but not with lymph node metastases", J. Biomed. Opt. **19**(12) (2014)

156. B. Banerjee et al., "Tryptophan autofluorescence imaging of neoplasms of the human colon", J. Biomed. Opt. **17**(1) (2012)

157. N. D. Kirkpatrick et al., "Endogenous fluorescence spectroscopy of cell suspensions for chemopreventive drug monitoring", Photochem. Photobiol. **81**(1), 125-34 (2005)

158. A. Khadjavi et al., "A high-throughput assay for the detection of Tyr-phosphorylated proteins in urine of bladder cancer patients", Biochem. Biophys. Acta. **1830**(6), 3664-9 (2013)

159. E. Birben, U. M. Sahiner, C. Sackesen, S. Erzurum & O. Kalayci, "Oxidative stress and antioxidant defense", World Allergy Organ J. **5**(1), 9-19 (2012)

160. T. S. Blacker & M. R. Duchen, "Investigating mitochondrial redox state using NADH and NADPH autofluorescence", Free Radic. Biol. Med. **100**, 53-65 (2016)

161. T. S. Blacker et al., "Separating NADH and NADPH fluorescence in live cells and tissues using FLIM", Nat. Commun. **29** (2014)

162. J. A. Palero et al., "In vivo monitoring of protein-bound and free NADH during ischemia by nonlinear spectral imaging microscopy", Biomed. Opt. Express **2**(5), 1030-9 (2011)

163. A. Ruck, C. Hauser, S. Mosch & S. Kalinina, "Spectrally resolved fluorescence lifetime imaging to investigate cell metabolism in malignant and nonmalignant oral mucosa cells", J. Biomed. Opt. **19**(9) (2014)

164. M. C. Skala et al., "In vivo multiphoton fluorescence lifetime imaging of protein-bound and free NADH in normal and pre-cancerous epithelia", J. Biomed. Opt. **12**(2) (2007)

165. K. Drozdowicz-Tomsia et al., "Multiphoton fluorescence lifetime imaging microscopy reveals free-to-bound NADH ratio changes associated with metabolic inhibition", J. Biomed. Opt. **19**(8) (2014)

166. K. Steenkeste et al., "Ex vivo fluorescence imaging of normal and malignant urothelial cells to enhance early diagnosis", Photochem. Photobiol. **83**(5), 1157-66 (2007)

167. J. Horilova, B. Cunderlikova & A. Marcek Chorvatova, "Time- and spectrally resolved characteristics of flavin fluorescence in U87MG cancer cells in culture", J. Biomed. Opt. **20**(5) (2015)

168. Z. Ablonczy et al., "The utilization of fluorescence to identify the components of lipofuscin by imaging mass spectroscopy", Proteomics **14**(7-8), 936-44 (2014)

169. A. Stojanovic, A. E. Roher & M. J. Ball, "Quantitative analysis of lipofuscin and neurofibrillary tangles in the hippocampal neurons of Alzheimer disease brains", Dementia **5**(5) (1994)

170. A. C. Grey, R. K. Crouch, Y. Koutalos, K. L. Schey & Z. Ablonczy, "Spatial localization of A2E in the retinal pigment epithelium", Invest. Ophthalmol. Vis. Sci. **52**(7), 3926-33 (2011)

171. M. Perse, R, Injac & A. Erman, "Oxidative status and lipofuscin accumulation in urothelial cells of bladder in aging mice", PLoS One **8**(3) (2013)

172. J. M. Watson et al., "Two-photon excited fluorescence imaging of endogenous contrast in a mouse model of ovarian cancer", Lasers Surg. Med. **45**(3), 155-66 (2013)

173. M. Inaguma & K. Hashimoto, "Porphyrin-like fluorescence in oral cancer: in vivo fluorescence spectral characterization of lesions by use of near-ultraviolet excited autofluorescence diagnosis system and separation of fluorescent extracts by capillary electrophoresis", Cancer **86**(11), 2201-11 (1999)

174. H. N. da Rocha Filho et al., "Expression of genes involved in porphyrin biosynthesis pathway in the human renal cell carcinoma", J. Fluoresc. **25**(5), 1363-9 (2015)

175. L. C. Courrol et al., "Study of blood porphyrin spectral profile for diagnosis of tumor progression", J. Fluoresc. **17**(3), 289-92 (2007)

176. M. H. Bellini et al., "Correlation between autofluorescence intensity and tumor area in mice bearing renal cell carcinoma", J. Fluoresc. **18**(6), 1163-8 (2008)

177. K. Koenig & H. Schneckenburger, "Laser-induced autofluorescence for medical diagnosis", J. Fluoresc. **4**(1), 17-40 (1994)

178. S. N. Datta, C. S. Loh, A. J. MacRobert, S. D. Whatley & P. N. Matthews, "Quantitative studies of the kinetics of 5-aminolaevulinic acid-induced fluorescence in bladder transitional cell carcinoma", Br. J. Cancer **78**(8), 1113-8 (1998)

179. K. S. Litvinova, D. A. Rogatkin, O. A. Bychenkov & V. I. Shumskiy, "Chronic hypoxia as a factor of enhanced autofluorescence of endogenous porphyrins in soft biological tissues", Proc. SPIE **7547** (2010)

180. A. C. Croce & G. Bottiroli, "Autofluorescence spectroscopy and imaging: a tool for biomedical research and diagnosis", Eur. J. Histochem. **58**(4), 2461 (2014)

181. I. Miranda-Lorenzo et al., "Intracellular autofluorescence: a biomarker for epithelial cancer stem cells", Nat. Methods **11**(11), 1161-9 (2014)

182. V. Masilamani et al., "Cancer detection by native fluorescence of urine", J. Biomed. Opt. **15**(5) (2010)

183. A. Birkova et al., "Changes in urine autofluorescence in ovarian cancer patients", Neoplasma **61**(6), 724-31 (2014)

184. Z. Steffekova, A. Birkova, A. Bomba & M. Marekova, "Early diagnosis of colorectal cancer in rats with DMH induced carcinogenesis by means of urine autofluorescence analysis", Photochem. Photobiol. **90**(3), 682-5 (2014)

185. M. Al-Salhi, V. Masilamani, T. Vijmasi, H. Al-Nachawati & A. P. VijayaRaghavan, "Lung cancer detection by native fluorescence spectra of body fluids - a preliminary study", J. Fluoresc. **21**(2), 637-45 (2011)

186. A. G. Anwer, P. M. Sandeep, E. M. Goldys & S. Vemulpad, "Distinctive autofluorescence of urine samples from individuals with bacteriuria compared with normals", Clin. Chim. Acta **401**(1-2), 73-5 (2009)

187. M. G. Vander Heiden, L. C. Cantley & C. B. Thompson, "Understanding the Warburg effect: the metabolic requirements of cell proliferation", Science **324**(5930), 1029-33 (2009)

188. A. Chiarugi, C. Dolle, R. Felici & M. Ziegler, "The NAD metabolome - a key determinant of cancer cell biology", Nat. Rev. Cancer **12**(11), 741-52 (2012)

189. A. Varone et al., "Endogenous two-photon fluorescence imaging elucidates metabolic changes related to enahnced glycolysis and glutamine consumption in precancerous epithelial tissues", Cancer Res. **74**(11), 3067-75 (2014)

190. J. H. Ostrander et al., "Optical redox ratio differentiates breast cancer cell lines based on estrogen receptor status", Cancer Res. **70**(11), 4759-66 (2010)

191. Q. Liu et al., "Compact point-detection fluorescence spectroscopy system for quantifying intrinsic fluorescence redox ratio in brain cancer diagnostics", J. Biomed Opt. **16**(3) (2011)

192. L. A. Sordillo, Y. Pu, P. P. Sordillo, Y. Budansky & R. R. Alfano, "Optical spectral fingerprints of tissues from patients with different breast cancer histologies using a novel fluorescence spectroscopic device", Technol. cancer Res. Treat. **12**(5), 455-61 (2013)

193. I. Georgakoudi et al., "NAD(P)H and collagen as in vivo quantitative fluorescent biomarkers of epithelial precancerous changes", Cancer Res. **62**(3), 682-7 (2002)

194. I. B. C. Matheson & J. Lee, "Reaction of chemical acceptors with singlet oxygen produced by direct laser excitation", Chem. Phys. Lett. **7**(4), 475-6 (1970)

195. S. D. Zakharov & A. I. Ivanov, "Light-oxygen effect in cells and its potential applications in tumour therapy", Lasers in Medicine **29**(12) (1999)

196. S. G. Sokolovski et al., "Infrared laser pulse triggers increased singlet oxygen production in tumour cells", Sci. Rep. **3**(3484) (2013)

197. F. Anquez, I. El Yazidi-Belkoura, S. Randoux, P. Suret & E. Courtade, "Cancerous cell death from sensitizer free photoactivation of singlet oxygen", Photochem. Photobiol. **88**(1), 167-74 (2012)

198. S. L. Jacques, "Optical properties of biological tissues: a review", Phys. Med. Biol. **58**(11), 37-61 (2013)

199. A. V. Dunaev et al., "Individual variability analysis of fluorescence parameters measured in skin with different levels of nutritive blood flow", Med. Eng. Phys. **37**(6), 574-83 (2015)

200. T. G. Phan & A. Bullen, "Practical intravital two-photon microscopy for immunological research: faster, brighter, deeper", Immunol. Cell Biol. **88**(4), 438-44 (2010)

201. I. V. Meglinski & S. J. Matcher, "Quantitative assessment of skin layers absorption and skin reflectance spectra simulation in the visible and near-infrared spectral regions", Physiol. Meas. **23**(4), 741-53 (2002)

202. S. Prince & S. Malarvizhi, "Monte Carlo simulation of NIR diffuse reflectance in the normal and diseased human breast tissues", Biofactors **30**(4), 255-63 (2007)

203. S. Palmer, K. Litvinova, A. Dunaev, S. Fleming, D. McGloin & G. Nabi, "Changes in autofluorescence based organoid model of muscle invasive urinary bladder cancer", Biomed. Opt. Express **7**(4), 1193-1200 (2016)

204. A. Mayevsky & B. Chance, "Oxidation-reduction states of NADH in vivo: from animals to clinical use", Mitochondrion **7**(5), 330-9 (2007)

205. N. Akbar et al., "In vivo noninvasive measurement of skin autofluorescence biomarkers relate to cardiovascular disease in mice", J. Microsc. **255**(1), 42-8 (2014)

206. O. D. Smirnova, D. A. Rogatkin & K. S. Litvinova, "Collagen as in vivo quantitative fluorescent biomarkers of abnormal tissue changes", J. Innov. Opt. Health Sci. **5**(2) (2012)

207. A. Mayevsky & B. Chance, "Oxidation-reduction states of NADH in vivo: from animals to clinical use", Mitochondrion **7**(5), 330-9 (2007)

208. A. V. Dunaev et al., "Substantiation of medical and technical requirements for noninvasive spectrophotometric diagnostic devices", J. Biomed. Opt. **18**(10) (2013)

209. V. Rajan, B. Varghese, T. G. van Leeuwen & W. Steenbergen, "Review of methodological developments in laser Doppler flowmetry", Lasers Med. Sci. **24**(2), 269-83 (2009)

210. M. K. Schilling et al., "Evaluation of laser doppler flowmetry for the study of benign and malignant gastric blood flow in vivo", Gut **45**(3), 341-5 (1999)

211. M. Kragh, B. Quistorff, M. R. Horsman & P. E. Kristiansen, "Acute effects of vascular modifying agents in solid tumours assessed by noninvasive laser Doppler flowmetry and near infrared spectroscopy", Neoplasia **4**(3), 263-7 (2002)

212. J. E. Batista, J. R. Wagner, K. M. Azadzoi, R. J. Krane & M. B. Siroky, "Direct measurement of blood flow in the human bladder", J. Urol. **155**(2), 630-3 (1996)

213. A. Humeau-Heurtier & M. Klonizakis, "Processing of laser Doppler flowmetry signals from healthy subjects and patients with varicose veins: information categorisation approach based on intrinsic mode function and entropy computation", Med. Eng. Phys. **37**(6), 553-9 (2015)

214. P. Irwin & N. T. Galloway, "Impaired bladder perfusion in interstitial cystitis: a study of blood supply using laser Doppler flowmetry", J. Urol. **149**(4), 890-2 (1993)

215. A. V. Dunaev et al., "Investigating tissue respiration and skin microhaemocirculation under adaptive changes and the synchronization of blood flow and oxygen saturation rhythms", Physiol. Meas. **35**(4), 607-21 (2014)

216. W. R. Wilson & M. P. Hay, "Targeting hypoxia in cancer therapy", Nat. Rev. Cancer **11**(6), 393-410 (2011)

217. S. Larre et al., "Screening for bladder cancer: rationale, limitations, whom to target and perspectives", Eur. Urol. **63**(6), 1049-58 (2013)

218. B. J. Schmitz-Drager et al., "Molecular markers for bladder cancer screening, early diagnosis, and surveillance: the WHO/ICUD consensus", Urol. Int. **94**(1), 1-24 (2015)

219. I. Karaoglu, A. G. van der Heijden & A. J. Witjes, "The role of urine markers, white light cystoscopy and fluorescence cystoscopy in recurrence, progression and follow-up of non-muscle invasive bladder cancer", World J. Urol. **32**(3), 651-9 (2014)

220. J. Parker and P. E. Spiess, "Current and emerging bladder cancer urinary biomarkers.", Scientific World Journal, 1103-12 (2011)

221. M. C. Skala et al., "*In vivo* multiphoton microscopy of NADH and FAD redox states, fluorescence lifetimes, and cellular morphology in precancerous epithelia", PNAS **104**(49), 19494-19499 (2007)

222. A. Walsh, R. S. Cook, B. Rexer, C. L. Arteaga & M. C. Skala, "Optical imaging of metabolism in HER2 overexpressing breast cancer cells", Biomed. Opt. Express **3**(1), 75-85 (2012)

223. A. V. Kuznetsov, R. Margreiter, A. Amberger, V. Saks & M. Grimm, "Changes in mitochondrial redox state, membrane potential and calcium precede mitochondrial dysfunction in doxorubicin-induced cell death", Biochem. Biophys. Acta **1813**(6), 1144-52 (2011)

224. B. Kierdaszuk, I. Gryczynski, A. Modrak-Wojcik, A. Bzowska, D. Shugar & J. R. Lakowicz, "Fluorescence of tyrosine and tryptophan in proteins using one- and two-photon excitation", Photochem. Photobiol. **61**(4), 319-324 (1995)

225. S. Palmer, K. Litvinova, E. U. Rafailov & G. Nabi, "Detection of urinary bladder cancer cells using redox ratio and double excitation wavelengths autofluorescence", Biomed. Opt. Express **6**(3), 977-86 (2015)

226. B. Thorell, "Flow-cytometric monitoring of intracellular flavins simultaneously with NAD(P)H levels", Cytometry **4**(1), 61-5 (1983)

227. V. L. Mosiman, B. K. Patterson, L. Canterero & C. L. Goolsby, "Reducing cellular autofluorescence in flow cytometry: an in situ method", Cytometry **30**(3), 151-6 (1997)

228. B. Barlogie et al., "Flow cytometry in clinical cancer research", Cancer Res. **43**(9), 3982-97 (1983)
229. C. A. Palmeira, P. A. Oliveira, F. Seixas, M. A. Pires, C. Lopes & L. Santos, "DNA image cytometry in bladder cancer: state of the art", Anticancer Res. **28**(1B), 443-50 (2008)
230. H. Ikehata & T. Ono, "The mechanisms of UV mutagenesis", J. Radiat. Res. **52**(2), 115-25 (2011)
231. J. R. Mourant, J. P. Freyer & T. M. Johnson, "Measurements of scattering and absorption in mammalian cell suspensions", Proc. SPIE **2679** (1996)
232. R. Rajasekaran, P. R. Aruna, D. Koteeswaran, G. Bharanidharan, M. Baludavid & S. Ganesan, "Steady-state and time-resolved fluorescence spectroscopic characterisation of urine of healthy subjects and cervical cancer patients", J. Biomed. Opt. **19**(3), 37003 (2014)
233. A. A. Salahudeen & C. J. Kuo, "Toward recreating colon cancer in human organoids", Nat. Med. **21**(3), 215-6 (2015)
234. D. Gao et al., "Organoid cultures derived from patients with advanced prostate cancer", Cell **159**(1), 176-87 (2014)
235. J. Leighton, R. Tchao & K. L. Tencer, "Organoid structure of normal rat bladder in unilaminar and bilaminar histophysiologic gradient culture: methods and obervations", In Vitro **3**(1), 183-97 (1984)
236. A. Huygens, A. R. Kamuhabwa, T. Roskams, B. Van Cleynenbreugel, H. Van Poppel & P. A. de Witte, "Permeation of hypericin in spheroids composed of different grade transitional cell carcinoma cell lines and normal human urothelial cells", J. Urol. **174**(1), 69-72 (2005)
237. A. J. Walsh et al., "Quantitative optical imaging of primary tumor organoid metabolism predicts drug response in breast cancer", Cancer Res. **74**(18), 5184-94 (2014)
238. H. Maeda, "The enhanced permeability and retention (EPR) effect in tumor vasculature: the key role of tumor-selective macromolecular drug targeting", Adv. Enzyme Regul. **41**, 189-207 (2001)
239. L. Shi et al., "Deep two-photon microscopic imaging through brain tissue using the second singlet state from fluorescent agent chlorophyll a in spinach leaf", J. Biomed. Opt. **19**(6) (2014)
240. I. Freitas et al., "Iron accumulation in mammary tumor suggests a tug of war between tumor and host for the microenvironment", Anticancer Res. **27**(5A), 3059-65 (2007)
241. D. M. Harris & J. Werkhaven, "Endogenous porphyrin fluorescence in tumours", Lasers Surg. Med. **7**(6), 467-472 (2005)
242. I. Rafailov et al., "A novel excitation-emission wavelength model to facilitate the diagnosis of urinary bladder diseases", Proc. SPIE **9303** (2015)
243. I. E. Rafailov et al., "Computational model of bladder tissue based on its measured optical properties", J. Biomed. Opt. **21**(2) (2016)
244. J. Hooda et al., " Enhanced Heme Function and Mitochondrial Respiration Promote the Progression of Lung Cancer Cells", PLoS One **8**(5) (2013)
245. H. Sies, " Strategies of antioxidant defense", Eur. J. Biochem. **215**(2), 213-9 (1993)
246. M. K. Kuimova, G. Yahioglu & P. R. Quilby, " Singlet oxygen in a cell: spatially dependent lifetimes and quenching rate constants", J. Am. Chem. Soc. **131**(1), 332-40 (2009)
247. E. Skovsen, J. W. Snyder, J. D. Lambert & P. R. Ogilby, " Lifetime and diffusion of singlet oxygen in a cell", J. Phys. Chem. B. **109**(18), 8570-3 (2005)
248. N. Shirasu, S. O. Nam & M. Kuroki, " Tumor-targeted Photodynamic Therapy", Anticancer Res. **33**(7), 2823-31 (2013)
249. M. D. Savellano & T. Hasan, " Photochemical targeting of epidermal growth factor receptor: a mechanistic study", Clin. Cancer Res. **11**(4), 1658-68 (2005)

250. E. O. Serebrovskaya, E. F. Edelweiss, O. A. Stremovskiy, K. A. Lukyanov, D. M. Chudakov & S. M. Devev, " Targeting cancer cells by using an antireceptor antibody-photosensitizer fusion protein", Proc. Natl. Acad. Sci. U. S. A. **106**(23), 9221-5 (2009)

251. E. D. Reich, R. Bachor, K. Miller, K. Koenig & R. E. Hautmann, " Liposome-administered tetramethylhematoporphyrin (TMHP) as a photodynamic agent for bladder tumor cells", Proc. SPIE **1881**(126) (1993)

252. T. Y. Ohulchanskyy et al., " Organically modified silica nanoparticles with covalently incorporated photosensitizer for photodynamic therapy of cancer.", Nano. Lett. **7**(9), 2835-42 (2007)

253. P. Juzenas et al., " Quantum dots and nanoparticles for photodynamic and radiation therapies of cancer.", Adv. Drug Deliv. Rev. **60**(15), 1600-14 (2008)

254. J. Ge et al., " A graphene quantum dot photodynamic therapy agent with high singlet oxygen generation.", Nat. Commun. **5:**4596 (2014)

255. K. Ogawa & Y. Kobuke, " Two-Photon Photodynamic Therapy by Water-Soluble Self-Assembled Conjugated Porphyrins.", Biomed. Res. Int. **125658** (2013)

256. C. L. Saw, P. W. Heng, W. W. Chin, K. C. Soo & M. Olivo, " Enhanced photodynamic activity of hypericin by penetration enhancer N-methyl pyrrolidone formulations in the chick chorioallantoic membrane model", Cancer Lett. **238**(1), 104-10 (2006)

257. S. D. Zakharov et al., " Structural rearrangements in the aqueous phase of cell suspensions and protein solutions induced by a light-oxygen effect", Quant. Electronics **33**(2) (2003)

258. S. Elmore, " Apoptosis: A Review of Programmed Cell Death", Toxicol. Pathol. **35**(4), 495-516 (2007)

259. P. A. Muller & K. H. Vousden, " p53 mutations in cancer", Nat. Cell Biol. **15**(1), 2-8 (2013)

260. A. M. Puzio-Kuter et al., " Inactivation of p53 and Pten promotes invasive bladder cancer", Genes Dev. **23**(6), 675-80 (2009)

261. W. X. Zong & C. B. Thompson, " Necrotic death as a cell fate", Genes Dev. **20**(1), 1-15 (2006)

262. C. M. Whitacre, T. H. Satoh, L. Y. Xue, N. H. Gordon & N. L. Oleinick, " Photodynamic therapy of human breast cancer xenografts lacking caspase-3.", Cancer Lett. **179**(1), 43-9 (2002)

263. F. A. Fitzpatrick, " Inflammation, carcinogenesis and cancer.", Int. Immunopharmacol. **1**(9-10), 1651-67 (2001)

264. R. N. Apte et al., " The involvement of IL-1 in tumorigenesis, tumor invasiveness, metastasis and tumor-host interactions.", Cancer Metastasis Rev. **25**(3), 387-408 (2006)

265. F. H. van Duijnhoven, R. I. Aalbers, J. P. Rovers, O. T. Terpstra & P. J. Kuppen, " The immunological consequences of photodynamic treatment of cancer, a literature review", Immunobiology **207**(2), 105-13 (2003)

266. P. Mroz, A. Szokalska, M. X. Wu & M. R. Hamblin, " Photodynamic Therapy of Tumors Can Lead to Development of Systemic Antigen-Specific Immune Response.", PLoS One **5**(12) (2010)

267. T. M. Sitnik & B. W. Henderson, " Effects of fluence rate on cytoxicity during photodynamic therapy.", Proc. SPIE **2972** (1997)

268. J. B. Jeeva & M. Singh, "Reconstruction of optical scanned images of inhomogeneities in biological tissues by Monte Carlo simulation", Comput. Biol. Med. **60**, 92-9 (2015)

269. S. Wang, J. Zhao, H. Lui, Q. He, J. Bai & H. Zeng, "Monte Carlo simulation of in vivo Raman spectral measurements of human skin with a multi-layered tissue optical model", J. Biophotonics **7**(9), 703-12 (2014)

270. V. P. Hart & T. E. Doyle, "Simulation of diffuse photon migration in tissue by a Monte Carlo method derived from the optical scattering of spheroids", Appl. Opt. **52**(25), 6220-9 (2013)

271. W. F. Cheong, S. A. Prahl & A. J. Welch, "A review of the optical properties of biological tissues", J. Quant. Electronics **26**(12), 2166-2185 (1990)

272. A. N. Bashkatov et al., "Optical properties of mucous membrane in the spectral range 350-2000nm", Opt. Spectroscopy **97**(6), 978-983 (2004)

273. H. W. Wang, Y. H. Wei & H. W. Guo, "Reduced nicotinamide adenine dinucleotide (NADH) fluorescence for the detection of cell death", Anticancer Agents Med. Chem. **9**(9), 1012-7 (2009)

274. Q. Wang, H. Yang, A. Agrawal, N. S. Wang & T. J. Pfefer, "Measurement of internal tissue optical properties at ultraviolet and visible wavelengths: Development and implementation of a fibreoptic-based system", Opt. Express **16**(12), 8685-703 (2008)

275. O. A'Amar, F. H. Guillemin, H. Begorre & E. Yvroud, "Autofluorescence spectroscopy of normal and pathological tissues of the bladder", Proc. SPIE **P63600/3197**, 41-49 (1997)

276. I. Georgakoudi et al., "Fluorescence, reflectance, and light-scattering spectroscopy for evaluating dysplasia in patients with Barrett's esophagus", Gastroenterology **120**(7), 1620-9 (2001)

277. J. L. Sandell & T. C. Zhu, "A review of in-vivo optical properties of human tissues and its impact on PDT", J. Biophotonics **4**(11-12), 773-87 (2011)

278. G. J. Muller & A. Roggan, "Dosimetry and computer based irradiation planning for laser-induced interstitial thermotherapy (LITT)" in "Laser-induced interstitial thermotherapy", SPIE Press, 114-159 (1995)

279. H. J. van Staveren, J. F. Beek, M. Keijzer & W. M. Star, "Integrating sphere effect in whole bladder wall photodynamic therapy at violet, green, and red wavelengths", Proc. SPIE **2323** (1995)

280. Z. Huang et al., "Laser-induced autofluorescence microscopy of normal and tumor human colonic tissue", Int. J. Oncol. **24**(1), 59-63 (2004)

281. P. Laguna et al., "Keratin expression profiling of transitional epithelium in the painful bladder syndrome/interstitial cystitis", Am. J. Clin. Pathol. **125**(1), 105-10 (2006)

282. Y. Wu & J. Y. Qu, "Autofluorescence spectroscopy of epithelial tissues", J. Biomed. Opt. **11**(5), 054023 (2006)

283. G. M. Palmer & N. Ramanujam, "Monte Carlo-based inverse model for calculating tissue optical properties. Part 1: Theory and validation on synthetic phantoms", Appl. Opt. **45**(5), 1062-71 (2006)

284. S. A. Prahl, M. J. C. van Gemert & A. J. Welch, "Determining the optical properties of turbid media by using the adding-doubling method", Appl. Opt. **32**(4), 559-568 (1993)